

Journal “Radioelectronics. Nanosystems. Information Technologies” (abr. RENSIT) publishes original articles, reviews and brief reports, not previously published, on topical problems in **radioelectronics (including biomedical) and fundamentals of information, nano- and biotechnologies**

**and adjacent areas of physics and mathematics.**

Designed for **researchers, graduate students, physics students of senior courses and teachers.**

It turns out **2 times a year** (that includes 2 issues)

Authors of journal are academicians, corresponding members and foreign members of Russian Academy of Natural Sciences (RANS) and their colleagues,

as well as other russian and foreign authors on presentation of their manuscripts by the members of RANS, which can be obtained by authors before sending articles to editors.

And also after its receiving - on recommendation of a member of editorial board of journal, or another member of Academy of Natural Sciences, that gave her opinion on article at request of editor.

The editors will accept articles in both **Russian and English** languages.

Articles are internally peer reviewed (**double-blind peer review**) by members of the Editorial Board.

Some articles undergo external review, if necessary.

Journal RENSIT is included in the **AJ and DB VINITI RAS** (<http://www.viniti.ru>), in the international abstracts database - **Ulrich’s International Periodicals Directory**, (USA, New York, <http://www.ulrichsweb.com>);

and DB **Russian Science Citation Index (RSCI)** [http://elibrary.ru/project\\_risc.asp](http://elibrary.ru/project_risc.asp)).

**Full-text content** is posted in the DB of the **Russian Scientific Electronic Library** - information resource on the Internet <http://elibrary.ru> and is available for registered users.

On journal's website <http://www.rensit.ru> posted metadata publications and **RENSIT - English version** (cover-to-cover translation) of journal, which is a party to **CrossRef**.

---

The founder - the **Russian Academy of Natural Sciences**  
Publisher - Publishing Center of the Russian Academy of Natural Sciences  
Publisher Address: 119002 Moscow, per. Sivtsev Vrazhek 29/16

## CONTENTS

### RADIOELECTRONICS

NONSTATIONARY REFLECTION OF A SUPERSHORT ELECTROMAGNETIC PULSES FROM THE LAYERED STRUCTURES

Alexey V. Trofimov, Anatoly V. Kozar' ..... 107

### NANOSYSTEMS

DIRAC MATERIAL GRAPHENE

Elena F. Sheka ..... 131

CAN GRAPHENE BILAYERS BE THE MEMBRANE MIMETIC MATERIALS? ION CHANNELS IN GRAPHENE-BASED NANOSTRUCTURES

Oleg V. Gradov, Margarita A. Gradova ..... 154

THE DISPERSIONS OF NANOPARTICLES IN WATER-ORGANIC SOLVENTS AS THE BASIS FOR THE SILVER NANO-INK FOR 2D PRINTING

Sergey V. Tkachev, Vitalii P. Kim, Alexey E. Kushnir, Denis Yu. Kornilov, Sergey P. Gubin ..... 171

### INFORMATION TECHNOLOGIES

THE USE OF PARALLEL PROGRAMMING TECHNOLOGIES FOR MODELING SEISMIC WAVES USING GRID-CHARACTERISTIC METHOD

Andrey M. Ivanov, Nikolay I. Khokhlov, Igor B. Petrov ..... 185

### NON-LINEAR THERMODYNAMICS

DETECTION AND INVESTIGATION OF ANOMALOUS (UNDAMPED) THERMAL WAVES

Vladimir I. Vysotskii, Alla A. Kornilova, Alexander O. Vasilenko, Mikhail V. Vysotskiy, Efim I. Hait, Nailia H. Volkova ..... 196

### FRACTALS IN PHYSICS

FOURIER IMAGES QUASISYMMETRY OF GENERALIZED TRIADIC KOCH PREFRACTALS

Galina V. Arzamastseva, Mikhail G. Evtikhov, Feodor V. Lisovsky, Ekaterina G. Mansvetova ..... 207

### THEORY OF EVOLUTION

EVOLUTIONARY ASPECTS OF THE GEL APPEARANCE AND ITS FUNCTIONS IN THE CELL CYTOPLASM

Alexander R. Zaritskii, Vladimir I. Grachev, Galina V. Zaitseva, Marina N. Kirichenko ..... 215

### CHRONICLE

GRAFENIKA (GRAPHENICS)

RUSSIAN GUBIN'S SEMINAR (MOSCOW)

Elena Yu. Buslaeva ..... 223

## RUSSIAN ACADEMY OF NATURAL SCIENCES

DEPARTMENT OF  
RADIOELECTRONICS,  
NANOPHYSICS AND  
INFORMATION TECHNOLOGIES  
PROBLEMS



# RENSIT:

RADIOELECTRONICS.  
NANOSYSTEMS.  
INFORMATION  
TECHNOLOGIES.

2016, VOL. 8, no. 2

FOUNDED IN 2009 - PRINT  
SINCE 2014 - PRINT&ON-LINE  
2 ISSUES PER YEAR  
MOSCOW

*Editor-in-Chief*

VLADIMIR I. GRACHEV  
grachev@cplire.ru

*Executive Secretary*

ROSTISLAV V. BELYAEV  
belyaev@cplire.ru

EDITORIAL COUNCIL

*Chairman*

Alexander S. Ilushin

*Deputy Chairman*

Sergey P. Gubin

Anatoly V. Andreev

Vitaly A. Barishpolets

Oleg V. Betzkiy

Vladimir A. Bushuev - *deputy chief*

Vladimir A. Cherepenin

Alexander S. Dmitriev

Yury K. Fetisov

Yaroslav A. Ilushin

Anatoly V. Kozar

Vladimir V. Kolesov - *deputy chief*

Alla A. Kornilova

Vladimir A. Makarov

Andrey I. Panas

Igor B. Petrov

Vyacheslav S. Rusakov

Alexander S. Sigov

Evgeny S. Soldatov

Lkhamsuren Enkhtor (Mongolia)

Yoshiyuki Kavazoe (Japan)

Kayrat K. Kadyrzhanov (Kazakhstan)

Peter Paul Mac Kenn (USA)

Deleg Sangaa (Mongolia)

Andre Skirtach (Belgium)

Enrico Verona (Italy)

Eugeny V. Ushpuras (Republic of Lithuania)

ISSN 2414-1267

The journal on-line is registered by the Ministry of Telecom and Mass Communications of the Russian Federation. Certificate E1 no. FS77-60275 on 19.12.2014

All rights reserved. No part of this publication may be reproduced in any form or by any means without permission in writing from the publisher.

©RANS 2016

EDITORIAL BOARD ADDRESS

218-219 of, 7 b., 11, Mokhovaya str.,

125009 Moscow, Russian Federation,

TEL. +7 495 629 3368

FAX +7 495 629 3678 GRACHEV

# NONSTATIONARY REFLECTION OF A SUPERSHORT ELECTROMAGNETIC PULSES FROM THE LAYERED STRUCTURES

Aleksey V. Trofimov, Anatoly V. Kosar'

Lomonosov Moscow State University, <http://www.msu.ru>

1/2, Leninskie Gory, 119991 Moscow, Russian Federation

[av.trofimov@physics.msu.ru](mailto:av.trofimov@physics.msu.ru), [avk@phys.msu.ru](mailto:avk@phys.msu.ru)

*Abstract.* Is carried out the theoretical and numerical study of non-stationary reflection of short and supershort electromagnetic pulses from a single-layer and multilayer interference structures, created test bench to measure of non-stationary reflection amplitude-modulated signal from the layered structure. It is shown that the envelope of the reflected signal substantially changes its appearance in the presence of even small losses in the non-reflection layers of the multilayer structure, the amplitude reflection coefficient depends linearly on the magnitude of the losses. At low loss in the layers of structure the envelope can be approximately described by the derivative of the N-incident signal envelope. Obtained the exact and approximate formulas that allow to calculate the characteristics of the multilayer interference structure, highly reflective matching the load to the waveguide, the waveguide due to a strong dispersion. It is shown that in multilayer interference structures with strong waveguide dispersion there is a significant increase in the amplitude and duration of the pulses of non-stationary reflection.

*Keywords:* electromagnetic ultrashort pulses of microwave, layered structure with strong losses and waveguide dispersion, transient reflectivity, the envelope of the reflected signal, highly reflective and load matching structure, multilayer interference filters

UDC 544.77, 53.098

*Bibliography* – 49 references

*Received* 13.12.2016

*RENSIT*, 2016, 8(2):107-130

DOI: 10.17725/rensit.2016.08.107

## CONTENTS

1. INTRODUCTION (107)
  2. NONSTATIONARY REFLECTION OF THE ELECTROMAGNETIC PULSE FROM THE SINGLE-LAYER STRUCTURE (111)
    - 2.1. Influence of layer losses on non-stationary reflection (111)
    - 2.2. The reflection from the layers  $N\lambda/2$  (116)
    - 2.3. Influence of waveguide dispersion (118)
    - 2.4. Experimental study of the signal reflection from the half-wave filter (119)
      - 2.4.1. Influence of losses in layer on the nonstationary reflection (120)
      - 2.4.2. Influence of layer thickness on the nonstationary reflection (121)
      - 2.4.3. Influence of the waveguide dispersion on the nonstationary reflection (121)
  3. NONSTATIONARY REFLECTION BY A STRONG WAVEGUIDE DISPERSION (123)
  4. NONSTATIONARY REFLECTION IN THE MULTILAYER INTERFERENCE FILTERS (125)
  5. CONCLUSION (127)
- REFERENCES (127)

## 1. INTRODUCTION

The main trend in the development of optical and microwave devices in the last decennary is a continuous decrease in the duration of their use in the electromagnetic pulses. Supershort electromagnetic pulses are increasingly used both for research and industry [1-3]. In connection with this generation are particularly relevant issues detection and control of such pulses. This tendency is observed in the literature devoted to research in the optical [4-14], in the millimeter and submillimeter ranges [15, 16].

Optical pulses having a duration of tens of femtoseconds to attoseconds units are used in the study of ultrafast processes in biology [1] and chemistry [2]. Large instantaneous pulse power is used in the study of nonlinear processes in semiconductor materials and devices [3]. In the

millimeter wave band the electromagnetic pulses of short duration have been applied too, in the first place - in radiolocation [15, 16].

Marked trends in the development of microwave and optical engineering lead to the need to create the new and to improvement the already existing devices to control of ultrashort electromagnetic pulses.

To control the signals of long duration multilayer interference structures are widely used (MIS). Today, MIS is actively used in devices operating both in the millimeter, and in the optical wavelength range. Methods of their analysis and synthesis worked out quite well.

Attempts to use MIS to control ultrashort pulses revealed the presence of a number of new effects [11, 17-20], not observed in the interaction with MIS signals of long duration. In the interaction of an electromagnetic signal with a multilayer structure interference of waves reflected from its layers, forms the past and reflected signals. At high incident signal duration time for establishing a stationary process in a multilayer structure is negligible compared with the duration of the signal, so the influence on the formation process of unsteady reflected and transmitted signals is not considered. For short pulses, which are defined as pulses with a duration of up to 100 periods of the electromagnetic field oscillations of [21], the duration of the transition process can be comparable to the duration of the signal, so the influence of non-stationary process accounting for forming the reflected and transmitted signals becomes necessary.

To date, research on the interaction of ultrashort pulses with multilayer interference structures are actively conducted in various directions. Deep enough to study the interaction of ultrashort pulses with mirrors on the basis of the MIS. Created multilayer mirrors, capable of not only effectively reflect short electromagnetic pulses, and even reduce the duration of the reflected signal, as compared to the incident signal [4-7].

The interaction of ultrashort pulses with non-reflective type structures on the basis of the MIS, in particular - with multilayer interference filters covered less extensively, although in this area a large number of publications [8-14] appeared in the last ten years.

Despite the high intensity of research of interaction of ultrashort electromagnetic pulses from the MIS, there are a number of phenomena that are not well understood and covered both in the domestic and foreign literature. One of such phenomena include the phenomenon of non-stationary reflection of electromagnetic pulses of short duration of the MIS. Lack of research on this subject in the first place, due to the peculiarities of observation of the phenomenon. For example, in the study of the processes occurring in the interaction of short electromagnetic pulses with multilayer mirrors, analyze non-stationary reflection process is quite difficult, as the intensity of the reflected signal from the primary mirror is many times higher signal intensity, formed as a result of non-stationary reflection.

In the vast majority of publications devoted to the issue of the interaction of electromagnetic pulses of short duration with non-reflective-type multi-layered structures, the reflected signal is regarded as undesirable. Therefore, the synthesis MIS reflected signal (including pulses having a generated during unsteady reflection) to be suppressed, typically numerical optimization algorithms, without analyzing the mechanism of its occurrence.

One of the first studies on the effects of non-stationary reflection of ultrashort pulses from the MIS non-reflective type, have been [17, 18, 22-24]. They first introduced the concept of "non-stationary reflection" and analyzed the processes taking place in the reflection of the electromagnetic pulse of short duration of the multi-layer structure.

As is well known [25], when electromagnetic wave is incident on a layered structure as a result of interference in its layers after a certain

time  $t_s$  in the stationary structure established electromagnetic field distribution. The amplitude of the wave reflected from the structure will tend to zero as a result of the negative interference of waves in the antireflection multilayer structure. However, if for some time  $t_p$  - less time to establish a stationary field distribution in  $t_s$  layers - a change of parameters (amplitude or phase) of the incident ultrashort pulse is disturbed amplitude-phase balance of interfering in a multilayer structure waves varies stationary distribution of the wave field in the structure  $t_p$  and it appears in the reflected signal over time. Thus, changes in the amplitude of the wave incident on the multilayer structure will change the amplitude of the signal reflected from the multilayer structure. In case, if no signal is stationary - for example, if the wave reflected from the antireflection structure or wave passed through the multilayer mirror - will be reflected (for antireflective structure) or past (for multilayer mirror) pulse signal of corresponding duration.

In [17] the analysis of non-stationary process of reflection was made on an example of a quarter of the film deposited on the substrate. An analytical solution for the amplitude envelope of the signal reflected from the structure with amplitude modulation in the following form

$$U(t) = \frac{r_0}{1-r_0^2} \left[ \sum_{n=1}^{\infty} \frac{1}{n!} \frac{d^n A(t)}{dt^n} (2k+1) \frac{T}{2} \right] e^{i\omega t}, \tag{1}$$

where  $U(t)$  - the envelope of the amplitude of the reflected wave,  $r_0$  - Fresnel reflection coefficient of the film material,  $A(t)$  - the envelope of the amplitude of the incident signal,  $T$  - wave period in the pulse oscillation,  $k = 0, 1, 2, \dots$  - the multiplicity of the film thickness of a quarter wavelength,  $\omega$  - angular frequency. In [17, 24] have been calculated according to the amplitude of the reflected signals at the drop of the bleaching pulse structure with trapezoidal and Gaussian envelope (**Fig. 1a, b**). Obtained in this work for some types of antireflection of periodic structures analytical expression can be used to analyze the time course-limited pulse amplitude.

In [18] analyzed the interaction of electromagnetic pulses with the phase and frequency modulation of a broad class of antireflective structures - thin-film interference aligner (TIS). Amplitudnospektralnyh theory, structural and invariant properties TIS was developed in [26, 27]. The paper deals with super-Gaussian pulse with an envelope type:

$$E_0 = A(t)e^{-i\varphi(t)} \tag{2}$$

$$A(t) = e^{\left(\frac{t}{\tau}\right)^{2p}}, \tag{3}$$

$\varphi(t)$  - a real time-varying phase. Assuming the quadratic phase modulation  $\varphi(t) = \alpha t^2/2$  [28, 29] (the most interesting from the point of view of applications) for the complex amplitude of the reflected wave was obtained by the following expression:

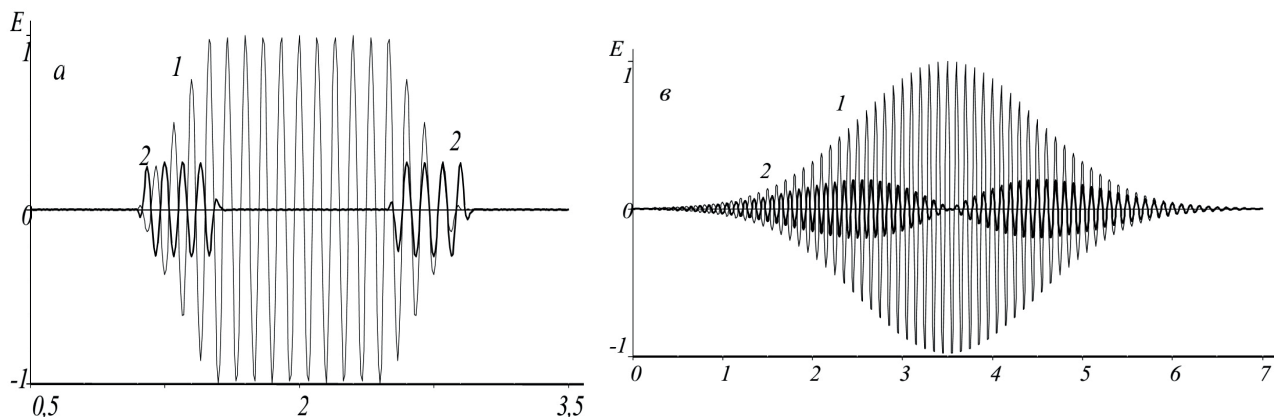


**Рис. 1.** Напряженности электрического поля отраженного сигнала для падающего импульса с трапецидальной огибающей (а) и с супергауссовой огибающей (1) падающего сигнала; 2) отраженного сигнала [24].

$$E_r(t) = r_0 \frac{A(t)e^{-i\varphi(t)} - A(t-\Delta t)e^{-i\varphi(t-\Delta t)}}{1 - r_0 e^{i[\varphi(t) - \varphi(t-\Delta t)]}}, \quad (4)$$

here  $\Delta t$  - transit time wave twice the film thickness. The expression for the envelope of the reflected wave of the FM pulse has the form [18]:

$$E_{or}(t) = |r_0| \frac{A(t)^2 - 2A(t)A(t-\Delta t)\cos(\varphi(t)) + A^2(t-\Delta t)}{1 - 2r_0^2 \cos(\varphi(t)) + r_0^4} \quad (5)$$

The results obtained in [18] analytical expressions allow you to select the time evolution of the phase modulation (FM) pulse. This follows from the fact that the analytical expression (4) is retained for the amplitude modulation of the phase information as a function of  $\varphi(t)$ . If using direct methods of correlation or received envelopes of the incident pulse  $A(t)$  and  $E_0$  is reflected, then, using (4), it is possible to determine the phase function  $\varphi(t)$ .

**Fig. 2** shows the results of calculation of the spectral method forms the reflected pulses from the FM film deposited on a substrate with  $ns = 3.42$ . In both cases, the pulse duration  $\tau$  was 7 ns, the carrier wavelength  $\lambda = 1.5$  microns; Gaussian pulse  $\alpha\tau^2 = 1$ , for a super-Gaussian pulse  $\alpha\tau^4 = 4$ , in the expression (3) the parameter  $p = 3$ . The envelope of the reflected pulses  $E_{0r}$  built according to the formula (5). The results obtained with the Fourier transform of the incident pulse taken as:

$$E(t) = A(t)e^{-i(\omega_0 t + \varphi(t))}. \quad (6)$$

In practice, often there are situations when the FM pulses acquire a flat or almost flat top. For this case, [18] the following ratio

$$E_r = \frac{r_0}{1 - r_0^2} \varphi(t). \quad (7)$$

This result (7) points to the prospects of the use of non-stationary reflection phenomenon to convert electromagnetic pulses.

In [18] it is noted that the TIS can be used to analyze the time dependence of the FM phase pulses and to produce ultrashort pulses with the above properties.

The phenomenon of non-stationary reflection effect causing his physical characteristics (absence of background reflection of the incident radiation, adequate dependence of its amplitude-time characteristics of the shape of the incident pulse and the physical properties of the framing structure of the media), not only relatively easy to obtain ultrashort electromagnetic pulses, but also to develop methods of analysis and the pulse parameters of transient processes in layered media.

It should be noted that the studies mentioned have not been given attention to a number of important details, such as - the influence of losses in the fibers of the structure and the process for the dispersion of a nonstationary reflection. Moreover, studies were analytical or numerical character -without experimental studies. All this causes concern and the need for further study of the phenomenon of non-stationary reflection, as well as the opportunities and conditions for its implementation.

The aim of this work is to conduct a detailed theoretical and experimental studies of the phenomenon of non-stationary reflection of

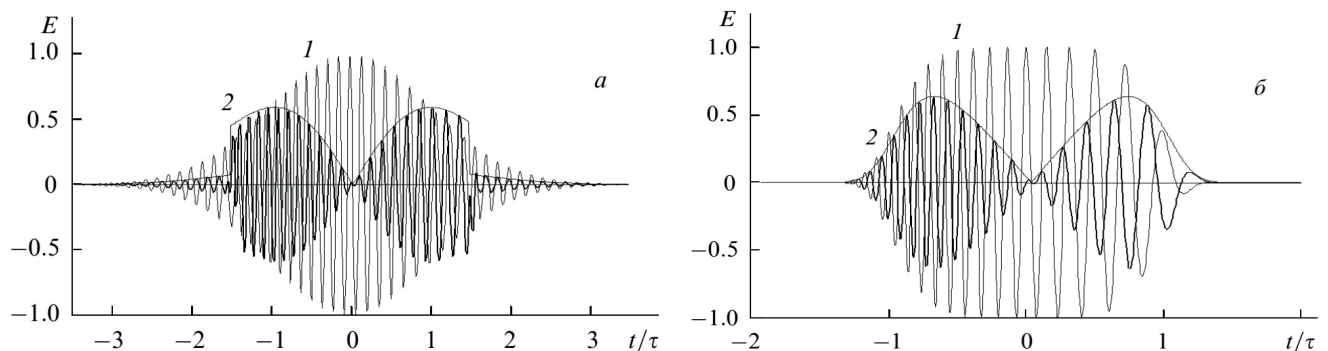


**Рис. 2.** Фазомодулированные падающий (1) и отраженный (2) импульсы с гауссовой (а) и супергауссовой (б) огибающими; отраженные импульсы увеличены в 7 раз (а) и в 2 раза (б) [24].

short and ultrashort pulses of electromagnetic interference multilayer structures, including an analysis of the impact of a strong waveguide dispersion, irregularities and losses in a multilayer structure on the formation of the reflected signal.

**2. NONSTATIONARY REFLECTION OF ELECTROMAGNETIC PULSE FROM THE SINGLE-WALLED STRUCTURES**

**2.1. THE IMPACT OF LOSSES IN THE LAYER ON THE NON-STATIONARY REFLECTION**

As used strukturny monolayer non-reflecting in a stationary mode dielectric layer whose thickness is a multiple of half wave optical thickness, placed between two identical characteristics in wave environments. This structure is the simplest implementation of a half-wave interference filter.

For the analysis of wave propagation through the layered structure of the losses the method of impedance characteristics [30-32]. At the same time the concept of impedance is introduced as the ratio of the tangential components of the electric and magnetic fields in this section of the layered structure.

Let some environments, which is a plane-parallel layer to the complex relative permittivity  $\epsilon = \epsilon' + i\epsilon''$  and thickness  $d$ , completely fills the cross section of a waveguide with a characteristic impedance of the  $Z_0$ , a regular on both sides. For further consideration, we introduce the index  $j$ , indicating the number of the layer. In this indexing will produce so that closest to the emission layer the source will have a maximum index. **Fig. 3** shows the direction of propagation of electromagnetic waves from the source and designated impedance layers  $Z_j$ , and input impedances at the boundary layers  ${}^jZ_{in}$ . The expressions for the propagation constant wave  $\gamma_j$  and  $Z_j$  impedance look like:

$$\gamma_j = \alpha_j + i\beta_j, \tag{8}$$

$$\alpha_j = \frac{2\pi}{\lambda} \sqrt{\frac{\sqrt{\epsilon_j''^2 + \Lambda_j^2} - \Lambda_j}{2}}; \beta_j = \frac{2\pi}{\lambda} \sqrt{\frac{\sqrt{\epsilon_j''^2 + \Lambda_j^2} + \Lambda_j}{2}}, \tag{9}$$

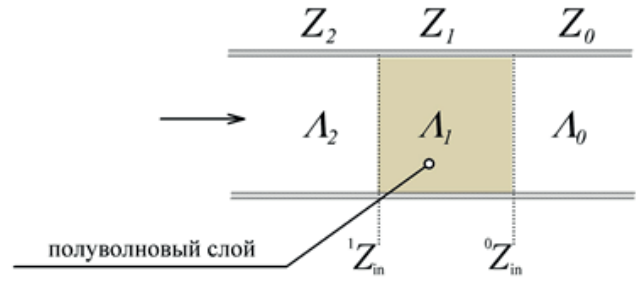


Рис. 3. Диэлектрический слой в волноводе.

$$Z_j = C_j + iD_j, \tag{10}$$

$$C_j = \sqrt{\frac{\sqrt{\epsilon_j''^2 + \Lambda_j^2} + \Lambda_j}{2(\epsilon_j''^2 + \Lambda_j^2)}}; D_j = \sqrt{\frac{\sqrt{\epsilon_j''^2 + \Lambda_j^2} - \Lambda_j}{2(\epsilon_j''^2 + \Lambda_j^2)}}, \tag{11}$$

For the analysis of multilayer structures installed in the waveguide must also take into account the effect of the waveguide dispersion. In this case:

$$\Lambda_j = \epsilon_j' - \left(\frac{\lambda}{\lambda_c}\right)^2, \tag{12}$$

$\lambda_c$  - critical wavelength in the waveguide mode for H10,  $\lambda_c = 2a$ ,  $a$  - the size of the wide wall of the waveguide,  $\lambda$  - the wavelength in free space.

The expression for the reflection coefficient at the interface between the waveguide and the portion of the free portion of the dielectric layer with the set can be written as:

$$r = \frac{{}^1Z_{in} - Z_0}{{}^1Z_{in} + Z_0}, \tag{13}$$

$$Z_0 = \frac{1}{\sqrt{1 - \frac{\lambda}{\lambda_c}}}. \tag{14}$$

The value  ${}^1Z_{in}$ , in the expression for the reflection coefficient, which can be calculated using the following recurrence relation:

$${}^1Z_{in} = \frac{{}^0Z_{in} + Z_1 th(\gamma_1 d)}{Z_1 + {}^0Z_{in} th(\gamma_1 d)} Z_1. \tag{15}$$

In this case, an isolated layer set in regular waveguide:

$${}^0Z_{in} = Z_0. \tag{16}$$

We estimate the impact of losses in a secluded dielectric half-wavelength layer on a range of non-stationary reflection amplitude-modulated signal. The imaginary part of the relative permittivity  $\epsilon''$ , is responsible for the

loss included in the expression for the layer of the impedance (10, 11) and the expression for the propagation constant (8, 9). To simplify the problem, take into account that the vast majority of materials used in the synthesis of multilayer structures exhibit low loss  $\epsilon''/\epsilon' \ll 1$ . Considering the loss of a plate with small, we introduce a small amount  $\xi_1 = \frac{\epsilon_1''}{\Lambda_1} \ll 1$ . Then, after simple transformations for the input impedance and the propagation constant, up to the first order, we obtain the following expressions:

$$Z_1 \approx \frac{1}{\sqrt{\Lambda_1}} + i \frac{\xi_1}{2\sqrt{\Lambda_1}}; \quad (17)$$

$$\gamma_1 \approx \frac{2\pi}{\lambda} \sqrt{\Lambda_1} \left( \frac{\xi_1}{2} + i \right). \quad (18)$$

For the reflection coefficient of the dielectric plate by substituting (17) and (18) into (15) and then into (13) we have:

$$r \approx \xi_1 \frac{\pi}{\sqrt{\Lambda_1}} \frac{(1 - Z_0^2 \Lambda_1)}{4Z_0}. \quad (19)$$

From the relation (19) shows that the losses in the case of small amplitude reflection coefficient depends linearly on the magnitude of losses in the layer. In addition, the reflection coefficient is purely real value and therefore, small losses in the fiber will not influence the phase relation between multipath waves, i.e. phase of the reflected signal pattern will be formed in the same manner as in the case of no loss.

The numerical calculation of the dependence of the reflection coefficient of a half-wave layer, mounted in a rectangular waveguide, provided  $v_0/v_s \approx 1.3$ , where  $v_s$  - critical frequency. Accounting waveguide dispersion leads to the fact that at the same offset from the center frequency  $v_0$  reflection coefficient has different values. The calculation showed that the minimum reflectance remains on the same frequency for different values of the imaginary part of the relative permittivity of the dielectric layer ( $\epsilon = 2 + 0.0i$ ,  $\epsilon = 2 + 0.01i$  and  $\epsilon = 2 + 0.05i$ ), which indicates the constancy phase balance in the layer of the interfering waves. The

negative value of  $r$  in the expression (19) shows that reflection from the layer occurs in antiphase with respect to the incident wave and the phase of the reflection coefficient  $\varphi_r = \pi$ . Thus, in the case of small losses in the half-wavelength layer violation occurs only balance the amplitude of the interfering wave, which in turn gives rise to a reflected signal.

The process of forming a reflected signal at falling amplitude modulated signal on a half-wave layer is lossy. considered as an example of a symmetric trapezoidal pulse with linear edges. Let the wave is incident on the half wave layer having a relative dielectric constant  $\epsilon = 2 + 0.05i$ . We assume that the length of the trapezoidal pulse  $\tau$  a lot more time passes wave double layer thickness. At the same time as a result of non-stationary reflection of electromagnetic pulse propagating toward the incident wave will be formed. We define a thickness equal to  $d = 30$  mm layer and the carrier frequency are chosen so that the layer will be a half-wave. **Fig. 4** shows the result of calculating the finite-difference time-domain method (Finite Difference Time Domain, FDTD, or Yee algorithm) [33, 34] the field strength of the reflected pulse  $E_r(t)$ . For clarity, the reflected signal amplitude is increased by 10 times.

Note that, when calculating the finite-difference time-domain method, and during the actual experiment, no ability to capture the reflected signal directly at the interface of the dielectric layer. From the moment the signal generation prior to fixation of the reflected pulse will take some time. There is always, however small, the distance of space between the generator and the dielectric layer, which is to overcome the wave before impact. In the case of the finite difference method is - the distance between the plane on which the initial value of the field  $E(t)$ , and the dielectric layer. As a rule, it is not less than 10 spatial grid cells, which are calculated. The presence of free space described by the site leads to an additional phase incursion between incident and reflected signals.

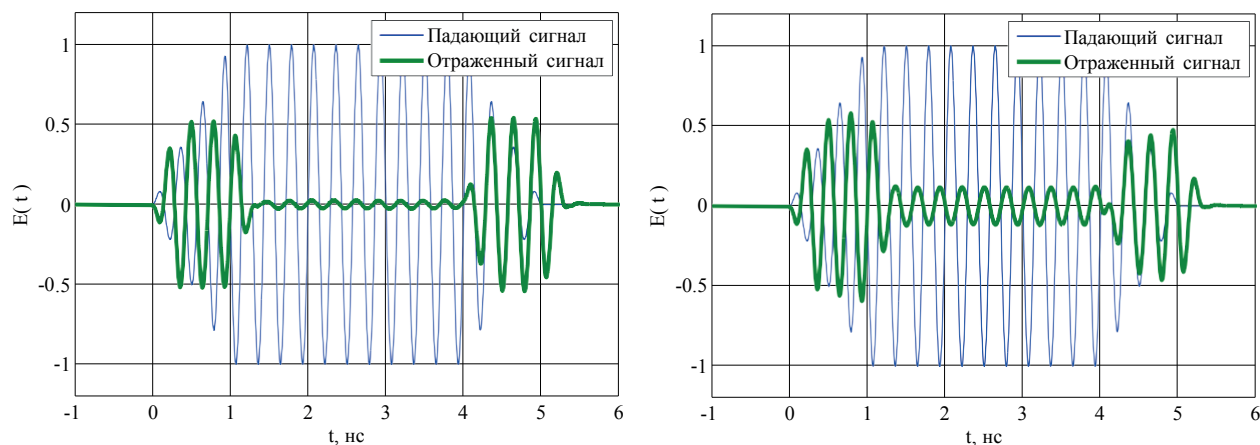


Рис. 4. Отраженные и падающие сигналы, рассчитанные методом конечных разностей во временной области, для случаев: а) отсутствия потерь в полуволновом слое, ( $\epsilon = 2 + 0.0i$ ); б) наличия потерь в полуволновом слое, ( $\epsilon = 2 + 0.05i$ ).

This phase shift complicates the analysis of the results, so for clarity in Fig. 4, it is compensated in such a way that the beginning of the reflected signal is combined with the beginning of the incident pulse.

For the analysis of the loss of influence on the process of unsteady reflection calculation  $E_r(t)$  of the field was conducted both in view of the losses in the half-wavelength layer, and excluding these losses. In the second case it was assumed that  $\epsilon'' = 0$ . In the absence of loss (Fig. 4a), according to the relation (19) layer is non-reflective structure. Therefore, in the area of the incident pulse of constant amplitude of the reflected signal is negligible. Thus pulses reflected in the falling signal edges, have a rectangular envelope (Fig. 4a).

The presence of even small losses in the layer leads to disruption of the amplitude balance of the interfering waves, whereby there is the appearance of the reflected signal in the incident pulse of constant amplitude, as shown in Fig. 4b. When taking into account losses, the pulses generated in the non-stationary reflection in the area of the incident signal fronts, changing its shape as compared to the pulses in the case of absence of loss (Fig. 4b). Impulse formed in the leading edge is different from the pulse trailing edge region, which is not observed in Fig. 4a. The reflected signal in the case of losses in the fiber, and in the case of the dielectric layer

without the loss consists of two pulses which are in antiphase.

We draw attention to a feature in the incident signal trailing edge in Fig. 4b. Despite the existence of loss at the time of the trailing edge of the reflection, there is a time when the amplitude of the reflected signal to zero, and the reflected signal phase changes by  $\pi$ . This shows that is currently running the amplitude balance condition interfering in the wave structure.

Impulse trapezoidal envelope is a convenient mathematical model for the analysis of non-stationary process of reflection, but in practice, these signals are used very rarely. This is due to the fact that the preparation of linear front in ultrashort pulse is quite a challenge. On the other hand trapezoidal pulse is a piecewise continuous function, which imposes additional restrictions when trying to pilot implementation.

For practical applications much more frequently used pulses with a Gaussian or super-Gaussian envelope. Therefore, on a par with trapezoidal pulses give the results of numerical modeling for Gaussian pulses.

In modeling the amplitude of the incident signal  $E_i(t)$  was set according to the following formula:

$$E_i(t) = e^{-\left(\frac{t_0-t}{\tau_1}\right)^{2p}} \cdot \sin(\omega t), \tag{20}$$

here  $p$  - an integer,  $\tau_1$  - scale factor, which determines the pulse duration,  $t_0$  - sets the

position of the pulse center of the timeline,  $\omega$  - normalized angular frequency. **Fig. 5** shows the results of numerical simulation of transient reflectivity of the dielectric layer  $c$  losses for a pulse with super-Gaussian envelope. The results were obtained for the values of  $p = 1$  (Gaussian pulse) and  $p = 6$  (super-gaussian pulse);  $t_0 = 6.5$ ,  $\tau_1 = 5$ . The amplitude of the reflected signal on all charts increased fivefold.

From Fig. 5 shows that all the features of the formation of the reflected signal in the presence of losses in the layer are observed for pulses with Gaussian and super-Gaussian envelope. Numerical calculation of finite-difference time-domain method allowed to obtain the amplitude of the time pulse generated in the non-stationary reflection on the dielectric plate with losses. The analysis of the results of numerical experiments revealed a number of new features in the

formation of the reflected pulse, which was not observed in the absence of losses.

For a more detailed analysis of non-stationary reflection process in the event of loss, we obtain an analytical expression for the reflected amplitude modulated signal.

For the convenience of further calculations proceed to dimensionless units. Let us introduce dimensionless time:

$$t = t' / \tau_0, \quad (21)$$

Here  $T_0$  - sets the scale of the timeline,  $t'$  - the time in seconds. For the amplitude of the reflected signal, without taking into account possible losses, in [35, 36] proposed an analytical solution of the form:

$$U(t) = \frac{r_0}{1 - r_0^2} [A(t) - A(t - \Delta t)] e^{i\omega t}, \quad (22)$$

here  $\omega$  - circular frequency of the signal in dimensionless units,  $r_0$  - Fresnel reflection

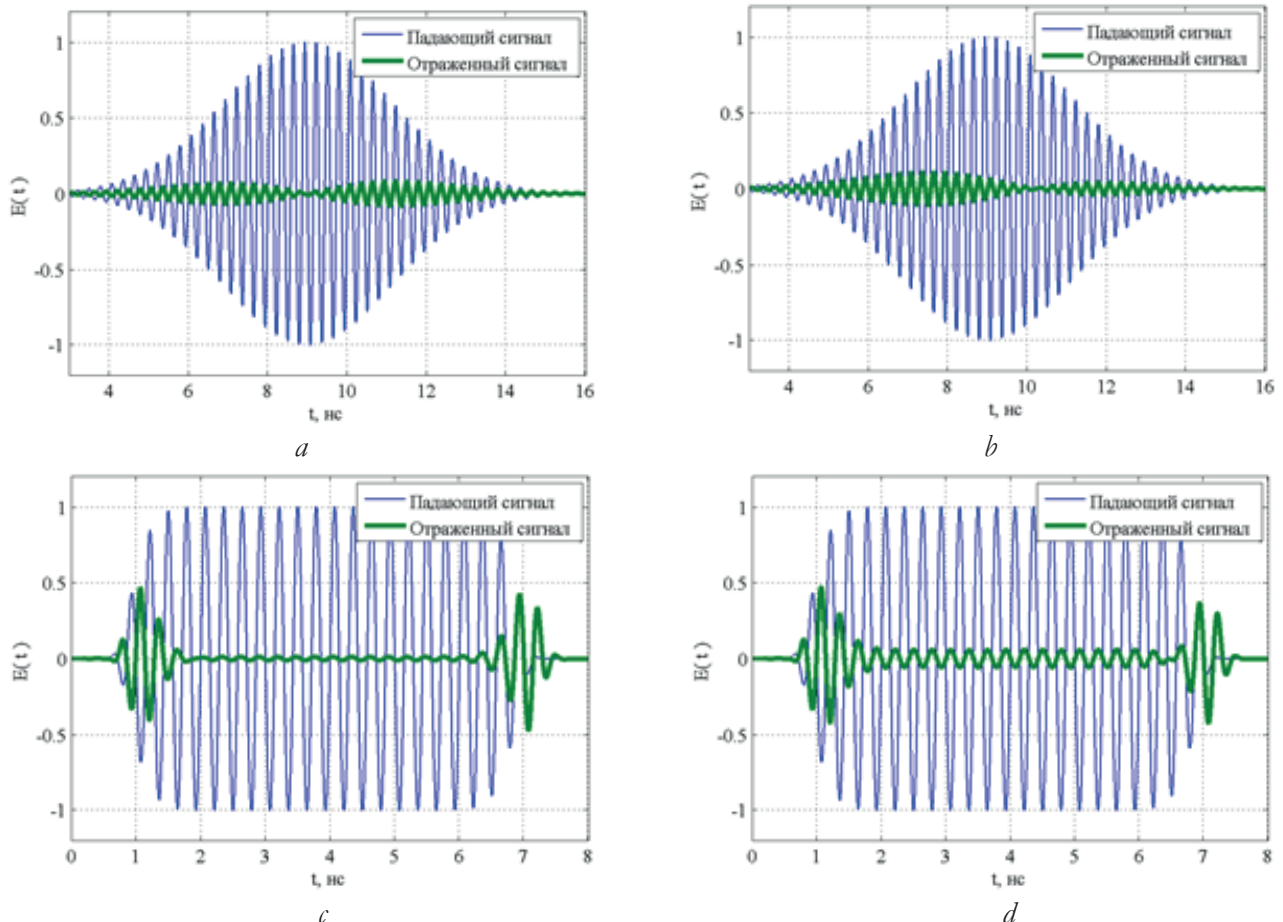


**Рис. 5.** Отраженные и падающие сигналы, рассчитанные методом конечных разностей для случая: а) отсутствия потерь в полуволновом слое  $\varepsilon = 2$ , гауссовой формы импульс; б) наличия потерь в полуволновом слое  $\varepsilon = 2 + 0.05i$ , импульс гауссовой формы; в) отсутствия потерь в полуволновом слое  $\varepsilon = 2$ , импульс супергауссовой формы; д) наличия потерь в полуволновом слое  $\varepsilon = 2 + 0.05i$ , импульс супергауссовой формы.

coefficient, by  $A(t)$  - is the dependence of the normalized incident signal amplitude versus time,  $\Delta t$  - twice the time of the film wave.

This result was obtained for an amplitude modulated signal reflected from the antireflection quarterwave film excluding possible losses therein. Equation (22) also holds for films fold thickness. In the derivation of the method of direct summation of interfering in a film of the waves and the approximation of slowly varying amplitudes. From the formula (22) shows that the reflected signal is the sum of two opposite signals. This representation is very convenient for the analysis of the formation of the reflected signal.

Accounting for small losses, as mentioned above, it leads to a change only the amplitude characteristics of interfering in the layer of waves. Applying the same approach as in [17], after simple calculations, you can get to a half-wave layer of lossy decision the following:

$$U(t) = \frac{r_0}{1-r_0^2} [A(t) - A(t-\Delta t)K] e^{i\omega t}, \quad (23)$$

Here, the coefficient  $K$  characterizes the energy loss in the propagation of the waves within the layer.

$$K = e^{-2\alpha d}. \quad (24)$$

Recall that  $\alpha$  - the real part of the propagation constant (9),  $d$  - plate thickness.

Analyze the formation of the reflected signal using the obtained expression (22) for example a trapezoidal signal envelope. Let trapezoidal signal has a duration  $\tau$ , and the slope angle of its edges equal to the absolute number of  $k = 1/s$ ,  $s$  - length fronts (Figure 6). Let the duration of the signal rise time  $\tau$  and  $s$  is much larger than the period of the carrier frequency. We denote the amplitude of the envelope of the signal as:

$$A(t) = \begin{cases} kt, & t_1 \leq t < t_3 \\ 1, & t_3 \leq t < t_5 \\ k(\tau - t), & t_5 \leq t < t_8 \end{cases} \quad (25)$$

In what follows we shall simply call the amplitude of the envelope amplitude, omitting the word "envelope" for short.

Given that relatively little time  $\Delta t$  the duration  $\tau$  of the signal, we expand the second term in formula (23) in a row:

$$A(t - \Delta t) = A(t) - \frac{dA}{dt} \Delta t. \quad (26)$$

The envelope of the reflected signal takes the following form:

$$U(t) = \frac{r_0}{1-r_0^2} \left[ A(t) - A(t)K + \frac{dA}{dt} \Delta t \right]. \quad (27)$$

For ease of analysis conditionally divide the duration of the incident signal at several intervals. **Fig. 6** shows the  $A(t)$  and  $A(t - \Delta t)$ , and their difference. In the time interval from  $t_1$  to  $t_2$  Fresnel reflection signal occurs. The time interval from  $t_1$  to  $t_2$  is equal to twice the transit time in the dielectric layer:

$$|t_1 - t_2| = \frac{2d\sqrt{\Lambda_1}}{c}. \quad (28)$$

In the time interval from  $t_2$  to  $t_3$  for the echo envelope obtain

$$U(t) = \frac{r_0}{1-r_0^2} [kt(1-K) + kK\Delta t]. \quad (29)$$

Then the slope of the envelope of the echo -  $k'$ , at the interval, we get:

$$k' = \frac{r_0}{1-r_0^2} (1-K)k. \quad (30)$$

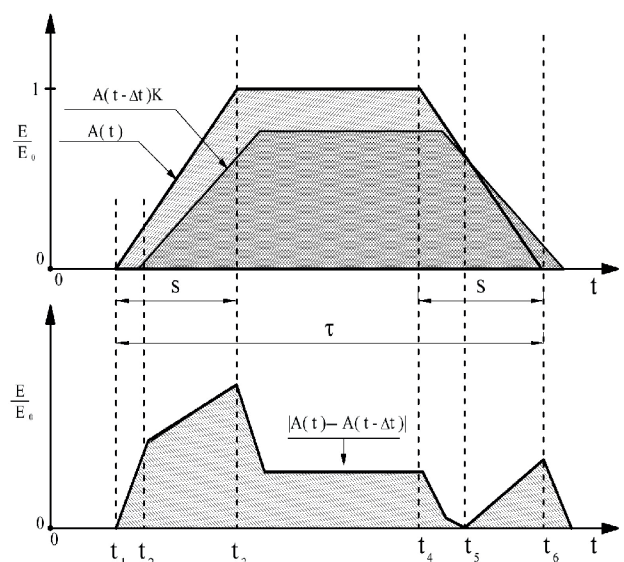


Рис. 6. Обозначения для расчета амплитуды отраженного сигнала.

Note that the tangent of the angle of inclination of the fronts of the reflected signal is not dependent on the duration of the falling edge of the signal. In the time interval from  $t_3$  to  $t_4$  we have:  $dA/dt = 0$ , therefore:

$$U(t) = \frac{r_0}{1-r_0^2} [A(t)(1-K)], \quad (31)$$

considering that  $A(t) = E_0$ , we obtain:

$$U(t) = \frac{r_0}{1-r_0^2} (1-K)E_0. \quad (32)$$

In the particular case, there are no losses in the layer, the expression (32) gives the well-known result:  $U(t) = 0$ .

In the time interval from  $t_4$  to  $t_6$ , the condition:  $dA/dt < 0$ . (33)

From Fig. 6 shows that there is always a time  $t_{min}$ , when

$$A(t_{min}) = A(t_{min} - \Delta t), \quad (34)$$

a reflected signal amplitude (23) has a local minimum. It is important to note that the function  $A(t)$  is not continuous, and depending on the time  $A(t)$  and  $A(t - \Delta t)$  can be different. For example, in the considered time interval from  $t_4$  to  $t_6$  are two possibilities:

$$A(t) = \frac{\tau - t}{s}, A(t - \Delta t) = 1; \quad (35)$$

$$A(t) = \frac{\tau - t}{s}, A(t - \Delta t) = \frac{\tau - t + \Delta t}{s}; \quad (36)$$

second embodiment is illustrated in Fig. 6.

Let us find out the minimum of reflection for any value  $t_{min}$  time for these two cases. Recall that the minimum amplitude of the reflected signal was observed by us in the numerical simulation of finite difference method (see. Fig. 4). In the first case we have:

$$\frac{\tau - t_{min}}{s} - K = 0, t_{min} = \tau - Ks. \quad (37)$$

This relation is valid only for the time  $\tau - s < t_5 < \tau - Ks$ . For the second case, substituting the explicit expression for the rear edge of the incident signal amplitude (36), we obtain:

$$A(t) = \frac{\tau - t}{s}, \frac{dA}{dt} = -k. \quad (38)$$

Then:

$$t_{min} = \tau - \frac{sKk\Delta t}{1-K}. \quad (39)$$

From the analysis it is clear that the resulting analytical expression (23) allows you to accurately calculate the amplitude of the reflected signal without resorting to numerical methods. Also, the analysis shows the possibility of determining the dielectric properties of the layer by measuring the parameters of the reflected pulse.

## 2.2. THE REFLECTION FROM THE LAYERS $N\lambda / 2$

Numerical simulation of non-stationary reflection amplitude modulated signal showed that the intensity of the reflected signal is only a few percent of the intensity of the incident. In the practice of the reflection phenomena of unsteady desirable that the amplitude of the formed pulses resulting in unsteady reflection was maximum, provided that the structure of the reflection coefficient at the carrier frequency of the pulse is close to zero.

In the formula (23) includes two parameters: the reflection coefficient  $r_0$  and twice the time  $\Delta t$  wave propagation through the layer. Changes in each of these parameters leads to a change in the amplitude of the reflected signal. We analyze the possibility of strengthening the non-stationary phenomenon reflected by changes in these parameters.

From the formula (23) shows that the increase in  $r_0$  will exacerbate the phenomenon of non-stationary reflection. Fresnel reflection coefficient  $r_0$  is given by the dielectric properties of the material of construction of the plate. It follows that the use dielectrics with high relative dielectric constant and low loss for the manufacture of the half-wave layer enables to enhance the effect of unsteady reflection. Unfortunately, materials with low loss and a high refractive index is extremely small. Task gain effective indicator on the border between the half-wave plate and the free space or waveguide line can be solved by installing a plate between the multilayer mirrors [38].

We turn now to the analysis of the possibility of strengthening the phenomenon of transient reflectivity due to changes in the propagation time wave in the dielectric layer.

From the expression (23) shows that the reflected signal amplitude can be increased by increasing the time of signal propagation in the structure. Indeed, the passage of the wave through the layer included in the expression for the envelope, and the amplitude of the reflected pulse is directly dependent on that time.

If we consider the process of non-stationary reflection from the layer thickness of a multiple of  $\lambda / 2$ , ie,  $d = N\lambda / 2$ , for example, when  $N > 3$  the contribution due to the propagation time may become significant. This is easily explained by the fact that the difference between  $A(t) - A(t + \Delta t)$ , a member of the formula (23) increases.

(22) for linearly rising edge should be that an increase in thickness of the plate twice will result in the same increase in the echo amplitude. For a plate thickness of  $\lambda$  Formula (23) takes the form:

$$U(t) = \frac{2r_0}{1-r_0^2} [A(t) - A(t - \Delta t)K_2] e^{i\omega t}, \tag{40}$$

here  $K_2$  is characterized by loss factor in the layer.

The amplitude of the echo pulse dependent on the difference between the two signals. By increasing the delay time between the waves reflected from the front and rear faces of the plate, this difference increases. The maximum pulse amplitude is reached when the delay time equal to the rise time. A further increase in travel time will not lead to an increase in the amplitude of the reflected signal, since the amplitude of the first term in the expression (23) will not increase.

**Fig. 7** shows the results of numerical modeling of the influence of the thickness of the dielectric layer on the amplitude of the reflected signal. For clarity, the amplitude of the reflected signal is increased 10 times. Thickness varied multiple of  $\lambda / 2$ . The simulation was performed by impedance characteristics and then applying the inverse Fourier transform. Results are given for a thickness of the dielectric layer 6 to  $\lambda \lambda$ . As

material for the dielectric layer was taken with a relative dielectric constant  $\epsilon = 2$  equal to  $+ 0.01i$ . The calculation was made without regard to the waveguide dispersion.

The initial calculation of the data was such that on the dielectric plate falling pulse with trapezoidal envelope. The carrier frequency corresponds to the frequency of the minimum reflection. With increasing layer thickness in a multiple number of times reflection zero frequency does not change.

As can be seen from the graphs in Fig. 7, by increasing the thickness increases the duration of the reflected pulse, as predicted. At a constant amplitude of the reflected signal amplitude should be minimized incident signal otherwise ceases to be non-reflective structure. As can be seen from Fig. 7, this requirement is fulfilled for the layers with a thickness of  $\lambda / 2$  to  $2\lambda$ , and partly for the layers  $4\lambda$  and  $8\lambda$ . For a layer thickness  $8\lambda$  amplitude reflected signal time to reach its maximum just at the moment when the amplitude of the incident signal becomes constant. In this case, a change in shape of the reflected signal as well as its duration.

The analysis showed that for increasing the intensity of the pulses generated in the non-stationary reflection AM signal, there are several possibilities.

Firstly, it is possible to reduce the length of the front structure of the incident pulse; secondly, to increase the time of the pulse through the

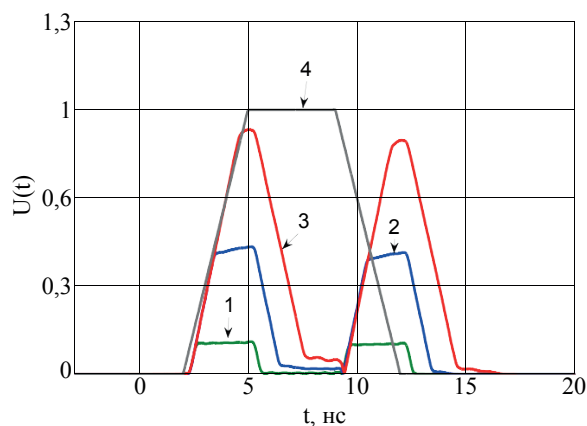


**Рис. 7.** Огибающие отраженного сигнала при разной оптической толщине диэлектрического слоя: 1 – толщина слоя  $d = \lambda$ ; 2 – толщина слоя  $d = 4\lambda$ ; 3 – толщина слоя  $d = 8\lambda$ ; 4 – падающий сигнал.

layer. On the other hand, it is important to remember that the increase in thickness leads to a multiple increase in the energy losses therein. As shown above, an increase in loss adversely affects the unsteady reflection phenomenon due to suppression of the interfering waves in the layer.

**2.3. INFLUENCE OF WAVEGUIDE DISPERSION**

In the experimental study of non-stationary process of reflection is convenient to use multilayer structures collected in the waveguide path. This approach allows to fix the layers of the multilayer structure at a desired distance from each other with high accuracy. It is necessary to take into account the effect of the waveguide dispersion in the non-stationary process of reflection.

The theoretical analysis of the influence of the waveguide dispersion in the non-stationary process of reflection amplitude-modulated signals. For this, consider a half-wave layer is established in a regular rectangular waveguide. Let waveguide excited fundamental mode H10. Let us write the dispersion relation by the wavelength dependence of the waveguide in a free frequency. To get fashion H10:

$$\lambda = \frac{c}{\nu} \sqrt{1 - \left(\frac{\nu_{c0}}{\nu}\right)^2} \quad (\nu \in \nu_{c0}, \nu_{c1}) \tag{41}$$

here - the speed of light,  $\nu$  - the frequency of the signal,  $\nu_{c0}$  - critical frequency for fashion H10,  $\nu_{c1}$  - critical frequency for the H01 mode. The relation shows that for  $\nu \rightarrow \infty \lambda = c / \nu$ , and the influence of the dispersion can be neglected. As is known [38], in the waveguide can simultaneously exist a large number of events, and at a frequency  $\nu > \nu_{c2}$  happen excitation of the second mode. Excitation of the second mode have a significant impact on the dispersion characteristics of the waveguide, complicating the analysis. The

optimum range of operating frequency is approximately in the range of  $1.25 \nu_{c0}$  to  $\nu_{c1}$ .

To analyze the effect of dispersion, we need the ability to change the carrier frequency of the signal from the region with weak dispersion to an area with strong. This requires that the reflectance of the layer had several minima in this frequency range as the carrier signal must coincide with a frequency of minimum reflectance.

Consider the process of transient reflectivity of the layer thickness in  $6\lambda$  installed in rectangular waveguide section  $23 \times 10$  mm 2. **Fig. 8** shows the reflection coefficient of the layer. The spectrum was calculated by the method of impedance characteristics.

Presented in Fig. 8 results show that in strong dispersion of the reflectance increases. It is also seen that in this range there are several frequencies, at which reflectance goes to zero.

For the frequencies corresponding to the zero reflection, calculated the reflected signal envelope. Let fall upon layer trapezoidal signal envelope. Let the carrier frequency of the signal as a  $\nu_0$ . The carrier frequency  $\nu_0$  express in terms of relative frequency  $\nu$ s critical for ease of analysis.

From the results presented in **Fig. 9** shows that the presence of the waveguide dispersion shape of the envelope of the signal changes. With

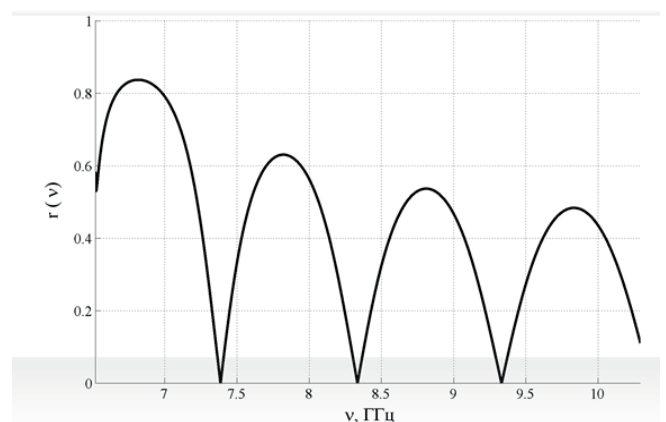


**Рис. 8.** *Спектр отражения от диэлектрической пластинки толщиной  $6\lambda$  в волноводе.*

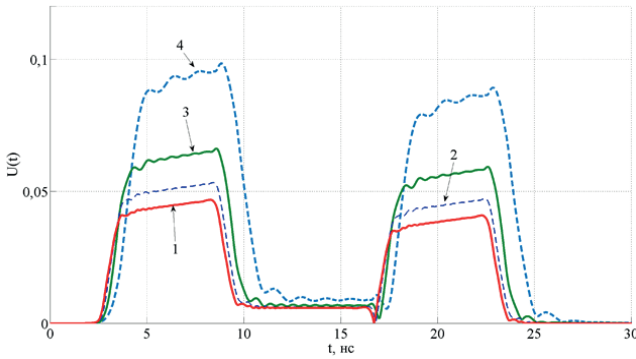


**Рис. 9.** Огибающие отраженного сигнала при различных значениях несущих частот падающего импульса, для случаев: 1) частота падающего импульса  $\nu_0 = 1.135\nu$ ; 2) частота падающего импульса  $\nu_0 = 1.128\nu$ ; 3) частота падающего импульса  $\nu_0 = 1.143\nu$ ; 4) частота падающего импульса  $\nu_0 = 1.159\nu$ .

increasing dispersion (approaching the critical wavelength), the amplitude of the reflected signal increases and increases its durability. Also in the area there are additional strong dispersion of the oscillation amplitude of the reflected signal. It is easy to note that at a frequency  $\nu_0 > 1.25\nu$ s envelope shape of the reflected signal does not change its nature. Unlike discussed in paragraph 2.2 the case of increasing signal propagation time through the structure, the approach to the critical frequency does not increase the losses in the layer.

Summarizing, we can say that the use of the phenomenon of waveguide dispersion and increased multiplicity layer can increase the amplitude of the signal generated in the non-stationary reflection. Increasing the thickness increases the loss in multilayer structures, which adversely affects the appearance of reflection unsteady. Using a waveguide dispersion allows more efficient to increase the amplitude of the reflected signal.

**2.4. Experimental study of the reflection signal from the half-wave filter**

The phenomenon of non-stationary reflection of short electromagnetic pulses from the layered structure was measured on the stand (Fig. 10), which consists of a vector network analyzer Rohde & Schwarz ZVB-20 with an attached rectangular waveguide into which the layered structure, completely filling

the cross-section. On the one hand excited waveguide coaxial-waveguide transition (OHR) with the whip antenna, on the other - enables consistent waveguide load. Stated dynamic range for ZVB-20 amounted to more than 125 dB [39]. When calibrating its input path used waveguide section with a loaded load. Spurious reflections arising waveguide system has been filtered in the time domain with a window function gated Hannah [40] using the inverse Fourier transform [41] The calibration signal.

The subject of the study was to analyze the envelope of the signal reflected from the plate. The experiment was conducted for plates made of dielectrics with different values of the relative permittivity. The materials were chosen: Teflon-4, polyamide-6 (caprolon), quartz brands KU and KB. Quartz and fluoroplastic-4 have low loss in the microwave wavelength range ( $\text{tg}(\delta) < 10^{-3}$ ). Kaprolon was chosen as the material having more losses than PTFE-4 and quartz.

The dependence of the complex reflection coefficient of frequency  $r(\nu)$ . Measurements were carried out in the frequency range from 6 GHz to 14 GHz, which covers the area H10 fashion the existence of frequencies for the connected waveguide section  $23 \times 10 \text{ mm}^2$ .

The measured reflectance was used in the next calculation of the envelope of the reflected pulse of short duration. Let a multilayered structure falls trapezoidal envelope signal. The amplitude of the signal can be written as:

$$E(t) = A(t) \cos(2\pi\nu t), \tag{42}$$

where  $\nu$  - the carrier frequency and  $A(t)$  is given by

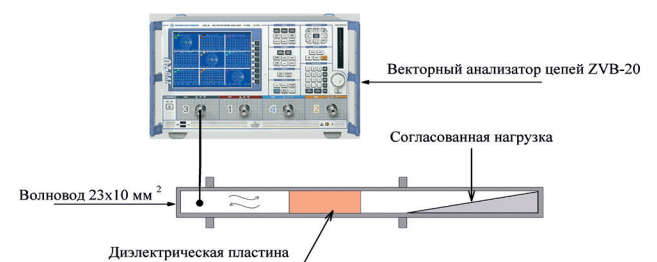


**Рис. 10.** Схема установки с однослойным фильтром.

$$A(t) = \begin{cases} \frac{t}{s}, & 0 \leq t < s, \\ 1, & s \leq t < (\tau - s), \\ \frac{\tau - t}{s}, & (\tau - s) \leq t < \tau, \end{cases} \quad (43)$$

here  $s$  - pulse rise time,  $\tau$  -Duration pulse level of -10dB.

If you know the reflection coefficient of the investigated multilayer structure  $r(\nu)$ , then to calculate the spectrum of the reflected signal, you can use the ratio:

$$H_g(\nu) = r(\nu) F(\nu). \quad (44)$$

Applying the inverse Fourier transform to the region  $H_g \nu$  positive frequencies obtain analytical signal:

$$h(t) = \frac{1}{\pi} \int_0^\infty H_g(\nu) e^{i2\pi\nu t} d(2\pi\nu). \quad (45)$$

Analytical Signal Module  $|h(\nu)|$  It is the desired envelope of the reflected pulse. Thus, by measuring the reflection coefficient  $r(\nu)$  in the positive frequency, we can obtain the envelope of the reflected pulse, and varying the parameters  $\nu$ ,  $\Delta t$ ,  $s$  possible to change the center frequency and duration of the incident signal and its fronts.

### 2.4.1. THE IMPACT OF LOSSES IN THE LAYER ON THE NON-STATIONARY REFLECTION

With unsteady reflection of electromagnetic pulses of short duration of the non-reflective multilayer structures such as play an important role in the loss of the layers of structures. For the experimental study of loss of influence in the layers in the process of non-stationary reflection of several materials were chosen. As dielectrics with low losses was chosen quite frequently used in microwave engineering material - Teflon-4. A material with a relatively high loss of polyamide-6 was selected.

For measuring the half-wave layer was placed in the middle of the free cross section of the waveguide  $23 \times 10 \text{ mm}^2$ . As the incident signal used trapezoidal electromagnetic pulse duration of 20 ns, the duration of the front and rear edges of which was 7 ns. **Fig. 11** in dashed lines

shows the experimentally obtained for the echo envelope half-wave layers made of polyamide and a fluoroplastic. For clarity, shows the envelope of the incident pulse, decreased in 10 times.

Also in Fig. 11 shows the results of a theoretical calculation. Theoretical curves were obtained by impedance characteristics then applying the inverse Fourier transform. In the calculation, the following values of the permittivity: polyamide-6,  $\epsilon = 2.98 + 0.037i$ , Teflon-4  $\epsilon = 2.03 + 0.003i$ .

As can be seen from Fig. 11, the theoretical calculation results are in good agreement with the experimental data. Comparing the results obtained for polytetrafluorethylene and polyamide, we see that the echo envelopes in the two cases differ.

In the case of a material with low losses (PTFE) shows that the reflected signal at constant amplitude of the incident pulse is practically absent. The reflected signal consists of two solitary pulses. The presence of small losses leads to the fact that the amplitude of these pulses is different and the shape of the envelopes of these pulses is different from the rectangular. This result shows that even with small losses in the structure layers, they must be taken into account.

With an increase in losses in the material is greatly increased amplitude in a reflected signal of the incident pulse of constant amplitude. With an increase in the imaginary part of relative

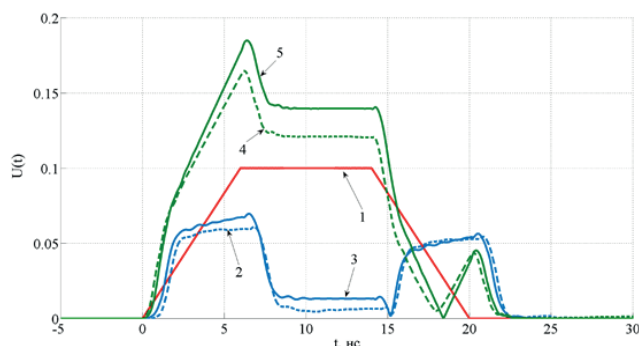


**Рис. 11.** Огибающая отраженного сигнала: 1 – падающий сигнал; 2 – экспериментальная кривая для слоя из фторопласта; 3 – теоретическая кривая для слоя из фторопласта; 4 – экспериментальная кривая для слоя из полиамида; 5 – теоретическая кривая для слоя из полиамида.

dielectric constant increases the difference pulses generated by reflection from the dielectric layer of the front and rear fronts of the incident signal. Fig. 11 clearly shows that even if losses in the half-wavelength layer exists a time when the reflected signal amplitude is close to zero.

**2.4.2. INFLUENCE OF LAYER THICKNESS ON NON-STATIONARY REFLECTION**

On amplitude reflected from the dielectric layer with signal loss affects the settling time of a stationary process in the layer. an increase of the reflected signal intensity at this time increases. For the experimental study of the effect of the dielectric plate optical thickness on the process of non-stationary reflection amplitude modulated signal used three samples made from PTFE. The thickness of the samples was 30 mm, 60 mm, 90 mm. The samples were mounted in a rectangular waveguide, completely filling the cross-section. For a frequency  $\nu = 8.4$  GHz, the wavelength in units of layers have a thickness of  $\lambda, 2\lambda, 3\lambda$ , respectively. In the experiment on a layer of the incident electromagnetic pulse with a trapezoidal envelope of 10 ns. Pulse rise time was 3 ns. The center frequency of the pulse  $\nu = 8.4$  GHz. **Fig. 12** shows the experimentally obtained envelopes of the reflected signal.

For clarity, shows the envelope of the incident signal, decreased in 10 times. From the results presented in Fig. 12 shows that with increasing layer thickness  $d = \lambda$   $d = 2\lambda$  to lead to an increase in the reflected signal amplitude is twice (40). On the other hand, a further increase of the layer thickness to  $3\lambda$   $2\lambda$  does not lead to a significant increase of the amplitude of the reflected signal and distorts the shape of the envelope in front of the incident pulse. This is because in this case the duration of the falling edge of the signal becomes comparable to the time of passage of a wave layer.

**2.4.3. INFLUENCE OF THE WAVEGUIDE DISPERSION IN THE NON-STATIONARY REFLECTION**

In the experimental study of non-stationary process of reflection is convenient to use

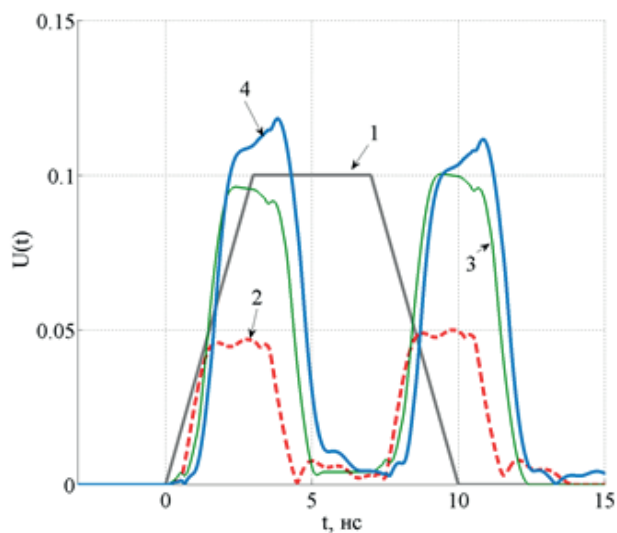


**Рис. 12.** Импульсы, отраженные от слоев различной толщины: 1 — падающий сигнал, 2 — толщина слоя  $d = \lambda$ ; 3 — толщина слоя  $d = 2\lambda$ ; 4 — толщина слоя  $d = 3\lambda$ .

multilayer structures collected in the waveguide path. This approach allows to fix the layers of the multilayer structure at a desired distance from each other with high accuracy. This raises the need to consider the influence of the waveguide dispersion in the non-stationary process of reflection.

One way analysis of variance effect on unsteady reflection process is to change the carrier frequency signal from the region with weak dispersion to an area with strong dispersion. Since the carrier frequency of the signal must coincide with a frequency of minimum reflectance MIS, it is necessary that the reflectance of the layer had several minima in this frequency range.

Consider the non-stationary process of reflection on the layer thickness of  $3\lambda$  mounted in a rectangular waveguide section  $23 \times 10$  mm 2. Said waveguide section has a cutoff frequency of  $6.5$  GHz  $\approx \nu_s$ . In the frequency range to the frequency and  $\nu_s \nu_{s2} \approx 14.4$  GHz it only excited fundamental mode H10. Waveguides of this section are applied, typically in the frequency range from 8 to 12 GHz. This is due to the fact that in the areas of 6.5-8 GHz significant impact on the dispersion of electromagnetic wave propagation in the waveguide, and in the 12-14.5 GHz band can be excited more waveguide mode. Excitation of higher mode significantly affect

the dispersion characteristics, leading to strong oscillations of the waveguide transmission ratio. Oscillations gain cause additional difficulties in dealing with applications.

**Fig. 13** shows the results of the experimentally measured reflection spectrum of the Teflon layer 90 mm thick, as well as the theoretical calculation. The calculation was made by the method of impedance characteristics for the value of  $\epsilon = 2.03 + 0.003i$ . At a frequency of 8.4 GHz, viewed dielectric layer has a thickness of  $3\lambda$ .

Fig. 13 that at the beginning and end of the frequency range of accuracy predicted by theory, the somewhat lower. This is due to the fact that the agreed load and coaxial-waveguide transition are designed to work in a range of 8-12 GHz. Outside this frequency range matching the quality falls. It also shows that in the strong waveguide dispersion coefficient of reflection increases.

In this range there are several values of the frequency at which the reflection coefficient vanishes. Frequencies minimum reflectance for the case have values: 8.38 GHz, 9.37 GHz, 10.4 GHz, 11.48 GHz and 12.55 GHz. We note that these frequencies are not equidistant. This effect is due to the presence of the waveguide dispersion. Let us write the dispersion relation by dependence of the group velocity of propagation of an electromagnetic pulse in the

waveguide on the frequency. To get fashion H10:

$$V = \frac{c}{n} \sqrt{1 - \left(\frac{v_c}{v}\right)^2}, \quad \text{by } v \in (v_c, v_{c1}); \quad (46)$$

here - the speed of light,  $v$  - the frequency of the signal,  $v_s$  - critical frequency for fashion H10,  $v_{c1}$  - critical frequency for fashion H01,  $n$  - refractive index of the substance filling the waveguide. From the relation (46) shows that the wave propagation velocity decreases when approaching to  $v_c$   $v$  and the layer becomes thicker as it for the incident wave, with the result that the resonances are often, but narrows the bandwidth.

For the frequencies corresponding to the zero reflection, will produce an experimental measurement of the envelope of the reflected signal. As in the case study of the effect of thickness on the process of reflection of non-stationary, use a trapezoidal pulse with an envelope 10 ns, c duration of 3 ns fronts. The carrier frequency  $v$  express in terms of relative frequency  $v_c$  critical for ease of analysis.

**Fig. 14** shows the envelope of the reflected signals fluoroplastic plates, for different values of carrier frequency. In addition, in the graph in Fig. 14 shows the envelope of the incident signal, decreased by 10 times. From the results presented in Fig. 14 shows that the presence of the waveguide dispersion of the signal envelope shape changes its form.

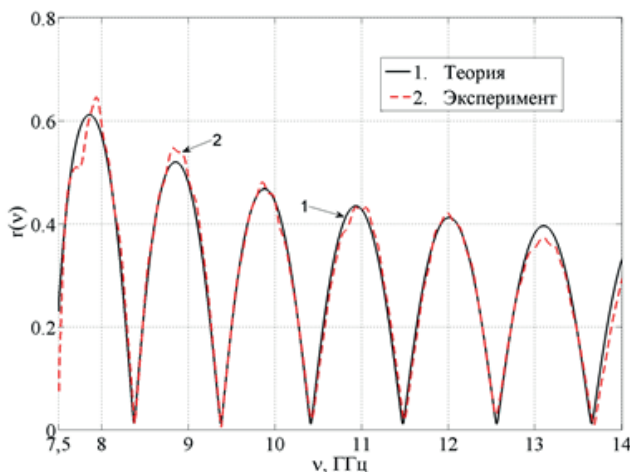


**Рис. 13.** Спектр отражения от тефлонового слоя: 1 – расчет методом импедансных характеристик; 2 – эксперимент.

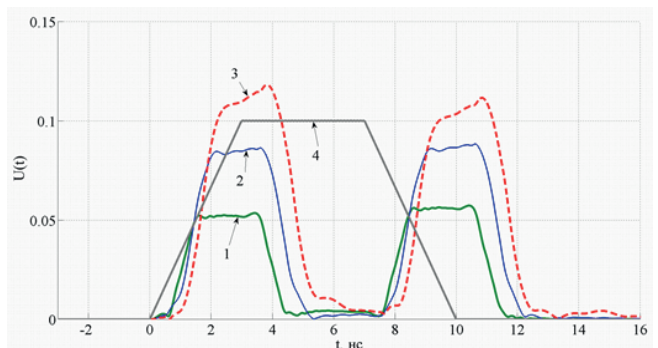


**Рис. 14.** Амплитуда огибающей отраженных сигналов для разного значения несущей частоты импульса: 1 – частота падающего импульса  $v = 1.92v_c$ ; 2 – частота падающего импульса  $v = 1.44v_c$ ; 3 – частота падающего импульса  $v = 1.29v_c$ ; 4 – падающий импульс.

With increasing dispersion (approaching the critical wavelength  $\nu \rightarrow \nu_c$ ) amplitude of the reflected signal increases and increases its durability. Also in the area there are additional strong dispersion of the oscillation amplitude of the reflected signal. It is easy to note that at a frequency  $\nu > 1.44 \nu_c$  envelope shape of the reflected signal does not change its nature. Unlike the above case of increasing the transit time through the structure, the approach to the critical frequency does not increase the losses in the layer.

### 3. NON-STATIONARY REFLECTION UNDER STRONG WAVEGUIDE DISPERSION

To enhance reflection unsteady - increasing pulse duration and intensity used line waveguide dispersion properties when introduced into the waveguide highly reflecting graphite loading of matching dielectric layer (Teflon) with small losses (**Fig. 15**). TO waveguide section  $23 \times 10$  mm<sup>2</sup> through a smooth transition waveguide connected waveguide sections  $16 \times 8$  mm<sup>2</sup> in order to reduce the impact of the effects associated with the excitation of the waveguide at frequencies close to the critical. Operating frequency range used by the OHR was from 8.15 GHz to 12.05 GHz, and the frequency at which the measurements were taken - from 8.5 GHz to 12 GHz. For the partial suppression of spurious reflections in the waveguide channel was introduced attenuator with low attenuation coefficient  $k \approx 1.5$  dB. The use of the attenuator has significantly increased the accuracy of the amplitude of the reflectance values of the agreed highly reflecting load,

thus making it difficult to measure its phase. Test stand allowed to obtain the dependence of the complex reflection coefficient of frequency.

The experiment was set in two stages. The first phase was measured reflectance of highly reflecting load and calculates the effective conductivity, as well as the measured cut-off frequency of the waveguide. The data used to calculate the thickness of the matching layer. In the second stage, building on the results of the calculation, it produces a series of dielectric layers. Next, we measured the reflectance of a harmonized system for layers of various thicknesses. Thus, the experimentally select the optimum thickness of the matching layer.

The results obtained in the first stage showed that the effective conductivity  $\sigma \approx 130$  load (ohm-m)<sup>-1</sup>, the critical frequency  $\nu_s = 9,339$  GHz. For this conductivity and the known thickness of the matching layer critical frequency was calculated, which was  $d = 7.715$  mm. When measuring the reflectance of the system matching layer minimum reflectance was obtained for the frequency  $\nu = 9.383$  GHz and a layer thickness of 8 mm, which agrees well with the theoretically calculated values.

**Fig. 16** shows the measurement results depending on the reflection coefficient of frequency for an agreed vysokotrazhayushey load and the result of numerical simulation.

As can be seen from Fig. 16, the results of a theoretical calculation are in good agreement with data obtained in the experiment. Considered the method of matching loads with highly reflective waveguide line is a simple, compact and easy to implement MIS. The proposed matching structure has a significant advantage over other types of MIS: choice of material for a quarter of the dielectric layer is limited almost exclusively the only requirement  $\epsilon l < 1/Z_s$ . Of course,

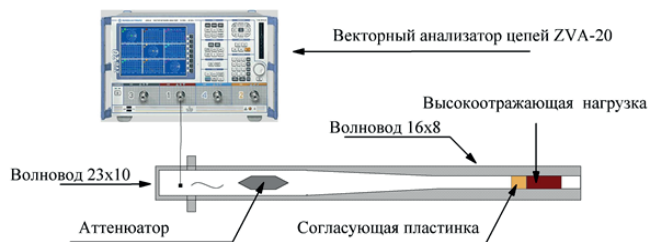


**Рис. 15.** Схема установки с высокоотражающей нагрузкой.

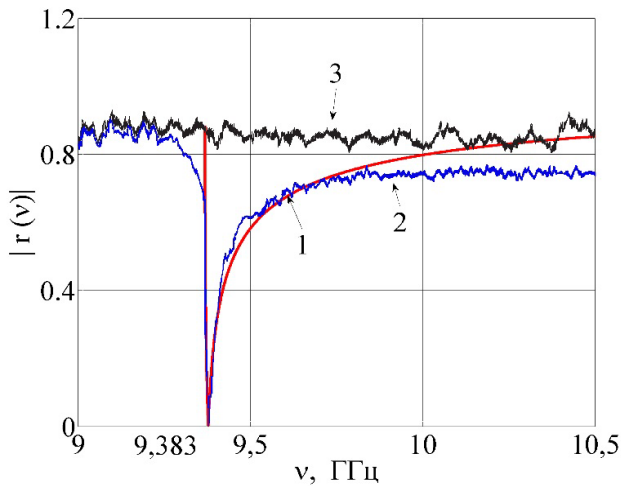


**Рис. 16.** Зависимость коэффициента отражения от частоты для согласованной нагрузки: 1 – расчет методом импедансных характеристик; 2 – экспериментально измеренный коэффициент отражения от согласованной высокоотражающей нагрузки; 3 – экспериментально измеренный коэффициент отражения от высокоотражающей нагрузки без согласующего слоя.

this loss in the fiber, as with any other method should be minimal.

When you study the influence of a strong waveguide dispersion in the process of reflection of non-stationary electromagnetic pulse from a highly reflecting agreed with the waveguide attenuator Load established between the OHR and the waveguide section with a matching structure was removed. The experiment measured the complex reflection

coefficient of the highly reflecting the agreed load  $r(\nu)$ . During the experiment, on the layer of the incident electromagnetic pulse with a super-Gaussian envelope. The duration of the incident pulse varied from 50 ns to 250 ns. Central pulse frequency coincides with the optimum coordination with the waveguide highly reflecting load  $\nu = 9.339$  GHz. **Fig. 17** shows the results of theoretical modeling and experimental envelopes received reflected pulses, and also shows the envelope of the incident signal  $U$  reduced by fourfold axis for clarity.

As can be seen from Fig. 17, the theoretical calculation results are in good agreement with the experimental data. It is evident that with a decrease in the duration of the incident pulse "distortion" of the reflected pulse is increased, which can be explained by the strong influence of the waveguide dispersion. As in the case of unsteady reflection without dispersion systems [17, 23, 42], the reflection signal formed by the structure discussed in the two pulse leading and trailing edges. Comparing the experimental results with the results for a system without dispersion [17, 23, 42], we see that the duration of these pulses has grown substantially. There is a time when the amplitude of the reflected signal tends to zero, but it occurs at the leading edge reflection and not adjustable, as

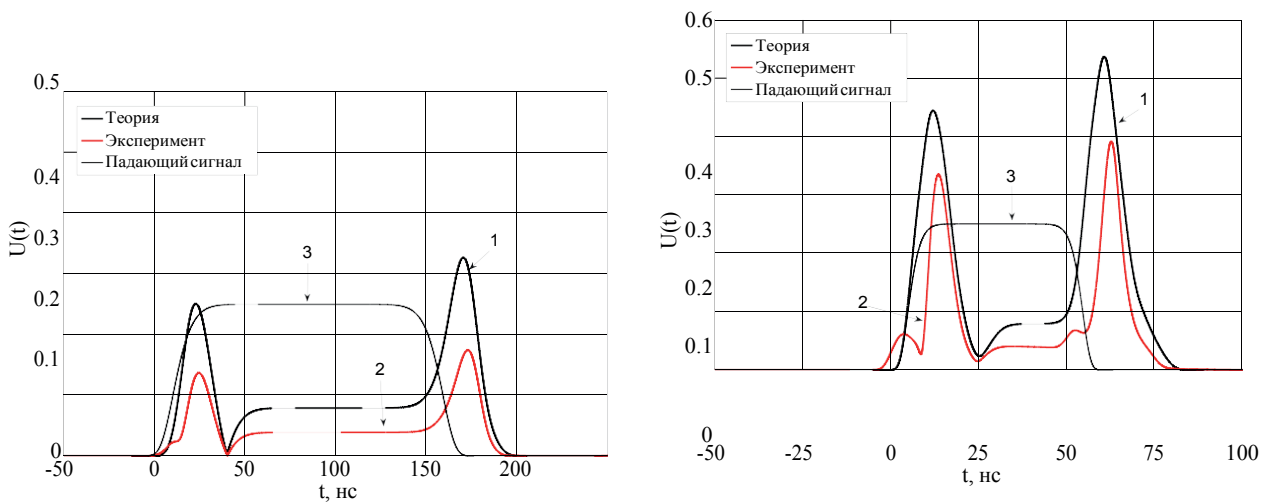


**Рис. 17.** Амплитуды огибающих отраженных сигналов от согласованной высокоотражающей нагрузки; а) длительность падающего импульса 150 нс.; б) длительность падающего импульса 50 нс.; 1 – теоретически рассчитанный отраженный сигнал; 2 – экспериментально измеренный отраженный сигнал; 3 – падающий импульс.

in the case of absence variance discussed in section 2. Another important feature when compared to systems without dispersion is a high intensity of reflected signals. From Fig. 17 shows that the maximum amplitude of the pulses generated during unsteady reflection reaches a value of 50% of the incident signal amplitude. Recall that the maximum value of the amplitude of the reflected signal, resulting in section 2, does not exceed 15% of the incident pulse amplitude. The high intensity of the reflected signal indicates the prospects of using strong waveguide dispersion to enhance the effects of non-stationary reflection. Studies have demonstrated the possibility in principle to provide the almost complete absorption of wave energy in highly reflective load, using interference phenomena in layered structures and waveguide dispersion properties of the line. In areas of changing the amplitude of the incident signal (front area) in the response generated short pulses whose duration corresponds to the duration of fronts. Unlike the case of the dispersion systems without return signal pulses generated at the time of the incident signal reflected fronts have a different amplitude for the leading and trailing edges. The amplitude of the first pulse is always smaller than the pulse amplitude formed trailing edge, and the envelope has a complex shape.

4. UNSTEADY REFLECTED IN THE MULTILAYER INTERFERENCE FILTERS

Unsteady reflection of the pulse signal of short duration in the multilayer structure of the non-reflective class as opposed to the signal reflection from one layer is characterized by a complex frequency dependency of the incident signal, as well as a significant dependence on the losses in the layers of the reflective structure.

In our paper [43] it was shown that the optimum condition for the non-stationary reflection from the multilayer structure is to use a band-pass filter of the second order with a maximally flat frequency response (AFR), well-known in the literature on the synthesis filters and antireflection coatings [44-46].

The simplest implementation of a multi-layer structure with a maximally flat frequency response of a filter consisting of two resonators, which is implemented between the critical connection [45, 47]. structure consisting of two half-wave lossless

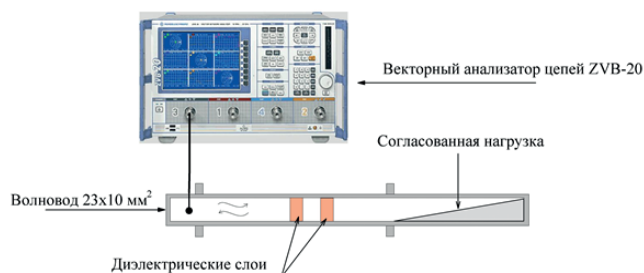


Рис. 18. Схема установки с многослойным фильтром. dielectric layers, which are arranged in the free space to each other at a distance of a quarter wave length (Fig. 18) was used.

In an ideal structure of the filter reflection from the layered structure can be calculated for the signal whose envelope has a symmetrical trapezoidal shape with linear edges. Let half-wave filter made of dielectric layers with a real and imaginary part of the relative dielectric constant equal to  $\epsilon' = 2$ ,  $\epsilon'' = 0.00$ , respectively. We assume that the length of the trapezoidal pulse  $\tau$  a lot more time passes wave double layer thickness. At the same time as a result of non-stationary reflection will be generated pulse propagating toward the incident wave. Define half-wave layers of equal thickness  $d = 30$  mm, while the thickness of the quarter-wave layer  $d_1 = 21$  mm.

Fig. 19 shows the result of calculation of the field  $E_r(t)$  of the reflected pulse finite-difference time-domain method tensions. For clarity, the reflected signal amplitude is increased by 20 times.

It can be seen that the reflected signal consists of four short pulses. The maxima of the reflected signal pulse corresponds to the time when the envelope of

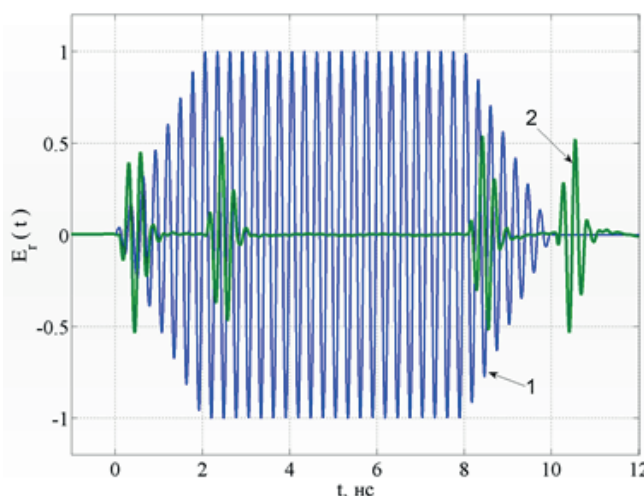


Рис. 19. Расчет поля  $E_r(t)$  отраженного импульса, методом конечных разностей во временной области: 1 – падающий сигнал; 2 – отраженный сигнал.

the incident signal has the maximum derivative. It also shows that the two central pulse have the same phase and are in antiphase with the first and last pulse.

In the practice of the multilayer structure may be necessary to include additional physical phenomena. For example, in the experimental conditions in the head space may be significant diffraction phenomenon on the edges of the plates and the deviation of the wave front of the incident plane. In addition, there will be additional requirements for accuracy and positioning of the plates to their thickness. Equally important, as it is evident from [42], is a real need to take account of losses in the layers of the multilayer structure.

Driving the practical implementation of the considered filter is strongly dependent on the frequency range for which it is applied. Thus in the optical domain using a substrate on which the layers are sequentially sputtered in the multilayer filter synthesis. In this case, the synthesis filter is necessary to consider not only the loss of structure layers, and the dispersion material as layers and the substrate. In the microwave range of wavelengths such structures can be realized in a waveguide. In this case, you must additionally consider the impact of the waveguide dispersion in the reflectance. On the other hand, it solves the problem of taking into account diffraction at the edges of plates and shapes of the incident wave front, as the plate completely covers the section of the waveguide.

In our case, the model was studied waveguide filter, as the most convenient for the pilot study. Consider this model more and carry out its numerical analysis based on the waveguide dispersion and loss of structure layers.

Let the layers are set in a free rectangular waveguide in which the excited fundamental mode H<sub>10</sub>. We assume that the layers are made of a dielectric with low losses.

Then the expression for the relative permittivity will be in the form  $\epsilon = \epsilon' - i\epsilon''$ , where  $\epsilon''$  and  $\epsilon'$  - imaginary and real part of the relative permittivity, respectively. We assume that the losses in the layers of the structure are small  $\epsilon''/\epsilon' < 1$ .

In [42] it was shown that the small loss in the sample do not affect its optical thickness, in this case - to the resonant frequency of a half-wave layer.

Then, to calculate the thickness of the layers can be taken into account only the waveguide dispersion. In this case, for the calculation of the layer thickness, we have:

$$d = \operatorname{Re}(Z) \frac{c}{2\nu}, \quad (47)$$

where  $\operatorname{Re}(Z)$  - the real part of the impedance layer.

Analysis of non-stationary reflection process requires a shift in the time domain. For this we use the inverse Fourier transform. As shown by numerical simulation method of impedance characteristics, the presence of losses in the structure of the layers leads to a reflection in the field of constant incident amplitude of the signal.

When measuring non-stationary reflection bandpass filter was used, consisting of two wave plates of fluoroplasta. Polyacetal has low loss in the microwave frequency range [48, 49]. The plates were mounted on a distance of a quarter wavelength from each other in the middle of the rectangular waveguide to minimize the influence of waves on the measured gap reflectance. The filter was tuned to the frequency 8.4 GHz and had the following geometrical dimensions: thickness fluoroplastic plates - 30.0 mm, the thickness of the air gap between the plates - 14.5 mm. The dielectric constant of PTFE for this frequency has been previously measured and accounted for  $\epsilon_1 = 2.05 - 0.015i$ .

The experiment measured the complex reflection coefficient of the structure. inverse Fourier transform was used to obtain the envelope of the reflected signal. **Fig. 20** shows the result of a theoretical model and experimentally measured envelope pulse reflected from the structure under study. As can be seen, the theoretical calculation results are in good agreement with the experimental data. Experimental results have shown that during unsteady reflection of an electromagnetic pulse from a three-layer filter with maximally flat frequency response are formed by four short pulse. The provisions of pulses coincides with the maximum derivative of the envelope of the incident signal. The signal generated during unsteady considered reflections from structures fundamentally different from the signal reflected from a single layer filter.

As in the case of half-wave filter, a loss of structure layers have a significant influence on the unsteady reflection. It also shows that there is a time

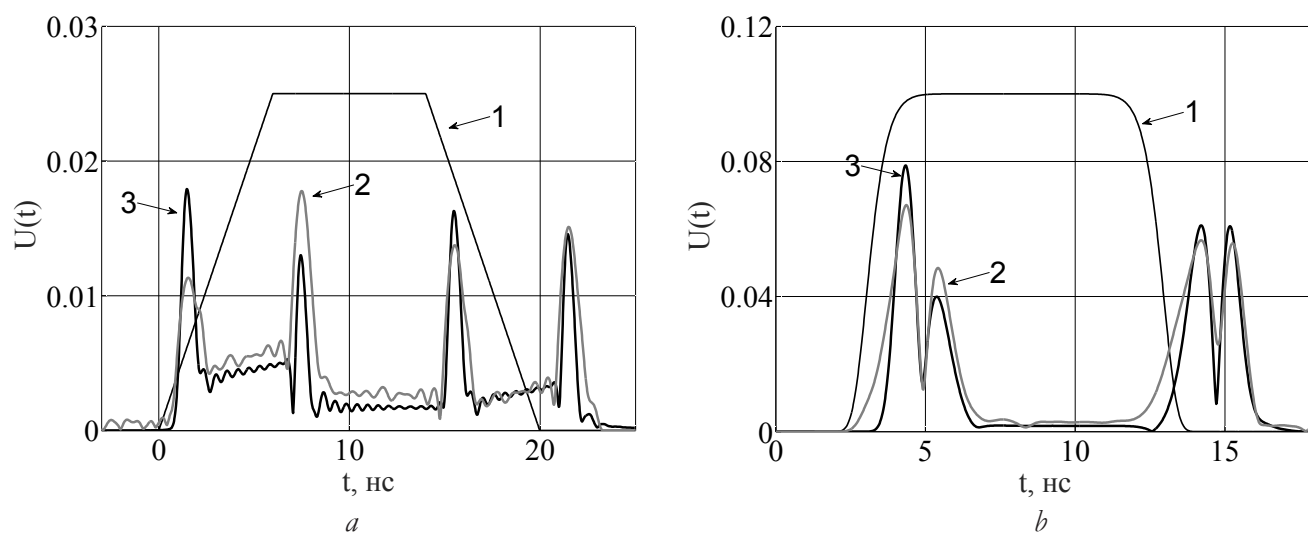


Рис. 20. Огибающая отраженного сигнала для падающего импульса с трапецидальной огибающей (а) и с супергауссовой огибающей (b) от трехслойного фильтра: 1 – огибающая падающего сигнала; 2 – эксперимент; 3 – теория.

when the amplitude of the reflected signal tends to zero.

### 5. CONCLUSION

This paper presents an overview of the main results of our studies in recent years the phenomenon of non-stationary reflection of short and ultrashort (about 100 periods of the field oscillations) of electromagnetic pulses of microwave laminates. This phenomenon is particularly observed in a contrasting comparability duration nonstationary transient interference waves in a multilayer structure with the duration of the incident pulse.

In the course of research it has been refined a theory of non-stationary reflection pulse signals from interference multilayer structures. The existing theoretical apparatus is supplemented with the influence on the process of non-stationary reflection losses in the layers of the multilayer interference structure and strong waveguide dispersion.

Developed experimental methods for studying non-stationary process of reflection of ultrashort electromagnetic pulses from multilayer interference structures in the microwave range. results of experimental observation of the phenomenon of non-stationary reflection amplitude modulated signal from interference multilayer structure obtained for the first time in the microwave range.

It was found that the reflection amplitude-modulated signal by a half-wave layer lossy always exists a time when the non-zero amplitude when the amplitude of the incident signal reflected signal tends to zero and that the phase changes by

$\pi$ . In the presence of small losses in the layers of the multilayer structure the amplitude reflection coefficient depends linearly on the magnitude of the losses, while the formation of the phase pattern of the interfering wave occurs in this case as well as in the absence of losses.

The task of matching loads with highly reflecting waveguide due to strong waveguide dispersion. The possibility to ensure complete containment of the incident wave energy into a load with virtually any reflectance via a matching structure consisting of only one layer, the thickness of which is close to a quarter-wave.

It revealed the presence of a more complex process in unsteady reflection multilayer structures with non-reflective class maximally flat frequency response, compared to multilayer structures having other functional dependence of the amplitude-frequency response.

It is shown that for small losses in the layers of the structure of a maximally flat frequency response envelope of the reflected signal can be approximately described by the N-th derivative of the envelope of the incident signal.

### REFERENCES

1. Petrich JW, Fleming GR. Ultrafast processes in biology. *Photochemistry and photobiology*, 1984, 40(6):775-780.
2. Kling MF, Vrakkin MJ. Attosecond Electron Dynamics. *Annual Review of Physical Chemistry*, 2008, 59(1):463-492.

3. Rulliere C. *Femtosecond Laser Pulses*. New York, Springer, 2004, 218 p.
4. Szipocs R., et al. Chirped multilayer coatings for broadband dispersion control in femtosecond lasers. *Photochemistry and photobiology*, 1994, 19(3):201-203.
5. Kartner FX, Matuschek N, Schibli T, Keller U. Design and fabrication of double-chirped mirrors. *Optics Letters*, 1977, 22(11):831-833.
6. Matuschek N, Kartner FX, Keller U. Analytical design of double-chirped mirrors with custom-tailored dispersion characteristics. *IEEE Journal of Quantum Electronics*, 1999, 35(2):129-137.
7. Vernon SP, et. al. Chirped multilayer coatings for increased x-ray throughput. *Optics Communications*, 1993, 18:672-674.
8. Dadashadze N, Romanov OG. Otrazhenie opticheskikh impulsov ot mnogosloynnykh dielektricheskikh struktur i microrezonatorov: chislennoe reshenie uravneniy Maksvella [Reflection optical pulses from multilayer dielectric structures and microcavities: numerical solution of Maxwell's equations]. *Vestnik BGU*, 2014,1(1):825-834 (in Russ.).
9. Dennis WM, Liebig C. Simulation of High Intensity Ultrashort Pulse Interactions with Dielectric Filters. *Proc. of SPIE*, 2007:5989-23.
10. Liebig CM, Dennis WM. Simulation of interactions of high-intensity ultrashort pulses with dielectric filters. *Optical Engineering*, 2007, 46(2):023801.
11. Dunning Sarah. Optimizing Thin Film Filters for Ultrashort Pulse Shaping. *Ph.D. thesis*, The University of Georgia, 2003.
12. Michielssen E, Ranjithan S, Mittra R. Optimal multilayer filter design using real coded genetic algorithms. *IEE Proceedings-J. Optoelectronics*, 1992, 139(6):413-420.
13. Chen LR. Ultrashort optical pulse interaction with fibre gratings and device applications. *Ph.D. thesis*, University of Toronto, 1997.
14. Chen LR, Benjamin SD, et. al. Ultrashort pulse reflection from fiber gratings: a numerical investigation. *Journal of Lightwave Technology*, 1997, 15(8):1503-1512.
15. Bystrov RP, Cherepenin VA. Teoreticheskoe obosnovanie vozmozhnostey primeneniya metoda generatsii moshchnykh nanosekundnykh impulsiv elektromagnitnogo izlucheniya pri sozdanii radiolokatsionnykh sistem elektronnoy bor'by dlya porazheniya ob'ektov [The theoretical justification of the possibility of generating high-power nanosecond pulses of electromagnetic radiation to create radar systems of electronic warfare for the destruction of objects]. *Journal radioelektroniki* (IRE RAS, the network edition), 2010, 4 (in Russ.).
16. Schamiloglu E. *High Power Microwave Sources and Technologies*. New York, Wiley&Sons, 2001.
17. Kozar AV, Bobrovnikov YuA, Gorokhov PN. Yavlenie nestatsionarnogo otrazheniya elektromagnitnykh voln s izmenyayushchey amplitudey ot sloistykh struktur [The phenomenon of non-stationary reflection of electromagnetic waves with varying amplitude from layered structures]. *Izvestiya RAN, Ser. Fiz.*, 2002, 12(1823):201-213 (in Russ.).
18. Bobrovnikov YuA, Gorokhov PN, Kozar AV. Preobrazovanie impulsiv s pomoshch'yu tonkosloynnykh struktur [Conversion of pulses via thin-layered structures.]. *Kvantovaya elektronika*, 2003, 53(11):1019 (in Russ.).
19. Weiner MA. Ultrafast optical pulse shaping: A tutorial review. *Optics Communications*, 2011, 284:3669-3692.
20. Bushuev VA. Vremennaya kompressiya impulsiv rentgenovskogo lazera na svobodnykh elektronakh v usloviyakh breggovskoy difraktsii [Time compression of X-ray free-electron laser pulses under conditions of Bragg diffraction]. *Radioelektronika. Nanosistemy. Infomatsionnye tekhnologii* (RENSIT), 2014, 6(2):177-187 (in Russ.).
21. Dunning FB. *Atomic, Molecular, and Optical Physics: Electromagnetic Radiation*. London, Academic Press, 1997, 406 p.
22. Bobrovnikov YuA, Kozar AV, Gorokhov PN. Nestatsionarnoe otrazhenie elektromagnitnykh impulsiv ot prosvetlyayushchikh tonkosloynnykh struktur [Non-stationary reflection of electromagnetic pulses from the thin-layer anti-reflective structures]. *Trudy VIII Vserossiyskoy shkoly-seminara "Volnovye yavleniya v neodnorodnykh sredakh"*, Moscow, MGU im. Lomonosova Publ., 2002, 1(5):53-54 (in Russ.).
23. Bobrovnikov YuA, Kozar AV, Gorokhov PN. Yavlenie nestatsionarnogo otrazheniya elektromagnitnykh voln ot prosvetlyayushchikh

- tonkoslotnykh struktur [The phenomenon of non-stationary reflection of electromagnetic waves from the thin-layer anti-reflective structures]. *Sb. dokladov nauchnoy konferentsii "Lomonosovskie chteniya". Sektsiya fiziki, podseksiya optiki i laseroy fiziki*. Moscow, Lomonosov MGU Publ., 2004, 1:31-33 (in Russ.).
24. Kozar AV. Interferentsionnye yavleniya v sloistykh strukturakh i ikh primenenie v zadachakh priema signalov i diagnostiki neodnorodnykh sred [Interference phenomena in layered structures and their application to problems of signal reception and diagnostics of inhomogeneous media.]. *Ph.D. thesis*, Moscow, Lomonosov MGU Publ., 2004.
  25. Born M, Wolf E. *Principles of optics*. Oxford-London, Pergamon Press, 1964.
  26. Kozar AV. Spectral characteristics of thin-layer interference matching systems. *Optics and Spectroscopy*, 1988, 64(5):1130-1134.
  27. Kozar AV. Opticheskie i strukturnye svoystva tonkosloynnykh interferentsionnykh soglasovateley [Optical and structural properties of thin-layer interference matchers]. *Optika i spektroskopiya*, 1985, 59(5):1132-1136 (in Russ.).
  28. Akhmanov SA, Vysloukh VA, Chirkin AS. *Optika femtosekundnykh lazernykh impulsov* [Optics femtosecond laser pulses]. Moscow, Nauka Publ., 1988.
  29. Vinogradova MB, Rudenko OV, Sukhorukov AP. *Teoriya voln* [Wave Theory]. Moscow, Nauka Publ., 1990, 432 c.
  30. Chipman RA. *Transmission lines*. New York, McGraw-Hill book company, 1968.
  31. Peres PLD, de Souza CR, Bonatti IS. ABCD matrix: a unique tool for linear two-wire transmission line modelling. *Intern. J. of Electrical Engineering Education*, 2003, 40(3):220-229.
  32. Matey GL, Yang L, Dzhons EMT. *Filtry SVCH, soglasuyushchie tsepi, tsepi svyazi* [Microwave filters, matching networks, connection circuits]. Moscow, Svyaz' Publ., 1971.
  33. Yee K. Numerical solution of initial boundary value problems involving Maxwell's equations in isotropic media. *Optical Engineering*, 1966, 14(2):302-307.
  34. Weiland T. A discretization method for the solution of Maxwell's equations for six-component fields. *Electronics and Communications AEU*, 1977, 31(3):116-120.
  35. Brekhovskikh LV. *Volny v sloistykh sredakh* [Waves in Layered Media.]. Moscow, Nauka Publ., 1973, 343 c.
  36. Kozar AV, Kolesnikov BS, Pirogov YuA. O primenenii metoda impedansnykh kharakteristik dlya analiza rasprostraneniya voln v mnogoslownnykh strukturakh s pogloshcheniem [Application of the method of impedance characteristics for the analysis of wave propagation in multilayer structures with absorption]. *Vestnik Mosk. univ., ser. Fizika, astronomiya*, 1978, 19(2):76-83 (in Russ.).
  37. Tikhonravov AV, Trubetskov MK. Modern design tools and a new paradigm in optical coating design. *Applied Optics*, 2012, 51(30):7319-7332.
  38. Vainstein LA. *Elektromagnitnye volny* [Electromagnetic waves.]. Moscow, Radio i svyaz' Publ., 1988.
  39. Rohde and Schwarz. *ZVT Vector Network Analyzers Operating Manual*. Munich, Germany: Rohde&Schwarz GmbH, KG, 2011.
  40. Agilent *Time Domain Analysis Using a Network Analyzer*. Application Note 1287-12. Agilent Technologies, Inc, USA, 2007:1-48.
  41. Ayficher E, Dzhervis B. *Tsifrovaya obrabotka signalov: prakticheskiy podkhod* [Digital Signal Processing: A Practical Approach]. Moscow, ID "Vil'yams" Publ., 2004, 992 c.
  42. Kozar AV, Trofimov AV. Yavlenie nestatsionarnogo otrazheniya impulsnykh signalov ot sloistykh struktur s poteryami [The phenomenon of non-stationary reflection of pulse signals from the layered structures with losses.]. *Vestnik Mosk. univ., ser. Fizika, astronomiya*, 2013, 5:38-43 (in Russ.).
  43. Kozar AV, Trofimov AV, Potapov AA. Protsess nestatsionarnogo otrazheniya korotkikh elektromagnitnykh impulsov ot mnogoslownnykh filtrov s maksimalno ploskoy amplitudno-chastotnoy kharakteristikoy [The process of non-stationary reflection of short electromagnetic pulses from the multilayer filters with maximally flat amplitude-frequency response]. *Journal radioelektroniki (IRE RAS, the network edition)*, 2016, 4:1-17 (in Russ.).
  44. Macleod HA. *Thin-Film Optical Filters*. London, Macmillan, 1986, 772 p.

45. Feldstein AL, Yavich LR. *Sintez chetyrekhpolyusnikov i vos'mipolyusnikov na SVCH* [Synthesis of microwave quadri- and eightpoles]. Moscow, Svyaz' Publ., 1971, 352 c.
46. Krepelka J. Maximally flat antireflection coatings. *Jemná Mechanika A Optika*, 1992, 37:53-56.
47. Schulz U, Schallenberg UB, Kaiser N. Symmetrical periods in antireflective coatings for plastic optics. *Applied Optics*, 2003, 42(7):1346-1351.
48. Kikoin IK (ed.). *Tablitsy fizicheskikh velichin. Spravochnik* [Tables of physical quantities. Directory]. Moscow, Atomizdat Publ., 1976, 1008 c.
49. Bur AJ. Dielectric properties of polymers at microwave frequencies: a review. *Polymer*, 1985, 26(7):963-977.

## DIRAC MATERIAL GRAPHENE

Elena F. Sheka

Russian Peoples' Friendship University of Russia, <http://www.rudn.ru>

117198 Moscow, Russian Federation

sheka@icp.ac.ru

*Abstract.* The paper presents an overview on the spin-rooted properties of graphene, supported by numerous experimental and calculation evidence. Correlation of odd  $p_z$  electrons of the honeycomb lattice meets a strict demand “different orbitals for different spins”, which leads to spin polarization of electronic states, on the one hand, and generation of an impressive pool of local spins distributed over the lattice, on the other. These features characterize graphene as a peculiar semimetal with Dirac cone spectrum at particular points of the Brillouin zone. However, spin-orbit coupling (SOC), though small but available, supplemented by dynamic SOC caused by electron correlation, transforms graphene-semimetal into graphene-topological insulator (TI). The consequent topological non-triviality and local spins are proposed to discuss such peculiar properties of graphene as high temperature ferromagnetism and outstanding chemical behavior. The connection of these new findings with difficulties met at attempting to convert graphene-TI (usually taken as SM) into semiconductor one is discussed.

*Keywords:* graphene, Dirac fermions, quasi-relativistic description, hexagonal honeycomb structure, local spins, open-shell molecules, spin-orbital coupling, quantum spin Hall insulator, high temperature ferromagnetism, chemical activity

PACS: 51.05.ue

*Bibliography* – 79 references

Received 14.10.2016

RENSIT, 2016, 8(2):131-153

DOI: 10.17725/rensit.2016.08.131

### CONTENTS

1. INTRODUCTION (131)
2. RELATIVISTIC ELECTRONS OF GRAPHENE (132)
3. CHARACTERISTICS OF THE DIRAC CONE SPECTRA (133)
4. DIRAC FERMIONS AND TOPOLOGICAL NON-TRIVIALITY OF GRPHENE (135)
5. MOLECULAR ESSENCE AND TOPOLOGICAL CHARACTER OF GRAPHENE MAGNETISM (136)
  - 5.1. General Features of Experimental Observations (136)
  - 5.2. Magnetic Behavior of Graphene Molecules (137)
  - 5.3. High-Temperature Ferromagnetic Topological Insulating Phase of Graphene (139)
6. LOCAL SPINS IN GRAPHENE MOLECULE LANDSCAPE (142)
7. INTRODUCTION TO GRAPHENE COMPUTATIONAL SPIN CHEMISTRY (145)
8. COMMENTS ON CONVERTING GRAPHENE FROM SEMIMETAL TO SEMICONDUCTOR (146)

### 9. CONCLUSION (149)

### REFERENCES (150)

#### 1. INTRODUCTION

The current paper concerns three main issues underlying spin features of graphene: (1) a significant correlation of the  $p_x$  odd electrons, exhibited in terms of spin peculiarities of the unrestricted Hartree-Fock (UHF) solutions, (2) disputable spin-orbital coupling (SOC) and (3) the crucial role of the C=C bond length distribution over the body in exhibiting the spin-based features. Despite numerous and comprehensive studies of graphene performed during the last decade [1], the spin-rooted peculiarities, involved in the graphene physics and chemistry, still remain outside the mainstream. However, graphene is doubtlessly of a spin nature and the main goal of the paper is to clarify how deeply electronic states of graphene molecules and solids are spin-burdened.

## 2. RELATIVISTIC ELECTRONS OF GRAPHENE

Implementing Löwdin's statement "different orbitals for different spins" [2], non-relativistic correlation effects in electronic properties are well pronounced and form the ground for peculiarities of chemical [3, 4], magnetic [5], and mechano-chemical [6] behavior of graphene. In contrast, the relativistic SOC contribution related to graphene bodies consisting of light elements is expectedly small (see [7] and references therein). Despite this, the quasi-relativity theory has accompanied graphene crystal from the first consideration of its electronic structure [8, 9]. The primitive cell of graphene is simple and contains two atoms. However, these cells are additionally hexagonally configured to fit the honeycomb lattice, on the one hand, and to provide the hexagonal and flat first Brillouin zone (BZ), on the other. The BZ contains two nonequivalent sets of three vertices  $K$  and  $K'$  each while  $\Gamma$  point is located at the hexagon centre. In the tight-binding approach it is typical to separate the Hamiltonian for the  $\pi$  (odd  $p_z$ ) electrons from that for the  $\sigma$  electrons, which is strictly valid only for a flat graphene sheet. Thus obtained [10], the total band structure of graphene crystal is of particular image, typical view

of which is presented in **Figure 1a**. Since referring relativistic analogy concerns  $\pi$  bands, it is conventional to just consider the latter. The relevant low-energy quasiparticle states at the Fermi level, marked by a tinny band in the figure, form six pairs of touching cones with the tips at  $K$  ( $K'$ ), two pairs of which are shown in Fig. 1b. The total low-energy electronic spectrum of the graphene six pairs is described [11] as

$$E_1(k_0 + \kappa) = E^0 - \left(\frac{\hbar p_0}{m}\right) \kappa,$$

$$E_2(k_0 + \kappa) = E^0 + \left(\frac{\hbar p_0}{m}\right) \kappa. \quad (1)$$

Here  $E^0$  and  $k_0$  are the Fermi energy and quasiparticle momentum at points  $K$  ( $K'$ ) while the  $E_1$  and  $E_2$  spectra are related to the conducting and valence bands, respectively. A detailed description of parameter  $\hbar p_0/m$  is given in Ref. [11]. Equations (1) are well similar to those related to Dirac's massless fermions due to which the low-energy quasiparticles in the vicinity of  $K$  ( $K'$ ) points (Dirac points later) can formally be described by the Dirac-like Hamiltonian

$$\hat{H} = \hbar v_F \begin{pmatrix} 0 & k_x - ik_y \\ k_x + ik_y & 0 \end{pmatrix} = \hbar v_F \boldsymbol{\sigma} \cdot \mathbf{k}, \quad (2)$$

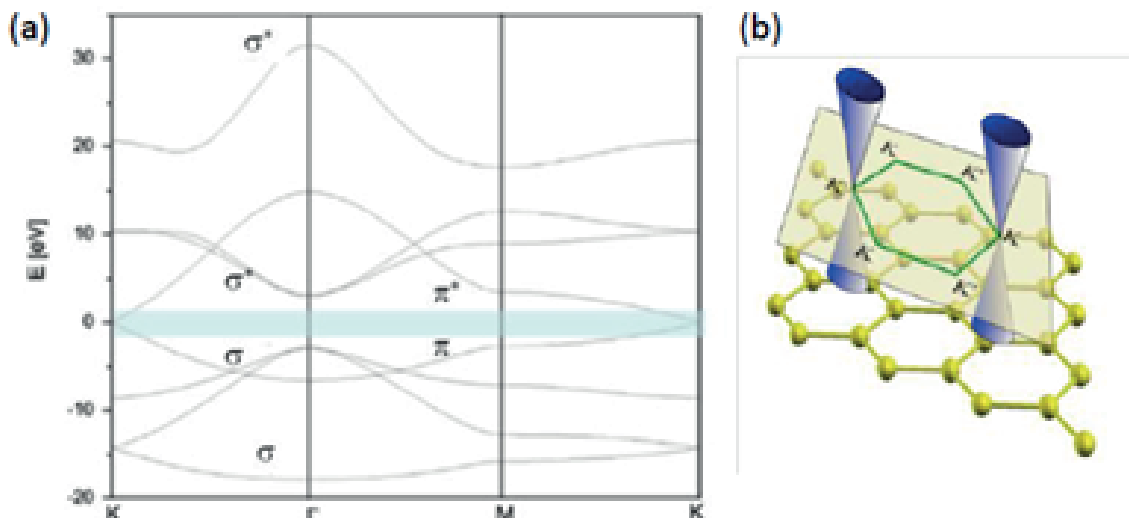


**Fig. 1.** (a) Widely presented view on the band structure of graphene. Fermi level is settled at zero. The bands below (above) the Fermi level are related to the valence (conductive) zones. (b) Two pairs of valence/conductive Dirac cones at  $K$  and  $K'$  points at the Fermi level.

where  $\mathbf{k}$  is the quasiparticle momentum,  $\sigma$  is the 2D Pauli matrix for pseudospins and the  $k$ -independent velocity  $v_F$  plays the role of the speed of light. The equation is a direct consequence of graphene's crystal symmetry that involves its honeycomb hexagonal lattice [9, 11]. Owing to this specific electron band structure, graphene was attributed to a Dirac material and until now graphene has been considered as a 'solid-state toy' for relativistic quantum mechanics [12-14]. Since the graphene massless Dirac fermions move with the Fermi velocity  $v_F \sim 10^6 \text{ ms}^{-1}$ , it is possible to mimic and observe quantum relativistic phenomena, even those unobservable in high energy physics, on table-top experiments at much lower energies due to the small value of the  $v_F/c$  ratio. Thus, a quite satisfactory consistency between theoretical predictions and experimental observations has even allowed one to speak about the observation of Dirac fermions in graphene. Taking them as physical reality, one has suggested a specific engineering of different Dirac fermions by modulating their Fermi velocity when attaching graphene to different substrates [15]. As seen in **Figure 2**, an impressive change of  $v_F$  from  $1.15 \cdot 10^6 \text{ ms}^{-1}$  to  $2.46 \cdot 10^6 \text{ ms}^{-1}$  is observed when substituting the  $\text{SiC}(000\bar{1})$  substrate by quartz.

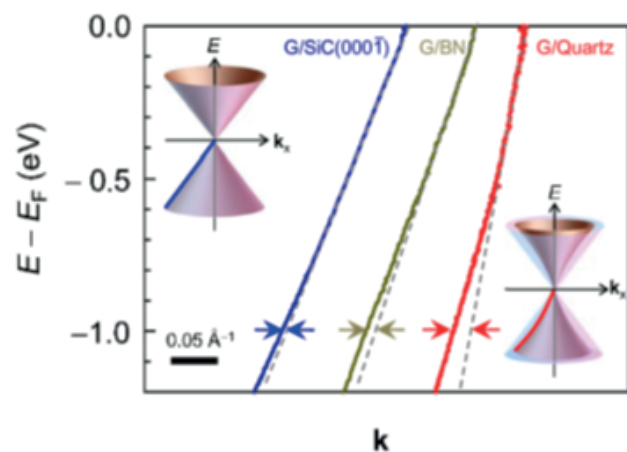


**Fig. 2.** Experimental  $E_2(k_0 + \kappa)$  dispersions for graphene on  $\text{SiC}(000\bar{1})$ , BN, and quartz. Insets exhibit changing in the graphene Dirac cones when going from weak (left) to strong (right) interaction with substrate [15].

### 3. CHARACTERISTICS OF THE DIRAC CONE SPECTRA

Dirac cones are a specific crystal symmetry effect, that suits any flat (even quasiflat) hexagonal arrangement of atoms similar to the honeycomb lattice that supply hexagonal BZ. Actually, the Dirac-fermion-like behavior of electronic states was observed for monolayers of silicon atoms on a  $\text{Ag}(111)$  surface voluntarily attributed to 'silicene' species [16] (see detailed discussion of the reality and virtuality of silicene in Ref. [17]). Similar behavior was predicted for higher tetrels of group 14 elements - germanene and stanene [18]. Particular attention should be given to a new class of artificial 'molecular graphenes' that mimic a honeycomb lattice structure. One of such 'molecule' was synthesized using individually placed carbon monoxide molecules on a  $\text{Cu}(111)$  surface [19]. A completed 'flake' of the molecular graphene is shown in topographic form in **Figure 3a**, demonstrating a perfect internal honeycomb lattice and discernible edge effects at the termination boundaries. In spite of the finite size of the structure obtained, due to which it should be attributed rather to 'molecular graphene' than to 'graphene crystal', as seen in Fig. 3b, two energy cones are characteristic for the energy band structure near the Fermi level. Estimations showed that the crystal-like behavior is well conserved when the molecule size is of 20 nm or more.

The other quite peculiar ability to create artificial graphene-like structure utilizes an optical honeycomb lattice to trap ultracold potassium atoms [20]. A Dirac-cone-like band structure is reproduced in this system as well. This optical method of creating the honeycomb lattice suggests a large possibility to investigate factors influencing the Dirac cones structure. Thus, by tuning the anisotropy of the lattice, the locations of the Dirac points may be shifted. When the anisotropy reaches a certain limit, the Dirac points merge and annihilate, while the evidence supporting the existence of a theoretically predicted topological phase

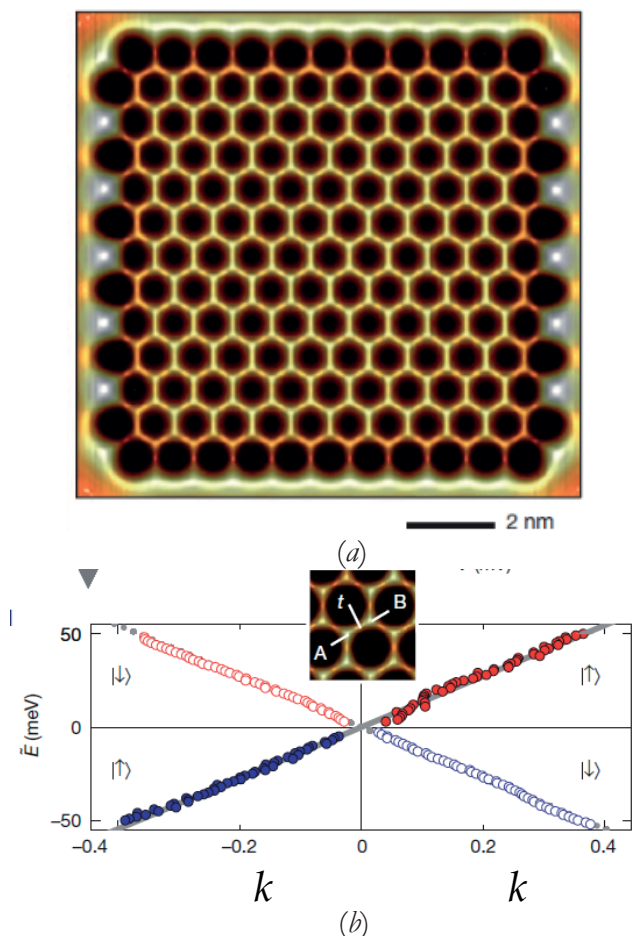


**Fig. 3.** (a) Constant current topograph of molecular graphene-like lattice composed of 1549 CO molecules (lattice constant,  $d=8.8 \text{ \AA}$ ). (b) Linearly dispersing quasi-particles revealed by the conductance spectra, plotted individually for sublattice A (filled circles: pseudospin  $s_x = +1/2$ ) and sublattice B (open circles: pseudospin  $s_x = -1/2$ ), measured at locations  $t$  illustrated in the inset. Adapted from Ref. [19].

transition was observed.

A number of theoretical suggestions on the Dirac-graphene-like structure is quite impressive. They cover virtual silicene, germanene, stannene (see review [21] and references therein), hydrogenated borophene [22] and arsenene [23]. All the Dirac species are described by hexagon packing of two-atom primitive cells. However, 'the primitive cell' may be considerably complicated as it takes place in the case of  $s$ -triazines with primitive cells composed of either  $C_6N_6$  or  $C_{12}N_6$ , and  $C_{24}N_6H_{12}$  molecular compositions [24], graphitic carbon nitride (GCN) with  $C_{14}N_{10}$  as a primitive cell [25], beautiful hexagon patterned lace of  $NiC_8S_2H_4$  molecules [26], the  $FeB_2$  monolayer with graphene-like boron sheet [27], an impressive number of MXenes [28] (a

new class of inorganic 2D compounds [29]), just appeared new compounds InSe [30] and so forth. The conservation of the hexagon packing of primitive cells mentioned above protects the presence of Dirac cones in the electronic spectra of all the species.

Virtually all the Dirac spectra discussed above were calculated not paying attention to if the studied system is open- or closed-shell one and exploiting closed-shell formalism. Only two calculations related to GCN  $C_{14}N_{10}$  [25] and metal-organic framework with primitive cell  $Ni_2C_{24}S_6H_{12}$  [26] were obtained taking into account that electrons with  $\alpha$  and  $\beta$  spins are correlated and separated in space. The open-shell approach immediately revealed the spin-polarization of the electronic spectra just doubling the band number and combining them in  $\alpha$  and  $\beta$  sets. **Figure 4a** presents the spin-polarized band structure of GCN while Fig. 4b is related to metal-organic framework. The configurations of the relevant primitive cells are shown under the spectra. Both primitive cells contain an even number of valence electrons,  $N^\alpha = N^\beta$  so that in neither case

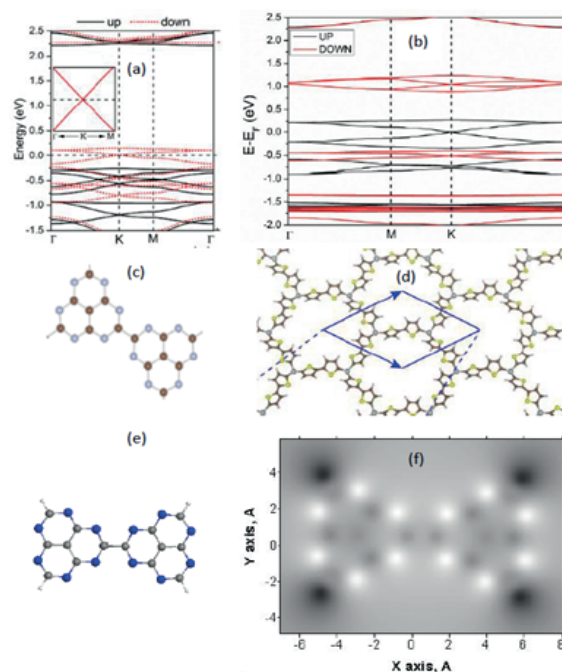


**Fig. 4.** Spin-polarized band structure and primitive cell of GCN  $C_{14}N_{10}$  (a) and (c) and  $Ni_2C_{24}S_6H_{12}$  (b) and (d). Adapted from Refs. [25] and [26], respectively. Equilibrium structure (e) and the ACS  $N_{DA}$  image map of local spin distribution (f) of the  $C_{14}N_{10}H_4$  molecule; UHF AM1 calculations.

are there unpairing free spins, since the total spin density is zero. In the case of GCN, the authors [25] explain the observed spin polarization from a chemical bonding analysis and attribute it to reducing the anti-bonding characteristics and density of states at Fermi level.

However, it is quite reasonable to suggest an alternative explanation and connect the obtained spin polarization caused by  $p_z$  electron correlation with the open-shell character of the electronic system of both cells [7]. In fact, as shown in Fig. 4e, in view of the UHF formalism the molecule  $C_{14}N_{10}H_4$ , that perfectly mimics the GCN primitive cell, is open-shell one with the total number of effectively unpaired electrons  $N_D = 5.34 e$  that are distributed as ‘local spins’ over nitrogen and carbon atoms with an average  $N_{DA}$  fractions of  $0.285 \pm 0.001 e$  and  $0.145 \pm 0.003 e$ , respectively (see Fig. 4f). Therefore, the band spin polarization becomes the manifestation of the electron correlation in 2D open-shell solids. As seen in Fig. 4, the spin polarization is well pronounced through over both BZs while at  $K$  points the Dirac spectra still remain gapless. Apparently, the feature is still caused by the hexagon packing of the molecules. Opening the gap at Dirac points needs the participation of SOC that has been so far ignored.

The disclosed connection between the open-shell character of the electronic system and spin polarization of the electronic band spectra brings us back to graphene. First, the character peculiarity was mentioned with relation to graphene magnetism and was illustrated by a convincing spin density map related to the rectangle graphene molecule (5, 5) NGr with five benzenoid units along the armchair and zigzag edges, respectively [5]. Second, it concerned the dispersion of the  $C=C$  bond length related to the body [31]. Now there is the third time when we have to realize the inevitability of spin polarization of the graphene electronic band structure. While the relevant results concerning the band structure of graphene are still in future,

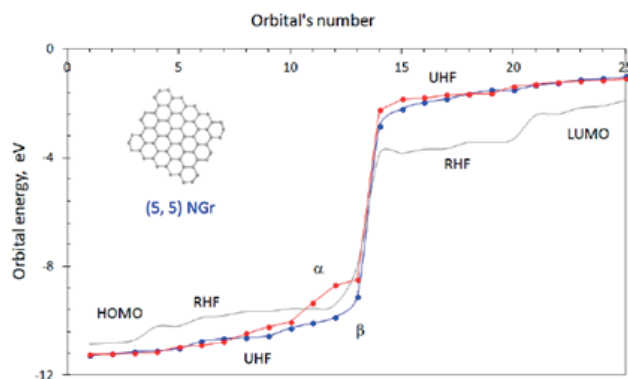


**Fig. 5.** Energies of 25 spinorbital in the vicinity of HOMO-LUMO gap of (5, 5) NGr molecule with bare edges; UHF AM1 calculations.

**Figure 5** presents the energy splitting related to a selected number of spinorbitals of the (5, 5) NGr molecule. A comparison of RHF and UHF results allows exhibiting correlation effects related to the studied open-shell molecule. The degeneracy of the RHF solution is caused by both high spatial ( $D_{2h}$ ) and spin symmetry of the molecule. As seen in the figure, when going from RHF to UHF formalism the UHF orbitals become clearly split into two families related to  $\alpha$  and  $\beta$  spins. The splitting value is different for different orbitals ranging from 0.02 eV to 1.12 eV. The orbitals splitting exhibits breaking spin symmetry that causes a remarkable distinguishing of orbitals related to different spins.

#### 4. DIRAC FERMIONS AND TOPOLOGICAL NON-TRIVIALITY OF GRAPHENE

As shown above, spin polarization does not affect the cones touching in the Dirac spectrum shown in Fig. 1 (see insert in Fig.4a) that may be violated by SOC only. At the same time, the intrinsic SOC of graphene is quite negligible due to which the gap emergence in its Dirac spectrum should be hardly expected. However, the electron correlation, which is significant, generates a dynamical SOC (see Ref. [32] and references therein) due to which it might be possible to expect some relativistic features, observable at even negligible intrinsic SOC but at a significant electron correlation. The first potential effect concerns the splitting of the

Dirac spectrum. To examine if the splitting can be observed for graphene experimentally, the team of Novoselov and Geim performed a particular investigation of how close one can approach the Dirac point [33]. It was shown that the approach value  $\delta E$  depends on quality and homogeneity of samples, on the resolution of experimental equipment, on temperature, and so forth. The best value  $\delta E$  related to free standing sample constitutes  $\sim 1$  meV at 4 K, thus establishing that there is no bandgap in graphene larger than 0.5 meV and that a combined SOC effect is less this value. Nevertheless, the finding does not disprove the existence of SOC as such, which may be important in the case of other effects, more sensitive to weak SOC. One of such potential effects concerns the topological non-triviality of graphene.

Actually, electron correlation and SOC are crucial characteristics of the topological non-triviality of 2D bodies. This question has been clear since the very time of the Dirac topological insulator (TI) discovery [34]. In the case of graphene, negligible SOC and complete ignorance of electron correlation, caused by calculations performed in the restricted formalism, were major obstacles to a serious discussion of this issue. However, the topological non-triviality covers a large spectrum of different topological states and phases involving both ideal Dirac TIs (or quantum spin Hall insulators – QSHI) and

other topological issues such as correlated topological band insulators, interaction-driven phase transitions, topological Mott insulators and fractional topological states [32] interrelation between which is determined by that one between SOC and correlation effects. **Figure 6** presents a phase diagram of topological states characteristic for 2D graphene-like honeycomb lattice (known as Kane-Mele model [9]) in relative coordinates of correlation energy ( $U$ ) and SOC ( $\lambda_{\text{SO}}$ ), which correspond to the Hubbard model. As seen in the figure, in the limit case  $\lambda_{\text{SO}} = 0$ , the relevant 2D structures should be attributed to either semimetal (SM) or quantum spin liquid (QSL) and antiferromagnetic Mott insulator (AFMI) with Heisenberg order ( $xyz$ ), depending on the correlation energy. The SOC increasing transforms SM solid and QSL into QSHI at a rather large scale of the correlation energy variation. When the value achieves the critical one shown by the straight line, the QSHI transforms into AFMI with easy plane order ( $xy$ ). In the limit case  $U = 0$ , the solid should behave as QSHI at all  $\lambda_{\text{SO}}$ .

Concerning graphene, recent estimation of  $U/t = 1.6$  [35] allows placing graphene far below the border with the QSL and AFM phases and attributing it to the SM phase if  $\lambda_{\text{SO}} = 0$ . However, the doubtless presence of the correlation of graphene  $p_z$  electrons causes unavoidable breaking of Kramers pairs of

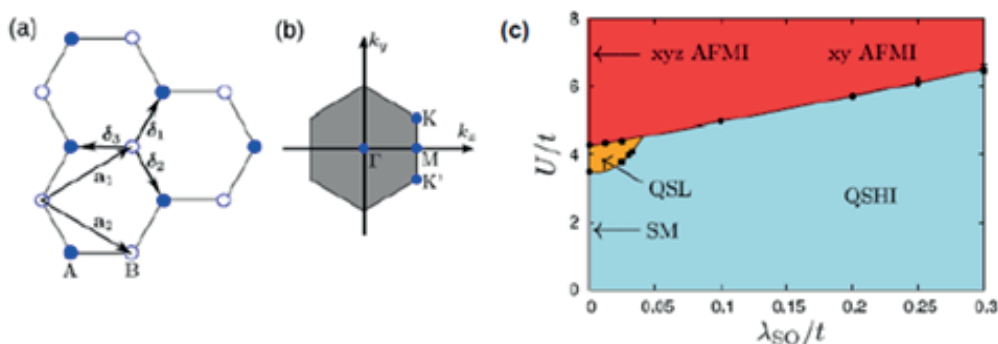


**Fig. 6.** (a) Kane-Mele model of the honeycomb lattice consisted of two sublattices A, B. (b) The hexagonal first Brillouin zone contains two nonequivalent Dirac points K and K'. (c) Phase diagram of the half-filled Kane-Mele-Hubbard model from quantum Monte Carlo simulations. Adapted from Ref. [32].

spinors [36], which violates the time-reversal symmetry, on the one hand, and stimulates the origin of dynamic SOC, on the other [32]. The findings shift graphene along the  $\lambda_{SO}/t$  axis in the depth of the QSHI phase thus providing a vivid topological non-triviality of graphene that might be revealed by not only the SOC-stimulated energy gap splitting. One of such topological effects has a direct bearing to peculiarities of graphene magnetism.

## 5. MOLECULAR ESSENCE AND TOPOLOGICAL CHARACTER OF GRAPHENE MAGNETISM

### 5.1. General Features of Experimental Observations

Repeatedly controlled extended graphene sheets are diamagnetic and magnetic response from large samples was empirically obtained only after either, say, heavy irradiation by proton beams or chemical modification (hydrogenation, oxidation and so forth) of graphite and/or graphene (see [37] and references therein). Thorough analysis, performed in each case, allowed excluding the impure origin of these features and attributing them to graphite/graphene itself, albeit induced by either micro- and/or nano-structuring of the samples or by defects of different topology created in due course of chemical modification (see some example [38-41]). It is important to mention that practically in all the cases a ferromagnetic response at room temperature was observed for graphene species with zero total spin density.

Another scenario concerns magnetic graphene of a paramagnetic behavior [40-42] recorded after either fluorination or bombarding graphene laminates consisting of 10-50 nm sheets by protons. The treatment provided the rupture of double  $C=C$  bonds inducing ‘spin-half paramagnetism’ in graphene. In both cases, the magnetization is weak and is characterized by one spin per approximately 1.000 carbon atoms. The ratio indicates that, in fact, the after-treatment magnetic crystal structure differs from

the pristine crystal structure and the difference concerns the unit cell that becomes  $\sim 33/2$  times larger than the previous one. Besides, the unit cell contains one additional spin thus lifting the spin multiplicity to doublet. Therefore, introduced adatoms and point defects cause a magnetic nanostructuring of the pristine crystal but with non zero spin density.

A doubtless confirmation that the nanostructuring of graphene sheets plays a large role in magnetization was obtained in the course of specifically configured experiments [43, 44]. Both cases concern meshed graphene or graphene in pores that were formed by either fully hydrogenated (oxidized) graphene discs in the first case or MgO nanoparticles in the second. A view on the sample and obtained results related to the first case can be obtained by looking at **Figure 7**. A large graphene sheet is put on porous alumina template (see Fig. 7a). The sample was subjected to either hydrogenation or oxidation through alumina pores thus leaving the graphene webs between the pores untouched. The web width  $W$  in a set of alumina templates differed by 10 to 50 nm. The ferromagnetic response of the webs at

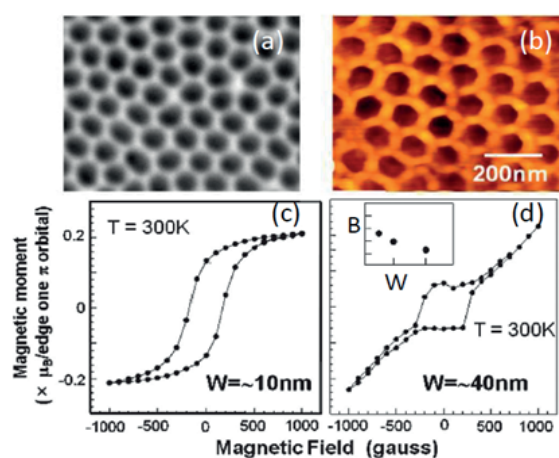


**Fig. 7.** (a) SEM image of nanoporous alumina template with mean pore diameter  $\sim 80$  nm and mean interpore spacing  $W \sim 20$  nm. (b) AFM image of graphene nanopore array formed by using (a) as an etching mask for the sample one-side hydrogenation. (c) and (d) Magnetization of monolayer graphene nanopore arrays at  $W \sim 10$  nm and 40 nm. Inset presents the dependence of the residual magnetization of graphene webs on their width  $W$ . Adapted from Ref. [43].

room temperature is presented in Figs. 7b and 7c at different web widths and the inset in Fig. 7c reveals the width dependence more clearly. In the second case, chemically modified dark disks in Fig. 7a were substituted with MgO nanoparticles, a set of which was covered by CVD grown graphene tissue [44]. The web width between the particles constituted  $\sim 10$  nm. The magnetic response from the sample is similar to that presented in Fig. 7b while the signal from much larger pieces  $\sim 100$  nm of technical graphene (reduced graphene oxide) was a few times less.

Therefore, nanosize occurrence and size-dependence, on the one hand, and high-temperature ferromagnetic character, on the other, are two peculiar features of zero-spin-density graphene magnetism. Evidently, the former concerns the magnetization magnitude and is associated with the molecular essence of graphene while the latter is relevant to the magnetism grounds and applies to its physics thus revealing the molecular-crystalline dualism of graphene once more.

## 5.2. Magnetic Behavior of Graphene Molecules

Zero-spin-density graphene implies the absence of free spins, since graphene belongs to a species for which  $N^\alpha = N^\beta$ . Usually such magnetic species were attributed to ‘singlet magnets’ (in terms of closed-shell approximation) and their magnetization was associated with the effect of the second order of perturbation theory (PT) implying the mixture of the ground singlet state with higher laying states of higher spin multiplicity. If the mixture is caused by the application of magnetic field, the effect is known as van Fleck magnetization [45]. However, graphene is an open-shell species due to which its singlet ground state has already been spin mixed due to odd  $p_z$  electron correlation. Since the spin contamination is the PT second order effect as well [7], there is no need to apply to the van Fleck effect to explain this magnetism. The magnetization ability of graphene has been

already ensured by its electronic system.

The observation of the PT second order contributions strongly depends on the energy denominator among other factors. For covalent species, triplet states are the main contributors due to which the energy denominator is  $2|J|$ , where  $J$  is the exchange integral that determines the energetic dependence of pure spin states in terms of the Heisenberg Hamiltonian  $H_{\text{ex}} = JS(S + 1)$ . The integral is usually referred to as the magnetic coupling constant [46]. A correct computation of the constant is quite complicated. Thankfully, about four decades ago Noodelman suggested a simple expression for the value determination for open-shell molecules in the framework of the broken spin symmetry approximation [46]

$$J = \frac{E^U(0) - E^U(S_{\text{max}})}{S_{\text{max}}^2} \quad (3)$$

Here,  $E^U(0)$  and  $E^U(S_{\text{max}})$  are energies of the UHF singlet and the highest-spin-multiplicity states, the latter corresponding to the  $S_{\text{max}}$  –pure-spin state. Thus obtained value is widely used and attributing it to molecular magnetism showed [48] that the measurable magnetization response can be fixed if  $|J| \leq |J_{\text{crit}}|$  where empirically estimated  $J_{\text{crit}}$  is of  $10^{-2} - 10^{-3}$  kcal/mol. Based on the molecular essence of graphene magnetism, let us look which  $J$  values can be expected for graphene molecules.

**Table 1** lists sets of three criterial quantities:  $\Delta E^{\text{RU}}$ ,  $\Delta \langle S \rangle^2$  and  $N_{\text{D}}$ , which characterize any open-shell molecule [4]. The

**Table 1**  
Identifying parameters of the odd electron correlation in rectangular nanographenes

$(n_x, n_y)$ NGrs	Odd electrons $N_{\text{odd}}$	$\Delta E^{\text{RU}}$ kcal/mol	$\delta E^{\text{RU}}, \%$	$N_{\text{D}}, e^-$	$\delta N_{\text{D}}, \%$	$\Delta \hat{S}_z^2$	$J$ , kcal/mol
(5,5)	88	307	17	31	35	15.5	-1.429
(7,7)	150	376	15	52.6	35	26.3	-0.888
(9,9)	228	641	19	76.2	35	38.1	-0.600
(11,10)	296	760	19	94.5	32	47.24	-0.483
(11,12)	346	901	20	107.4	31	53.7	-0.406
(15,12)	456	1038	19	139	31	69.5	-0.324

<sup>1</sup>AM1 version of UHF codes of CLUSTER-Z1 [49]. Presented energy values are rounded off to an integer.

<sup>2</sup>The percentage values are related to  $\delta E^{\text{RU}} = \Delta E^{\text{RU}}/E^{\text{RU}}(0)$  and  $\delta N_{\text{D}} = N_{\text{D}}/N_{\text{odd}}$ , respectively.

data were evaluated for a number of graphene molecules presented by rectangular ( $n_a$ ,  $n_z$ ) fragments ( $n_a$  and  $n_z$  count the benzenoid units along armchair and zigzag edges of the fragment, respectively). Consequently, the table as a whole presents the size dependence of the UHF peculiarities of the open-shell graphene molecules. As seen in the table, the parameters are certainly not zero, obviously greatly depending on the fragment size while their relative values are practically non size-dependent. Attention should be given to rather large  $N_D$  values, both absolute and relative, that manifest the measure of the  $p_z$  odd electrons correlation. It should be added as well that the relation  $N_D = 2\Delta\hat{S}^2$ , which is characteristic for spin contaminated solutions in the singlet state, is rigidly kept over all the molecules. The data are added by the magnetic constant  $J$  determined following Eq. 3.

As seen in Table 1, quantities  $\Delta E^{RU}$ ,  $N_D$  and  $\Delta\langle S \rangle^2$  gradually increase when the size grows due to increasing the number of atoms involved in the pristine structures. The relative parameters  $\delta E^{RU}$  and  $\delta N_D$  only slightly depend on the NGr size just exhibiting a steady growth of the parameters. In contrast,  $J$  values demonstrate quite different behavior. The values show a significant size-dependence, gradually decreasing by the absolute magnitude when the size grows. This dependence can be obviously interpreted as the indication of strengthening the electron correlation thus exhibiting the collective character of the event. The finding is expected to lay the foundation of peculiar size-effects for properties that are governed by these parameters, the first of which can be addressed to molecular ferrodiamagnetism. The diamagnetic behavior is provided by  $\sigma$  electrons while the ferromagnetic contribution is relevant to odd  $p_z$  ones.

As mentioned earlier, the primitive cell of graphene crystal, which determines the magnetic properties of an ideal crystal, involves two atoms joined by one  $C=C$  bond

of a benzenoid unit. The estimation of the  $|J|$  value for ethylene and benzene molecule with stretched  $C=C$  bonds up to  $1.42\text{\AA}$  in length gives  $|J|$  values of 13 kcal/mol and 16 kcal/mol, respectively. Despite the fact that ethylene and benzene molecules do not reproduce this cell exactly, a similar  $|J|$  constant of the cell is undoubted. Owing to this, the crystal should demonstrate the diamagnetic behaviour only. To provide a remarkable ‘ferrodiamagnetism’ means to drastically decrease the magnetic constant  $|J|$ . While this is impossible for a regular crystal, graphene molecules are more labile. Shown in Table 1, the smallest  $|J|$  of 0.3 kcal/mol is still large enough to provide a recordable magnetization of (15, 12) NGr molecular magnet, but the tendency is quite optimistic. Supposing the quantity to be inversely proportional to the number of odd electrons, it is possible to estimate the electron number which would satisfy  $|J_{crit}|$  of  $10^{-2} - 10^{-3}$  kcal/mol which gives us  $N \sim 10^5$ .

For rectangular NGr  $N$  odd electrons are supplied by  $N$  carbon atoms that, according to [50], is determined as

$$N = 2(n_a n_z + n_a + n_z). \tag{4}$$

To fit the needed  $N$  value, the indices  $n_a$  and  $n_z$  should be of hundreds, which leads to linear sizes of the NGr from a few units to tens nm. The estimation is rather approximate, but it, nevertheless, correlates well with the experimental observations of the ferromagnetism of activated carbon fibers consisting of nanographite domains of  $\sim 2$  nm in size [51] as well as with the data related to meshed graphene [43, 44] discussed earlier. The maximum effect was observed in [43] at the interpore distance of 20 nm after which the signal gradually decreased when the width increased. The behavior is similar to that obtained for fullerene oligomers [52], which led to the suggestion of a scaly mechanism of nanostructured solid state magnetism of the polymerized fullerene  $C_{60}$  that was confirmed experimentally.

The said above highlights another noteworthy aspect of the graphene magnetism attributing the phenomenon to size-dependent ones. The latter means that the graphene magnetization is observed for nanosize samples only, moreover, for samples whose linear dimensions fit a definite interval, while the phenomenon does not take place at either smaller or bigger samples size outside the critical region. Actually, an individual benzenoid unit (and benzene molecule) is only diamagnetic. When the units are joined to form a graphene-like benzenoid cluster, effectively unpaired electrons appear due to weakening the interaction between  $p_z$  odd electrons followed by stretching  $C=C$  bonds which causes the electrons correlation. The correlation accelerates when the cluster size increases, which is followed with the magnetic constant  $|J|$  decreasing until the latter achieves a critical value that provides a noticeable fixation of the spin mixing of the cluster ground state. Until the enlargement of the cluster size violates a molecular (cluster-like) behavior of odd electrons, the sample magnetization will grow. However, as soon as the electron behavior becomes spatially quantized, the molecular character of the magnetization will be broken and will be substituted by one determined by the electron properties of the primitive cell. Critical size parameters, controlling quantization of molecular properties depends on the kind of quasiparticles being considered. Addressing graphene magnetization, evidently it is Dirac fermions that control the quantizing and their mean free path  $l_{fm}$  determines the critical size parameter: when the cluster size exceeds  $l_{fm}$  the spatial quantization quenches the cluster magnetization.

Happily, just recently experimental data were published related to the study of size dependence of both the linearity of the fermion low-energy band  $E_{fm}(k)$  within the Dirac cones in the vicinity of the Fermi level and the shape of the spectrum. **Figure 8** presents a set of  $E_{fm}(k)$  spectra related to a polycrystalline graphene

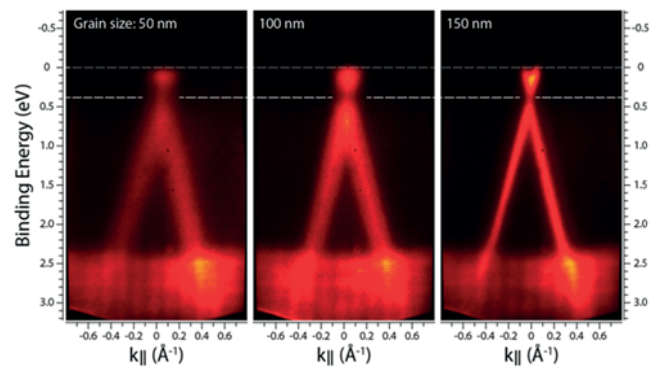


**Fig. 8.** Dirac's cones of continuous graphene film with average grain sizes of 50, 100, and 150 nm at the K point of graphene Brillouin zone obtained by ARPEES mapping.

Fermi energy is settled to zero. Adapted from Ref. [53].

sample consisting of grains of different sizes [53]. As seen in the figure, quantizing is well supported in grains of 150 nm, starts to be distorted in grains of 100 nm and is remarkably violated for grains of 50 nm. A considerable broadening of the spectrum in the last case allows putting the upper bound for  $l_{fm}$  around 50 nm. A comparable  $l_{fm}$  value of  $\sim 20$  nm follows from the data related to CO-hexagon structure [19].

Obviously, the transition from localized to quantized state is not abrupt. Thus at the pore width  $W = 40$  nm the residual magnetization only halves the maximum value at 20 nm (see inset in Fig. 7c) and continuous approaching zero may cover quite a large pore width. Actually, in the case of MgO pores [44], magnetization of rGO flakes with width  $\sim 100$  nm constitutes  $\sim 20\%$  of the value at the pore width of 10 nm. Nevertheless, the molecules linear size is evidently the governing factor for the magnitude of ferrodiamagnetism of pristine graphene.

### 5.3. High-Temperature Ferromagnetic Topological Insulating Phase of Graphene

If the discussion in the previous section allows one to understand when the magnetic behavior of graphene becomes measurable, it, however, does not answer the question of why the behavior is ferromagnetic and still exists at and above room temperature. In fact, it is difficult to expect ferromagnetism from a species with zero total spin density in the ground state.

Additionally, molecular magnetism is usually observed at quite low temperatures [48] and its fixation at room temperature seems highly unexpected. At the same time, there are physical objects for which high-temperature ferromagnetism is a characteristic mark. Thus, we come again to the peculiar Dirac materials known as TIs [34]. As shown in Section 4, quite considerable electron correlation and small, but available, intrinsic-dynamic SOC allow attributing graphene to weak QSHI. Evidently, the topological non-triviality is relevant to both crystalline and molecular graphene. Accepting this idea, let us see how it works with respect to the high-temperature ferromagnetism of graphene.

In view of electron correlation, graphene presents a honeycomb structure of carbon atoms with local spins distributed over them. The spin values are not integral and are determined by the relevant  $N_{DA}$  values forming an image ACS map similar to the one presented in Fig. 4f. Evidently, the exchange interaction between these local spins is responsible for the magnetic behavior of graphene. To determine the type of the behavior, let us use the formalism suggested for describing the magnetic impurities on the surface of a topological insulator [54]. In the presence of magnetic impurity or local spins, the main Hamiltonian describing the TI band structure in the form of Eq. 2 is substituted by a new one

$$H = \hbar v_F (\mathbf{k} \times \hat{\mathbf{z}}) \cdot \boldsymbol{\sigma} - H_{ex}, \quad (5)$$

where  $v_F$  is the Fermi velocity,  $\hat{\mathbf{z}}$  is the surface unit normal,  $\boldsymbol{\sigma}$  is the Dirac electron spin and

$$H_{ex} = \sum_r J_z s_z(\mathbf{r}) S_z(\mathbf{r}) + J_{xy} (s_x S_x + s_y S_y) \quad (6)$$

Here  $S_i(\mathbf{r})$  is the spin of a magnetic impurity located at  $\mathbf{r}$ ,  $s_i(\mathbf{r}) = \psi^*(\mathbf{r}) \sigma^i \psi(\mathbf{r})$  is the spin of the surface electrons and  $J_z$  and  $J_{xy}$  are the coupling parameters. When the impurity spin is polarized in the  $z$  direction the second term in Eq. 6 disappears. As every magnetic impurity opens a local gap in its vicinity, one may expect the system to be gapped everywhere, at least in the mean-field level. However, this

is not necessarily true if the magnetization of magnetic impurities is non-uniform. Meeting the problem and comparing the formation of magnetic domain wall and ferromagnetic arrangement, the authors [54] came to the conclusion that the magnetic impurities must be ferromagnetically coupled.

Sharing this viewpoint, a similar Hamiltonian  $H_{ex}$  was suggested to describe the Dirac-fermion-mediated ferromagnetism in a topological insulator [55]. The Hamiltonian  $H_{ex}$  reads

$$H_{ex} = J n_s \bar{S}_z \sigma_z. \quad (7)$$

Here  $\sigma_z$  is the  $z$  component of the electron spin and  $n_s$  is the areal density of localized spins with an average  $z$  component  $\bar{S}_z$ .  $J$  describes the exchange coupling between the  $z$  components of the Dirac electron spin  $\boldsymbol{\sigma}$  and the local spin  $\mathbf{S}$ , locking  $\boldsymbol{\sigma}$  perpendicular to the momentum  $\mathbf{k}$ . Following the same conclusion that every local spin opens the gap and the system must be gapped everywhere, we have to accept the necessity of a ferromagnetic configuration for local spins. Apparently, it is the consequence that explains ferromagnetic behavior of pure graphene samples.

Highly convincing evidence, strongly supporting suggestion that graphene is a typical TI, was received in the most recent [56]. **Figure 9** presents a molecular complex, presented by *Er*(trensal) single-ion magnets that was adsorbed on graphene/Ru(0001), on graphene/Ir(111) and on bare Ru(0001) substrates. On graphene, the molecules self-assemble into dense and well-ordered islands with their magnetic easy axes perpendicular to the surface. In contrast, on bare Ru(0001) the molecules are disordered exhibiting only weak directional preference of the easy magnetization axis. Accordingly, the ferromagnetic response is spin polarized in the two former cases while unpolarized in the case of the Ru(0001) substrate and additionally twice less by magnitude. Therefore, the topologically trivial bare ruthenium surface

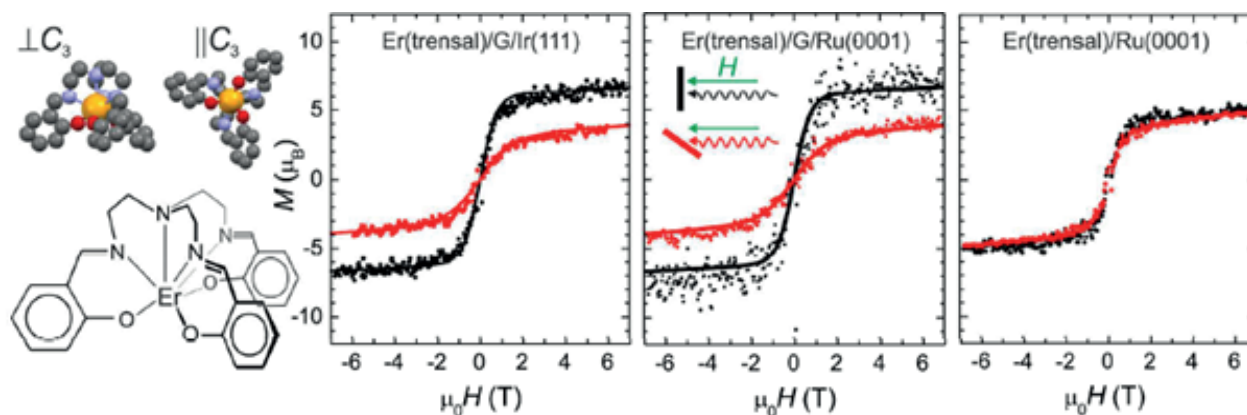


**Fig. 9.** Structural views and scheme of the molecular magnet *Er(trensyl)*. Coloring: orange: Er; blue: N; red: O; grey: C; H atoms are omitted for clarity. From left to right: magnetization curves at normal (black) and grazing (red) orientation of magnetic field with respect to the substrate surface. Adapted from Ref. [56].

has no effect on the molecular impurity ordering while the addition of a monolayer graphene covering leads to ferromagnetic ordering of the impurity characteristic for topologically non-trivial substrates, which were discussed above. Not only ordering but enhancement of ferromagnetic response evidences the TI nature of the graphene component of the hybrid substrates. In fact, the substitution of ruthenium by iridium has no additional effect so that all the observed peculiarities are caused by graphene layer. As for the response enhancement,  $J_z \langle s_z \rangle$  in the right-hand part of Eq. 7 acts as an effective magnetic field to magnetize the magnetic impurities. At the same time,  $J_z \langle s_z \rangle$  acts as the effective magnetic field to polarize the electron spin of TI. Obviously, such a double action of the exchange coupling leads to the enhancement of the magnetic response. When magnetic impurities form a continuous adlayer, additional enhancement should be expected due to the magnetic proximity effect (see the last publication [57] and references therein). Therefore, empirically confirmed graphene behaves as a typical TI, which leads to a severe reconsideration of its physical properties discussed mainly without taking into account this drastically important fact.

## 6. LOCAL SPINS IN GRAPHENE MOLECULE LANDSCAPE

The local spins of graphene, which are actively involved in the manifestation of its topological non-triviality discussed above, are associated with effectively unpaired  $p_z$  electrons and are one of the most important consequences of the UHF formalism applied to the graphene molecule open-shell ground state [3]. As seen in Table 1, bare graphene molecules are characterized by rather large total numbers of such electrons  $N_D$  that constitute more than one third of the total number of the odd  $p_z$  electrons. It means that the molecules are strongly radicalized thus exhibiting high chemical activity. While the total number of effectively unpaired electrons is the quantitative measure of the activity of the whole molecule, or *molecular chemical susceptibility* (MCS) introduced in [58], their partitioning over molecule atoms describes the *atomic chemical susceptibility* (ACS) in terms of  $N_{DA}$  due to which image maps of their distribution over atoms present a chemical portrait of the associated molecules [59]. Such maps of graphene molecules have a very particular, but therewith standard image which allows both disclosing the local spin distribution over atoms and considering chemical activity of the molecules at the quantitative level.

**Figure 10** presents the  $N_{DA}$  distribution (the ACS  $N_{DA}$  image map below) over atoms of the (11, 11) NGr bare molecule. As seen in the

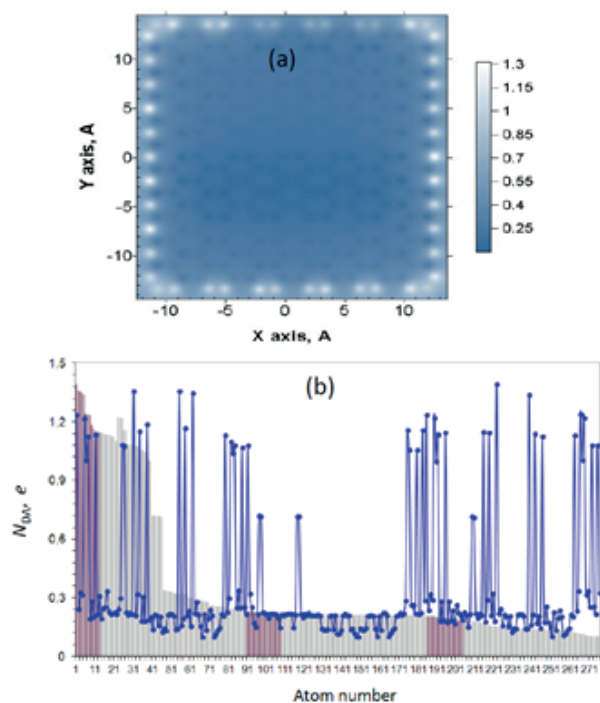


**Fig. 10.** (a) Equilibrium structure and ACS  $N_{DA}$  image map of the (11, 11) NGr molecule with bare edges. Scale bar matches  $N_{DA}$  values in e. (b)  $N_{DA}$  plotting from output file (curve with dots) and max  $\rightarrow$  min  $N_{DA}$  distribution (histogram). For the first 46 atoms: the histogram reveals first 22 zigzag edge atoms while next 24 bars (from 23 to 46) are related to armchair edge atoms. UHF AM1 calculations. figure, according to this parameter, the graphene molecule is definitely divided into two drastically different parts, namely, the circumference involving 46 edge atoms and internal honeycomb zone, or basal plane. Since the difference of the maximum  $N_{DA}$  values in the two areas is six-fold, the basal plane is practically invisible in Fig. 10a, while keeping a considerable  $N_{DA}$  of  $\sim 0.2$  e in average. The value rising over the average occurs only for 40 atoms adjacent to the molecule perimeter of edge atoms, for which  $N_{DA}$  varies from 0.34 e to 0.22 e. This atom fraction is clearly seen in the histogram in Fig. 10b at atom numbers from 47 to 86.

Presented in the figure is the chemical portrait of the bare (11, 11) NGr molecule. As seen from the histogram in Fig. 10b, the chemical activity of the graphene molecule atoms greatly varied within both the circumference and basal plane, more significantly within the first one. In the histogram the most intense 46 edge atoms

belong to 22 and 24 atoms related to zigzag and armchair edges, respectively. For zigzag atoms  $N_{DA}$  values fill the region 1.39-1.10 e, while the latter for armchair atoms is much wider and constitutes 1.22-0.71 e.

Qualitatively, the picture is typical for graphene sheets of any size. Modern fascinating experimental techniques allow confirming the above statement. Thus, as shown in [3, 7], the advanced atom-resolved AFM is able to fix local spins in a pentacene molecule when using a CO-terminated gold tip. Since this experiment provides monitoring of the molecule chemical activity, a close similarity of the AFM image and the relevant ACS  $N_{DA}$  map occurred quite expected. Happily, such a justification is available now for (n, 3) graphene nanoribbon as well [60]. As in the case of pentacene, the scanning transmission electron microscope (STEM) image of the nanoribbons (Figure 11a) is in good consent with the calculated  $N_{DA}$  map of the (15, 3) NGr molecule (Fig. 11b) thus, in particular, evidently justifying a peculiar two-zone character of the graphene pool of effectively unpaired electrons.

The variety of electron densities of carbon atoms along and perpendicular to the edges of

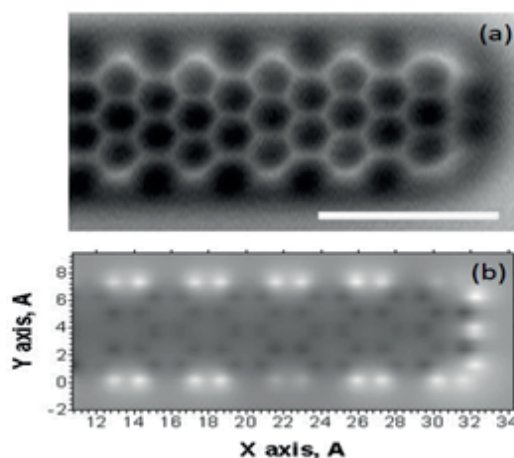


**Fig. 11.** (a) Constant-height high-resolution AFM image of the zigzag end of graphene nanoribbon obtained with CO-terminated tip. White scale bar: 1 nm. Adapted from Ref. [60]. (b) ACS  $N_{DA}$  image map of one of the zigzag ends of the (15, 3) NGr molecule with bare edges. UHF AM1 calculations.

a graphene flake has been clearly demonstrated just recently by site-specific single-atom electron energy loss spectroscopy (EELS) using the annular dark field (ADF) mode of a low-voltage STEM [61]. **Figure 12** discloses a highly informative picture related to the states of carbon atoms in the vicinity of zigzag and armchair edges. As seen in the figure, the site-dependent peculiarities are observed in the low-energy parts of the EELS spectra, which present  $K$ -edges of the carbon EELS signals. All the low-energy spectra involve a characteristic EELS peak  $P_b$  at 285 eV related to the excitation transformation of a core  $s$ -electron to an unoccupied  $\sigma^*$  orbital. Additional peaks at 281 eV ( $P_z$ ) and 282.8 eV ( $P_a$ ) for the zigzag and armchair edge atoms, respectively, are caused by the  $s$  electron excitation to an unoccupied  $p_z^*$  orbital and the change to the profile of the EELS is related to variations in the local density of states. The peaks are well pronounced for edge atoms (spectrum 1), significantly decreasing in intensity for adjacent atoms (spectrum 2) and practically fully vanishing for carbon atoms on the flake basal plane (spectra 3 and 4). Additionally,

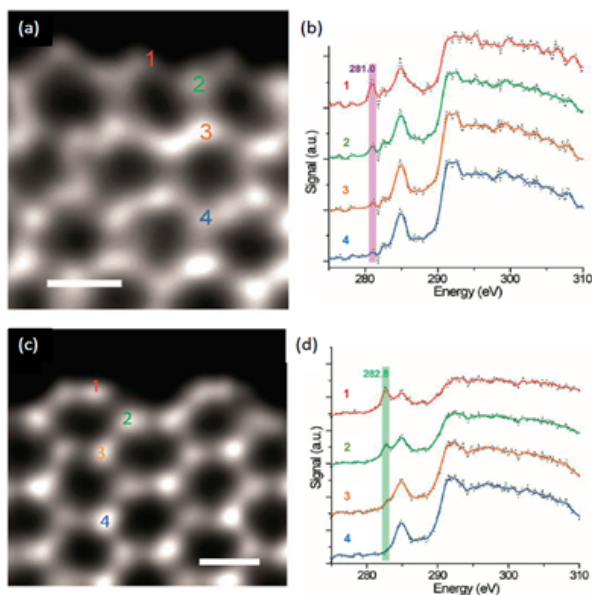


**Fig. 12.** STEM-EELS mapping of graphene edges. (a) ADF-STEM image and (b) EELS of zigzag edge from the regions numbered in (a). (c) ADF-STEM image and (d) EELS of armchair edge from the regions numbered in (d). White scale bar: 2 Å. Numbers and their colors on ADF-STEM images and EELS spectra coincide. Adapted from Ref. [61].

EELS spectra across the edge vary markedly for both zigzag and armchair atoms. As seen in **Figure 13a**, the spectra of two neighboring zigzag atoms (8 and 10) differ so greatly that the peak  $P_z$  is substituted by the peak  $P_a$ . The latter structure is conserved for the adjacent atom 9, albeit with changes in the intensity distribution between  $P_a$  and  $P_b$  peaks. EELS spectra in Fig. 13b exhibit the difference in the behavior of the neighboring armchair atoms expressed in changing the  $P_a/P_b$  intensities ratio.

The discussed spectral features are well consistent with the conclusion obtained from the above analysis of the  $N_{DA}$  distribution in Fig. 10b. Thus, first, the chemical bonding of zigzag and armchair edge atoms is different, bigger in the latter case, which is consistent with the lower chemical activity of the armchair edge atoms compared with the zigzag ones. Second, atoms of the adjacent-to-edge rows demonstrate a transient state between the edge and bulk one that correlates well with the activity of 40 adjacent atoms (from 47 to 86) in the histogram

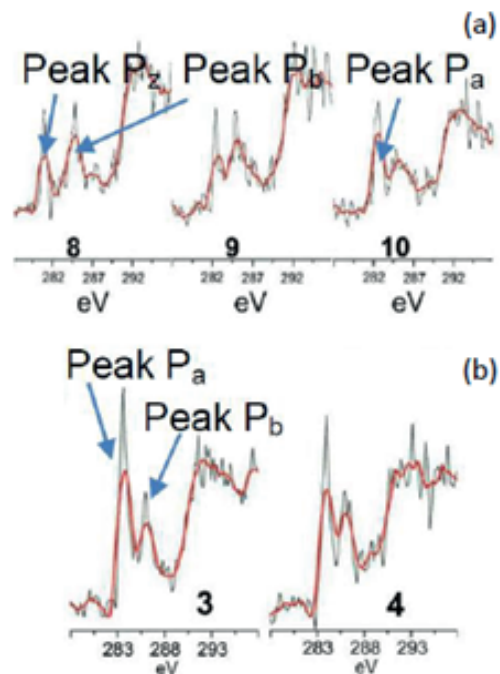


**Fig. 13.** EELS spectra at the edges of graphene flake. (a) Neighboring zigzag atoms (atoms 8 and 9) and adjacent atom between them (atom 9). (b) Neighboring armchair atoms (atoms 3 and 4).  $P_z$ ,  $P_a$  and  $P_b$  match peaks at 281 eV, 282.8 eV, and 285 eV, respectively. Adapted from Ref. [61].

in Fig. 10*b*. Third, inside the region, the perimeter of which is formed by adjacent atoms, the carbon atoms can be attributed to the basal-plane ones. Fourth, the electron density as well as ACS  $N_{DA}$  of the edge, adjacent, and bulk atoms significantly varies thus demonstrating that the atom groups are not rigidly standardized and might be very sensitive to external actions due to which graphene molecules are very changeable.

The two-zone electron density image of bare graphene molecule is not new. This feature lays the foundation of a large number of theoretical-computational considerations concerning the particular role of edge atoms in graphene begun in 1996 [62] and lasting until today (see a collection of papers [63-66] and references therein). The graphene objects studied were mainly pencil-made with a regular honeycomb structure described by standard  $C=C$  bonds of 1.42 Å in length and identical zigzag and armchair edge atoms. The results obtained concern the two-zone electronic structure and the attribution of the edge atoms peculiarity to the expected particular magnetic behavior of graphene flakes and, particularly, nanoribbons. However, the latter expectations proved quite illusive and as shown experimentally, the magnetic behavior of graphene samples is not directly connected with peculiar features of their edge atoms. It is worthwhile to keep in mind a skeptical comment of Roald Hoffmann concerning his “Small but strong lessons from chemistry to nanoscience” [67]: “There is a special problem that theory has with unterminated structures – ribbons cut off on the sides, polymers lacking ends. If passivation is not chosen as a strategy, then the radical lobes of the unterminated carbon atoms, or undercoordinated transition metals, will generate states that are roughly in the middle energetically, above filled levels, below empty levels in a typical molecule that has a substantial gap between filled and unfilled levels. If such levels – states, the physicists call them – are not identified as “intruder” states, not really real, but arising from the artifact of termination, they may be mistaken for real states

in the band gap, important electronically. And if electrons are placed in them, there is no end to the trouble one can get into. These band gap states are, of course, the origin of the reactivity of the terminated but not passivated point, line, or plane. But they have little to do with the fundamental electronic structure of the material”.

## 7. INTRODUCTION TO GRAPHENE COMPUTATIONAL SPIN CHEMISTRY

Modern chemistry is heavily occupied with revealing reliable qualitative and better quantitative descriptors which can point to the consequences of chemical reactions. UHF formalism of open-shell molecules suggests unique quantitative descriptors MCS  $N_D$  and ACS  $N_{DA}$ . For molecules with even number of electrons  $N_{DA}$  is identical to the atom free valence [68]. Consequently, free valence of atom  $A$ ,  $V_A^{free}$ , is defined as

$$V_A^{free} = N_A^{val} - \sum_{B \neq A} K_{AB}. \quad (8)$$

Here  $N_A^{val}$  is the number of valence electrons of atom  $A$  and  $\sum_{(B \neq A)} K_{AB}$  presents a sum over the generalized bond index

$$K_{AB} = |P_{AB}|^2 + |D_{AB}|^2, \quad (9)$$

where the first term is the Wiberg bond index while the second term is determined by taking into account the spin density matrix. The  $V_A^{free}$  distribution (curve with dots) alongside with the ACS  $N_{DA}$  (histogram) for the (5, 5) NGr molecule is shown in **Figure 14**. As seen in the figure, the

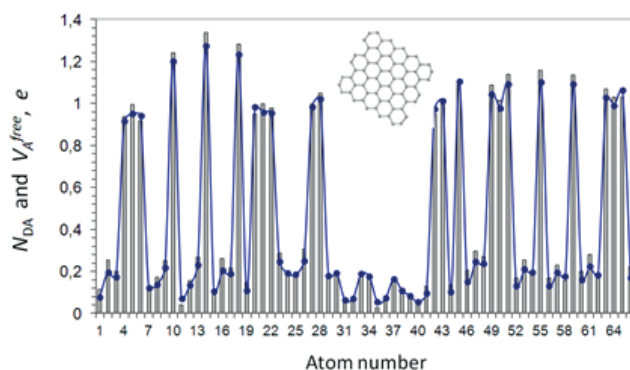


**Fig. 14.** ACS  $N_{DA}$  (histogram) and free valence  $V_A^{free}$  (curve with dots) distributions over atoms of the (5, 5) NGr molecule. Inset: equilibrium structure of the (5, 5) NGr molecule. UHF AM1 calculations.

first steps of any chemical reaction occur at the molecule periphery. Since this reactivity area is largely spread in space, the formation of the first monoderivative does not inhibit the molecule reactivity so that the reaction will continue until the reaction ability is satisfied. This means that any chemical modification of graphene starts as polyderivatization of the pristine molecule at its circumference.

The excellent agreement of  $N_{DA}$  and  $V_A^{free}$  values shows that the former is actually a quantitative ACS measure and can serve a quantitative descriptor of the molecule target atoms, for which atom-atom contacts are the most desirable in addition reactions. Thus, the values distribution over molecule atoms forms a unique ACS  $N_{DA}$  map, which opens a transparent methodology of a successive algorithmic computational synthesis of any graphene polyderivatives, just selecting the graphene core atom at each step by the largest  $N_{DA}$  value. A successive use of this methodology was shown on examples of the hydrogenation [69] and oxidation [70] of the (5, 5) NGr molecule.

As it turns out, already the first addition of any reactant, or modifier, to the edge atom of graphene molecule, chosen by the highest ACS, causes a considerable change in the pristine ACS  $N_{DA}$  image map thus allowing the exhibition of the second edge atom with the highest ACS to proceed with the chemical modification and so forth. This behavior is common to graphene molecules of any size and shape. In what follows, the behavior feature will be demonstrated on the example of the (5, 5) NGr molecule that was chosen to simplify the further presentation. **Figure 15** presents a set of (5, 5) NGr polyhydrides and polyoxides obtained in the course of the first stage of the relevant per step reactions that concern framing the bare molecule. Two important conclusions follow from the figure. First, in spite of the seemingly local change of the molecule structure caused by the addition, the second target carbon atoms does not correspond to the atom that

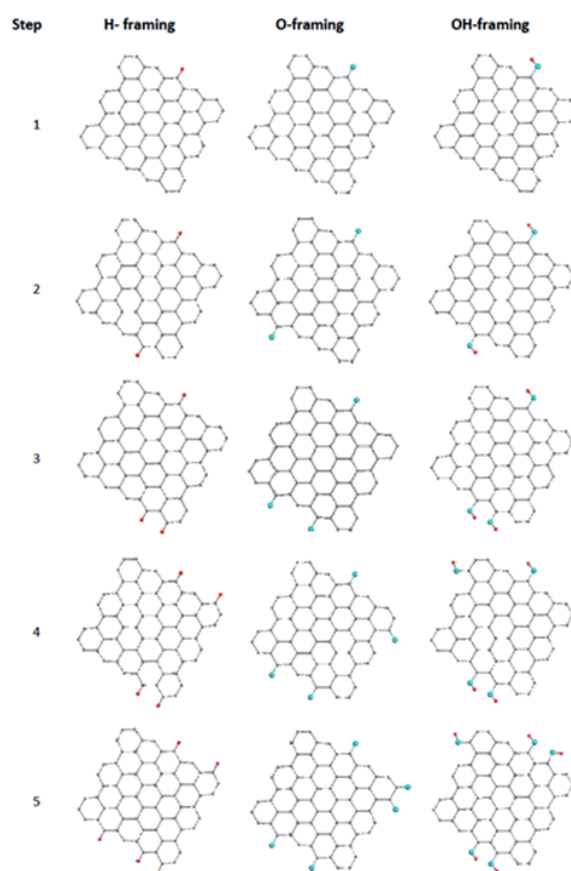


**Fig. 15.** Equilibrium structures of the (5,5) NGr polyhydrides and polyoxides related to 1st, 2nd, 3rd, 4th, and 5th steps obtained in the course of the relevant stepwise reactions. Gray, blue, and red balls mark carbon, oxygen, and hydrogen atoms, respectively. UHF AM1 calculations.

is the second one of the highest activity in the  $N_{DA}$  list of the pristine molecule. Second, this atom position, as well as the sequence of steps, varies depending on the chemical nature of the addends. Both features are the result of the redistribution of  $C=C$  bond lengths over the molecule, thus revealing the collective action of its unpaired electrons and/or local spins.

## 8. COMMENTS ON CONVERTING GRAPHENE FROM SEMIMETAL TO SEMICONDUCTOR

Despite its numerous extraordinary properties and huge potential for various applications, one of the greatest challenges in using graphene as an electronic material is the lack of a sizable bandgap. Accordingly, graphene is intrinsically a zero-gap QSHI, but a semimetal in the view of most. The gap absence significantly limits the use of graphene in many applications where

semiconducting materials with a suitable bandgap are required. Researchers have been searching for effective ways to produce semiconducting graphene and have developed various methods to generate a bandgap in graphene. Despite extensive investigation in the laboratory, the production of semiconducting graphene still faces many challenges. A detailed description of problems on the way as well as suggestions for their resolving is given in review [71]. Let us look at the problems from the viewpoint of obvious ‘underwater stones’ provided by the common properties of the graphene chemistry.

When categorizing methods to produce semiconducting graphene, three groups were classified: (1) morphological patterning of graphene sheets into nanoribbons, nanomeshes, or quantum dots to induce quantum confinement and edge effects; (2) chemical modification, doping, or surface functionalization of graphene to intentionally interrupt the connectivity of the  $\pi$  electron network; and (3) other methods, e.g., use of two graphene layers arranged in Bernal stacking (or AB stacking) to break the lattice symmetry, and applying mechanical deformation or strain to graphene.

Following the scheme proposed in [71] and shown in **Figure 16**, techniques of the first group meet problems concerning the basic edge property of the graphene molecule that is obviously a dangling-bond effect. Actually, cutting graphene sheets into nanoribbons increases the number of dangling bonds and, consequently, the number of unpaired

electrons  $N_D$  thus enhancing the ribbon’s radical properties. In its turn, the extra radicalization greatly promotes various chemical reactions in the ribbon’s circumference leading to a significant and sometimes even drastic reconstruction of the pristine graphene structure. Inserting nanomeshes results in the same effect due to the highly active periphery of the formed holes. Deposition of nanosize quantum dots highly disturbs the graphene substrate, changing the  $C=C$  bond length distribution, and thus causing the  $N_D$  growth if even not contributing by their own unpaired electrons. Therefore, cutting and drilling create a big ‘edges problem’ and do not seem to be proper technologies for the desired transformation of the graphene electronic system.

The chemical modification of graphene is not only a subject of interesting chemistry but has been repeatedly suggested as an efficient tool for the semimetal-semiconductor transferring needed for high-performance electronics [71]. It should be noted that these suggestions are based on results of computational studies that concern pencil-drawn pictures of graphene fragments including those or other chemical modifiers artificially spread over graphene sheets (see, for example, Refs. [72] and [73]). These and many other virtual structures, regularly distributed in space by applying periodic boundary conditions, exhibit electronic properties that are so badly needed for the application. However, the empirical reality is much less promising since so far none of regularly chemically modified graphene structure has been obtained. And the collective behavior of graphene unpaired electrons, protesting against any response localization, is the main reason for the failure.

The desired regular structures of chemically modified graphene are related to the graphene polyderivatives that are formed with the participation of carbon atoms on the basal plane. However, as was shown earlier, reactions at the circumference precede those at the basal plane. Moreover, the latter cannot begin until

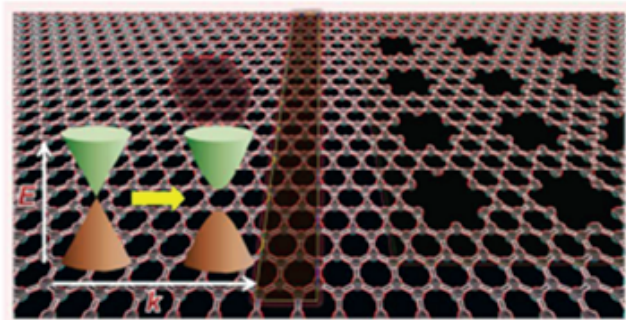


**Fig. 16.** A schematic view of morphological patterning of a graphene sheet. Adapted from Ref. [71].

the former are completed. In the predominant majority of the studied cases, the completion of the circumference reactions means the completion of framing of the studied molecules. A thorough study of the circumference reactions has disclosed a very exciting feature: the framing of graphene molecules promotes the molecule cracking. **Figure 17** presents a set of ACS  $N_{DA}$  maps related to mono-hydrogen terminated ( $H_1$ -terminated below) NGr molecules of different sizes. The ACS maps of all the pristine molecules are of an identical pattern characteristic for the (11, 11) NGr molecule shown in Fig. 10 just scaled according to the molecule size. As seen in the figure, the ACS maps of  $H_1$ -terminated polyderivatives show a peculiar two-part division related to (15, 12) ( $3.275 \times 2.957 \text{ nm}^2$ ) and (11, 11) ( $2.698 \times 2.404 \text{ nm}^2$ ) NGr molecules in contrast to the maps of (9, 9) ( $1.994 \times 2.214 \text{ nm}^2$ ), (7, 7)

( $1.574 \times 1.721 \text{ nm}^2$ ), and (5, 5) ( $1.121 \times 1.219 \text{ nm}^2$ ) NGr molecules. Apparently, the finding demonstrates the ability of graphene molecules to be divided when their linear size exceeds 1-2 nm. The cracking of pristine graphene sheets in the course of chemical reaction, particularly during oxidation, was repeatedly observed. A peculiar size effect was studied for graphene oxidation in [74] and fluorination in [75]. During 900 sec of continuous oxidation, micrometer graphene sheets were transformed into  $\sim 1 \text{ nm}$  pieces of graphene oxide. Obviously, the tempo of cracking should depend on particular reaction conditions, including principal and service reactants, solvents, temperature, and so forth (see [76, 77]). Probably, in some cases, cracking can be avoided. Apparently, this may depend on particular conditions of the inhibition of the edge atoms reactivity. However, its ability caused by the inner essence of the electron correlation is an imminent threat to the stability and integrity of the final product.

In some cases, the cracking is not observed when graphene samples present membranes fixed over their perimeter on solid substrates. Therewith, the reactivity of circumference atoms is inhibited and the basal plane is the main battlefield for the chemical modification. Still, as in the case of circumference reactions considered earlier, the highest ACS retains its role as a pointer of the target carbon atoms for the subsequent reaction steps. However, the situation is much more complicated from the structural aspect viewpoint. The addition of any modifier to the carbon atom on the basal plane is accompanied by the  $sp^2 \rightarrow sp^3$  transformation of the valence electrons hybridization so that for regularly packed chemical derivatives, the benzenoid skeleton of pristine graphene should be substituted with the cyclohexanoid one related to the formed polyderivatives. When benzene molecules and, subsequently, benzenoid units are monomorphic, cyclohexanes, and thus cyclohexanoid units, are highly heteromorphic. Not very big difference in the conformers free

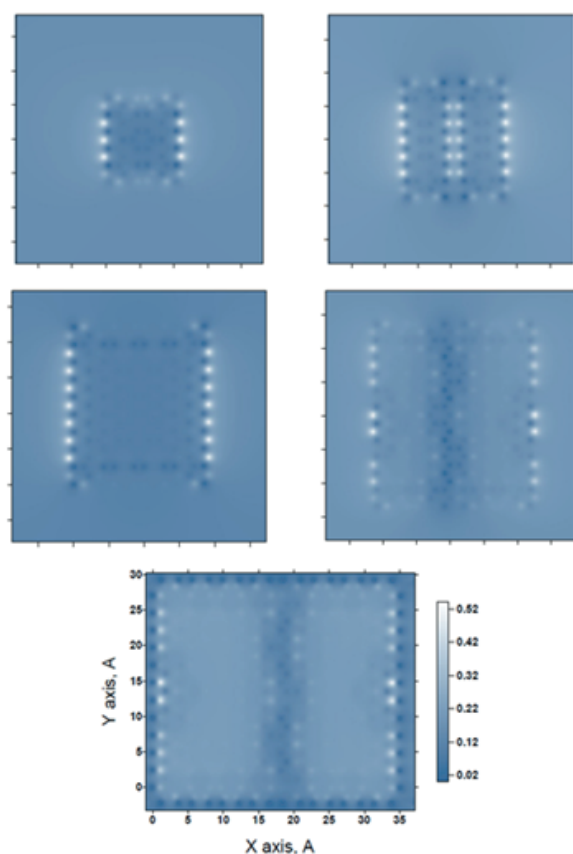


**Fig. 17.** ACS  $N_{DA}$  image maps over atoms of the (5, 5), (7, 7), (9, 9), (11, 11), and (15, 12) NGr molecules with  $H_1$ -terminated edges. All the images are given in the same space and  $N_{DA}$  scales shown on the bottom. UHF AM1 calculations.

energy allows coexisting cyclohexanoids of different structures thus making the formation of a regular structure a rare event. Actually, the regular crystalline-like structure of a graphene polyhydride, known as graphane, was obtained experimentally under particular conditions only when hydrogenating fixed graphene membranes accessible to hydrogen atoms from both sides [78]. In the same experiment, fixed membranes accessible to hydrogen atoms from one side showed an irregular amorphous-like structure. The empirical findings were supported by computations based on the consideration of stepwise hydrogenation of fixed and free standing membranes accessible to hydrogen atom from either two or one sides [69].

As shown above, it is possible to proceed with the chemical modification of graphene within the basal plane only after a complete inhibition of high chemical activity of atoms at the circumference. Despite the fact that the  $N_{DA}$  values within the area are much less than at a bare circumference, as seen in Fig. 10b, they still constitute  $\sim 0.3-0.1 e$  that is quite enough to maintain active chemical modification. However, the reality drastically differs from the desired chemical patterning of graphene sheets whose virtual image presents the final product of the patterning as regular carpets similar to the flowerbeds of French parks. The reality is more severe and closer to designs characteristic of English parks. The matter is that the collective of unpaired electrons, which strictly controls the chemical process at each step, has no means by which to predict the modifier deposition sites many steps forward. And it is clear why. Each event of the modifier deposition causes an unavoidable structure deformation due to local  $sp^2 \rightarrow sp^3$  transformation in the place of its contact with graphene. The relaxation of the deformation, as was seen in Fig. 15, extends over a large area, which, in turn, is accompanied by the redistribution of  $C=C$  bond lengths. Trying to construct a patterning, it is impossible, while not making calculations, to guess exactly at

which carbon atom the maximum reactivity will concentrate, highlighting the latter as a target atom to the next deposition. Therefore, even two simultaneous depositions cannot be predicted, not to mention such complex as quantum dots or nanoribbons. That is why a desired regular chemical patterning of graphene basal plane exists only virtually. The real situation was studied in detail in the case of graphene hydrogenation [79], exhibiting the gradual filling of the basal plane with hydrogen at random. Final products of the addition reactions on basal planes of graphene strongly depend on the addends being used. None of the regular motives were observed in any of the cases in the course of stepwise reactions.

As for use of graphene bi- and multilayers and applying mechanical deformation or strain to graphene, each of the techniques has its own limitations since again any structural changing affects the pool of effectively unpaired electrons (local spins) whose reaction is complex and nonlocal as well as practically unpredictable.

## 7. CONCLUSION

Graphene is a deeply spin-rooted species, starting with the quasi-relativistic description of the electronic state of graphene's hexagonal honeycomb structure and finishing with topological non-triviality of graphene crystals and molecules. The latter is convincingly supported by the magnetic behavior of graphene molecules and is the consequence of local spin emergence over carbon atoms subordinated to zero spin density of the species. Local spins form the groundwork for a computational spin chemistry of graphene and free from the illusions associated with the tuned morphological and chemical modification of graphene towards its converting from gapless QSHI to semiconductor.

## ACKNOWLEDGEMENTS

The author takes the opportunity to express her deep gratitude to I.S. Burmistrov and Yu.E. Lozovik for fruitful and stimulating discussions.

## REFERENCES

1. *Graphene Science Handbook: 6-volume set*. Eds. Aliofkhazraei M, Ali N, Miln WI, Ozkan CS, Mitura S, Gervasoni J. CRC Press, Taylor and Francis Group, Boca Raton, 2016.
2. Löwdin P-O. Correlation problem in many-electron quantum mechanics. 1. Review of different approaches and discussion of some current ideas. *Adv. Chem. Phys.*, 1958, 2:209-322.
3. Sheka EF. The uniqueness of physical and chemical natures of graphene: Their coherence and conflicts. *Int. J. Quant. Chem.*, 2014, 114:1079-1095.
4. Sheka EF. Computational strategy for graphene: Insight from odd electrons correlation. *Int. J. Quant. Chem.*, 2012, 112:3076-3090.
5. Sheka EF, Chernozatonskii LA. Chemical reactivity and magnetism of graphene. *Int. J. Quant. Chem.*, 2010, 110:1938-1946.
6. Sheka EF, Popova NA, Popova VA, Nikitina EA, Shaymardanova LKh. Structure-sensitive mechanism of nanographene failure. *J. Exp. Theor. Phys.*, 2011, 112:602-611.
7. Sheka EF. Spin effects of  $sp^2$  nanocarbons in light of unrestricted Hartree-Fock approach and spin-orbit coupling theory. In: *Advances in Quantum Methods and Applications in Chemistry, Physics, and Biology* (Tadjer, A., Brändas, E.J., Maruani, J., Delgado-Barrío, G., ed.). Progress in Theoretical Chemistry and Physics 31, Springer, Switzerland, 2016:xxx-yyy.
8. Wallace PR. The band theory of graphite. *Phys. Rev.*, 1947, 71:622-634.
9. Kane CL, Mele EJ. Quantum spin Hall effect in graphene. *Phys. Rev. Lett.*, 2005, 95:226801.
10. Guzmàn-Verrí GG. Electronic Properties of Silicon-Based Nanostructures. *MS thesis*, Wright State University, Dayton, 2006.
11. Slonczewski JC, Weiss PR. Band structure of graphite. *Phys. Rev.*, 1957, 109:272-279.
12. Katsnelson MI. Graphene: carbon in two dimensions. *Materials Today*, 2007, 10:20-27.
13. Geim AK, Novoselov KS. The rise of graphene. *Nat. Mat.*, 2007, 6:183-191.
14. Kim P. Graphene and relativistic quantum physics. *Matiere de Dirac, Seminaire Poincare XVIII*, 2014:1-21.
15. Hwang C, Siegel DA, Mo S-K, Regan W, Ismach A, Zhang Y, Zettl A, Lanzara A. Fermi velocity engineering in graphene by substrate modification. *Sci. Rep.*, 2012, 2:590.
16. Kara A, Enriquez H, Seitsonen AP, Lew Yan Voon LC, Vizzini S, Aufray B, Oughaddou H. A review on silicene – new candidate for electronics. *Surf Sci. Rep.*, 2012, 67:1-18.
17. Sheka EF. Silicene is a material phantom. *Nanosyst. Phys. Chem. Math.*, 2016, 7:983-1001.
18. Zhang R-W, Ji W-X, Zhang C-W, Li P, Wang P-J. Prediction of flatness-driven quantum spin Hall effect in functionalized germanene and stanene. *Phys. Chem. Chem. Phys.*, 2016, 18:28134-28139.
19. Gomes KK, Mar W, Ko W, Guinea F, Manoharan HC. Designer Dirac fermions and topological phases in molecular graphene. *Nature*, 2012, 483:307-311.
20. Tarruell L, Greif D, Uehlinger T, Jotzu G, Esslinger T. (2012). Creating, moving and merging Dirac points with a Fermi gas in a tunable honeycomb lattice. *Nature*, 2012, 483:302-306.
21. Bhimanapati GR, Lin Z, Meunier V, Jung Y, Cha J, Das S, Xiao D, Son Y, Strano MS, Cooper VR, Liang L, Louie SG, Ringe E, Zhou W, Sumpter BG, Terrones H, Xia F, Wang Y, Zhu J, Akinwande D, Alem N, Schuller JA, Schaak RE, Terrones M, Robinson JA. (2015). Recent advances in two-dimensional materials beyond graphene, *ACS Nano*, 2015, 9:11509-11539.
22. Xu L-C, Du A, Kou L. Hydrogenated borophene as a stable two-dimensional Dirac material with an ultrahigh Fermi velocity. *Phys. Chem. Chem. Phys.*, 2016, 18:27284-27289.
23. Wang C, Xia Q, Nie Y, Rahman M, Guo G. Strain engineering band gap, effective mass

- and anisotropic Dirac-like cone in monolayer arsenene. *AIP Advances*, 2016, 6:035204.
24. Wang A, Zhang X, Zhao M. Topological insulator states in a honeycomb lattice of s-triazines. *Nanoscale*, 2014, 6:11157-11162.
  25. Zhang X, Wang A, Zhao M. Spin-gapless semiconducting graphitic carbon nitrides: A theoretical design from first principles. *Carbon*, 2015, 84:1-8.
  26. Wei L, Zhang X, Zhao M. Spin-polarized Dirac cones and topological nontriviality in a metal-organic framework  $\text{Ni}_2\text{C}_{24}\text{S}_6\text{H}_{12}$ . *Phys. Chem. Chem. Phys.*, 2016, 18:8059-8064.
  27. Zhang H, Li Y, Hou J, Du A, Chen Z. Dirac state in the  $\text{FeB}_2$  monolayer with graphene-like boron sheet. *Nano Lett.*, 2016, 16:6124-6129.
  28. Si C, Jin K-H, Zhou J, Sun Z, Liu F. Large-gap quantum spin hall state in MXenes: d-Band topological order in a triangular lattice. *Nano Lett.*, 2016, DOI: 10.1021/acs.nanolett.6b03118.
  29. Naguib M, Mochalin VN, Barsoum MW, Gogotsi Y. 25th Anniversary Article: MXenes: A new family of two-dimensional materials. *Adv. Mat.*, 2014, 26:992-1005.
  30. Bandurin DA, Tyurnina AV, Yu GL, Mishchenko A, Zólyomi V, Morozov SV, Kumar RK, Gorbachev RV, Kudrynskiy ZR, Pezzini S, Kovalyuk ZD, Zeitler U, Novoselov KS, Patané A, Eaves L, Grigorieva IV, Fal'ko VI, Geim AK, Cao Y. High electron mobility, quantum Hall effect and anomalous optical response in atomically thin InSe. *Nat. Nanotech.*, 2016, DOI: 10.1038/NNANO.2016.242.
  31. Sheka EF. Stretching and breaking of chemical bonds, correlation of electrons, and radical properties of covalent species, *Adv. Quant. Chem.*, 2015, 70:111-161.
  32. Hohenadler M, Assaad FF. Correlation effects in two-dimensional topological insulators, *J. Phys.: Condens. Matter*, 2013, 25:143201 (31pp).
  33. Mayorov AS, Elias DC, Mukhin IS, Morozov SV, Ponomarenko LA, Novoselov KS, Geim AK, Gorbachev RV. How close can one approach the Dirac point in graphene experimentally? *Nano Letters*, 2012, 12:4629-4634.
  34. *Topological Insulators: Fundamentals and Perspective*. Eds. Ortman F, Roche S, Valenzuela SO, Molenkamp LW. Wiley: Chichester, 2015.
  35. Schüler M, Rösner M, Wehling TO, Lichtenstein AI, Katsnelson MI. Optimal Hubbard models for materials with nonlocal Coulomb interactions: graphene, silicene and benzene. *Phys. Rev. Lett.*, 2013, 111:036601.
  36. Bučinský L, Malček M, Biskupič S, Jayatilaka D, Büchel GE, Arion VB. Spin contamination analogy, Kramers pairs symmetry and spin density representations at the 2-component unrestricted Hartree–Fock level of theory. *Comp. Theor. Chem.*, 2015, 1065:27-41.
  37. Yazyev OV. Emergence of magnetism in graphene materials and nanostructures. *Rep. Prog. Phys.*, 2010, 73:05650130.
  38. Esquinazi P, Spemann D, Hohne R, Setzer A, Han KH, Butz T. Induced magnetic ordering by proton irradiation in graphite. *Phys. Rev. Lett.*, 2003, 91:227201.
  39. Sepioni M, Nair RR, Rablen S, Narayanan J, Tuna F, Winpenny R, Geim AK, Grigorieva IV. Limits on intrinsic magnetism in graphene, *Phys. Rev. Lett.*, 2010, 105:207205.
  40. Nair RR, Sepioni M, Tsai I-L, Lehtinen O, Keinonen J, Krasheninnikov AV, Thomson T, Geim AK, Grigorieva IV. Spin-half paramagnetism in graphene induced by point defects. *Nat. Phys.*, 2012, 8:199-202.
  41. Eng AYS, Poh HL, Sanek F, Marysko M, Matejkova S, Sofer Z, Pumera M. Searching for magnetism in hydrogenated graphene: Using highly hydrogenated graphene prepared via birch reduction of graphite oxides. *ACS Nano*, 2013, 7:5930-5939.
  42. Nair RR, Tsai I-L, Sepioni M, Lehtinen O, Keinonen J, Krasheninnikov AV, Castro Neto AH, Katsnelson MI, Geim

- AK, Grigorieva IV. Dual origin of defect magnetism in graphene and its reversible switching by molecular doping. *Nat. Commun.*, 2013, 4:2010.
43. Tada K, Haruyama J, Yang HX, Chshiev M, Matsui T, Fukuyama H. Ferromagnetism in hydrogenated graphene nanopore arrays. *Phys. Rev. Lett.*, 2011, 107:217203.
44. Ning G, Xu C, Hao L, Kazakova O, Fan Z, Wang H, Wang K, Gao J, Qian W, Wei F. Ferromagnetism in nanomesh graphene. *Carbon*, 2013, 51:390-396.
45. Van Fleck JH. *The Theory of Electric and Magnetic Susceptibilities*. Oxford, 1932.
46. Adamo C, Barone V, Bencini A, Broer R, Filatov M, Harrison NM, Illas F, Malrieu JP, Moreira I.de PR. Comment on "About the calculation of exchange coupling constants using density-functional theory: The role of the self-interaction error". [*J. Chem. Phys.*, 2005, 123:164110]. *Journ. Chem. Phys.*, 2006, 124:107101.
47. Noodleman L. Valence bond description of antiferromagnetic coupling in transition metal dimmers. *J. Chem. Phys.*, 1981, 74:5737-5742.
48. Kahn O. *Molecular Magnetism*. VCH, New York, 1993.
49. Zayets VA. *CLUSTER-Z1: Quantum-Chemical Software for Calculations in the s,p-Basis*. Kiev, Institute of Surface Chemistry Nat Ac Sci of Ukraine, 1990.
50. Gao X, Zhou Z, Zhao Y, Nagase S, Zhang SB, Chen ZJ. Comparative study of carbon and BN nanographenes: Ground electronic states and energy gap engineering. *Phys. Chem. A*, 2008, 112:12677.
51. Enoki T, Kobayashi Y. Magnetic nanographite: an approach to molecular magnetism. *J. Mat. Chem.*, 2005, 15:3999.
52. Sheka EF, Zayets VA, Ginzburg IYa. Nanostructural magnetism of polymeric fullerene crystals. *J. Exp. Theor. Phys.*, 2006, 103:728-739.
53. Nai CT, Xu H, Tan SJR, Loh KP. Analyzing Dirac cone and phonon dispersion in highly oriented nanocrystalline graphene. *ACS Nano*, 2016, 10:1681-1689.
54. Liu Q, Liu C-X, Xu C, Qi X-L, Zhang S-C. Magnetic impurities on the surface of a topological insulator. *Phys. Rev. Lett.*, 2009, 102:156603.
55. Checkelsky JG, Ye J, Onose Y, Iwasa Y, Tokura Y. Dirac-fermion-mediated ferromagnetism in a topological insulator. *Nature Phys.*, 2012, 8:729-733.
56. Dreiser J, Pacchioni GE, Donati F, Gragnaniello L, Cavallin A, Pedersen KS, Bendix J, Delley B, Pivetta M, Rusponi S, Brune H. Out-of-plane alignment of Er(trensal) easy magnetization axes using graphene. *ACS Nano*, 2016, 10:2887-2892.
57. Katmis F, Lauter V, Nogueira FS, Assaf BA, Jamer ME, Wei P, Satpati B, Freeland JW, Eremin I, Heiman D, Jarillo-Herrero P, Moodera JS. A high-temperature ferromagnetic topological insulating phase by proximity coupling. *Nature*, 2016, 533:513-516.
58. Sheka EF. Chemical susceptibility of fullerenes in view of Hartree-Fock approach. *Int. J. Quant. Chem.*, 2007, 107:2803-2816.
59. Sheka EF. Chemical portrait of fullerenes. *J. Struct. Chem.*, 2006, 47:593-599.
60. van der Lit J, Boneschanscher MP, Vanmaekelbergh D, Ijäs M, Uppstu A, Ervasti M, Harju A, Liljeroth P, Swart I. Suppression of electron-vibron coupling in graphene nanoribbons contacted via a single atom. *Nat. Commun.*, 2013, 4:2023.
61. Warner JH, Lin Y-C, He K, Koshino M, Suenaga K. Atomic level spatial variations of energy states along graphene edges. *Nano Lett.*, 2014, 14:6155-6159.
62. Nakada K, Fujita M. Edge state in graphene ribbons: Nanometer size effect and edge shape dependence. *Phys. Rev. B*, 1996, 54:17954-17961.
63. Barnard AS, Snook IK. Modelling the role of size, edge structure and terminations on the electronic properties of graphene

- nano-flakes. *Modelling Simul. Mater. Sci. Eng.*, 2011, 19:054001.
64. Acik M, Chabal YJ. Nature of graphene edges: A review. *Jpn. J. Appl. Phys.*, 2011, 50:070101.
65. Mishra PC, Yadav A. Polycyclic aromatic hydrocarbons as finite size models of graphene and graphene nanoribbons: Enhanced electron density edge effect. *Chem. Phys.*, 2012, 402:56-68.
66. Ang LS, Sulaiman S, Mohamed-Ibrahim MI. Effects of size on the structure and the electronic properties of graphene nanoribbons. *Monatsh. Chem.*, 2013, 144:1271-1280.
67. Hoffmann R. Small but strong lessons from chemistry for nanoscience. *Ang. Chem. Int. Ed.*, 2013, 52:93-103.
68. Mayer I. On bond orders and valences in the ab initio quantum chemical theory. *Int. J. Quant. Chem.*, 1986, 29:73-84.
69. Sheka EF, Popova NA. Odd-electron molecular theory of the graphene hydrogenation. *J. Mol. Model.*, 2012, 18:3751-3768.
70. Sheka E, Popova N. Molecular theory of graphene oxide. *Phys. Chem. Chem. Phys.*, 2013, 15:13304-13332.
71. Lu G, Yu K, Wen Z, Chen J. Semiconducting graphene: converting graphene from semimetal to semiconductor. *Nanoscale*, 2013, 5:1353-1367.
72. Chernozatonski LA, Sorokin PB, Belova EE, Brüning J. Superlattices consisting of 'lines' of adsorbed hydrogen atom pairs on graphene, *JEPT Lett.*, 2007, 85:77-81.
73. Lu N, Huang Y, Li H-b, Li Z, Yang J. First principles nuclear magnetic resonance signatures of graphene oxide. *J. Chem. Phys.*, 2010, 133:034502.
74. Pan S, Aksay IA. Factors controlling the size of graphene oxide sheets produced via the graphite oxide route. *ACS Nano*, 2011, 5:4073-4083.
75. Nebogatikova NA, Antonova IV, Prinz VYa, Kurkina II, Vdovin VI, Aleksandrov GN, Timofeev VB, Smagulova SA, Zakirova ER, Kesler VG. Fluorinated graphene dielectric films obtained from functionalized graphene suspension: preparation and properties. *Phys. Chem. Chem. Phys.*, 2015, 17:13257-13266.
76. Wang X, Bai H, Shi G. Size fractionation of graphene oxide sheets by pH-assisted selective sedimentation. *J. Am. Chem. Soc.*, 2011, 133:6338-6342.
77. Kang JH, Kim T, Choi J, Park J, Kim YS, Chang MS, Jung H, Park K, Yang SJ, Park CR. The hidden second oxidation step of Hummers method. *Chem. Mat.*, 2016, 28:756-764.
78. Elias DC, Nair RR, Mohiuddin TMG, Morozov SV, Blake P, Halsall MP, Ferrari AC, Boukhvalov DW, Katsnelson MI, Geim AK, Novoselov KS. Control of graphene's properties by reversible hydrogenation: evidence of graphane. *Science*, 2009, 323:610-613.
79. Balog R, Jorgensen B, Nilsson L, Andersen M, Rienks E, Bianchi M, Fanetti M, Lægsgaard E, Baraldi A, Lizzit S, Slijivancanin Z, Besenbacher F, Hammer B, Pedersen TG, Hofmann P, Hornekær L. Bandgap opening in graphene induced by patterned hydrogen adsorption. *Nature Mat.*, 2010, 9:315-319.

# CAN GRAPHENE BILAYERS BE THE MEMBRANE MIMETIC MATERIALS? ION CHANNELS IN GRAPHENE-BASED NANOSTRUCTURES

**Oleg V. Gradov**

Institute of Energy Problems of Chemical Physics, Russian Academy of Sciences, <http://www.inepcp.ru>  
117829 Moscow, Russian Federation  
[gradov@chph.ras.ru](mailto:gradov@chph.ras.ru)

**Margaret A. Gradova**

Semenov Institute of Chemical Physics, Russian Academy of Sciences, <http://www.chph.ras.ru>  
119991 Moscow, Russian Federation  
Institute of Energy Problems of Chemical Physics, Russian Academy of Sciences, <http://www.inepcp.ru>  
117829 Moscow, Russian Federation  
[gradova@chph.ras.ru](mailto:gradova@chph.ras.ru)

---

*Abstract.* The prospects of application of graphene and related structures as the membrane mimetic materials, capable of reproducing several biomembrane functions up to the certain limit, are analyzed in the series of our papers. This paper considers the possibility of the ion channel function modeling using graphene and its derivatives. The physical mechanisms providing selective permeability for different membrane mimetic materials, as well as the limits of the adequate simulation of the transport, catalytic, sensing and electrogenic properties of the cell membrane ion channels using bilayered graphene-based structures are discussed.

*Keywords:* ion channels, graphene, channel mimetics, nanopores, kapillarchemie, size-dependent electrochemistry, electric double-layer capacitor, ISFET & ChemFET

**PACS: 81.05.ue**

*Bibliography - 171 references*

*Received 14.11.2016*

*RENSIT*, 2016, 8(2):154-170

**DOI: 10.17725/rensit.2016.08.154**

---

## CONTENTS

1. INTRODUCTION (154)
  2. SEMIPERMEABILITY AND THE ION CHANNELS (154)
  3. PORES AND ION CHANNELS IN GRAPHENE-BASED NANOSTRUCTURES (158)
  4. CONCLUSION (161)
- REFERENCES (161)

## 1. INTRODUCTION

In [1] provides an overview of membrane models – semi-synthetic, synthetic, biogenic, semiconducting, superconducting, ferroelectric - and the related membrane mimetic materials from phospholipid bilayers and Langmuir films to multilayer nanofilms and ferromagnetic structures, along with the consideration of the problems of ambiguity models, completeness the membrane mimetic materials modeling, functional and substrate equivalence of the membrane mimetic materials. The use of

analogical functional similarity criteria for the analysis of possibility of consideration of graphene, particularly the two-layer graphene as the membrane mimetic material - the subject of this work, with a focus on the analysis of it key property – permeability for ions, water and other organic matter.

## 2. SEMIPERMEABILITY AND THE ION CHANNELS

A well known flexibly adjustable semipermeability towards various agents is characteristic for the graphene-oxide membranes in organic solvents, with the size of the nanochannels providing either transport or blocking of several agents, which can be narrowed down by the thermal annealing or extended by solvation, thereby changing the boundary of the transmitted agent's size selectivity [2]. This corresponds to

the well known models of the “size / solubility” – regulation of the sodium ion channels [3] and good approximations of the kinetic regimes depending on the ionic radius [4]. As a particular case of the applicability of the quantitative relations between the structure and biological activity (QSAR) [5], the analysis principles for the functional adjustability of the ion channels by the sink parameters, with the membrane pores corresponding to the drains, and the size of particles penetrating through those pores, in the case of the graphene layers fail to describe the membrane permeability, since the membrane considered performs a biological function despite the fact that its chemical composition is far from bioorganic one, and hence, is not included into the ion channel databases [6] which could be used to obtain QSAR data.

It is noteworthy that similar problems with the QSAR approaches earlier emerged in the analysis of the lipid nanopores operating as the ion channels of the cell membranes without any conventional ion channel components [7] due to their size corresponding to the ion radius. (Typically even at the dependence of the several ion channel group input on the ionic radius complex biochemical and crystallographic models are applied up to the homohexamer one [8], i.e. compatible with the QSAR principles based on the analysis of the conformation and steric accessibility of the channelome biomacromolecules).

In connection with the above contradiction it is also worth to mention the known data on the ionic permeability of the synthetic filters which have never been analyzed using QSAR methods for the similar reasons: it was shown that the ions penetrating through the synthetic PET filters are selected by the mechanisms providing the biomimetic and membrane mimetic kinetics with the discrete fast transitions between the conductivity levels and parametric selectivity of the ion fluxes, as well as inhibition by divalent cations, similar to the cell ion channels [9, 10].

Thus, it is possible to work out the criteria for verification of the biomimetic nature of the membrane mimetic models, based on the idea about the gradations of the ion channel efficiency according to the conductivity and bioelectric response generated, rather than on the conventional statement about the discrete transition between the excited states («all-or-none law» [11, 12]), typical for the deterministic model of the electrophysiological potential generation.

It is reasonable, since it has been shown earlier that the ion channel states (which are the prototypes of the membrane mimetic, or even channel mimetic models [13-15]) with a low ion conductivity in fact are not “closed”, but are changing within several gradations providing qualitatively (“ion-selectively”) and quantitatively (according to the permeability) distinguishable types of the membrane-electrophysical or electrophysiological response, which is the main cause for the specific channelome noises at the patch-clamp registograms [16]. Of course, this does not mean the close similarity between the biological and synthetic membrane structures or the possibility to reduce the channelome molecular machinery to the simple porous structure, but it indicates the general operation principles of the non-specific physical mechanisms at the nanoscale where the size effects are physically-determined and chemically-independent, i.e. are little if any influenced by the chemical composition of the medium and macromolecular morphology of the biopolymers (in a conventional meaning of this term introduced by P.J. Flory [17, 18], a Nobel prize winner and the author of the Flory-Huggins equation which is formally similar to the Van der Waals equation, and hence, can be applied at the physical scale considered in this paper).

For the above reasons, biomimetic interpretation and assigning of the specific membrane properties to graphene and other layered membrane mimetic materials

with the pore size corresponding to the ion radii, although does not contradict to the experimental data, in fact is a logical error of the inversion type, arising from the mixing of the deductive and inductive predicates: graphene and the cell membrane with the similar pore size obviously subject to the same physical and chemical principles (which is manifested in the similarity of the solvation regulation and the electrophysical response), and hence, in this aspect “graphene can be considered as a membrane mimetic material to the same extent as the biological membrane can be considered as a graphene-mimetic”.

This suggests that the similarity problem (including the above mentioned QSAR) for such structures, if considered from the standpoint of molecular biology rather than biophysical and biocolloid chemistry, becomes incorrect. According to the classical colloid and capillary chemistry principles [19, 20] it is possible to determine the efficiency limits of the sorption processes within the pores and channels of the particular diameter, which is usually applied in cytophysiology [21] (the Freundlich adsorption isotherm [22] is named after Herbert Freundlich – the founder of the capillary chemistry and a pioneer of the capillary-chemical approaches in physiology). Thus, it is more appropriate to address the problem of channelomics of the graphene-oxide membrane mimetic materials from the standpoint of the size effects inherent to the former in the aspects of adsorption, filtration and size separation of the particles /ions, rather than in the framework of the specialized (supra)molecular structures which satisfy the similarity conditions to the specific cytophysiological structure performing the physical and chemical separation mechanism (i.e. “a similarity of the general phenomenon to its particular manifestation”).

The effects of the size-dependent penetration of the chemical agents through the graphene layers are well known in nanochemistry [23, 24]. Reactivity towards

different gases [25] and electrochemical properties of the nanoelectrode graphene layers [25] also depend on the pore diameter. The above phenomenon known as “size-dependent electrochemistry” is a conceptual continuation of the Freundlich’s “Kapillarchemie”. This approach is widely applicable not only in the chemistry of the carbon structures, but also in the nanostructural materials science as a whole.

Regarding the carbon structures related to graphene, nanoelectrochemistry based on the size effects was applied in the studies on the multilayered carbon nanotubes [27] and a fully or partially reduced graphite oxide [28] which is an electrode material for electrochemical double-layer capacitors [29] often considered as the biological membrane bilayer model [30-34], as well as the layered supercapacitors of EDLC-type (“electric double-layer capacitor”) with the pronounced relation between the ion and pore sizes [35] similar to the biological membranes and membrane mimetic materials considered above. By the way, this is a reduced graphite oxide which is used as an electrode material in such supercapacitors [36], allowing the EDLC-based membrane models to mimic not only the energy storage function, but also a number of biochemical receptor functions, such as recognition and detection of the specific mediators/neurotransmitters/neurohormones (e.g. dopamine – [37-39]), performed on the basis of the electrochemical principles without any specific biomacromolecular agents [40-42] (in particular, due to the thickness-dependent hydrophobic properties of graphene, which is formally similar to the size-dependent properties of the “trans-graphene transport” of differently charged biomolecular agents through the pores in its hydrophobic surface [43, 44], which makes the problem of designing the graphene-based sensitive biomimetic materials soluble and similar to the design of the receptor mimetic peptides [45] based on the hydrophobic interaction simulations).

To date, all the exceptions from this reductionistic rule, actually, confirm the rule, since the range of charge, mass and other physical and chemical parameters of the substances used in the composite techniques as well as the degrees of their biochemical (or immunochemical in the case of such detection principles) affinity differ by orders of magnitude: aptamers/nucleic acids [46, 47]; conductive polymers, such as polypyrrole (both at graphene and pyrolytic graphite) [48-51]; porphyrins and their derivatives, qualitatively different in their physical and chemical properties and aggregation behavior in solutions [52-54]; aminosugars - linear polysaccharide derivatives, such as chitosan [55, 56] used for immobilization; polymer electrolytic membranes, particularly those based on fluoride containing copolymers – fluorocarbon vinyl esters containing sulfonic groups (e.g. a well known nafion), including those with the composite impregnation by several inorganic components and structure-modifying agents [57-60]; inorganic particles and clusters themselves – gold, copper, nickel and zinc oxide nanoparticles [61-68]; graphene-doping chemical elements, such as nitrogen [69, 70]. Although the above list is not complete, it fully represents the range of different mass and charge parameters for a number of molecules in the membrane mimetic structures performing receptor functions based on graphene and its derivatives. Despite the fact that in some cases electrophysical response has not been directly registered (detected only from the secondary indicators, such as redox-dependent fluorescence), the above information can be sufficient to prove by contradiction the correctness of the reductionistic model which does not require any bioorganic or macromolecular agents for performing the receptor functions by the membrane mimetic materials.

It is noteworthy that graphene-based nanostructures are often used in designing of both n-layered supercapacitors and sensors to various agents operating without enzymes

[71]. In such sensors graphene is only a kind of supercapacitor material – there are biosensors [72], gaze [73] and humidity [74] sensors (also capable of the energy storage) based on the non-graphene supercapacitor membrane coatings. Wherein, from the standpoint of the channelomics of such membrane mimetic materials, it should be mentioned that supercapacitor sensor membranes can separate ions, synthetic and biological molecules [75], promote dissociation of salts producing energy [76] due to the ion gradient (similar to the above cited Mitchell chemiosmotic model). Thus, energy supplying and sensing properties of the graphene-based membrane mimetic materials, which are phenomenologically similar to a number of fundamental properties inherent to the biomembranes, are provided by the electrophysical mechanisms (the molecule polarity, hydrophobicity and a number of properties related to the uncompensated charge interactions, in particular, coordination). It is not reasonable to consider the biosensor properties of the graphene-based membrane mimetic materials in this section, since they will be considered in details below, as well as the chemosensor ones, but the sensor properties of the supercapacitor-based membrane mimetic materials were discussed here for the reason of extrapolation of the ion channel- / membrane mimetic modeling criteria and the search for the general basis of the sensor, ion-selective and electrophysical properties of the model system.

The aforementioned correlations between the electric and transport (ion-selective) properties require the example of their cooperative interaction. To date there are well known graphene-based ion-selective field-effect transistors (ISFET) sensitive to the proton concentration [77], which clearly correlates to the chemiosmotic model of the membrane electrogenesis, as well as with the model of biomembrane as the transistor structure known since 1960-th [78]. In such models the ion

transport, sensing properties and changing of the sensor electric parameters are synchronized and interdependent. By the way, for all chemically-selective field-effect transistors (ChemFET), and particularly for the ion-selective field-effect transistors (ISFET) [79, 80], there is no difference between the “membrane selectivity” and the “sensor electric response specificity” [81]. In recent years the ion sensing functions in microfluidic and even nanofluidic chemometric systems (labs-on-a-chip) are performed by the ionic transistors based on the ion concentration polarization by an ion exchange membrane [82], capable of performing electrogenic ion exchange and sensing with the electric response. Similar functions can be performed by the graphene or graphene oxide-based ion exchangers and composite ion-exchange materials [83-85], whereby the principles of synchronization of various aspects of their activity as multifunctional membrane mimetic materials can be realized using graphene and its analogs/derivatives applicable as FET. It should be noted that for performing of the most of the above mentioned functions graphene-based structures should possess only the FET properties, but not the whole ChemFET. There are sensors based on the graphene-containing FET structures (non-positioned as a ChemFET), but applied for the redox-sensing [86], aptasensing [87], electrochemical biosensing [88], metal ion sensing [89], as well as for design of the components of the bioelectronic “nose” [90]. This is due to the qualitative dependence of the graphene-based FET response on the ambient liquid and vapor media conditions [91], which may be due to the increased mobility of the charge carriers (holes), the decrease in the residual charge carrier concentration and changes in the molecular transport, induced by the charged defects (so-called perforation) near the surfaces of the active layers. The above effects result from the charge transport, as well as the molecule orientation induced by the charge near the FET surface [92], but it requires the

presence of the vacant pores and charge defects in the membrane mimetic surface similar to the structural and electrophysiological features of biomembranes with the electrogenic properties, ionic transport and spatial molecule orientation in the controlling electric field are coupled and colocalized [93]).

### 3. PORES AND ION CHANNELS IN GRAPHENE-BASED NANOSTRUCTURES

Let us consider here the question about the presence of pores and the ion channel analogs (or the possibility of their realization) in graphene and its products, precursors and related compounds. There are known gaze-transport [94] and ion-transport [95] channels in the laminar graphene oxide and graphene-based nanostructures of the electrophysical destination used in electrotechnics for designing of the lithium-ion batteries. All the phenomena of the selective ion penetration through the graphene structures are based on the above channel operation. In literature one can find the description of all kinds of the ion channels implemented on the basis of the graphene nanopores/nanochannels [96, 97]: for alkali metals [98], including biomimetic (bioinspired) analogs of the sodium and potassium channels [99] (as well as the other alkali metals, such as lithium, rubidium, and caesium [100-102], as follows from the thermodynamic calculations for the monovalent cations [103] and quantum chemical simulations for a number of the alkali metal ions [104], which can also operate in the channel, but their Clark is too low, and hence, does not allow to perform any significant functions at the macroscopic scale at the organism or the whole biosphere level), for the chloride ions [105] (the analogs of the known chloride ion channels [106, 107]), etc.

Consideration of the “exotic” pores and channels in graphene operating with the rubidium, gadolinium and other rare earth element ions [108, 109] is beyond the scope of

this paper for the purpose of maintenance of the biomimetic functional analogy.

In the synthesis of the biomimetic graphene-based ISFET structures an important aspect is the compatibility with the channelome, since the carbon nanostructure-based ISFET are used in the electrophysical studies in neurocytology [110] by contact formation with the neurons, which serve as the ion-exchange structures between the channelome and FET, and are responsive to the extracellular medium and the mediated stimulation/inhibition of the ion-transport channel activity [111]. Recent data on the possibility of the biomimetic ion channel function modeling and their introduction into the graphene capsules and membrane-like structures, by 2015 made it possible to consider the graphene-based capsules with the ion-selective channels as the embryo protocells [112, 113]. Though the above interpretation is doubtful, given that the early protocell models were actually simple phospholipid membrane structures [114-116], a membrane mimetic nature of this abstraction is clear, while it is not a breakthrough among the numerous non-lipid [117], membrane-free [118] and electrostatically-gated [119], inorganic [120, 121] mineral [122, 123] and other protocells, illustrating the recent tendency to the biomembrane substitution by its functional alternative.

However, it is evident that the synthetic functional model operates differently from its prototype, while providing chemical sensing in the vicinity of the graphene surfaces [124]: selective particle transport through the graphene layers can be performed accordingly not only to the particle charge or mass [125], but also to its spin [126], which is fundamentally different from the conventional physics of the biomembrane prototypes (although spin labels and other methods of the spin chemistry are often used in biophysics and cytophysiology for studying the ion channel properties and membrane permeability [127-131]). Thus, here we speak about the transduction of the physical

agents rather than chemical (ionic) carriers of the QSPR/QSAR-coupled chemical parameters and physiological properties. In this case a model can be considered objective only if it is adequate to the biological prototype by the formation mechanism; functionally different models are based on different principles, and hence, reproduce the properties of the prototype only to the extent determined by the difference in their formation mechanisms.

There are known works on the graphene nanofluidic channel formation by scrolling graphene layers into a tube [132]. In biological systems there is an analogous example of the model channel formation via self-assembly (folding) of the cyclic peptide nanotubes [133] formed directly in the course of their interaction with the ligand [134] (as a supramolecular response [135] to the above interaction). Similarly occurs self-assembly of the model ion channel networks based on liquid-crystalline bicontinuous cubic phases [136] or columnar phases based on crown ethers in lipid bilayers [137]. The ion channel assembly from dendrimers is slightly different due to their branched structure [138], but this special case can not be implemented using graphene membrane mimetic structures, and hence, is beyond the scope of our paper. Another different mechanism of the membrane self-assembly, and hence, the membrane channel assembly, occurs under the templating conditions, which is simulated by the formation of the graphene films on various catalytic and ultramicrostructured surfaces (e.g. for obtaining FET and other ion-selective structures [139, 140]).

Catalytic structuring of the subsurface layer [141] is an inevitable condition for the on-surface synthesis. Templating on the inorganic catalytic surfaces is essential for the synthesis of a variety of inorganic catalytically-active (to a certain extent of self-assembly even autocatalytically-active) redox-surfaces [142]; similar requirements are in the synthesis of the layers with channels, mediated by the templating metal surfaces

[143]. In such syntheses vacancies serve as the precursors (seeds) for the channel formation and are also involved in the determination and direction of the surface structuring forms under the phase transitions [144]. A similar but qualitatively opposite role is played by the metal ions: surfactant templating on the molten salt surfaces with the metal adducts leads to the formation of the metallotropic liquid-crystalline phases [145]. Given the applicability of the catalytic templating methods for the synthesis of the graphene-oxide nanostructures [146], it is possible to design graphene-based biomimetic/membrane mimetic surfaces with the ion channel function performed by the structures formed via templating and related mechanisms. This will correspond both to the template-associated synthesis of the peptide ion channel-mimicking systems [147] and to the formation of the synthetic inorganic transmembrane tubes and channels under the lipid templating [148], i.e. it will be substrate-independent from the biomolecular and supramolecular carriers, as well as from the organic/inorganic composition of the ion channel-mimicking structure as a whole, which is a prerequisite for the agent modeling of their functional mimetics.

Addressing the problem of catalysis in the ion channel mimetic self-assembly, including graphene-based structures, it is necessary to point out the catalytic function of the channels-prototypes. Catalytically-active are both cationic (e.g. calcium channels [149], characterized by the coupling of their catalytic and transport functions in the ATP-mediated  $\text{Ca}^{2+}$ -transport), and anionic [150] ion channels and membrane ion pumps. Many specific regulators of the ion transport and permeability, such as CFTR – cystic fibrosis transmembrane conductance regulator [151, 152], catalytic and the channel opening/closing regulation functions are also coupled. ATP-sensitive potassium channels (sometimes referred to as KATP/KATP or sarcKATP in sarcolemma, mitoKATP in chondriome, nucKATP at the nucleus depending on their

localization), also possess catalytic activity [153, 154]. A similar situation occurs with the redox-regulators and the iron metabolism mediators – ferritin-based ion channels [155], as well as with their synthetic derivatives and analogs made from nanostructures [156].

In general, synthetic catalytically-active pores [157] with the ion selectivity similar to their biological prototype are capable of performing the ion channel functions with the same (bio) catalytic function. The possibility of the above principle implementation using the agent models is determined by several conditions. Firstly, both for the potassium [158] and sodium [159] channels with the opposite operation modes (potassium channels are opened while the sodium ones are closed, since the cell resting potential parameters are close to the Nernst equilibrium potential of the potassium ions) catalysis plays an important role. Secondly, catalytic functions are characteristic both for the cationic and anionic channels (the term “chloride ion channels” in this case is not fully appropriate, since the same channels provide transport of the  $\text{HCO}_3^-$ ,  $\text{I}^-$ ,  $\text{SCN}^-$  and  $\text{NO}_3^-$  anions). Thirdly, most of the model ion-selective systems are equally sensitive to most of the monovalent cations [160]. On the other hand, catalytic functions and the ligand recognition can be performed almost without any ion channels based on the pi-cation interactions [161]. At the same time coupling between the potential generation phases and catalytic cycles in the membrane can be provided by the lipids, e.g. by a phospholipid PI(4,5)P2 (phosphatidylinositol 4,5-bisphosphate) [162, 163]. Thus, the nature and structure of the agent itself are not significant for mimicking its function, while the adequate function reproduction is the key similarity criterion of the biomimetic model to its biological prototype.

Another characteristic example is the operation of the water channel associated with the catalytically-active sites [164] and their mimicking within the graphene layer or graphite surface in the form of the water transpiration

channels [165, 166], which can be reproduced (with the presence of the driving gradient) beyond the structural modeling and design/synthesis of the ion channel mimetics by means of the simple passive membrane model with its permeability dependent on the ion size, and water permeability within the same channels and the surface features [167]. This corresponds to the membrane pore model and the model of the non-selective independent ion channels with their permeability determined by the ion and molecule size. However, the native water channels – integral proteins aquaporins – also perform the pore functions, while some of them depending on the molecular size and shape also allow penetration of glycerin, ammonia, urea and carbon dioxide through the membrane [168].

#### 4. CONCLUSION

In a general case, agent functional modeling of the ion channels using graphene-based structures is not only possible, but also satisfies the requirement for the colocalization of the ion-selective and electrogenic functions, resulting from the analysis of the biophysical prototype (membrane) functions. Good examples of such structures with colocalization are the channels in the graphene-based ISFET – ion-selective field-effect transistors [169, 170] considered above. However, there are two aspects of electrogenesis, which can not be neglected during the analysis of the ion channel operation in graphene-based ISFET. One of them is the electrical double layer, which is the absolute theoretical limit of the nanoelectric system design, and the other one is the double layer nature of the biological membrane as a capacitor (which is required for modeling its periodical discharge in the form of the action and breakdown potentials in the area of the membrane pore formation), which should correspond to the double-layered structure of the graphene-based agent membrane mimetic material. Then the logic “performance” and the “duty cycle” of the graphene ion channel operation [171] in the electrogenic medium

– graphene bilayer – will possess a higher degree of similarity with its biological prototype. A detailed consideration of the electrical double layer as a driving force of the electrogenic processes and membrane mimetic structures, along with the consideration of the differences between the double-layered and multi-layered graphene-based structures and their single-layer analogs in the membrane mimetic aspect will be given in the next part of this paper.

#### REFERENCES

1. Gradov OV. Membrannye modeli i anzats dvukhsloynogo grafena kak membranomimetika [Can graphene bilayers be the membrane mimetic materials?]. *Radioelektronika. Nanosistemy. Informatsionnye tekhnologii (RENSIT)*, 2016, 8(1):25-38 (in Russ.); DOI: 10.17725/rensit.2016.08.025.
2. Huang L, Li Y, Zhou Q, Yuan W, Shi G. Graphene Oxide Membranes with Tunable Semipermeability in Organic Solvents. *Adv Mater.*, 2015, 27(25):3797-3802.
3. Courtney KR. Sodium channel blockers: the size/solubility hypothesis revisited. *Mol. Pharmacol.*, 1990, 37(6):855-859.
4. Courtney KR. Size-dependent kinetics associated with drug block of sodium current. *Biophys. J.*, 1984, 45(1):42-44.
5. Courtney KR. Quantitative structure/activity relations based on use-dependent block and repriming kinetics in myocardium. *J. Mol. Cell Cardiol.*, 1987, 19(3):319-330.
6. Le Novère N, Changeux JP. The Ligand Gated Ion Channel database: an example of a sequence database in neuroscience. *Philos. Trans. R. Soc. Lond. B: Biol Sci.*, 2001, 356(1412):1121-1130.
7. Pakhomov AG, Bowman AM, Ibey BL, Andre FM, Pakhomova ON, Schoenbach KH. Lipid nanopores can form a stable, ion channel-like conduction pathway in cell membrane. *Biochem. Biophys. Res. Commun.*, 2009, 385(2):181-186.
8. Cruickshank CC, Minchin RF, Le Dain AC, Martinac B. Estimation of the pore size of

- the large-conductance mechanosensitive ion channel of *Escherichia coli*. *Biophys. J.*, 1997, 73(4):1925-1931.
9. Lev AA, Korchev YE, Rostovtseva TK, Bashford CL, Edmonds DT, Pasternak CA. Rapid switching of ion current in narrow pores: implications for biological ion channels. *Proc. Biol. Sci.*, 1993, 252(1335):187-192.
  10. Korchev YE, Bashford CL, Alder GM, Apel PY, Edmonds DT, Lev AA, Nandi K, Zima AV, Pasternak CA. A novel explanation for fluctuations of ion current through narrow pores. *FASEB J.*, 1997, 11(7):600-608.
  11. Osterhout WJ. Nature of the action current in nitella: V. Partial response and the all-or-none law. *J. Gen. Physiol.*, 1943, 27(1):61-68.
  12. Osterhout WJ. Apparent violations of the all-or-none law in relation to potassium in the protoplasm. *J. Gen. Physiol.*, 1954, 37(6):813-824.
  13. Steinle ED, Mitchell DT, Wirtz M, Lee SB, Young VY, Martin CR. Ion channel mimetic micropore and nanotube membrane sensors. *Anal. Chem.*, 2002, 74(10):2416-2422.
  14. Guo W1, Tian Y, Jiang L. Asymmetric ion transport through ion-channel-mimetic solid-state nanopores. *Acc. Chem. Res.*, 2013, 46(12):2834-2846.
  15. Wirtz M, Martin CR. Nanotube Membrane Sensors: Resistive Sensing and Ion Channel Mimetics. *Sens. Upd.*, 2002, 11(1):35-64.
  16. Korchev YE, Bashford CL, Alder GM, Kasianowicz JJ, Pasternak CA. Low conductance states of a single ion channel are not 'closed'. *J. Membr. Biol.*, 1995, 147(3):233-239.
  17. Flory PJ. Molecular morphology in amorphous and glass polymers. *Journ. Non-Crystal. Sol.*, 1980, 42(1-3):117.
  18. Flory PJ, De Yeung Y. Molecular morphology in semicrystalline polymers. *Nature*, 1978, 272:226-229.
  19. Freundlich H. *Kapillarchemie; eine Darstellung der Chemie der kolloide und verwandter Gebiete, Band 1*. Leipzig, Akademische Verlagsgesellschaft, 1930, 566 p.
  20. Freundlich H. *Colloid & capillary chemistry*. New York, E.P. Dutton & Company, 1922, 883 p.
  21. Freundlich H. *Kapillarchemie und Physiologie*. Dresden, Theodor Stienkopff, 1914, 48 p.
  22. Freundlich H. Die Adsorption in Lösungen. *Z. Phys. Chem.*, 1906, 57(A):385-470.
  23. Plant SR, Cao L, Yin F, Wang ZW, Palmer RE. Size-dependent propagation of Au nanoclusters through few-layer graphene. *Nanoscale*, 2014, 6(3):1258-1263.
  24. Jeon KJ, Lee Z. Size-dependent interaction of Au nanoparticles and graphene sheet. *Chem. Commun.*, 2011, 47(12):3610-3612.
  25. Si C, Zhou G. Size-dependent chemical reactivity of porous graphene for purification of exhaust gases. *J. Chem. Phys.*, 2012, 137(18):184309-1-184309-6.
  26. Zhang B, Fan L, Zhong H, Liu Y, Chen S. Graphene nanoelectrodes: fabrication and size-dependent electrochemistry. *J. Am. Chem. Soc.*, 2013, 135(27):10073-10080.
  27. Cardoso RM, Montes RH, Lima AP, Dornellas RM, Nossol E, Richter EM, Munoz RA. Multi-walled carbon nanotubes: Size-dependent electrochemistry of phenolic compounds. *Electrochim. Acta*, 2015, 176:36-43.
  28. Tran MH, Yang CS, Yang S, Kim IJ, Jeong HK. Size dependent electrochemical properties of reduced graphite oxide. *Chem. Phys. Lett.*, 2014, 608:207-212.
  29. Hantel MM, Kaspar T, Nesper R, Wokaun A, Kötz R. Partially reduced graphite oxide as an electrode material for electrochemical double-layer capacitors. *Chemistry*, 2012, 18(29):9125-9136.
  30. Rao S, Lu S, Guo Z, Li Y, Chen D, Xiang Y. A light-powered bio-capacitor with nanochannel modulation. *Adv. Mater.*, 2014, 26(33):5846-5850.

31. Lamport DT, Varnai P, Seal CE. Back to the future with the AGP-Ca<sup>2+</sup> flux capacitor. *Ann. Bot.*, 2014, 114(6):1069-1085.
32. Kim I, Warshel A. A Microscopic Capacitor Model of Voltage Coupling in Membrane Proteins: Gating Charge Fluctuations in Ci-VSD. *J. Phys. Chem. B.*, 2016, 120(3):418-432.
33. Ray S, Kassan A, Busija AR, Rangamani P, Patel HH. The plasma membrane as a capacitor for energy and metabolism. *Am. J. Physiol. Cell Physiol.*, 2016, 310(3):C181-C192.
34. Gimsa J, Wachner D. A unified resistor-capacitor model for impedance, dielectrophoresis, electrorotation, and induced transmembrane potential. *Biophys. J.*, 1998, 75(2):1107-1116.
35. Largeot C, Portet C, Chmiola J, Taberna PL, Gogotsi Y, Simon P. Relation between the ion size and pore size for an electric double-layer capacitor. *J. Am. Chem. Soc.*, 2008, 130(9):2730-2731.
36. Lobato B, Vretenár V, Kotrusz P, Hulman M, Centeno TA. Reduced graphite oxide in supercapacitor electrodes. *J. Coll. Interf. Sci.*, 2015, 446:203-207.
37. Kannan PK, Moshkalev SA, Rout CS. Highly sensitive and selective electrochemical dopamine sensing properties of multilayer graphenenanobelts. *Nanotechn.*, 2016, 27(7):075504-1-075504-9.
38. Qian T, Yu C, Wu S, Shen J. Gold nanoparticles coated polystyrene/reduced graphite oxide microspheres with improved dispersibility and electrical conductivity for dopamine detection. *Coll. Surf. B: Biointerfaces*, 2013, 112:310-314.
39. Qian T, Wu S, Shen J. Facilely prepared polypyrrole-reduced graphite oxide core-shell microspheres with high dispersibility for electrochemical detection of dopamine. *Chem. Commun.*, 2013, 49(41):4610-4612.
40. Feng X, Zhang Y, Zhou J, Li Y, Chen S, Zhang L, Ma Y, Wang L, Yan X. Three-dimensional nitrogen-doped graphene as an ultrasensitive electrochemical sensor for the detection of dopamine. *Nanoscale*, 2015, 7(6):2427-2432.
41. Bagherzadeh M, Heydari M. Electrochemical detection of dopamine based on pre-concentration by graphene nanosheets. *Analyst*, 2013, 138(20):6044-6051.
42. Cheemalapati S, Palanisamy S, Mani V, Chen SM. Simultaneous electrochemical determination of dopamine and paracetamol on multiwalled carbon nanotubes/graphene oxide nanocomposite-modified glassy carbon electrode. *Talanta*, 2013, 117:297-304.
43. Munz M, Giusca CE, Myers-Ward RL, Gaskill DK, Kazakova O. Thickness-Dependent Hydrophobicity of Epitaxial Graphene. *ACS Nano*, 2015, 9(8):8401-8411.
44. Schneider GF, Xu Q, Hage S, Luik S, Spoor JN, Malladi S, Zandbergen H, Dekker C. Tailoring the hydrophobicity of graphene for its use as nanopores for DNA translocation. *Nat. Commun.*, 2013, 4:2619.
45. Martin-Moe SA, Lehr R, Cauley MD, Moe GR. Hydrophobic interactions and the design of receptor mimetic peptides. *Pept. Res.*, 1995, 8(2):70-76.
46. Wang X, You Z, Sha H, Cheng Y, Zhu H, Sun W. Sensitive electrochemical detection of dopamine with a DNA/graphene bilayer modified carbon ionic liquid electrode. *Talanta*, 2014, 128:373-378.
47. Liu S, Xing X, Yu J, Lian W, Li J, Cui M, Huang J. A novel label-free electrochemical aptasensor based on graphene-polyaniline composite film for dopamine determination. *Biosens. Bioelectron.*, 2012, 36(1):186-191.
48. Qian T, Yu C, Wu S, Shen J. In situ polymerization of highly dispersed polypyrrole on reduced graphite oxide for dopamine detection. *Biosens. Bioelectron.*, 2013, 50:157-160.
49. Qian T, Wu S, Shen J. Facilely prepared polypyrrole-reduced graphite oxide core-shell microspheres with high dispersibility for electrochemical detection of dopamine. *Chem. Commun.*, 2013, 49(41):4610-4612.

50. Si P, Chen H, Kannan P, Kim DH. Selective and sensitive determination of dopamine by composites of polypyrrole and graphene modified electrodes. *Analyst*, 2011, 136(24):5134-5138.
51. Mao H, Liang J, Ji C, Zhang H, Pei Q, Zhang Y, Zhang Y, Hisaeda Y, Song XM. Poly(zwitterionic liquids) functionalized polypyrrole/graphene oxide nanosheets for electrochemically detecting dopamine at low concentration. *Mater. Sci. Eng. C: Mater. Biol. Appl.*, 2016, 65:143-150.
52. Wu L, Feng L, Ren J, Qu X. Electrochemical detection of dopamine using porphyrin-functionalized graphene. *Biosens. Bioelectron.*, 2012, 34(1):57-62.
53. Sakthinathan S, Lee HF, Chen SM, Tamizhdurai P. Electrocatalytic oxidation of dopamine based on non-covalent functionalization of manganese tetraphenylporphyrin/reduced graphene oxide nanocomposite. *J. Coll. Interf. Sci.*, 2016, 468:120-127.
54. Yan X, Gu Y, Li C, Tang L, Zheng B, Li Y, Zhang Z, Yang M. Synergetic catalysis based on the proline tailed metalloporphyrin with graphene sheet as efficient mimetic enzyme for ultrasensitive electrochemical detection of dopamine. *Biosens. Bioelectron.*, 2016, 77:1032-1038.
55. Niu X, Yang W, Guo H, Ren J, Yang F, Gao J. A novel and simple strategy for simultaneous determination of dopamine, uric acid and ascorbic acid based on the stacked graphene platelet nanofibers/ionic liquids/chitosan modified electrode. *Talanta*, 2012, 99:984-988.
56. Weng X, Cao Q, Liang L, Chen J, You C, Ruan Y, Lin H, Wu L. Simultaneous determination of dopamine and uric acid using layer-by-layer graphene and chitosan assembled multilayer films. *Talanta*, 2013, 117:359-365.
57. Ku S, Palanisamy S, Chen SM. Highly selective dopamine electrochemical sensor based on electrochemically pretreated graphite and nafion composite modified screen printed carbon electrode. *J. Coll. Interf. Sci.*, 2013, 411:182-186.
58. Zhang W, Zheng J, Shi J, Lin Z, Huang Q, Zhang H, Wei C, Chen J, Hu S, Hao A. Nafion covered core-shell structured  $\text{Fe}_3\text{O}_4$ @graphene nanospheres modified electrode for highly selective detection of dopamine. *Anal. Chim. Acta.*, 2015, 853:285-290.
59. Liu CY, Liu ZY, Peng R, Zhong ZC. Quasireversible Process of Dopamine on Copper-Nickel Hydroxide Composite/Nitrogen Doped Graphene/Nafion Modified GCE and Its Electrochemical Application. *J. Anal. Meth. Chem.*, 2014, 2014:724538.
60. Ly SY, Park, Won D. Diagnosis of Dopamine in Brain Neuro Cell Using a Nafion-immobilized Carbon Electrode. *Med. Chem.*, 2012, Sep 10. [Preprint].
61. Yang L, Huang N, Lu Q, Liu M, Li H, Zhang Y, Yao S. A quadruplet electrochemical platform for ultrasensitive and simultaneous detection of ascorbic acid, dopamine, uric acid and acetaminophen based on a ferrocene derivative functional Au NPs/carbon dots nanocomposite and graphene. *Anal. Chim. Acta.*, 2016, 903:69-80.
62. Wang P, Xia M, Liang O, Sun K, Cipriano AF, Schroeder T, Liu H, Xie YH. Label-Free SERS Selective Detection of Dopamine and Serotonin Using Graphene-Au Nanopyramid Heterostructure. *Anal. Chem.*, 2015, 87(20):10255-10261.
63. Li C, Zhao J, Yan X, Gu Y, Liu W, Tang L, Zheng B, Li Y, Chen R, Zhang Z. Tremella-like graphene-Au composites used for amperometric determination of dopamine. *Analyst*, 2015, 140(6):1913-1920.
64. Yan Y, Liu Q, Wang K, Jiang L, Yang X, Qian J, Dong X, Qiu B. Enhanced peroxydisulfate electrochemiluminescence for dopamine biosensing based on Au nanoparticle decorated reduced graphene oxide. *Analyst*, 2013, 138(23):7101-7106.
65. Chen X, Zhang G, Shi L, Pan S, Liu W, Pan H. Au/ZnO hybrid nanocatalysts

- impregnated in N-doped graphene for simultaneous determination of ascorbic acid, acetaminophen and dopamine. *Mater. Sci. Eng. C: Mater. Biol. Appl.*, 2016, 65:80-89.
66. He P, Wang W, Du L, Dong F, Deng Y, Zhang T. Zeolite A functionalized with copper nanoparticles and graphene oxide for simultaneous electrochemical determination of dopamine and ascorbic acid. *Anal. Chim. Acta.*, 2012, 739:25-30.
67. Liu B, Ouyang X, Ding Y, Luo L, Xu D, Ning Y. Electrochemical preparation of nickel and copper oxides-decorated graphene composite for simultaneous determination of dopamine, acetaminophen and tryptophan. *Talanta*, 2016, 146:114-121.
68. Liu CY, Liu ZY, Peng R, Zhong ZC. Quasireversible Process of Dopamine on Copper-Nickel Hydroxide Composite/Nitrogen Doped Graphene/Nafion Modified GCE and Its Electrochemical Application. *J. Anal. Meth. Chem.*, 2014, 2014:724538.
69. Sheng ZH, Zheng XQ, Xu JY, Bao WJ, Wang FB, Xia XH. Electrochemical sensor based on nitrogen doped graphene: simultaneous determination of ascorbic acid, dopamine and uric acid. *Biosens. Bioelectron.*, 2012, 34(1):125-131.
70. Thanh TD, Balamurugan J, Lee SH, Kim NH, Lee JH. Effective seed-assisted synthesis of gold nanoparticles anchored nitrogen-doped graphene for electrochemical detection of glucose and dopamine. *Biosens. Bioelectron.*, 2016, 81:259-267.
71. Madhu R, Veeramani V, Chen SM, Manikandan A, Lo AY, Chueh YL. Honeycomb-like Porous Carbon-Cobalt Oxide Nanocomposite for High-Performance Enzymeless Glucose Sensor and Supercapacitor Applications. *ACS Appl. Mat. Interf.*, 2015, 7(29):15812-15820.
72. Mousty C, Leroux F. LDHs as electrode materials for electrochemical detection and energy storage: supercapacitor, battery and (bio)-sensor. *Rec. Pat. Nanotech.*, 2012, 6(3):174-192.
73. Liu Y, Jiao Y, Zhang Z, Qu F, Umar A, Wu X. Hierarchical SnO<sub>2</sub> nanostructures made of intermingled ultrathin nanosheets for environmental remediation, smart gas sensor, and supercapacitor applications. *ACS Appl. Mat. Interf.*, 2014, 6(3):2174-2184.
74. Must I, Johanson U, Kaasik F, Põldsalu I, Punning A, Aabloo A. Charging a supercapacitor-like laminate with ambient moisture: from a humidity sensor to an energy harvester. *Phys. Chem. Chem. Phys.*, 2013, 15(24):9605-9614.
75. Meng JP, Gong Y, Lin Q, Zhang MM, Zhang P, Shi HF, Lin JH. Metal-organic frameworks based on rigid ligands as separator membranes in supercapacitor. *Dalton Trans.*, 2015, 44(12):5407-5416.
76. Sales BB, Saakes M, Post JW, Buisman CJ, Biesheuvel PM, Hamelers HV. Direct power production from a water salinity difference in a membrane-modified supercapacitor flow cell. *Envir. Sci. Technol.*, 2010, 44(14):5661-5665.
77. Kiani MJ, Ahmadi MT, Karimi Feiz Abadi H, Rahmani M, Hashim A, Che Harun FK. Analytical modelling of monolayer graphene-based ion-sensitive FET to pH changes. *Nanoscale Res. Lett.*, 2013, 8(1):173-1-173-9.
78. Johnson RN, Hanna GR. Membrane model: a single transistor analog of excitable membrane. *J. Theor. Biol.*, 1969, 22(3):401-411.
79. Sibbald A, Covington AK, Carter RF. Simultaneous on-line measurement of blood K<sup>+</sup>, Ca<sup>2+</sup>, Na<sup>+</sup>, and pH with a four-function ChemFET integrated-circuit sensor. *Clin. Chem.*, 1984, 30(1):135-137.
80. Sibbald A, Covington AK, Carter RF. Online patient-monitoring system for the simultaneous analysis of blood K<sup>+</sup>, Ca<sup>2+</sup>, Na<sup>+</sup> and pH using a quadruple-function ChemFET integrated-circuit sensor. *Med. Biol. Eng. Comput.*, 1985, 23(4):329-338.
81. Costa J, Fernandes M, Vieira M, Lavareda G, Karmali A. Membrane selectivity versus

- sensor response in hydrogenated amorphous silicon ChemFETs using a semi-empirical model. *J. Nanosci. Nanotechnol.*, 2011, 11(10):8844-8847.
82. Sun G, Senapati S, Chang HC. High-flux ionic diodes, ionic transistors and ionic amplifiers based on external ion concentration polarization by an ion exchange membrane: a new scalable ionic circuit platform. *Lab Chip.*, 2016, 16(7):1171-1177.
83. Mo Y, Wan Y, Chau A, Huang F. Graphene/Ionic liquid composite films and ion exchange. *Sci. Rep.*, 2014, 4:5466-1-5466-8.
84. Chen G, Zhai S, Zhai Y, Zhang K, Yue Q, Wang L, Zhao J, Wang H, Liu J, Jia J. Preparation of sulfonic-functionalized graphene oxide as ion-exchange material and its application into electrochemiluminescence analysis. *Biosens. Bioelectron.*, 2011, 26(7):3136-3141.
85. Zhang S, Shao Y, Liu J, Aksay IA, Lin Y. Graphene-polypyrrole nanocomposite as a highly efficient and low cost electrically switched ion exchanger for removing  $\text{ClO}_4^-$  from wastewater. *ACS Appl. Mat. Interf.*, 2011, 3(9):3633-3637.
86. Park JW, Park SJ, Kwon OS, Lee C, Jang J. Polypyrrole nanotube embedded reduced graphene oxide transducer for field-effect transistor-type  $\text{H}_2\text{O}_2$  biosensor. *Anal. Chem.*, 2014, 86(3):1822-1828.
87. Kwon OS, Park SJ, Hong JY, Han AR, Lee JS, Lee JS, Oh JH, Jang J. Flexible FET-type VEGF aptasensor based on nitrogen-doped graphene converted from conducting polymer. *ACS Nano*, 2012, 6(2):1486-1493.
88. Farid S, Meshik X, Choi M, Mukherjee S, Lan Y, Parikh D, Poduri S, Batteredene U, Huang CE, Wang YY, Burke P, Dutta M, Strocio MA. Detection of Interferon gamma using graphene and aptamer based FET-like electrochemical biosensor. *Biosens. Bioelectron.*, 2015, 71:294-299.
89. Park JW, Park SJ, Kwon OS, Lee C, Jang J. High-performance  $\text{Hg}^{2+}$  FET-type sensors based on reduced graphene oxide-polyfuran nanohybrids. *Analyst*, 2014, 139(16):3852-3855.
90. Park SJ, Kwon OS, Lee SH, Song HS, Park TH, Jang J. Ultrasensitive flexible graphene based field-effect transistor (FET)-type bioelectronic nose. *Nano Lett.*, 2012, 12(10):5082-5090.
91. Worley BC, Kim S, Park S, Rossky PJ, Akinwande D, Dodabalapur A. Dramatic vapor-phase modulation of the characteristics of graphene field-effect transistors. *Phys. Chem. Chem. Phys.*, 2015, 17(28):18426-18430.
92. Min M, Seo S, Lee J, Lee SM, Hwang E, Lee H. Changes in major charge transport by molecular spatial orientation in graphene channel field effect transistors. *Chem. Commun.*, 2013, 49(56):6289-6291.
93. Strejčková A, Staničová J, Jancura D, Miškovský P, Bánó G. Spatial orientation and electric-field-driven transport of hypericin inside of bilayer lipid membranes. *J. Phys. Chem. B.*, 2013, 117(5):1280-1286.
94. Shen J, Liu G, Huang K, Jin W, Lee KR, Xu N. Membranes with fast and selective gas-transport channels of laminar graphene oxide for efficient  $\text{CO}_2$  capture. *Angew. Chem. Int. Ed. Engl.*, 2015, 54(2):578-582.
95. Chen XC, Wei W, Lv W, Su FY, He YB, Li B, Kang F, Yang QH. A graphene-based nanostructure with expanded ion transport channels for high rate Li-ion batteries. *Chem. Commun.*, 2012, 48(47):5904-5906.
96. Sun P, Zhu M, Wang K, Zhong M, Wei J, Wu D, Xu Z, Zhu H. Selective ion penetration of graphene oxide membranes. *ACS Nano*, 2013, 7(1):428-437.
97. Sint K, Wang B, Král P. Selective ion passage through functionalized graphene nanopores. *J. Am. Chem. Soc.*, 2008, 130(49):16448-16449.
98. Boukhvalov DW, Virojanadara C. Penetration of alkali atoms throughout a graphene membrane: theoretical modeling. *Nanoscale*, 2012, 4(5):1749-1753.
99. He Z, Zhou J, Lu X, Corry B. Bioinspired graphene nanopores with voltage-tunable

- ion selectivity for Na<sup>+</sup> and K<sup>+</sup>. *ACS Nano*, 2013, 7(11):10148-10157.
100. Grahame-Smith DG, Wang H. Comparison of the actions of lithium, rubidium, and caesium on rat brain 5-HT function: pharmacological implications of ion channel function. *Clin. Neuropharmacol.*, 1992, 15(Suppl. 1):614A-615A.
101. Boccaccio A, Conti F, Olivera BM, Terlau H. Binding of kappa-conotoxin PVIIA to Shaker K<sup>+</sup> channels reveals different K<sup>+</sup> and Rb<sup>+</sup> occupancies within the ion channel pore. *J. Gen. Physiol.*, 2004, 124(1):71-81.
102. Mao G, Winokur MJ, Karasz FE. Dual alkali-metal-ion channel structures in poly(p-phenylenevinylene). *Phys. Rev. B: Cond. Matt.*, 1996, 53(2):R463-R467.
103. Miller C, Stahl N, Barrol M. A thermodynamic analysis of monovalent cation permeation through a K<sup>+</sup>-selective ion channel. *Neuron*, 1988, 1(2):159-164.
104. Billes F, Mohammed-Ziegler I, Mikosch H. Transportation behavior of alkali ions through a cell membrane ion channel. A quantum chemical description of a simplified isolated model. *J. Mol. Model.*, 2012, 18(8):3627-3637.
105. Hilder TA, Gordon D, Chung SH. Synthetic chloride-selective carbon nanotubes examined by using molecular and stochastic dynamics. *Biophys. J.*, 2010, 99(6):1734-1742.
106. Middleton RE, Pheasant DJ, Miller C. Homodimeric architecture of a ClC-type chloride ion channel. *Nature*, 1996, 383(6598):337-340.
107. Li Y, Yeo GF, Milne RK, Madsen BW, Edeson RO. Burst properties of a supergated double-barrelled chloride ion channel. *Math. Biosci.*, 2000, 166(1):23-44.
108. Franco A, Winegar BD, Lansman JB. Open channel block by gadolinium ion of the stretch-inactivated ion channel in mdx myotubes. *Biophys. J.*, 1991, 59(6):1164-1170.
109. Wang K, McIlvain B, Tseng E, Kowal D, Jow F, Shen R, Zhang H, Shan QJ, He L, Chen D, Lu Q, Dunlop J. Validation of an atomic absorption rubidium ion efflux assay for KCNQ/M-channels using the ion Channel Reader 8000. *Assay Drug Dev. Technol.*, 2004, 2(5):525-534.
110. Massobrio G, Massobrio P, Martinoia S. Modeling the neuron-carbon nanotube-ISFET junction to investigate the electrophysiological neuronal activity. *Nano Lett.*, 2008, 8(12):4433-4440.
111. Martinoia S, Massobrio P. ISFET-neuron junction: circuit models and extracellular signal simulations. *Biosens. Bioelectron.*, 2004, 19(11):1487-1496.
112. Li Z, Wang C, Tian L, Bai J, Yao H, Zhao Y, Zhang X, Cao S, Qi W, Wang S, Shi K, Xu Y, Mingliang Z, Liu B, Qiu H, Liu J, Wu W, Wang X, Wenzhen A. An embryo of protocells: The capsule of graphene with selective ion channels. *Sci. Rep.*, 2015, 5:10258-1-10258-14.
113. Li Z, Wang C, Tian L, Bai J, Yao H, Zhao Y, Zhang X, Cao S, Qi W, Wang S, Shi K, Xu Y, Mingliang Z, Liu B, Qiu H, Liu J, Wu W, Wang X, Wenzhen A. Corrigendum: An embryo of protocells: The capsule of graphene with selective ion channels. *Sci. Rep.*, 2015, 5:12386.
114. Stillwell W. Facilitated diffusion as a method for selective accumulation of materials from the primordial oceans by a lipid-vesicle protocell. *Orig. Life.*, 1980, 10(3):277-292.
115. Liu J, Stace-Naughton A, Jiang X, Brinker CJ. Porous nanoparticle supported lipid bilayers (protocells) as delivery vehicles. *J. Am. Chem. Soc.*, 2009, 131(4):1354-1355.
116. Walde P. Building artificial cells and protocell models: experimental approaches with lipid vesicles. *Bioessays*, 2010, 32(4):296-303.
117. Li M, Huang X, Tang TY, Mann S. Synthetic cellularity based on non-lipid micro-compartments and protocell models. *Curr. Opin. Chem. Biol.*, 2014, 22:1-11.

118. Koga S, Williams DS, Perriman AW, Mann S. Peptide-nucleotide microdroplets as a step towards a membrane-free protocell model. *Nat. Chem.*, 2011, 3(9):720-724.
119. Li M, Harbron RL, Weaver JV, Binks BP, Mann S. Electrostatically gated membrane permeability in inorganic protocells. *Nat. Chem.*, 2013, 5(6):529-536.
120. Cooper GJ, Kitson PJ, Winter R, Zagnoni M, Long DL, Cronin L. Modular redox-active inorganic chemical cells: iCHELLs. *Angew. Chem. Int. Ed. Engl.*, 2011, 50(44):10373-10376.
121. Kumar RK, Li M, Olof SN, Patil AJ, Mann S. Artificial cytoskeletal structures within enzymatically active bio-inorganic protocells. *Small*, 2013, 9(3):357-362.
122. Gupta VK. Emergence of photoautotrophic minimal protocell-like supramolecular assemblies, "Jeewanu" synthesised photo chemically in an irradiated sterilised aqueous mixture of some inorganic and organic substances. *Orig. Life Evol. Biosph.*, 2014, 44(4):351-355.
123. Kaur G, Rath G, Heer H, Goyal AK. Optimization of protocell of silica nanoparticles using 3<sup>2</sup> factorial designs. *AAPS PharmSciTech.*, 2012, 13(1):167-173.
124. Yasaei P, Kumar B, Hantehzadeh R, Kayyalha M, Baskin A, Reprin N, Wang C, Klie RF, Chen YP, Král P, Salehi-Khojin A. Chemical sensing with switchable transport channels in grapheme grain boundaries. *Nat. Commun.*, 2014, 5:4911.
125. Rickhaus P, Liu MH, Makk P, Maurand R, Hess S, Zihlmann S, Weiss M, Richter K, Schönenberger C. Guiding of Electrons in a Few-Mode Ballistic Graphene Channel. *Nano Lett.*, 2015, 15(9):5819-5825.
126. Cantele G, Lee YS, Ninno D, Marzari N. Spin channels in functionalized graphene nanoribbons. *Nano Lett.*, 2009, 9(10):3425-3429.
127. Archer SJ, Ellena JF, Cafiso DS. Dynamics and aggregation of the peptide ion channel alamethicin. Measurements using spin-labeled peptides. *Biophys. J.*, 1991, 60(2):389-398.
128. Perozo E, Cuello LG, Cortes DM, Liu YS, Sompornpisut P. EPR approaches to ion channel structure and function. *Novartis Found Symp.*, 2002, 245:146-168.
129. Holt SA, Le Brun AP, Majkrzak CF, McGillivray DJ, Heinrich F, Lösche M, Lakey JH. An ion-channel-containing model membrane: structural determination by magnetic contrast neutron reflectometry. *Soft Matter*, 2009, 5(13):2576-2586.
130. Endeward B, Butterwick JA, MacKinnon R, Prisner TF. Pulsed electron-electron double-resonance determination of spin-label distances and orientations on the tetrameric potassium ion channel KcsA. *J. Am. Chem. Soc.*, 2009, 131(42):15246-15250.
131. Dellisanti CD, Ghosh B, Hanson SM, Raspanti JM, Grant VA, Diarra GM, Schuh AM, Satyshur K, Klug CS, Czajkowski C. Site-directed spin labeling reveals pentameric ligand-gated ion channel gating motions. *PLoS Biol.*, 2013, 11(11):e1001714, 1-14.
132. Mirsaidov U, Mokkaapati VR, Bhattacharya D, Andersen H, Bosman M, Özyilmaz B, Matsudaira P. Scrolling graphene into nanofluidic channels. *Lab Chip*, 2013, 13(15):2874-2878.
133. Montenegro J, Ghadiri MR, Granja JR. Ion channel models based on self-assembling cyclic peptide nanotubes. *Acc. Chem. Res.*, 2013, 46(12):2955-2965.
134. Mayer M, Semetey V, Gitlin I, Yang J, Whitesides GM. Using ion channel-forming peptides to quantify protein-ligand interactions. *J. Am. Chem. Soc.*, 2008, 130(4):1453-1465.
135. Sánchez-Quesada J, Isler MP, Ghadiri MR. Modulating ion channel properties of transmembrane peptide nanotubes through heteromeric supramolecular assemblies. *J. Am. Chem. Soc.*, 2002, 124(34):10004-10005.

136. Ichikawa T, Yoshio M, Hamasaki A, Mukai T, Ohno H, Kato T. Self-organization of room-temperature ionic liquids exhibiting liquid-crystalline bicontinuous cubic phases: formation of nano-ion channel networks. *J. Am. Chem. Soc.*, 2007, 129(35):10662-10663.
137. Cazacu A, Tong C, van der Lee A, Fyles TM, Barboiu M. Columnar self-assembled ureido crown ethers: an example of ion-channel organization in lipid bilayers. *J. Am. Chem. Soc.*, 2006, 128(29):9541-9548.
138. Nyitrai G, Keszthelyi T, Bóta A, Simon A, Tóke O, Horváth G, Pál I, Kardos J, Héja L. Sodium selective ion channel formation in living cell membranes by polyamidoamine dendrimer. *Biochim. Biophys. Acta.*, 2013, 1828(8):1873-1880.
139. Abhilash TS, De Alba R, Zhelev N, Craighead HG, Parpia JM. Transfer printing of CVD graphene FETs on patterned substrates. *Nanoscale*, 2015, 7(33):14109-14113.
140. Ping J, Wang Y, Ying Y, Wu J. Application of electrochemically reduced graphene oxide on screen-printed ion-selective electrode. *Anal. Chem.*, 2012, 84(7):3473-3479.
141. Lukas M, Meded V, Vijayaraghavan A, Song L, Ajayan PM, Fink K, Wenzel W, Krupke R. Catalytic subsurface etching of nanoscale channels in graphite. *Nat. Commun.*, 2013; 4:1379.
142. Choi BS, Kim SM, Gong J, Lee YW, Kang SW, Lee HS, Park JY, Han SW. One-pot self-templating synthesis of Pt hollow nanostructures and their catalytic properties for CO oxidation. *Chemistry*, 2014, 20(37):11669-11674.
143. Yang F, Zhou S, Wang H, Long S, Liu X, Kong Y. A metal-assisted templating route ( $S^0M^+I$ ) for fabricating thin-layer CoO covered on the channel of nanospherical-HMS with improved catalytic properties. *Dalton Trans.*, 2016, 45(15):6371-6382.
144. Li Y, Guijarro N, Zhang X, Prévot MS, Jeanbourquin XA, Sivula K, Chen H, Li Y. Templating Sol-Gel Hematite Films with Sacrificial Copper Oxide: Enhancing Photoanode Performance with Nanostructure and Oxygen Vacancies. *ACS Appl. Mat. Interf.*, 2015, 7(31):16999-17007.
145. Martin JD, Keary CL, Thornton TA, Novotnak MP, Knutson JW, Folmer JC. Metallotropic liquid crystals formed by surfactant templating of molten metal halides. *Nat. Mater.*, 2006, 5(4):271-275.
146. Moon GH, Shin Y, Choi D, Arey BW, Exarhos GJ, Wang C, Choi W, Liu J. Catalytic templating approaches for three-dimensional hollow carbon/graphene oxide nano-architectures. *Nanoscale*, 2013, 5(14):6291-6296.
147. Chaloin L, Méry J, Van Mau N, Divita G, Heitz F. Synthesis of a template-associated peptide designed as a transmembrane ion channel former. *J. Pept. Sci.*, 1999, 5(9):381-391.
148. Wang Y, Ma S, Su Y, Han X. Palladium nanotubes formed by lipid tubule templating and their application in ethanol electrocatalysis. *Chemistry*, 2015, 21(16):6084-6089.
149. Inesi G, Kirtley ME. Coupling of catalytic and channel function in the  $Ca^{2+}$  transport ATPase. *J. Membr. Biol.*, 1990, 116(1):1-8.
150. Hsu CM, Rosen BP. Characterization of the catalytic subunit of an anion pump. *J. Biol. Chem.*, 1989, 264(29):17349-17354.
151. Ramjeesingh M, Li C, Garami E, Huan LJ, Galley K, Wang Y, Bear CE. Walker mutations reveal loose relationship between catalytic and channel-gating activities of purified CFTR (cystic fibrosis transmembrane conductance regulator). *Biochemistry*, 1999, 38(5):1463-1468.
152. Csanády L, Vergani P, Gadsby DC. Strict coupling between CFTR's catalytic cycle and gating of its  $Cl^-$  ion pore revealed by distributions of open channel burst durations. *Proc. Nat. Acad. Sci. USA*, 2010, 107(3):1241-1246.
153. Bienengraeber M, Alekseev AE, Abraham MR, Carrasco AJ, Moreau C, Vivaudou M,

- Dzeja PP, Terzic A. ATPase activity of the sulfonyleurea receptor: a catalytic function for the KATP channel complex. *FASEB J.*, 2000, 14(13):1943-1952.
154. Park S, Lim BB, Perez-Terzic C, Mer G, Terzic A. Interaction of asymmetric ABCC9-encoded nucleotide binding domains determines KATP channel SUR2A catalytic activity. *J. Proteome Res.*, 2008, 7(4):1721-1728.
155. Behera RK, Theil EC. Moving  $\text{Fe}^{2+}$  from ferritin ion channels to catalytic OH centers depends on conserved protein cage carboxylates. *Proc. Nat. Acad. Sci. USA*, 2014, 111(22):7925-7930.
156. Theil EC. Ferritin protein nanocages use ion channels, catalytic sites, and nucleation channels to manage iron/oxygen chemistry. *Curr. Opin. Chem. Biol.*, 2011, 15(2):304-311.
157. Sakai N, Sordé N, Matile S. Synthetic catalytic pores. *J. Am. Chem. Soc.*, 2003, 125(26):7776-7777.
158. Sharma V, Wikström M. The role of the K-channel and the active-site tyrosine in the catalytic mechanism of cytochrome c oxidase. *Biochim. Biophys. Acta.*, 2016, 1857(8):1111-1115.
159. Chakrabarti N, Ing C, Payandeh J, Zheng N, Catterall WA, Pomès R. Catalysis of  $\text{Na}^+$  permeation in the bacterial sodium channel Na(V)Ab. *Proc. Nat. Acad. Sci. USA*, 2013, 110(28):11331-11336.
160. Lim C, Dudev T. Potassium Versus Sodium Selectivity in Monovalent Ion Channel Selectivity Filters. *Met. Ions Life Sci.*, 2016, 16:325-347.
161. Zacharias N, Dougherty DA. Cation- $\pi$  interactions in ligand recognition and catalysis. *Trends Pharmacol Sci.*, 2002, 23(6):281-287.
162. Okamura Y. Lipids: PI couples voltage to catalysis. *Nat. Chem. Biol.*, 2010, 6(5):315-316.
163. Kohout SC, Bell SC, Liu L, Xu Q, Minor DL, Isacoff EY. Electrochemical coupling in the voltage-dependent phosphatase Ci-VSP. *Nat. Chem. Biol.*, 2010, 6(5):369-375.
164. Dhindwal S, Priyadarshini P, Patil DN, Tapas S, Kumar P, Tomar S, Kumar P. Ligand-bound structures of 3-deoxy-D-manno-octulosonate 8-phosphate phosphatase from *Moraxella catarrhalis* reveal a water channel connecting to the active site for the second step of catalysis. *Acta Crystallogr. D: Biol. Crystallogr.*, 2015, 71(2):239-255.
165. Marti J, Nagy G, Gordillo MC, Guàrdia E. Molecular simulation of liquid water confined inside graphite channels: thermodynamics and structural properties. *J. Chem. Phys.*, 2006, 124(9):94703-1-94703-7.
166. Thekkethala JF, Sathian SP. Thermal transpiration through single walled carbon nanotubes and graphene channels. *J. Chem. Phys.*, 2013, 139(17):174712-1-174712-9.
167. Leung SS, Sindhikara D, Jacobson MP. Simple Predictive Models of Passive Membrane Permeability Incorporating Size-Dependent Membrane-Water Partition. *J. Chem. Inf. Model.*, 2016, 56(5):924-929.
168. Kreida S, Törnroth-Horsefield S. Structural insights into aquaporin selectivity and regulation. *Curr. Opin. Struct. Biol.*, 2015, 33:126-134.
169. Jang M, Trung TQ, Jung JH, Kim BY, Lee NE. Improved performance and stability of field-effect transistors with polymeric residue-free graphene channel transferred by gold layer. *Phys. Chem. Chem. Phys.*, 2014, 16(9):4098-4105.
170. Ramesh P, Itkis ME, Bekyarova E, Wang F, Niyogi S, Chi X, Berger C, de Heer W, Haddon RC. Electro-oxidized epitaxial graphene channel field-effect transistors with single-walled carbon nanotube thin film gate electrode. *J. Am. Chem. Soc.*, 2010, 132(41):14429-14436.
171. Li SL, Miyazaki H, Hiura H, Liu C, Tsukagoshi K. Enhanced logic performance with semiconducting bilayer graphene channels. *ACS Nano*, 2011, 5(1):500-506.

# THE DISPERSIONS OF NANOPARTICLES IN WATER-ORGANIC SOLVENTS AS THE BASIS FOR THE SILVER NANO-INK FOR INK-JET PRINTING

**Sergey V. Tkachev, Sergey P. Gubin**

"AkKo Lab" LLC, <http://akkolab.ru/en>

129110 Moscow, Russian Federation

Kurnakov Institute of General and Inorganic Chemistry, Russian Academy of Sciences, <http://www.igic.ras.ru>

117991 Moscow, Russian Federation

[tkachev\\_svmsu@mail.ru](mailto:tkachev_svmsu@mail.ru), [gubin@igic.ras.ru](mailto:gubin@igic.ras.ru)

**Vitalii P. Kim, Alexey E. Kushnir, Denis Yu. Kornilov**

"AkKo Lab" LLC, <http://akkolab.ru/en>

[vp.kim@physics.ms.u.ru](mailto:vp.kim@physics.ms.u.ru), [kushnir.a.e@gmail.com](mailto:kushnir.a.e@gmail.com), [kornilovdenis@rambler.ru](mailto:kornilovdenis@rambler.ru)

*Abstract.* The work is aimed to solve the problem of developing functional silver nano-ink applied in ink-jet technology in printed flexible electronics, as well as to demonstrate printing results and their discussion. The development of functional compounds for printing is a fundamentally new approach to the production of flexible electronic devices for the military and civil industry. As a part of the work special attention is paid to the preparation of aqueous and organic dispersions of silver nanoparticles, the study of the various factors which affect the size and characteristics of the nanoparticles, methods of concentrating the standard dispersions to obtain nano-ink, printing the conductive structures by synthesized nano-ink and research of the printed elements' properties. These results give an opportunity to develop silver nano-ink and adapt it for printing on various substrates (including flexible polymeric ones) by specialized equipment.

*Keywords:* silver nano-ink, aqueous dispersions, ink-jet printing, conductive structures, polymeric substrate, flexible printed electronics

UDC 546.57, 621.3.049.7

*Bibliography* – 8 references

*Received* 5.12.2016

*RENSIT*, 2016, 8(2):171-184

DOI: 10.17725/rensit.2016.08.171

## CONTENTS

- |   |  |
|---|--|
| <ol style="list-style-type: none"> <li>1. INTRODUCTION (171)</li> <li>2. THE EXPERIMENTAL SECTION (174)               <ol style="list-style-type: none"> <li>2.1. PREPARATION OF DILUTE AQUEOUS DISPERSIONS OF SILVER NANOPARTICLES (174)</li> <li>2.2. PREPARATION OF SILVER NANO-INK (174)</li> </ol> </li> <li>3. RESULTS AND DISCUSSION (174)               <ol style="list-style-type: none"> <li>3.1. INK-JET PRINTING WITH USE OF SILVER NANO-INK (176)</li> <li>3.2. TREATMENT OF SUBSTRATES IN PLASMA (177)</li> <li>3.3. THERMAL TREATMENT (178)</li> <li>3.4. PRINTING OF THE CONDUCTIVE LINES ON THE ITO SURFACE WITH THE USE OF SILVER NANO-INK (178)</li> </ol> </li> </ol> | <ol style="list-style-type: none"> <li>3.5. PRINTING OF THE CONDUCTIVE LINES ON THE SILICON SURFACE WITH THE USE OF SILVER NANO-INK (180)</li> <li>3.6. PRINTING OF THE HEATING ELEMENTS ON THE POLYMER FILM (181)</li> <li>3.7. PRINTING OF THE COMPLEX-GEOMETRY CONDUCTIVE BOARDS ON DIFFERENT SUBSTRATES (181)</li> <li>3.8. PRINTING ON TEXTILE GOODS WITH THE USE OF SILVER NANO-INK (182)</li> </ol> <ol style="list-style-type: none"> <li>4. CONCLUSION (182)</li> <li>REFERENCES (183)</li> </ol> <ol style="list-style-type: none"> <li>1. INTRODUCTION<br/>Printed flexible electronics is a new perspective direction on development of microelectronic flexible devices by the printing additive</li> </ol> |
|---|--|

technologies of the next generation including ink-jet printing [1]. Nowadays major foreign corporations, interested commercial organizations and separate research groups are working at creation and development of flexible electronic devices by the method of precision additive printing with the use of specialized printers.

Intensive development of the mentioned direction in microelectronics is caused by sharp monthly increase in the number of scientific publications devoted to creation of printing microelectronic devices.

Use of the additive printing is urgent due to the following advantages: increasing technological capabilities to use the flexible electronic devices; simplification of technological cycle of design and manufacture of electronic circuit boards; reduction in the number of technological operations; reduce in energy costs; significant improvement of the environmental safety of the technological process.

Nowadays considerable work of scientists and designers in the sphere of printed and flexible electronics is aimed at development of new functional materials – nano-ink which would give an opportunity to excel the corresponding solid state electronic analogs produced with the use of the traditional methods in some crucial parameters. Thus, depending on the aim of use, nano-ink for special purposes is being developed. They are the following: the conductive on the basis of metal nanoparticles (mainly silver nanoparticles), semiconductive, magnetic and carbon ones on the basis of graphene and related nanoobjects and nanotubes [2-3]. It should be noted that the majority of printed electronic tasks require silver nano-ink.

Thus, this article presents the results of developments of the "AkKo Lab" LLC

company and their discussion. They include creation of silver nano-ink adapted for printing on the available high-technology equipment Dimatix Materials Printer 2831 and also the results of various structures' printing on the different-nature substrates.

In terms of chemistry, silver nano-ink is highly concentrated dispersions of silver nanoparticles. As a rule, mass content of silver nanoparticles in such systems accounts for more than 5-10 wt%. It is obvious that synthesis of dilute dispersions of silver nanoparticles is quite well-developed nowadays, and there are a great number of various methods and options to obtain them. However, there are some problems related to production of highly concentrated dispersions of silver nano-ink applied particularly to print the conductive lines by ink-jet printing method. Besides that, to use nano-ink in cartridges of the ink-jet printers Dimatrix, the following requirements should be fulfilled: the used nano-ink should have viscosity 10-20 cP, surface tension 28-33 dynes/cm and pH 4-9, particle size (preferably less than 50 nm) ensuring successful ink's passage through the nozzles of the size about 17  $\mu\text{m}$  and also absence of harmful and poisonous substances in nano-ink composition.

It is also necessary to notice that the nano-ink use in printing on the basis of various nanoobjects is justified by the precision microprint and the unique properties of nanomaterials in comparison with similar compact substances. It is worth noticing that nowadays on the world market there is only some simpler nano-ink (according to its composition), mainly silver one [4]. As a rule, the main difficulties at synthesis of nano-ink adapted for ink-jet printing are the following: stabilization of individual nanoparticles

at increase in their concentration in dispersion (up to several tens of mass percentage of the substance), achievement of the required surface tension, nano-ink viscosity. These difficulties are being solved by not only selection of the conditions for synthesis realization (duration, temperature, components concentration), but also by choice of various kinds of surfactants, solvents. In general, the great number of methods is original because nano-ink is a complex multi-component solution.

The work innovation is in the development of new, original according to their composition, highly concentrated dispersions of functional silver nanoparticles which allow producing elements of flexible microelectronic devices by the method of ink-jet printing.

Nowadays such large companies as "Fujifilm", "Novacentrix", "Ceradrop" and the others produce and supply the printers capable to print pictures of any geometry using nano-ink. Moreover, refill of the corresponding cartridge is possible using any nano-ink meeting the printing requirements; the substrates choice is not limited. Now printing accuracy of such printers does not exceed several microns, and minimum size of an individual drop is more than 15  $\mu\text{m}$ . This is due to the sizes of the cartridge nozzles, surface tension and nano-ink viscosity, the adhesive properties of the substrate and precision of the stepper motors of the printer. Nowadays, using such printed installations and nano-ink, specializing companies and individual research teams print the majority of microelectronics' element base: capacitors, accumulators, conductive lines, LEDs and the others [5-7]. Besides, some experiments on printing LEDs, transistors on the flexible transparent polymer substrates are described

in literature. Large-scale production with the application of printing additive technologies is possible using roll-to-roll technology where the roll of the required material is applied as a substrate. This technology is suitable to print and carry out the following temperature (thermal, light, etc.) treatment of electronic devices with the feed rate of the substrate as several meters per a minute.

Combination of functional nano-ink (with characteristics of conductors, semiconductors and dielectrics) with the modern printed installations may reduce the cost of the electronic products significantly, increase efficiency of their production, give an opportunity to produce flexible electronic devices.

Ink-jet printing technology differs from the traditional technologies of electronic industry (photolithography, etc.) in the low production cost, possibility to work with any substrate type, and substrates in this technology do not experience significant impacts. Thus, the technology gives an opportunity to produce flexible transparent electronic devices with relatively low cost. The final product in the ink-jet printing is batteries, accumulators, capacitors, thin-film transistors, displays, sensors, antennas, solar batteries, the connecting elements in chips, etc. [8]

The problem statement in this work is the need to arrange mass production of silver nano-ink which is stable during storage and transportation and suitable for ink-jet printing of the conductive structures on the various substrates (including flexible ones) using modern 2D printers.

The article shows how to solve the assigned task by the approaches and methods of colloidal chemistry, gives the results

of some elements' printing, presents their measured characteristics.

## 2. EXPERIMENTAL SECTION

The initial reagents for the silver nano-ink synthesis were silver nitrate (chemically pure, «Bertuz» JSC), silver acetate ( $\geq 99.0\%$ , CAS-No.: 563-63-3, Sigma Aldrich), tri-sodium citrate 2-hydrate (99.0%, CAS-No.: 6132-04-3, Panreac), sodium borohydride (96%, CAS-No.: 16940-66-2, Panreac), ethylene glycol (analytically pure, CAS-No.: 107-21-1, «Ekos-1» JSC) and deionized water.

### 2.1. PREPARATION OF DILUTE AQUEOUS DISPERSIONS OF SILVER NANOPARTICLES

In a typical synthesis, 4 g of sodium citrate was dissolved in deionized water in a flat-bottomed flask at continuous stirring. Next, a solution containing 0.5 g of silver nitrate and silver acetate in deionized water was added to sodium citrate solution in small portions at constant stirring. Additionally 0.2 M aqueous sodium borohydride solution was prepared. Further, freshly prepared sodium borohydride solution was added dropwise to a solution containing sodium citrate, nitrate and silver acetate. The obtaining dispersion of silver nanoparticles acquired an intense dark brown color. As a result, the standard aqueous dispersions of silver nanoparticles containing 0.03 wt% silver nanoparticles were obtained.

### 2.2. PREPARATION OF SILVER NANO-INK

To synthesize silver nano-ink, the standard dispersion of silver nanoparticles was centrifuged at 15 000 rpm for 20 min. Further the supernatant was decanted and the obtaining highly concentrated liquid of silver nanoparticles was collected. Then centrifugation step was repeated again. Further surfactants were added to the

resulting silver nanoparticles concentrate. They included ethylene glycol which is needed to stabilize the obtained silver nanoparticles. Then, the obtained highly concentrated dispersion of the nanoparticles in ethylene glycol was passed through the filter with a pore size of 0.22  $\mu\text{m}$ . As a result, the targeted silver nano-ink was obtained.

The morphology, composition and structure of the obtaining nano-objects in the work were examined by scanning electron microscopy SEM (the scanning probe microscope Carl Zeiss Supra 40- 30- 87, Germany), atomic force microscopy AFM (the atomic force microscope Solver P47, «NT-MDT» Co, Russia), transmission electron microscopy TEM (the transmission electron microscope JEOL 2000FX, Germany), the powder X-ray diffraction XRD (the diffractometer Bruker Advanced 8 at  $\text{CuK}\lambda$  radiation and  $\lambda=1,5418 \text{ \AA}$ ), spectrophotometry (the spectrophotometer Leki SS2107UV, «LOIP» JSC, Russia)

## 3. RESULTS AND DISCUSSION

It should be noted that the structure and the spectral properties of nanoparticles depend significantly not only on composition and the characteristics of the dispersion where they are dispersed but also on the synthesis conditions, use of one or another stabilizer, solvent, concentration of initial reagents, etc. Due to the fact that nanoparticles are generated using standard methodologies, it is still being discussed if it is possible to keep the composition, structure and specific optical physical characteristics of initial nanoparticles when they become final product – highly concentrated dispersions of these nanoparticles – nano-ink. The authors would like to confirm the possibility to prepare silver nano-ink from standard silver dispersions

in aqueous dispersion keeping their main characteristics and also to show and discuss the results of conductive structures' printing with the use of synthesized nano-ink on the printer Dimatix Materials Printer 2831.

**Figure 1** presents typical absorption spectra depending on wavelength for diluted samples of standard dispersion of silver nanoparticles and nano-ink produced from the given dispersion. Absorption extremum takes place at wavelength of 388 nm which corresponds to the average nanoparticles size of 10 nm, according to the literature data.

Spectral analysis shows that operations of centrifugation and concentration of standard dispersion of silver nanoparticles lead to not only increase in concentration of the targeted nanoparticles in nano-ink but more noticeable monodispersion of the end product in comparison with initial dispersion.

According to the data of XRD analysis, reflections of crystal structure of silver nanoparticles isolated both from standard dispersion of silver nanoparticles and from silver nano-ink and after that prepared at 100°C are equal to the phase of massive silver (the card PDF#030921, database of the International Centre for Diffraction Data).

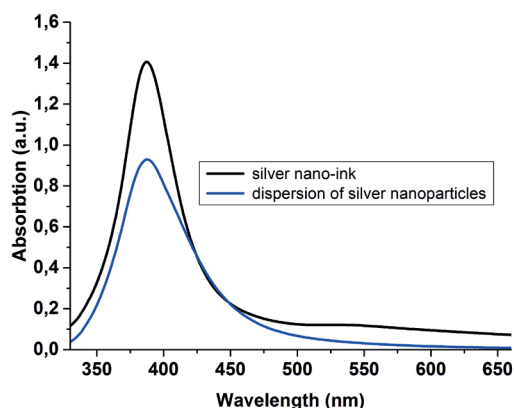


**Fig. 1.** Typical absorption spectra of diluted dispersions of silver nanoparticles and nano-ink.

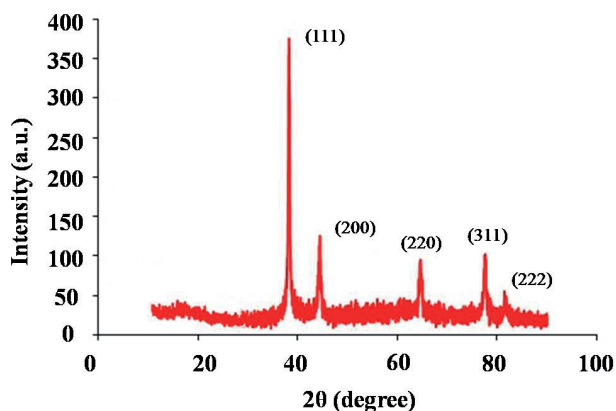


**Fig. 2.** XRD pattern of silver nano-ink produced by thermal treatment of silver inks' aliquot at temperature 100°C for 30 min.

**Figure 2** gives diffraction pattern of silver nano-ink produced by thermal treatment of silver inks' aliquot at temperature 100°C.

Analysis of silver nano-ink samples by the transmission electron microscopy method shows that dispersions of silver nanoparticles and nano-ink consist of isotropic nanoparticles (**Figure 3**). It should be noticed that the particles' shape is quite uniform and close to the spherical one. According to the results of the electron-diffraction pattern obtained by TEM method, silver nano-ink has crystal nature. Thus, ring-shaped reflections on the electron-diffraction pattern identify the phase of compact silver and the sample's single-phase state.

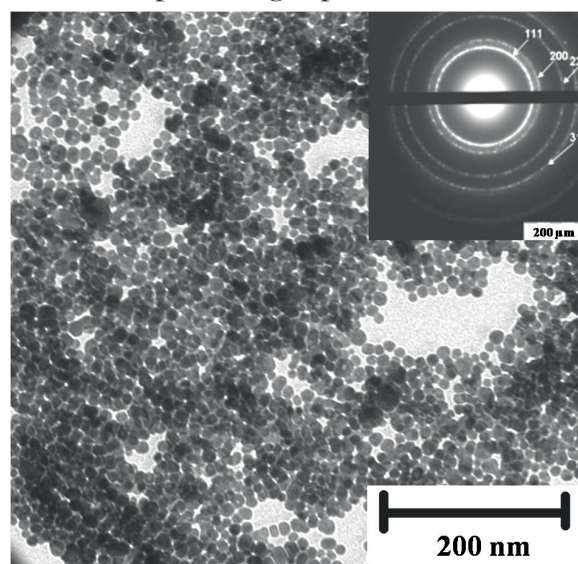


**Fig. 3.** TEM-image and electron diffraction of silver nanoparticles from silver nano-ink.

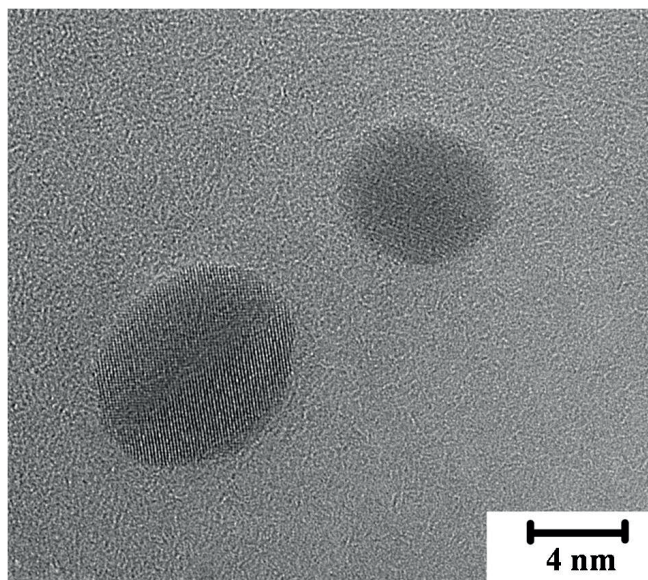


Fig. 4. HRTEM - high resolution image of silver nanoparticles from silver nanoparticles' dispersion.

It is shown that the results obtained using TEM technique correspond with the spectrophotometry results.

Figure 4 presents the high resolution transmission electron microscopy (HRTEM) for two silver nanoparticles. The structure and the shape of nanoparticles are distinct in the picture.

According to the histogram (Figure 5) of silver nanoparticles' distribution at sizes, it was stated that the average silver nanoparticles size accounts for  $10 \pm 2$  nm and the range of

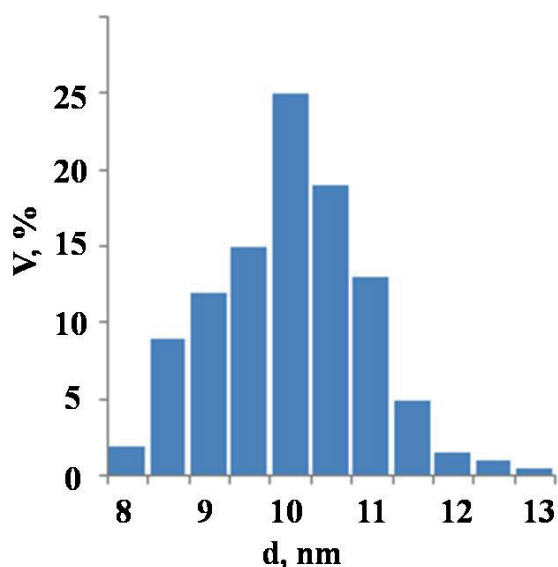


Fig. 5. The histogram of silver nanoparticles' distribution at sizes.

nanoparticles distribution at sizes is quite narrow.

Some physical properties of the produced nano-ink were investigated. Thus, viscosity of synthesized silver nano-ink accounted for 17-20 cP, surface tension – 28-30 mN/m.

Thereby, standard dispersions of silver nanoparticles and silver nano-ink were studied and characterized. It was ascertained that the developed silver nano-ink met the requirements for 2D ink-jet printing completely.

### 3.1. INK-JET PRINTING WITH USE OF SILVER NANO-INK

Ink-jet printing by synthesized nano-ink was implemented using the printer (Fujifilm Dimatix Inc) Dimatix DMP-2831 equipped with the 16-nozzles cartridge and the silicon MEMS printer head; a nominal drop volume of every nozzle is up to 10 pl (Figure 6).

The main printing parameters are the volume of the ink drop formed in the printer's cartridge nozzle and the distance between two next drops on the substrate. The drop's volume – up to 10 pl – is optimal due to the use of silver nano-ink with the size up to 12 nm mainly. At this drop volume, the lateral drop size on the substrate's surface does not exceed 20 μm which characterizes print resolution at this method.



Fig. 6. Ink-jet printing equipment – Fujifilm Dimatix-2831.

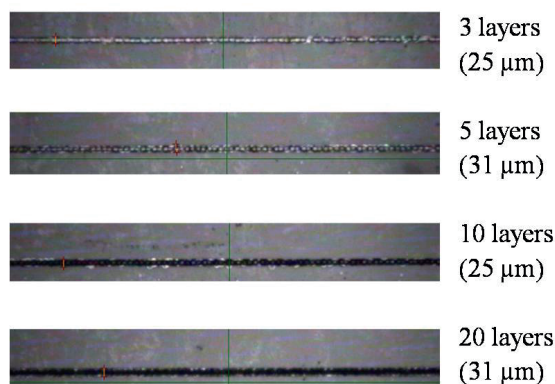


**Fig. 7.** Image of the lines with different number of layers printed by silver nano-ink on the polymer film; the image was obtained using the optical microscope (the line width is given in brackets).

In order to obtain continuous lines, printing may be done in several passes. **Figure 7** shows the lines printed using silver nano-ink with different number of layers, printing was done 3; 5; 10 and 20 times. However, the printed line widened insignificantly: from 25 μm to 31 μm.

**Figure 8** shows a photograph of the printed silver lines on flexible polymer films. The width of the narrowest line is 30 μm.

**3.2. TREATMENT OF SUBSTRATES IN PLASMA**

As the applied printed technology is based on ink-jet principle, one of conditions for printing is suitable surface characteristics of the substrates, particularly the contact wetting angle (or limiting wetting angle) of the substrate surface. If the substrate surface is hydrophobic, shrinking of the printed structure into individual drops may take place which is the reason for crippling of the printed structures. To solve the task of the substrates hydrophilization,



**Fig. 8.** The photograph of the printed silver lines on flexible polymer films. The width of the narrowest line is 30 μm.

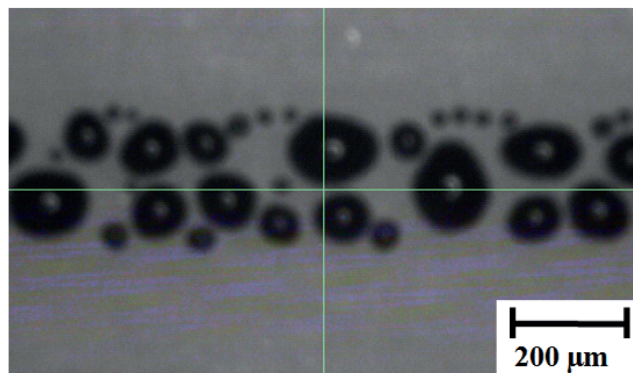


**Fig. 9.** Image of the 200 μm-width line printed by silver nano-ink on the polyimide film; image is obtained by optical microscopy method.

treatment of the substrate in plasma is applied. Thus, experiments on plasma influence of surface characteristics of ceramic and polyimide substrates were carried out using the equipment “Tantec VacuLAB”. At printing, nano-ink formed isolated drops on the substrates which had not been treated in plasma (**Figure 9**).

If plasma influences ceramic and polyimide substrates, contact wetting angle of the latter one increases, surface characteristics become hydrophilic. **Figure 10** shows the printed lines on the plasma-treated surfaces.

Thus, the presented technology of the surfaces hydrophilization widens the range of the substrates’ types applied in the technology of ink-jet printing of the electronic components.

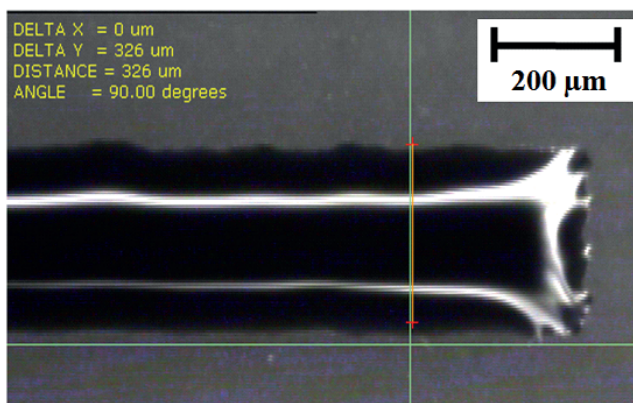


**Fig. 10.** Image of the 200 μm-width line printed by silver nano-ink on the polyimide film; the image is obtained by optical microscopy method.

### 3.3. Thermal treatment

To bond the individual silver nanoparticles and then to form the single metal structure, it is necessary to heat particles by means of thermal treatment or high-energy optical pulses.

**Figure 11** presents the images of scanning electron microscopy of the lines printed by silver nano-ink at different annealing temperature.

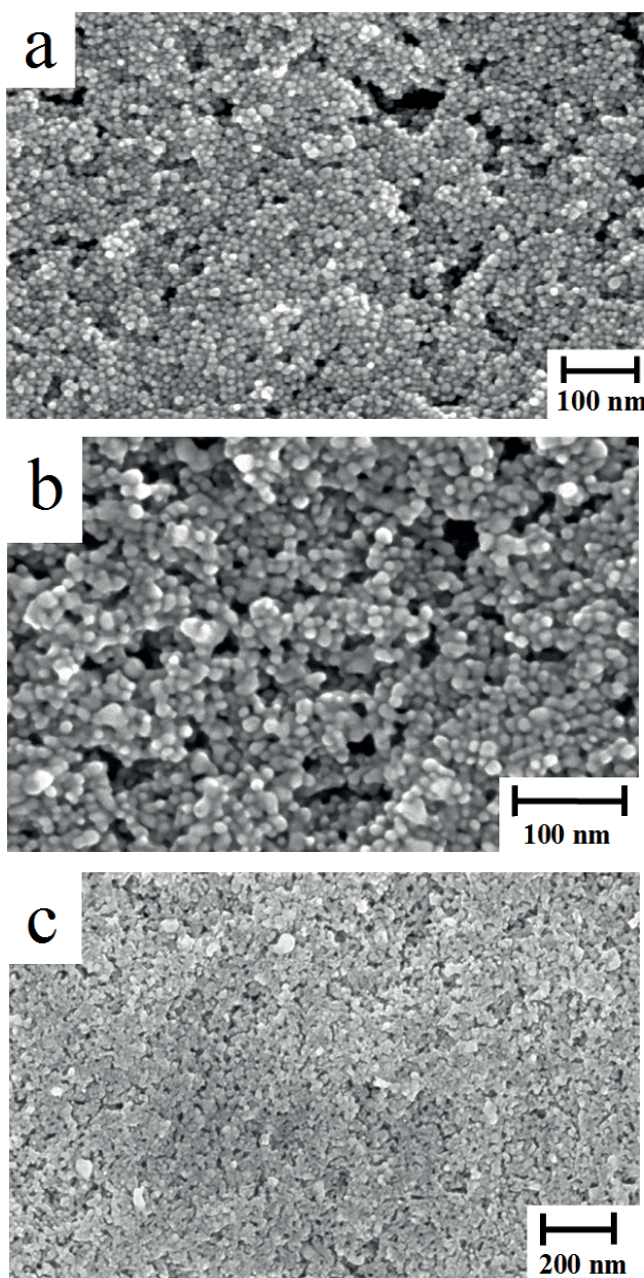


**Fig. 11.** SEM-images of silver nano-ink: a – without thermal treatment; b – thermal treatment at 90°C; c – thermal treatment at 150°C.

It should be noticed that melting point of massive silver is 962°C. The given pictures show that silver nanoparticles start sintering between each other at 90°C. The reason for this is the heightened surface energy of nanoparticles. Taking into consideration that such heating (about 90°C) does not destroy the majority of polymeric films, this technology may be successfully applied to create the metal conductive structures on the flexible polymer films.

Measurements of resistivity of the structures printed by silver nano-ink were carried out at different annealing temperatures (**Figure 12**).

The result is that the value of silver nano-ink resistivity at annealing temperature 400°C accounts for 0.025 Ohm·mm<sup>2</sup>/m. Meanwhile, the value of massive silver is 0.015 Ohm·mm<sup>2</sup>/m. This confirms almost complete sintering of nanoparticles massive into the single structure.

### 3.4. PRINTING OF THE CONDUCTIVE LINES ON THE ITO SURFACE WITH THE USE OF SILVER NANO-INK

Printing by silver nano-ink was implemented on the silicon substrate covered by ITO layer with the use of the Fujifilm Dimatix 2831 printer. The ITO – Indium Tin Oxide – layer

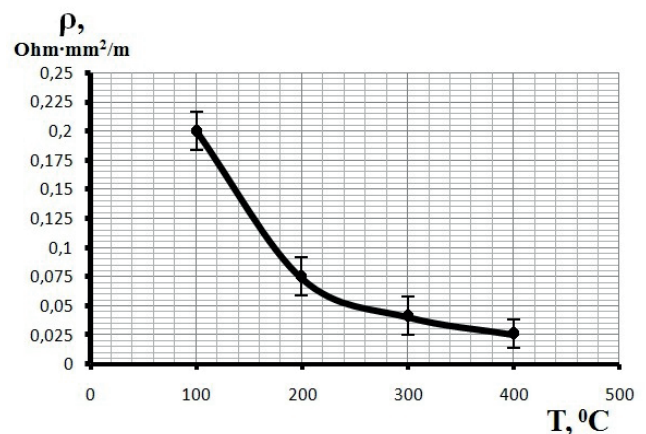


**Fig. 12.** The plot of resistivity of the structures printed by silver nano-ink at annealing temperature from 100°C to 400°C.

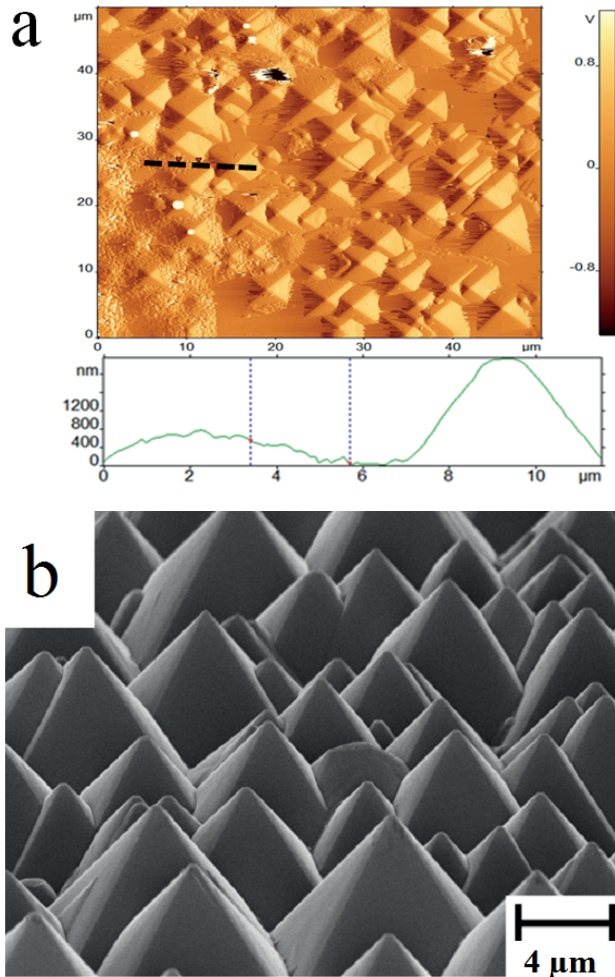


**Fig. 13.** Images of ITO surface: a – a top view (obtained by the AFM method), b – a side view (obtained by the SEM method). consists of 90 wt%  $\text{In}_2\text{O}_3$  and 10 wt%  $\text{SnO}_2$ . The ITO layer is optically transparent and electroconductive.

Surface of the given substrates and the structure of the printed lines were investigated by the scanning electron microscopy and atomic force microscopy (Figures 13-16).

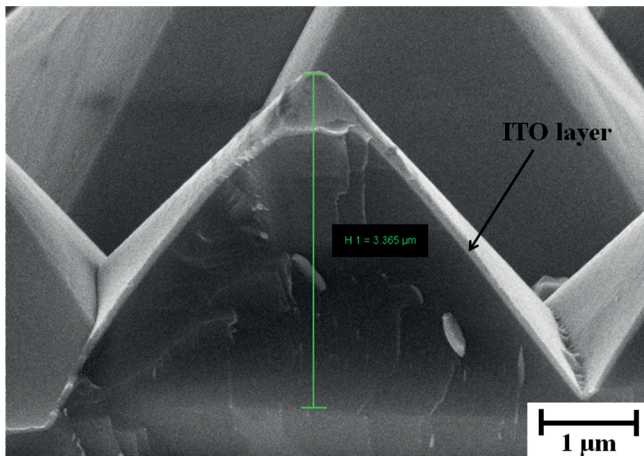


**Fig. 14.** SEM – image of the surface cleavage.

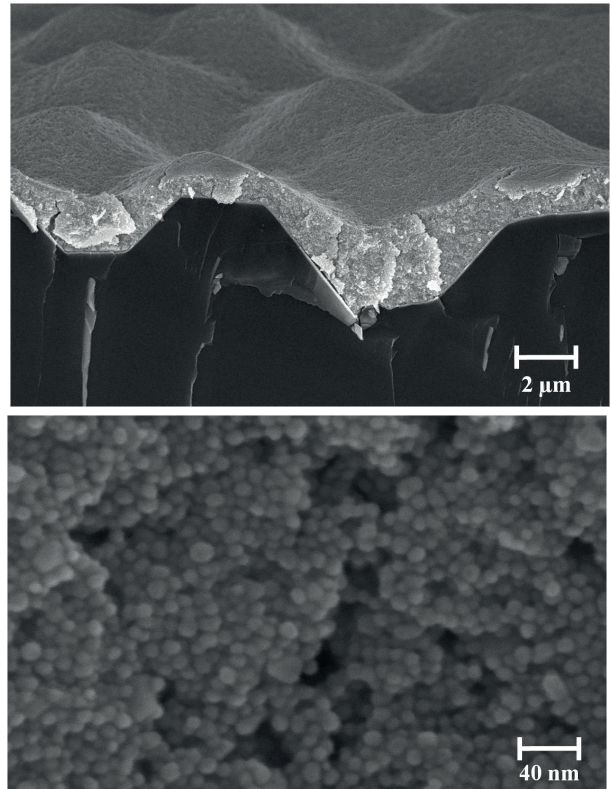


**Fig. 15.** SEM-images of the printed annealed conductive elements on the ITO surface: at the top – a side view, on the down – a top view.

The width of the printed silver conductive lines is from 100  $\mu\text{m}$  up to 2 mm, and the height of the obtained structures does not

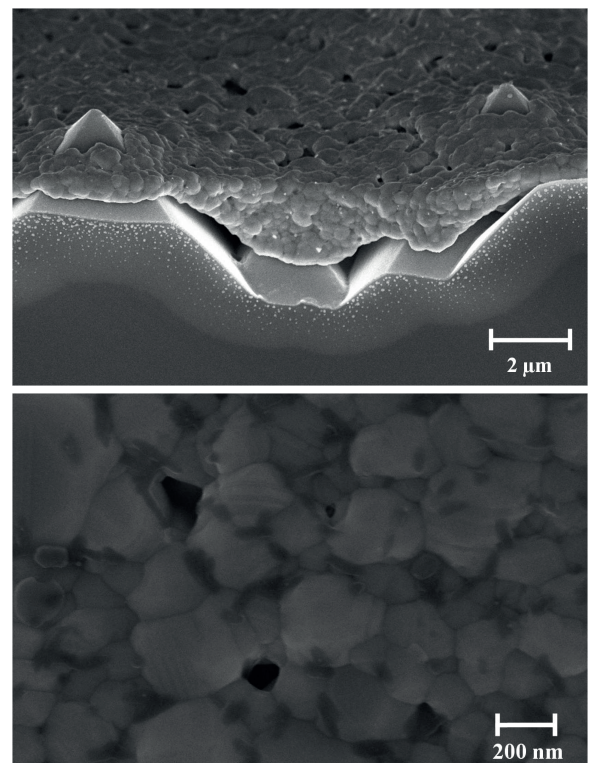


**Fig. 16.** SEM - images of the printed annealed conductive elements on the ITO surface which were annealed at temperature 120°C for 15 min: at the top – a side view, on the down – a top view.



**Fig. 17.** Image of the printed conductive elements on the silicon substrate (by size 15 cm × 20 cm) covered by ITO layer.

exceed 2 μm (**Figure 17**). The printed lines were annealed at temperature 120°C for 15 min. The printed lines resistivity is on average 2 Om/cm.

Thus, it was proved that the technology of ink-jet printing with the use of nano-ink on the basis of conductive nanoparticles may be used in perspective to create conductive circuit wiring on the substrates covered by the ITO layer, particularly on solar sells.

### 3.5. PRINTING OF THE CONDUCTIVE LINES ON THE SILICON SURFACE WITH THE USE OF SILVER NANO-INK

As nowadays silicon is widely used in the electronic industry, the utterly important task

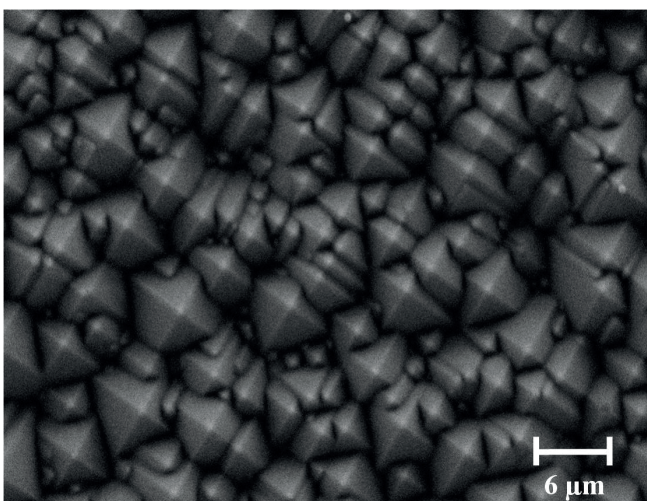


**Fig. 18.** SEM-image of the silicon substrate's surface

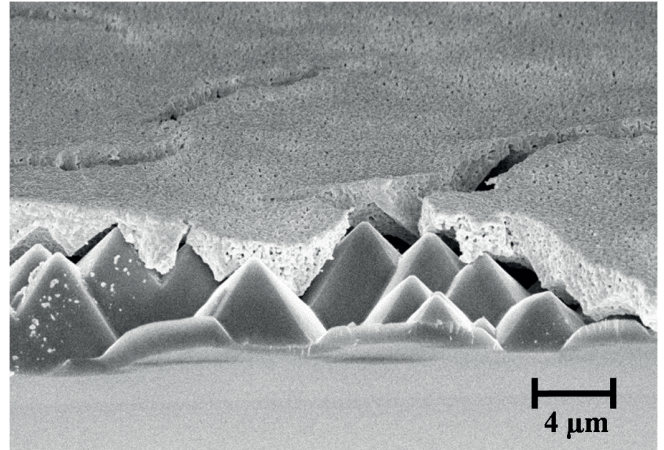


**Fig. 19.** SEM-image of the printed silver line on the silicon substrate (annealing temperature is 195°C, 60 min)

is testing of silicon substrates (**Figure 18**) in the technology of ink-jet printing of the electronic devices' components.

A number of experiments on silver nano-ink printing were carried out with the use of Fujifilm Dimatix DMP – 2831 equipment on the silicon substrates' surface (**Figures 19, 20**).

The presented above images show that silver nano-ink sinters into the single structure after thermal treatment. This confirms the possibility to apply the present approach to produce electronic devices on the silicon substrates.

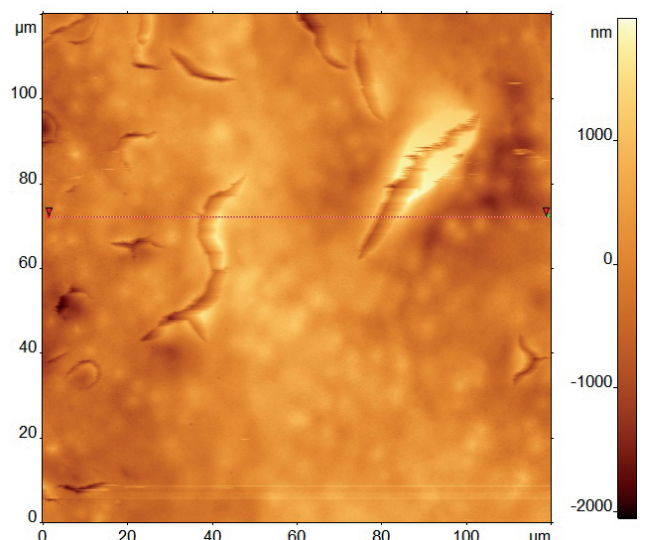


**Fig. 20.** AFM – image of the topology of the printed silver line's surface on the silicon substrate (annealing temperature is 195°C, 60 min).



Fig. 21. Image of the sample – a heating element printed on the polymer film by silver nano-ink.

### 3.6. PRINTING OF THE HEATING ELEMENTS ON THE POLYMER FILM

Ink-jet printing by metal-containing nano-ink may be also applied to produce heating elements (Fig. 21).

The experiments showed that such elements printed by synthesized silver nano-ink had resistance 30 Om. It should be noted that maximum heating temperature was 50°C and 70°C at voltage 12V, 18V correspondingly.

### 3.7. PRINTING OF THE COMPLEX-GEOMETRY CONDUCTIVE BOARDS ON DIFFERENT SUBSTRATES

Silver conductive boards were printed on the polymer films using the special high-precision ink-jet printer Fujifilm Dimatix 2831. It should be noted that the picture may have any geometry with the resolution

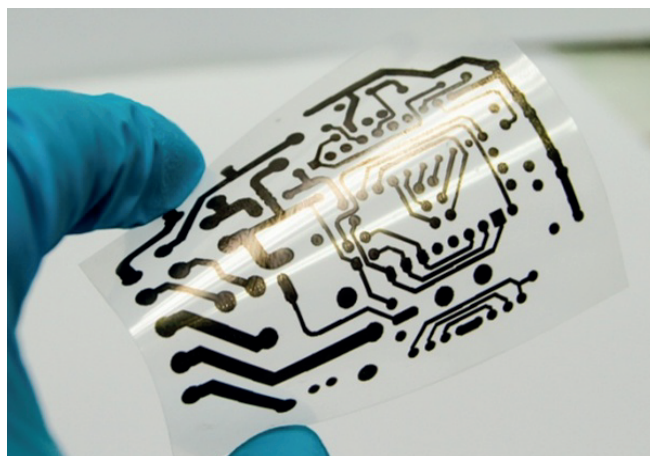


Fig. 22. Image of the conductive board printed using silver nano-ink on the polymer film.

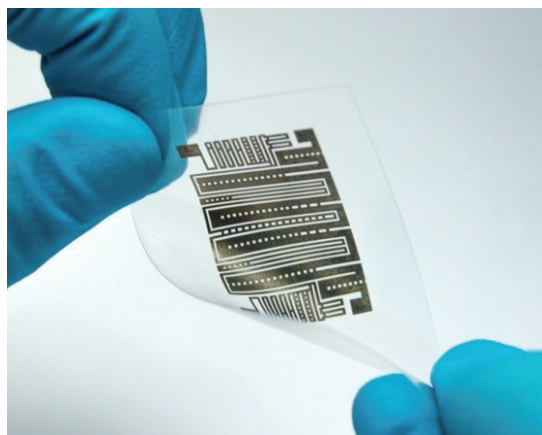


Fig. 23. Image of the conductive board printed using silver nano-ink on the polymer film.

up to 20 μm (Fig. 22, 23). Conductivity, in turn, is defined by the number of the deposited substances and annealing temperature. Due to the melting of the flexible polymer films at temperature 200°C, printing of conductive elements on polymer substrates is possible only using conductive nanoparticles, because their melting temperature is significantly lower than one of the massive analogs. Thus, the melting temperature of massive silver is 962°C, but silver nanoparticles start sintering at the temperature 90°C.

The model samples of the RFID-antenna (Radio Frequency Identification) and conductive accumulator coverings were also printed (Figure 24) Polyimide film,

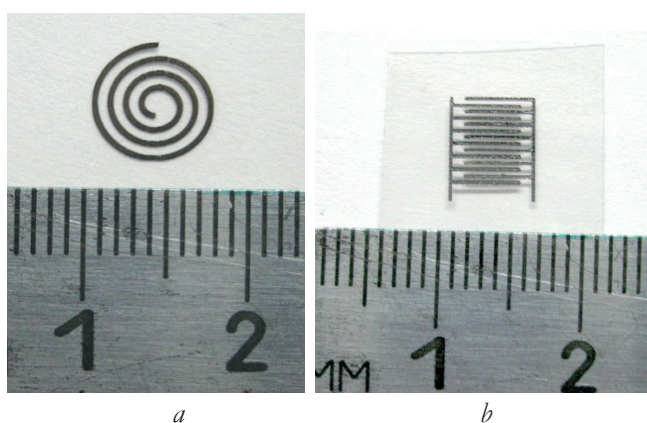


Fig. 24. Images of the RFID-antenna (a) and the conductive accumulator coverings (b) printed using silver nano-ink on the polymer film.



**Fig. 25.** Image of the conductive lines printed by silver nano-ink on the polyimide film.

ceramics, glazed paper, glass were also used as a substrate (**Fig 25, 26**).

The surface of glass and polyimide film was treated with solvents: isopropyl alcohol, acetone, chloroform and surface-active substances. Thus, the substrates' surface was degreased and got hydrophilic properties.

Nowadays ceramics is widely used in the electronic industry, mainly as a hard substrate of the electronic devices' elements. This is the reason for the choice of the ceramic surface. As ceramics has the porous structure, the adjacent conductive elements were short-circuited in ceramics structural pores. The problem was solved by supply of voltage which is needed to burn such "bridges". The possibility to solder to the printed structure was experimentally proved. This confirms the perspectives of realization into the existing technological cycles on production of the electronic devices' elements on ceramics.

Nowadays glazed paper is not used in electronic industry. However, the presented

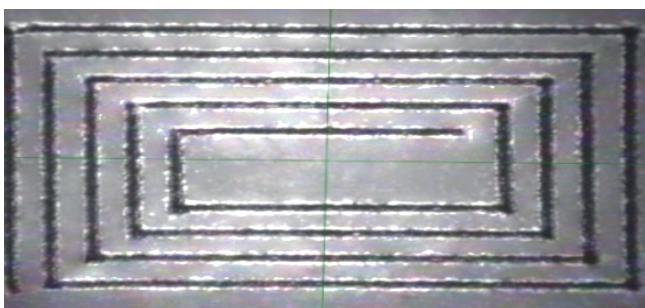


**Fig. 26.** Image obtained by the optical microscopy method of the RFID antenna by silver nano-ink on the polyimide film.

substrate has one obvious advantage: due to its porous structure and the glazed layer on the surface, silver nano-ink' solvent is immediately absorbed into the structure, but silver nanoparticles remain on the surface. Thus, there is a possibility to draw, print conductive elements directly on paper without additional post-printing treatment.

### 3.8. PRINTING ON TEXTILE GOODS WITH THE USE OF SILVER NANO-INK

Printing on textile goods with the use of silver nano-ink was carried out (**Figure 27**). The presence of the final samples' electronic conduction is caused by continuous multiple coating consisted from the layers of the annealed metal nanoparticles on the cloth's surface. The stability of the sample's parameters to bending and interaction with water is unsatisfactory. The reason for this is crippling of the layer from annealed silver nanoparticles. The low adhesion degree is presumably caused by the significant number of nanoparticles' layers.

### 4. CONCLUSION

The "AkKo Lab" LLC company has developed the methodology of silver nano-ink production. In terms of colloid chemistry, the developed nano-ink

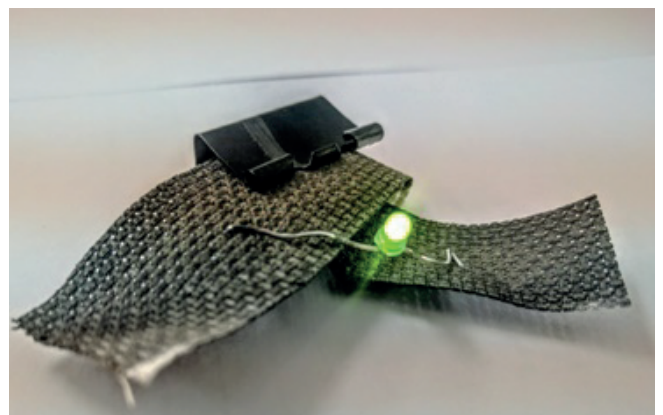


**Fig. 27.** Printing on textile goods with the use of silver nano-ink.

represents highly concentrated dispersions of silver nanoparticles. According to the data of transparent electron microscopy and scanning electron microscopy, silver nanoparticles in nano-ink have the shape close to spherical one. Besides, silver nanoparticles are characterized by quite the narrow range of particles' distribution at sizes – from 8 to 12 nm.

Silver nano-ink was adapted to print on the high-technology printer Dimatix Material Printer DMP-2831. Printing of different conductive structures on different nature substrates was worked through. They are ceramics, glass, ITO layer, flexible polymer films, textile goods. It was shown that printing quality depends on the wide range of the parameters: the substrate's nature, nano-ink adhesion to the substrate's surface, printing temperature, the number of printing passes.

It should be noted that printing is possible almost on any surface. However, to print successfully, it is necessary to treat printing surface beforehand by a physical (particularly by treatment in plasma) or a chemical method (treatment by surface-active substances, alcohols, etc.) in order to make the surface wet for nano-ink and suitable to print.

The important property of the developed nano-ink is quite low sintering temperature of silver nanoparticles. Thus, the sintering temperature of silver nano-ink into the conductive layer is significantly lower than the melting temperature of its compact analog and accounts for about 100°C.

Silver nano-ink developed by the "AkKo Lab" LLC company passed tests in the Fujifilm Dimatix Inc. company in California (the USA) and was highly estimated. Silver nano-ink is a commercial product and is

supplied to the final customers in Russia and abroad.

The obtained results show the perspective to apply the technology of the ink-jet printing by the metal-containing nano-ink to produce the electronic devices, including those on flexible substrates.

*This work was partly supported by the fund of assistance to innovation, project number 0016302.*

## REFERENCES

1. Kamyshny A, Steinke J, Magdassi S. Metal-based Inkjet Inks for Printed Electronics. *The Open Applied Physics Journal*, 2011, 4:19-36.
2. Finn DJ, Lotya M, Coleman JN. Inkjet Printing of Silver Nanowire Networks. *ACS Appl. Mater. Interfaces*, 2015, 7(17):9254-9261.
3. Torrisi F, Hasan T, Wu W, Sun Z, Lombardo A, Kulmala TS, Hsieh G-W, Jung SJ, Bonaccorso F, Paul PJ, Chu DP, Ferrari AC. Ink-Jet Printed Graphene Electronics. *ACS Nano*, 2012, 6(4):2992-3006.
4. Tobjork D, Osterbacka R. Paper electronics. *Advanced materials*, 2011, 23:1935-1961.
5. Gaikwad AM, Whiting GL, Steingart DA, Arias AC. Highly Flexible, Printed Alkaline Batteries Based on Mesh-Embedded Electrodes. *Advanced materials*, 2011, 23:3251-3255.
6. Hildera M, Winther-Jensen B, Clarka NB. Paper-based, printed zinc-air battery. *Journal of Power Sources*, 2009, 194:1135-1141.
7. Park J, Moon J, Shin H, Wang D, Park M. Direct-write fabrication of colloidal photonic crystal microarrays by ink-jet printing. *Journal of Colloid and Interface Science*, 2006, 298:713-719.

8. Jillek W, Yung WKC. Embedded components in printed circuit boards: a processing technology review. *International Journal of Advanced Manufacturing Technology*, 2005, 25:350-360.

# THE USE OF PARALLEL PROGRAMMING TECHNOLOGIES FOR MODELING SEISMIC WAVES USING GRID-CHARACTERISTIC METHOD

<sup>1</sup>Andrey M. Ivanov, <sup>1</sup>Nikolay I. Khokhlov, <sup>1,2</sup>Igor B. Petrov

<sup>1</sup>Moscow Institute of Physics and Technology, <http://mipt.ru>  
141701 Dolgoprudny, Moscow region, Russian Federation

<sup>2</sup>Scientific Research Institute of System Analysis, Russian Academy of Sciences, <https://www.niisi.ru>  
117218 Moscow, Russian Federation

[ip-e@mail.ru](mailto:ip-e@mail.ru), [k\\_h@inbox.ru](mailto:k_h@inbox.ru), [petrov@mipt.ru](mailto:petrov@mipt.ru)

*Abstract.* The paper deals with the problem of modeling seismic wave propagation in solid deformable bodies. The state of these bodies can be represented as a solution of hyperbolic system of equations. Grid-characteristic method is used to find the solution. This formulation of physical problem is used to demonstrate the use of technologies of parallel programming for shared memory systems using OpenMP and POSIX Threads technology. To achieve high performance, vector SSE and AVX instructions of CPU is used. In addition, GPU implementation is written using CUDA and OpenCL technologies. Results of multi-GPU parallelisation is also obtained. Use of NVIDIA GPUDirect technology that allows GPUs to make data exchanges directly through the PCI Express bus is considered. The paper demonstrates achieved acceleration and percentage of the theoretically possible performance. The paper demonstrates achieved acceleration and percentage of the theoretically possible performance. The paper describes the optimizations, which allowed us to achieve the obtained acceleration results.

The study was financially supported by RFBR as part of a research project number 15-07-01931 A.

*Keywords:* mathematical modeling, parallel programming, grid-characteristic method, shared memory, seismic, vectorization, GPU, CUDA, OpenCL

UDC 519.633

*Bibliography* - 20 references

Received 25.11.2016

*RENSIT*, 2016, 8(2)185-195

DOI: 10.17725/[rensit.2016.08.185](https://doi.org/10.17725/rensit.2016.08.185)

## CONTENTS

1. INTRODUCTION (185)
2. MATHEMATICAL MODEL (186)
3. NUMERICAL METHOD (186)
4. STATEMENT OF PROBLEM (187)
5. PARALLELIZATION TEST CONDITIONS (187)
6. OPTIMIZATION PROCESS (188)
7. PARALLEL ALGORITHM (188)
8. GPU OPTIMIZATIONS (189)
  - 8.1. TRANSFERRING IMPLEMENTATION FROM CPU TO GPU – CUDA1 (190)
  - 8.2. STRUCTURE OF ARRAYS AND SEQUENTIAL MEMORY ACCESS – CUDA2 (191)
  - 8.3. KERNEL CALL PARAMETERS – CUDA3 (191)
  - 8.4. BLOCK SIZES – CUDA4 (192)
  - 8.5. USING OPENCL1 (192)
9. MULTIPLE GPUS (192)
10. CONCLUSION (193)
- REFERENCES (194)

## 1. INTRODUCTION

The problem of wave propagation in linear-elastic medium is of interest in seismology and geophysics. With the increasing performance of modern computer systems and the possibility of parallel execution of the program code, it is possible to carry out computer modeling of seismic waves with great precision. The question is how to efficiently use the available computing resources.

The first solution to this problem is to use of technologies of parallel programming for shared memory systems. The article [1] considers the problem of modeling effects of parallelization occurring in the ground during an earthquake, using OpenMP. With regard to other problems of mathematical modeling, there is the paper [2]

about application of OpenMP technology to parallelize finite element method on unstructured grids.

The second approach is parallelization on modern GPUs. There are a lot of papers on this subject. For example, parallelization of finite difference method on the GPU with CUDA technology [4] is considered in the article [3]. There are studies [5, 6] where the problem of reverse time migration is solved on a cluster of GPUs.

Finally, a third approach is parallelism in distributed memory systems. CPUs and GPUs may also be used in such systems. In paper [7], finite-difference method of viscoelastic environment modeling is parallelized using MPI [8] technology. The work [9] considers spectral elements method for the simulation of wave propagation in the asteroid. In addition, the work [10] compares the performance of parallelizing on GPU with use of CPU clusters. The study [11] demonstrates the use of the hybrid OpenMP + MPI systems for seismic finite-difference modeling.

There are also other approaches, a detailed consideration of which is beyond the scope of this article. For example there are the use of the FPGA [12] and ASIC [13].

In this paper we consider the solution of hyperbolic systems of equations that describes the behavior of waves in elastic solid bodies. To find the solution of this system grid-characteristic method [14–16] is used. Calculations are made on the explicit scheme, because in this case program responds well to parallelization. Solution of the problem is parallelized using shared memory systems with OpenMP, POSIX Threads technologies [17] and on GPUs using CUDA, OpenCL [18].

## 2. MATHEMATICAL MODEL

Environment behavior is described by the model of an ideal isotropic linear-elastic material. We consider the two-dimensional problem. The following system of partial differential equations

describes the state of the elementary volume of elastic material in the approximation of small deformations:

$$\begin{aligned} \rho \frac{\partial v_x}{\partial t} &= \frac{\partial \sigma_{xx}}{\partial x} + \frac{\partial \sigma_{xy}}{\partial y}, & \rho \frac{\partial v_y}{\partial t} &= \frac{\partial \sigma_{xy}}{\partial x} + \frac{\partial \sigma_{yy}}{\partial y}, \\ \frac{\partial \sigma_{xx}}{\partial t} &= (\lambda + 2\mu) \frac{\partial v_x}{\partial x} + \lambda \frac{\partial v_y}{\partial y}, \\ \frac{\partial \sigma_{yy}}{\partial t} &= \lambda \frac{\partial v_x}{\partial x} + (\lambda + 2\mu) \frac{\partial v_y}{\partial y}, \\ \frac{\partial \sigma_{xy}}{\partial t} &= \mu \left( \frac{\partial v_x}{\partial x} + \frac{\partial v_y}{\partial y} \right), \end{aligned}$$

where  $\rho$  is the density of the medium;  $\lambda, \mu$  are Lamé parameters;  $v_x$  and  $v_y$  are the horizontal and vertical components of the velocity of the particles of the medium;  $\sigma_{xx}, \sigma_{yy}, \sigma_{xy}$  are the components of the stress tensor.

This system can be presented in the matrix form:

$$\frac{\partial \mathbf{u}_p}{\partial t} + A_{pq} \frac{\partial \mathbf{u}_q}{\partial x} + B_{pq} \frac{\partial \mathbf{u}_q}{\partial y} = 0, \quad (1)$$

where  $\mathbf{u}$  is the vector of 5 independent variables  $\mathbf{u} = (\sigma_{xx}, \sigma_{yy}, \sigma_{xy}, v_x, v_y)^T$ . The explicit form of the matrices  $A_{pq}, B_{pq}$  is presented in [19]. Hereinafter we mean summation over repeated indices. The eigenvalues of matrices  $A_{pq}$  and  $B_{pq}$  are as follows:  $s_1 = -c_p, s_2 = -c_s, s_3 = 0, s_4 = c_s, s_5 = c_p$ , where  $c_p$  and  $c_s$  are the propagation speeds of elastic P-waves and S-waves in the medium.

## 3. NUMERICAL METHOD

Using coordinate-wise splitting we can reduce the problem of constructing a difference scheme for the system of equations (1), to the problem of constructing a difference scheme for system of the form:

$$\frac{\partial \mathbf{u}_p}{\partial t} + A_{pq} \frac{\partial \mathbf{u}_q}{\partial x} = 0, \quad (2)$$

For hyperbolic system of equations (2) matrix  $\mathbf{A}$  can be represented as  $\mathbf{A} = \mathbf{R}\mathbf{\Lambda}\mathbf{R}^{-1}$ , where  $\mathbf{\Lambda}$  is a diagonal, the elements of which are the eigenvalues of  $\mathbf{A}$ , and  $\mathbf{R}$  is the matrix consisting of right eigenvectors of  $\mathbf{A}$ . We introduce new

variables:  $\mathbf{w} = \mathbf{R}^{-1}\mathbf{u}$  (the so-called Riemann invariants). Then the system of equations (2) will be reduced to a system of 5 independent scalar advection equations.

Let's reduce a third-order accuracy scheme to the numerical solution of one-dimensional linear advection equation  $u_t + au_x = 0$ ,  $a > 0$ ,  $\sigma = a\tau/h$ ,  $\tau$  is a time step,  $h$  is step on coordinate:

$$u_m^{n+1} = u_m^n + \sigma(\Delta_0 + \Delta_2)/2 + \sigma^2(\Delta_0 - \Delta_2)/2 + \frac{\sigma(\sigma^2 - 1)}{6}(\Delta_1 - 2\Delta_0 + \Delta_2), \quad (3)$$

$$\Delta_0 = u_{m-1}^n - u_m^n,$$

$$\Delta_1 = u_{m-2}^n - u_{m-1}^n,$$

$$\Delta_2 = u_m^n - u_{m+1}^n.$$

Scheme (3) is stable to Courant numbers not bigger than 1. A grid-characteristic criterion of monotony is used, it is based on the characteristic property of the accurate solutions:

$$\min(u_{m-1}^n, u_m^n) \leq u_m^{n+1} \leq \max(u_{m-1}^n, u_m^n).$$

In places where this criterion is met, the order of scheme falls to the second one.

Once the values of the Riemann invariants on the next time step are found, the solution:  $\mathbf{u}^{n+1} = \mathbf{R}\mathbf{w}^{n+1}$ .

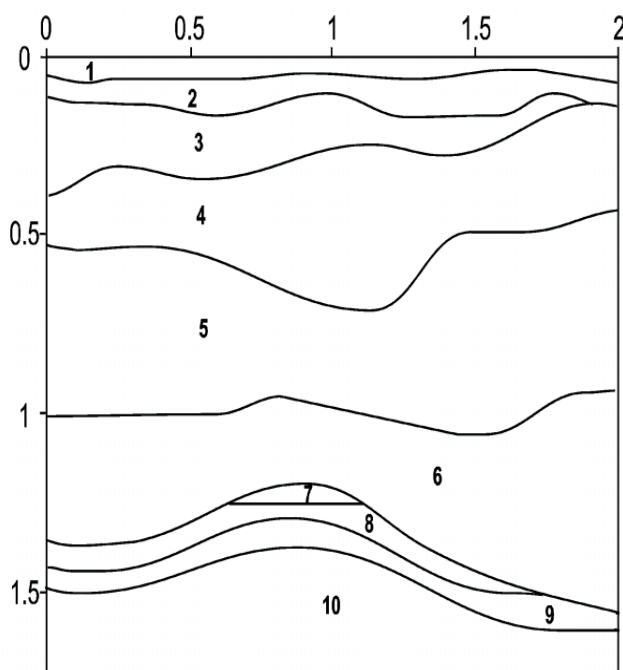


Fig. 1. Geological model of anticlinal trap [20].

#### 4. STATEMENT OF PROBLEM

Test model is shown in Fig. 1. The dimensions are given in kilometers. A non-reflecting boundary condition is set for bottom and side borders and free boundary is set for the top. The source of perturbations is a vertical force applied to the site from 925.7 m to 974.1 m on the day surface; its amplitude is set by Ricker pulse frequency of 40 Hz. The calculation results are presented in Fig. 2.

#### 5. PARALLELIZATION TEST CONDITIONS

All the CPU tests were carried out on the one test task. The two-dimensional test problem with the number of nodes 4000×4000 is considered. 100 time steps were carried out. All calculations were performed both with a single, and a double accuracy. In this paper only double-precision charts are given. Each grid point stored 5 floating point variables. Grid size in memory is 305 MB for computing with single precision and 610 MB for the calculations with double accuracy.

The next compiler optimization fl were used: -fno-tree-vectorize to restrict vectorization, -fopenmp and -pthread to specify parallelization technology, -O2 to use standard optimizations,

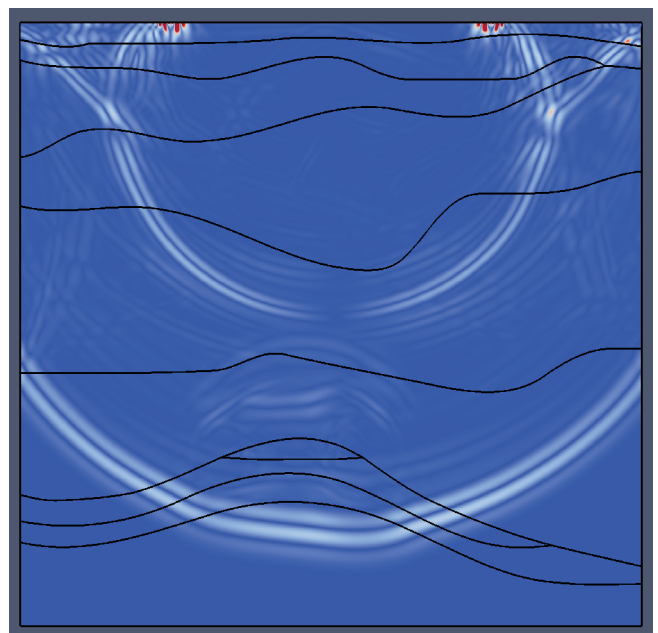


Fig. 2. The calculation result is the wave pattern in time moment  $t = 0.38$  s.

Table 1  
CPUs are used for parallelization tests

Name (notation)	Clock rate, GHz	Cache, kB	Processors and cores	Compilers	Performance, GFLOPS
AMD Opteron 6272 (a64)	2.1	2048	8 processors with 8 cores	gcc4.4.6	1075.2
Intel Xeon E5-2697 (i24)	2.7	30720	2 processors with 12 cores	gcc4.4.7, icc15.0.0	518.4
AMD Opteron 8431 (a48)	2.4	512	8 processors with 6 cores	gcc4.4.7	921.6

-msse, -mavx to specify a set of vectorization instructions.

Calculations were made on CPUs presented in Table 1. Compilers on charts are denoted as gcc and icc. Vector instructions sets are denoted as sse or avx.

All the CPU tests were carried out with another parameters. The two-dimensional test problem with the number of nodes 4096×4096 is considered. 6500 time steps were carried out. All calculations were performed both with a single (SP), and a double (DP) accuracy. Each grid point stored 5 floating point variables. Grid size in memory is 320 MB for computing with single precision and 640 MB for the calculations with double accuracy. Characteristics of used GPUs is shown in Table 2.

### 6. OPTIMIZATION PROCESS

The sequential version of the algorithm was written first. Recalculation of grid nodes was carried out in two steps. In the step X algorithm bypasses the grid by the columns, then by the rows. In the step Y it firstly bypasses the grid by the rows, then by the columns. It was

Table 2  
Characteristics of GPUs

GPU	Cores	Clock rate, MHz	GFLOPS (SP)	SP:DP	GFLOPS (DP)
GeForce GT 640	384	900	691	24	29
GeForce GTX 480	480	1401	1345	8	168
GeForce GTX 680	1536	1006	3090	24	129
GeForce GTX 760	1152	980	2258	24	94
GeForce GTX 780	2304	863	3977	24	166
GeForce GTX 780 Ti	2880	876	5046	24	210
GeForce GTX 980	2048	1126	4612	32	144
Tesla M2070	448	1150	1030	2	515
Tesla K40m	2880	745	4291	3	1430
Tesla K80	2496	562	2806	1.5	1870
Radeon HD 7950	1792	800	2867	4	717
Radeon R9 290	2560	947	4849	8	606

measured the number of arithmetic operations in the code and using this value we obtained the theoretical value of required FLOPS. It was 262 to recalculate one grid node. On the charts, this version is denoted as simple.

Next, an attempt was made to optimize the step Y. The sequence of nodes access was changed so that it coincided with the access order in step X. Thus the memory access was became sequential, leading to a more efficient use of cache memory. Furthermore, by replacing the arithmetical operations by equivalent, the required amount of FLOPS has been reduced to 190 for single node recalculation. The designation of this version on the charts is cf.

Then the cycles where grid nodes are recalculated were vectorized. It was done with the help of the OpenMP technology directives (#pragma omp simd), appearing in the standard 4.0. Explicitly defined a set of instructions to be used: SSE or AVX. These measurements were made only on Intel Xeon E5-2697.

Based on the frequency of each individual processor core, its peak performance can be obtained. Thus, the percentage of peak performance was calculated for serial version for each test (Fig. 3).

### 7. PARALLEL ALGORITHM

The algorithm has been parallelized using OpenMP and POSIX Threads technologies. Each program version has been parallelized separately to be able to observe the effects of

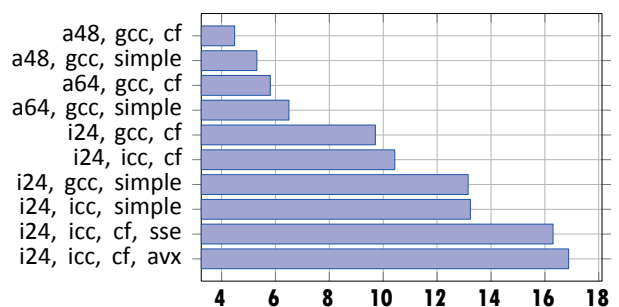


Fig. 3. Percentage of peak performance.

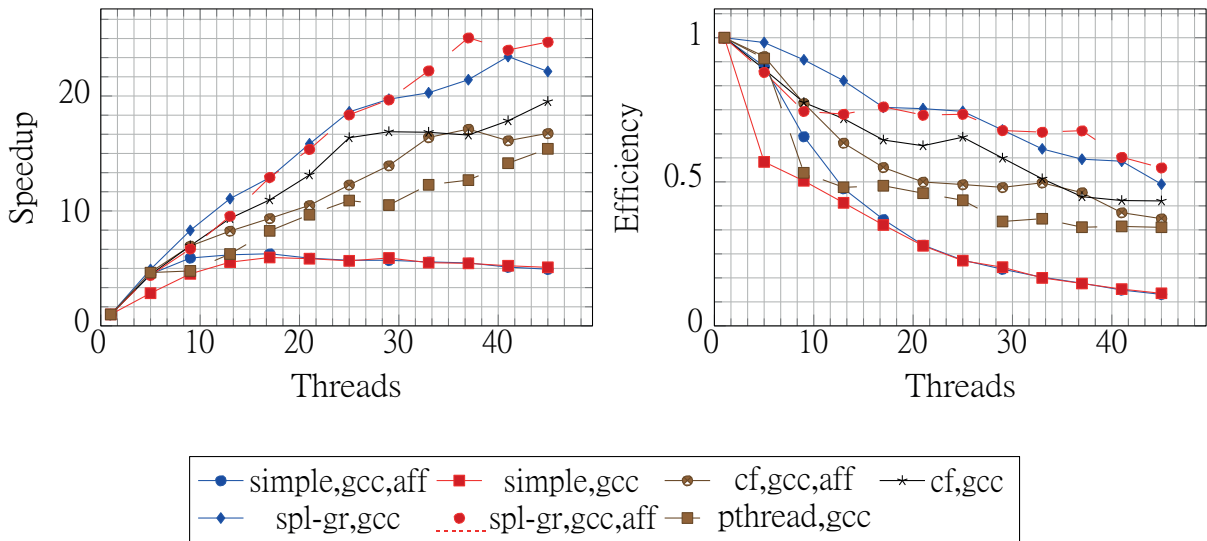


Fig. 4. Parallelization results on AMD Opteron 8431.

sequential code optimization on the efficiency of its parallelization.

Optimization of already parallel code has been made. Each thread allocates memory, which is only necessary to recalculate nodes in its part of grid. On the charts, this version is indicated as spl-gr. In the theory, this should lead to an increase in performance in NUMA systems, since a memory which is allocated on a specific thread is placed in the local memory of this thread according to OpenMP standard. Performance is increased because local memory access consumes less amount of time.

Separate measurements, where change of processor cores was forbidden for threads,

were made. In other words a "binding" of threads to specific processor cores was made. This is done to reduce the time costs. Without this binding, the optimization where the grid is divided into separate parts for different processes ceases to make sense. The results are shown in Fig. 4 - 7.

Next, OpenMP version of the code with grid splitting between the threads has been rewritten to use POSIX Threads as a parallelization technology.

8. GPU OPTIMIZATIONS

The CPU optimized version of this program was taken as the basis for the algorithm implementation on GPUs. The most

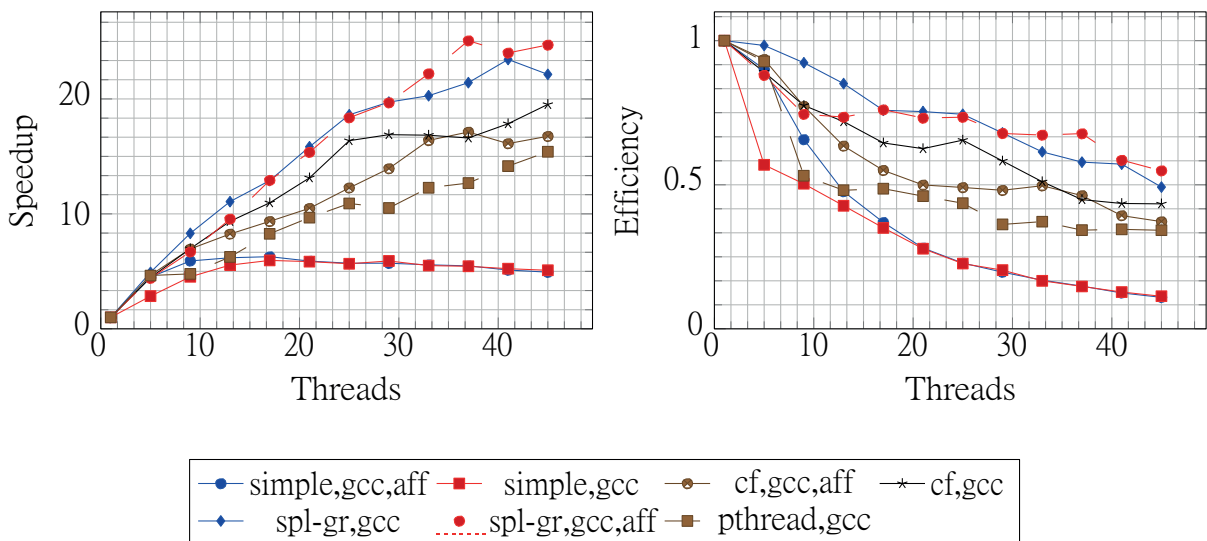


Fig. 5. Parallelization results on AMD Opteron 6272.

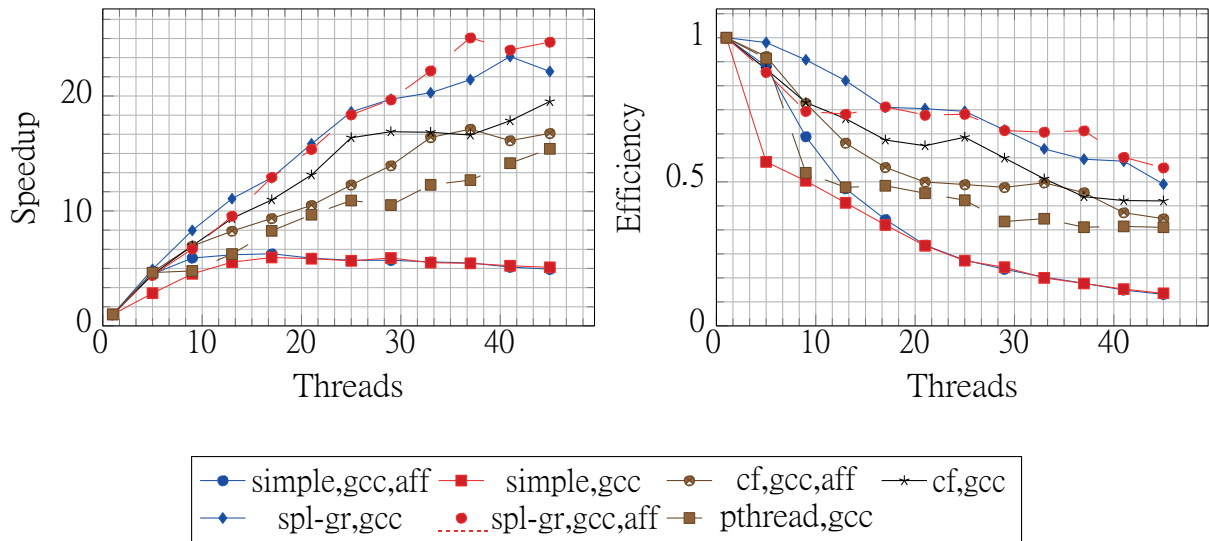


Fig. 6. Parallelization results on Intel Xeon E5-2697 (without affinity).

computationally expensive parts of the algorithm were optimized. As the spatial coordinate splitting was used, two steps were required to transfer the entire grid: on the  $X$  axis and  $Y$  axis. At that the number of arithmetic floating point operation was calculated, required for the conversion of one grid point in two steps – 190 Flops. Therefore, by knowing the number of grid nodes, the number of time steps, the theoretical amount of GFlops consumed by algorithm, can be determined. Next, knowing the number of stream processors in GPU, its clock frequency and the number of FMA (fused multiply-add) processors in a single processor, we calculated a peak performance for each GPU. The real

algorithm tests on GPUs have shown lower values of performance.

Fig. 8 shows a test result. The percentage of the peak performance of algorithms was estimated as the ratio between two values – theoretically required amount of Flops for grid recalculation and real consumed amount of Flops.

### 8.1. Transferring implementation from CPU to GPU – cuda1

In the original version, the algorithm was redesigned for execution on GPUs using CUDA technology, but it is not optimized for execution on GPUs. In this technology, the graphic processor was assigned 2 times more memory than required to store the computational grid.

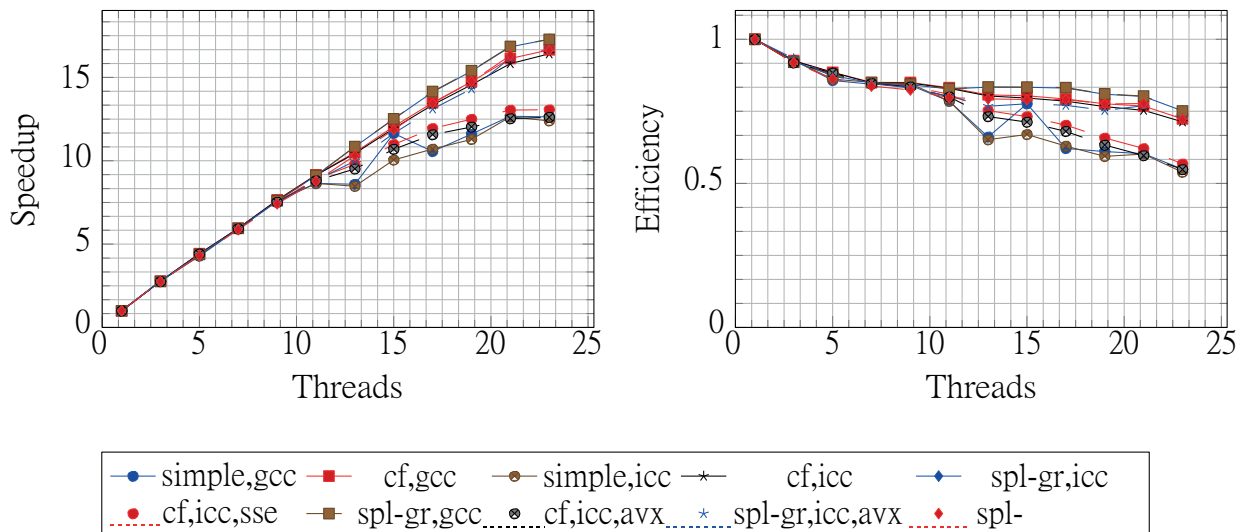


Fig. 7. Parallelization results on Intel Xeon E5-2697 (with affinity).

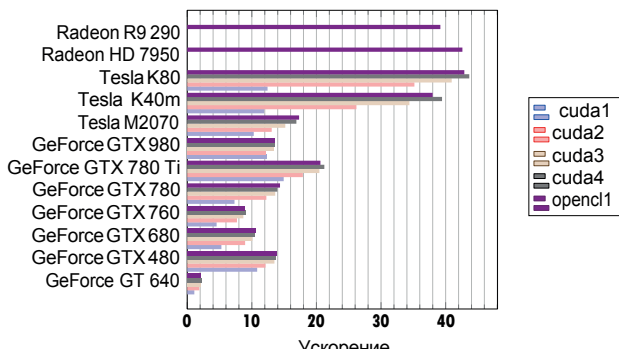


Fig. 8. Percentage of peak performance.

It is a standard practice when working with the algorithm designing technologies for GPUs. As a result, only the synchronization is performed between function calls that run on GPU (CUDA kernels). This was done due to the fact that global synchronization of all graphics processor causes large time delays, so these delays were inserted between calls of kernels. Thus, it became possible to reduce the number of global synchronization up to two times by one time step. Architecture of CUDA stream processors means that in one CUDA unit, flows that perform the same code on different areas of memory are executed simultaneously, if there are no branches in the program code. Therefore, a situation when all flows wait for completion of one occurs only if this flow executes any operations that differ from the rest.

All operations on the memory assigning on GPU and calls of functions running on the graphic processor, are produced by the host – CPU. Operations of memory grid copying from the host memory and back require a lot of time, so the grid is copied once from the host memory to GPU memory, before the start of the main computing, and once at the end from the GPU memory to host memory. Number of steps by the time and computational grid size was such that the time required for calculations far exceeds the time required to copy it.

Data can be stored in grid in two ways: in the form of the array of structures and in the form

of arrays structure. The structure in this case means vector  $u$ , consisting of 5 components. In the original version, data in the computational grid were organized as an array of structures, i.e. data in a particular node are stored sequentially in the memory. To set the boundary conditions of the task, the behavior other than required by other flows at the boundary of the computational grid was required. To handle the grid boundaries in the kernel code, the code section with five conditional blocks "if-else" is inserted in the algorithm. Several options of the unit size were considered for this version. It was found that the optimal size is 16x16, at which operation time was minimal.

**8.2. Structure of arrays and sequential memory access – cuda2**

Shared memory was used in the next optimization of CUDA block. This is due to the fact that the latency during the interaction with this memory is less than the interaction with the global memory. Optimization means there is only one reading from the global memory at each step along X and Y at the beginning of a function call that is running on the GPU and the data is copied in total memory. Immediately after that all the flows are synchronized in the block; after that, all calculations are performed on the data in the shared memory block. At the end of kernel, the result is written to the second copy of the computational grid in the global memory. Another optimization was the selection of a different storing method of the calculated grid in GPU memory – array structure. After that, calls to the global memory become coalesced which led to the increase in performance. The above mentioned optimizations reduced the number of if-else blocks for grid boundaries processing up to 2.

**8.3. Kernel call parameters – cuda3**

Before that, additional information, such as grid size, material, variables values, resulting from intermediate calculations valid along all time

steps were passed to the structure in the GPU global memory as a pointer. All flows constantly addressed the same memory section. Such data were calculated on the CPU in CUDA3 algorithm version once before the execution of code on GPU and were transferred through the parameters of kernel call. It was expected that each flow would create a local copy of these values.

**8.4. Block sizes – cuda4**

It was important to choose the dimensions of the blocks so that the graphics processor would be constantly loaded, that is, there were no part-time loaded flow processors. It was also important to choose the block sizes multiple of the warp sizes, as the sequential access to memory is carried out within a warp. Another reason is that the flows of a warp can execute code simultaneously on different memory sections, if there are no branches.

In CUDA4 version, block sizes are selected so as to satisfy the above mentioned requirements and minimize the number of nodes which require memory exchanging between the memory blocks. At the step on *X* axis to convert each node of the computational grid, values in two adjacent nodes on the *X* axis are required, and at step on *Y*-axis, two adjacent nodes on the *Y*-axis are required. Therefore, one should choose the block sizes so that the number of nodes that require values in the adjacent blocks would be smaller. It was necessary, since the adjacent blocks of nodes require more memory in a general memory block.

If, for example, we take a block of  $M \times N$  times, then in step *X* for storage of nodes of adjacent blocks  $4N$ , additional nodes are required, and in step *Y* –  $4M$ . Therefore, in step *X*, the size equal to  $256 \times 1$  has been selected, as a result, block required only 4 additional nodes in memory. In step *Y*, the block size was set as  $16 \times 16$  to reach a compromise between the number of additional memory (64 grid nodes) and the requirements for the serial memory access.

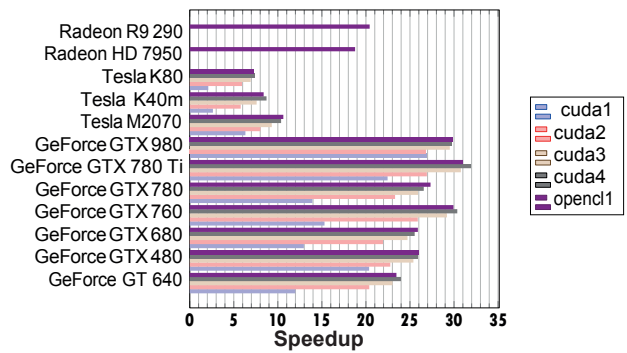


Fig. 9. Acceleration on GPU compared to CPU core.

**8.5. Using opencl**

The next step was to create the OpenCL implementation of this algorithm. Optimized version of the CUDA4 algorithm was taken as the basis for this. Acceleration test results for all implementations are shown in Fig. 9. The maximum obtained acceleration compared with a single CPU on one graphic CPU – 55 times on the GeForce GTX 780 Ti in the computations of single precision and 44 times at Tesla K80 in double precision computations.

It good results for AMD devices should be noted, in spite of the fact that cheap desktop card were used, they showed good results on implementations of single-precision and double-precision.

**9. MULTIPLE GPUs**

The algorithm has been parallelized to run on multiple graphics processors. The most optimized version was used to perform several unused GPU. At that the computational grid was divided into several equal-sized rectangular areas. The division was made on the *Y* axis, due to the selected size of the block on *X* axis.

Tests with multiple GPUs were carried out only for the same GPUs. This was made due to the fact that by using GPUs of different performance, faster processors will cause downtime of slower graphics processors, and the effect of their simultaneous use may be less noticeable. Synchronization of computational grid between GPUs was carried out by sharing through host memory (CPU). Moreover synchronization was performed only once at each

time step before the step on  $Y$  axis. If the grid size is  $M \times N$ , and the number of processors is  $D$ , the number required for the synchronization of grid nodes equals  $4M(D - 1)$ .

Also, the version based on GPUDirect was implemented. The main advantage of GPUDirect technology in problem solution is the ability to transfer data, which is located in GPU memory directly without the involvement of the host via PCI Express bus, i.e., there is no need to copy data from the first graphics processor to the host, and then from the host to the other GPU. Test results are shown in Fig. 10.

The result of using CUDA technology does not differ significantly, when host memory is used as an exchange buffer. The result for OpenCL technology is a little worse.

10. CONCLUSION

This paper shows how the capabilities of CPU are involved in the solution of problems with seismic grid-characteristic method.

Highest percentage of peak performance of the processor has been obtained in sequential version. It was 22% for the calculations in single precision and 17% for double precision computations with cache memory access optimizations and use of AVX instruction set.

The maximum speedups was on AMD Opteron 6272 – up to 37 times with 64 cores, on AMD Opteron 8431 – up to 25 times on 48 cores, and on Intel Xeon E5-2697 – up to 1710 times on 24 cores.

Thus, we demonstrated, that in systems with shared memory, the main limitation to the growth of speedup with the increase of number of threads is the maximum speed of interaction with the memory. Separation of memory between threads allows processor cores to access only local memory, so memory access is faster. Binding threads to specific cores reduces the number of memory used to maintain the coherence of cores cache, which is also leads to increased performance. It should be noted that the implementation of a parallel version using POSIX Threads is more complicated than using of OpenMP, but does not provide a significant performance increase or efficiency of parallelization.

In addition, we described methods that allow achieving the highest performance of the algorithm when computing on the GPU. The problem of effective GPU memory use both in case of using one GPU, and in case of multiple GPUs is also studied. The influence of different optimizations on the performance of the algorithm was considered. The maximum acceleration obtained on graphic CPU compared with a single CPU – 55 times on GeForce GTX 780 Ti when computing with a single precision and 44 times at Tesla K80 at double precision computations. We managed to achieve the performance of 460 GFlops for single accuracy, and the maximum performance of 138 GFlops for double accuracy was obtained. Maximum achieved acceleration of the graphics processors is 7.1 times for 8 GPUs for double precision. GPUDirect technology raised acceleration to 10% of what has been achieved without the calculations with a single precision.

Based on these results we can draw come to a conclusion that GPUs can be used for the solution of such problems. The results are similar for other tasks, which use similar numerical methods (finite volume method, finite difference methods). It is also worth noting that there are good results for the AMD

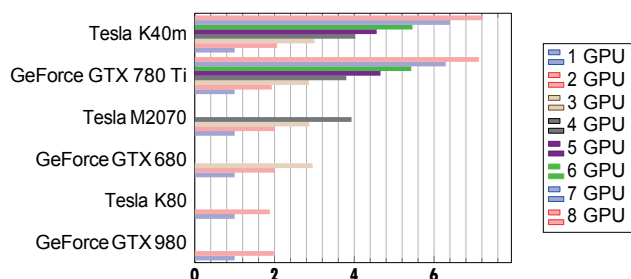


Fig. 10. Acceleration using GPUDirect.

processors and OpenCL technology, while CUDA technology for NVidia GPUs is used in most works.

## REFERENCES

1. Caserta A, Ruggiero V, Lanucara P. Numerical modelling of dynamical interaction between seismic radiation and near-surface geological structures: a parallel approach. *Computers and geosciences*, 2002, 28, 9:1069-1077.
2. Guo X, Lange M, Gorman G, Mitchell L, Weiland M. Developing a scalable hybrid MPI/OpenMP unstructured finite element model. *Computers and Fluids*, 2015, 110:227-234.
3. Micikevicius P. 3D finite difference computation on GPUs using CUDA. *Proceedings of 2nd workshop on general purpose processing on graphics processing units*. ACM, 2009:79-84.
4. Nickolls J, Buck I, Garland M, Skadron K. Scalable parallel programming with CUDA. *Queue*, 2008, 6, 2:40-53.
5. Abdelkhalek R, Calendra H, Coulaud O, Latu G, Roman J. Fast seismic modeling and reverse time migration on a GPU cluster. *HPCS'09 Intern. Conf. on High Performance Computing and Simulation*, IEEE, 2009:36-43.
6. Foltinek D, Eaton D, Mahovsky J, Moghaddam P, McGarry R. Industrial-scale reverse time migration on GPU hardware. *2009 SEG Annual Meeting - Society of Exploration Geophysicists*. 2009.
7. Bohlen T. Parallel 3-D viscoelastic finite difference seismic modelling. *Computers and Geosciences*, 2002, 28, 8:887-899.
8. Gropp W, Lusk E, Doss N, Skjellum A. A high-performance, portable implementation of the MPI message passing interface standard. *Parallel computing*, 1996, 22, 6:789-828.
9. Martin R, Komatitsch D, Blitz C, Le Goff N. Simulation of seismic wave propagation in an asteroid based upon an unstructured MPI spectral-element method: blocking and non-blocking communication strategies. *Intern. Conf. on High Performance Computing for Computational Science*. Springer, Berlin Heidelberg, 2008:350-363.
10. Rostrup S, De Sterck H. Parallel hyperbolic PDE simulation on clusters: Cell versus GPU. *Computer Physics Communications*, 2010, 181, 12:164-179.
11. Aochi H, Dupros F. MPI-OpenMP hybrid simulations using boundary integral equation and finite difference methods for earthquake dynamics and wave propagation: Application to the 2007 Niigata Chuetsu-Oki earthquake. *Procedia Computer Science*, 2011, 4:1496-1505.
12. Vanderbauwhede W, Benkrid K. *High-performance computing using FPGAs*. New York, Springer, 2013.
13. Krueger J, Donofrio D, Shalf J, Mohiyuddin M, Williams S, Olike L, Pfreundt FJ. Hardware/software co-design for energy-efficient seismic modeling. *Proceedings of 2011 Intern. Conf. for High Performance Computing, Networking, Storage and Analysis*. ACM, 2011, 73 p.
14. Petrov IB, Favorskaya AV, Sannikov AV, Kvasov IE. Grid-characteristic method using high-order interpolation on tetrahedral hierarchical meshes with a multiple time step. *Mathematical Models and Computer Simulations*, 2013, 5, 5:409-415.
15. Golubev VI, Petrov IB, Khokhlov NI. Numerical simulation of seismic activity by the grid-characteristic method. *Computational Mathematics and Mathematical Physics*, 2013, 53, 10:1523-1533.
16. Beklemysheva KA, Petrov IB, Favorskaya AV. Numerical simulation of processes in solid deformable media in the presence of dynamic contacts using the grid-characteristic method. *Mathematical Models and Computer Simulations*, 2014, 6, 3:294-304.

17. Butenhof DR. *Programming with POSIX threads*. Addison-Wesley Professional, 1997, 400 p.
18. Munshi A. The opencl specification. *2009 IEEE Hot Chips 21 Symposium (HCS)*. IEEE, 2009, 314 p.
19. LeVeque RJ. *Finite volume methods for hyperbolic problems*. Cambridge university press, 2002, 558 p.
20. Carcione JM, Herman GC, ten Kroode APE. Review Article: Seismic modeling. *Geophysics*, 2002, 67, 4:1304-1325.

## DETECTION AND INVESTIGATION OF ANOMALOUS (UNDAMPED) THERMAL WAVES

Vladimir I. Vysotskii, Anton O. Vasilenko, Mikhail V. Vysotsky

Shevchenko Kiev National University, <http://www.univ.kiev.ua>

64/13, st. Vladimirskaia, 01601 Kyiv, Ukraine

[vivysotskii@gmail.com](mailto:vivysotskii@gmail.com), [vivysotskii@gmail.com](mailto:vivysotskii@gmail.com), [mih1984@gmail.com](mailto:mih1984@gmail.com)

Alla A. Kornilova, Efim I. Hait, Nailia H. Volkova

Lomonosov Moscow State University, <http://www.msu.ru>

1/2, Leninskie Gory, 119991 Moscow, Russian Federation

[prfnart@mail.ru](mailto:prfnart@mail.ru), [haitov5@yandex.ru](mailto:haitov5@yandex.ru), [haitov5@yandex.ru](mailto:haitov5@yandex.ru)

*Abstract.* Results of the detection and study of fundamentally new physical phenomenon - generating undamped temperature waves, which can exist in different environments only at certain frequencies, the value of which depends on the time of the local relaxation of thermal excitations in these environments (the thermalization time) are presented. In the air, under normal conditions, the minimal frequency of such wave corresponds to 70-90 MHz and in metals and semiconductors it is  $10^{12}$ -  $10^{14}$  Hz. In the experiments these waves are generated via cavitation processes and registered in the air at a distance of 2 m and this distance is limited only by the experimental conditions

*Keywords:* cavitation, shock waves, acoustic detector, thermal wave, the heat equation, thermal relaxation

PACS: 47.55.Bx; 43.25.Yw; 43.25.Ed; 44.10.+i; 62.50.Ef; 66.70.-f

*Bibliography* – 22 references

*Received* 03.12.2016

*RENSIT*, 2016, 8(2):196-206

DOI: 10.17725/rensit.2016.08.196

### CONTENTS

1. INTRODUCTION (196)
  2. THE THERMAL DIFFUSIVITY EQUATION AND ITS SOLUTIONS FOR SYSTEMS WITH MEMORY (197)
  3. REGISTRATION AND STUDY OF UNDAMPED TEMPERATURE WAVES IN CAVITATION EXPERIMENTS (199)
  4. CONCLUSION (203)
- REFERENCES (205)

### 1. INTRODUCTION

In our previous studies [1-6] various radiative processes that accompany the cavitation of liquid jet exiting under pressure from a narrow channel were considered. At the time of these studies we have observed non-trivial physical processes during the interaction of this jet with the target. In particular the excitation of shock waves in this target and generation of pulsed X-ray and high-frequency (in the range 70-90 MHz) radiations from the opposite surface of the target have been observed.

High-frequency radiation were recorded by an acoustic sensor at a distance of 2 m from the target. This fact is paradoxical since it is well known that the absorption coefficient of hypersound in air in normal conditions is  $\delta(\omega) \approx 10^{-12} \omega^2 \text{sm}^{-1}$  (1) and in this frequency range is equal to a very large value  $\delta(\omega) \approx 10^4 \text{cm}^{-1}$ , while the path length does not exceed a few microns. In addition as a sensor wideband acoustic detector with a resonant frequency of 1-2 MHz was used, which sensitivity in the hypersound range  $\omega \gg 1 \text{MHz}$  is low. Herewith we had taken every precaution to make it impossible any path of signal from source to detector, except the direct propagation in the air. Further analysis has shown that the registered radiation is not the hypersound, but the thermal (temperature) radiation, which has a non-damped character. The physical mechanism of excitation and propagation of such waves is discussed below.

**2. THE THERMAL DIFFUSIVITY EQUATION AND ITS SOLUTIONS FOR SYSTEMS WITH MEMORY**

Let's consider the background, rationale, and "weak" places of the classical heat equation, the solution of which leads to the thermal waves.

For decades in the analysis of heat conduction problem the classical Fourier hypothesis was used, according to which the non-stationary heat flow  $\vec{q}(\vec{r}, t)$  is proportional to the temperature gradient  $\vec{q}(\vec{r}, t) = -\lambda grad(T(\vec{r}, t))$ , (2) and extends in the direction of reduction of this gradient (eg, [7-9]). Here,  $\lambda$  is the coefficient of thermal conductivity.

If we combine (2) with the energy conservation law for the local area (the continuity equation) in a medium with a volume density  $\rho$  and heat capacity  $c_v$ ,

$$\rho c_v \frac{\partial T(\vec{r}, t)}{\partial t} = div \vec{q}(\vec{r}, t), \tag{3}$$

we can get a classic parabolic equation for the temperature field

$$\rho c_v \frac{\partial T(\vec{r}, t)}{\partial t} = \lambda div \{ grad [T(\vec{r}, t)] \}. \tag{4}$$

In the one-dimensional case the solution of this equation is a superposition of colliding plane waves

$$\begin{aligned} T(\omega, x, t) &= A_\omega e^{i(\omega t - kx)} + B_\omega e^{i(\omega t + kx)} \equiv \\ &\equiv A_\omega e^{-\delta x} e^{i(\omega t - \kappa x)} + B_\omega e^{\delta x} e^{i(\omega t + \kappa x)}, \\ k &= \kappa(1 - i), \kappa = Re k = \sqrt{\omega / 2G}, \delta = Im k = \sqrt{\omega / 2G}. \end{aligned} \tag{5}$$

Here,  $G = \lambda / \rho c_v$  – thermal diffusivity coefficient

This solution shows that the temperature waves, produced on the basis of the system of equations (2-4) are characterized by a very strong damping with a factor  $\delta = \sqrt{\omega / 2G}$ , which is exactly equal to the wave number  $\kappa$ .

It is obvious that the solution (5) with such ratio of wave number and the absorption coefficient at which virtually complete absorption of wave occurs on a spatial interval of the wavelength can be called wave only with great approximation.

Such "standard" solutions are well known. They, in particular, are regarded as illustrations in any textbook on mathematical physics and are used for solving of some applications (in particular, the problem of propagation of extremely low-frequency temperature wave in soil,

which is caused by seasonal temperature variations with a period of 1 year). Analysis of the initial equations (2)-(4) shows that at least two important conditions are used there: the principle of local thermodynamic equilibrium and the principle of locality. The principle of locality allows to use the energy conservation equation in differential (local) form instead of the conservation of energy equation in integral form. The principle of local thermodynamic equilibrium justifies the possibility of describing of non-equilibrium system, in which there is a temperature gradient, concentration gradient, etc., through the introduction of local equilibrium states of smaller subsystems. These very important principles are valid only for slow processes, when the relaxation time of subsystems to equilibrium state  $\tau$  is much shorter than the characteristic time of the process (eg, the duration of the heat front for pulse impact or oscillation period for harmonic thermal effects).

In the 50s of the 20th century in the works of Cattaneo and Vernotte attempts to consider non-stationary heat transfer processes have been made, which has led to the hyperbolic equation for the temperature field [10, 11]. Hyperbolic and nonlinear parabolic models of heat transfer for the purpose of the analysis of the new heat transfer modes, including the mode with escalation were also considered [12]. Unfortunately, these and similar "incomplete" methods and models do not allow to use the thermal processes for the efficient processing of the experimental data, related to the interaction of fast particles with the environment (for example, crystalline targets).

This issue is discussed in details in our works [13-16]. Methods discussed below show that more correct and adequate is the revision of the basic ratios and initial concepts, which are used without limits of obtaining the "standard" initial relations (2-4). The main of them relates to the hypothesis of the use of locally equilibrium (thermalized) environment for the receiving of these relations. To make this circumstance correct we need to evaluate a real time of thermal relaxation in different environments [17, 18].

In plasma the time of formation of equilibrium (Maxwellian) distribution within the electronic subsystem in a small area equals

$$\tau^{(ee)} \approx \sqrt{m_e} (k_B T_e)^{3/2} / 4\pi\Lambda n_e e^4, \quad (6)$$

where  $n_e$ ,  $m_e$ ,  $T_e$  – respectively, the electron concentration, mass of electron and electron temperature,  $\Lambda \approx 15$  – "coulomb" logarithm.

For the ionic subsystem in plasma the relaxation time equals  $\tau^{(ii)} \approx \sqrt{m_i / m_e} \tau^{(ee)}$ .

Close to this value relaxation time, which determines the "maxwellization" of electron gas on the levels of energy in the conduction band, adjacent to the Fermi level, approximately equals  $\tau \approx 10^{-14}$ - $10^{-12}$  seconds.

In the air the relaxation time  $\tau \approx (1.5-2) \cdot 10^{-8}$  sec is defined as by the duration of "maxwellization" process of gas translational degrees of freedom  $\tau_{\max}$  as by the much longer relaxation time of molecules vibrational and rotational degrees of freedom. With the change of temperature and, especially, density and composition of the air (e.g., at the presence of water vapor), the value of  $\tau$  can vary within a wide range ( $\tau \approx 10^{-7}$ - $10^{-8}$  s).

It is also evident that the relaxation time has to depend on the intensity of the thermal wave and on the temperature of medium in which the wave propagates. The solution of such nonlinear problem is an extremely difficult problem.

It is obvious that for thermal processes, which occur slowly than the given values  $\tau$ , taking into account of relaxation is negligible because for the description of such processes it is always possible to use equilibrium characteristics.

The simplest account of the temperature relaxation process (without nonlocality and time heterogeneity of the process of temperature formation) can be carried out using a modified equation of continuity

$$\rho c_v \frac{\partial T(\vec{r}, t + \tau)}{\partial t} = -\text{div} \vec{q}(\vec{r}, t), \quad (7a)$$

corresponding to the integral relation

$$\frac{\partial}{\partial t} \int_V W_T(\vec{r}, t + \tau) dV = - \int_S \vec{q}(\vec{r}, t) \vec{n} dS, \quad (7b)$$

which has been obtained by integration of the differential relation (7a) using the Gauss formula.

Here  $W_T(\vec{r}, t + \tau) = \rho c_v T(\vec{r}, t + \tau)$  – the volume density of the thermal energy;  $\vec{n}$  – normal vector to the surrounding the volume  $V$  surface.

Formula (7b) shows that the change in the total heat energy at time  $t + \tau$  in the small volume  $V$  is determined by the energy flow  $\vec{q}(\vec{r}, t)$  via the surface  $S$ , the bounding this volume, corresponding to the previous point of time  $t$ .

Substituting equation (2) to (7a), we obtain the thermal diffusivity equation with delay  $\tau$ , which is in one-dimensional case in a homogeneous medium has the form

$$\frac{\partial T(x, t + \tau)}{\partial t} = G \frac{\partial^2 T(x, t)}{\partial x^2}. \quad (8)$$

The solution of equation (8) is determined by the superposition of temperature waves

$$T(\omega, x, t) = A_\omega \exp\left[-\kappa \frac{\cos \omega \tau}{\sqrt{1 + \sin \omega \tau}} x\right] \exp\left\{i(\omega t - \kappa \sqrt{1 + \sin \omega \tau} x)\right\} + B_\omega \exp\left[\kappa \frac{\cos \omega \tau}{\sqrt{1 + \sin \omega \tau}} x\right] \exp\left\{i(\omega t + \kappa \sqrt{1 + \sin \omega \tau} x)\right\}, \quad (9)$$

$\cos \omega \tau \geq 0, \kappa = \sqrt{\omega / 2G},$

obtained for the first time in [13-16]. Each of these waves is fundamentally different from the temperature waves, corresponding to "standard" solution (5).

For waves determined by solution (9), the damping coefficient

$$\delta = \kappa \frac{\cos \omega \tau}{\sqrt{1 + \sin \omega \tau}} = \sqrt{\omega / 2G} \frac{\cos \omega \tau}{\sqrt{1 + \sin \omega \tau}} \quad (10a)$$

depends both on the coefficient thermal diffusivity  $G = \lambda / \rho c_v$ , so and on the time of delay  $\tau$  and the wave frequency  $\omega$ . At extremely low values of  $\omega \tau \ll 1$  from (10a), we can find

$$\delta \approx \sqrt{\omega / 2G} (1 - \omega \tau / 2). \quad (10b)$$

At  $\tau = 0$  the solutions (5) and (10a,b) coincide.

In **Figure 1** the frequency dependences of the absorption coefficient of the "conventional" thermal waves in a medium with no delay (at  $\tau = 0$ ) and the same wave with a delay ( $\tau \neq 0$ ) (10) are presented. The absorption coefficient has a physical sense only when  $\delta / \kappa \geq 0$  (in the upper half-plane of Fig. 1). For graphics (1) the value of  $\tau$  is a formal parameter, which is needed for comparison of (1) and (2) within the same scale.

It can be seen that for an arbitrary value  $\tau$  the absorption coefficient of thermal waves in an

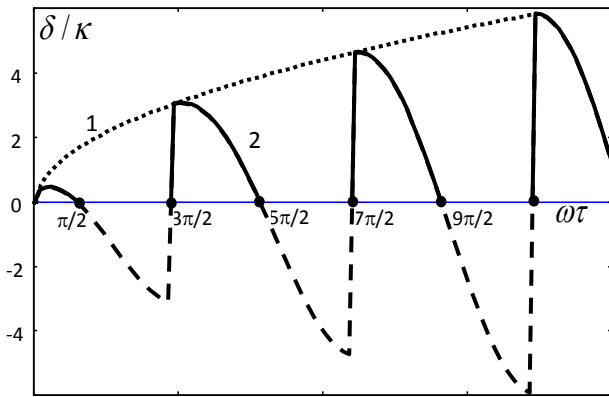


Fig. 1. The frequency dependence of the normalized absorption coefficient of the temperature wave: 1 - a solution (5) of the "classical" thermal diffusivity equation (4), corresponding to  $\tau = 0$ ; 2 - solution (10) of the thermal diffusivity equation (8) with an arbitrary delay  $\tau$ .

environment with a delay  $\tau \neq 0$  is always less than a medium without such delay. From the analysis of the solution (9) follows that heat waves can exist only if  $\cos\omega\tau \geq 0$ , which corresponds to the physical result – the wave in the medium is damped in the propagation direction. Excitation of temperature waves with a frequency corresponding to the condition  $\cos\omega\tau < 0$  in the equation (9) is impossible, since the existence of such waves is contrary to the principle of causality – their amplitude increases in the propagation direction.

To the waves with frequencies  $\omega_n = (n + 1/2)\pi/\tau, n = 0, 1, 2, \dots$  (11) which correspond to conditions  $\cos\omega_n\tau = 0$ , wave numbers  $k_n = \pm\kappa_n\sqrt{2}$  are real and damping coefficient  $\delta$  (10a) is zero, and the general solution of equation (9) in this case has the form of a superposition of the direct and inverse undamped temperature waves

$$T(\omega_n, x, t) = A_{\omega_n} \exp\{i(\omega_n t - \kappa_n \sqrt{2}x)\} + B_{\omega_n} \exp\{i(\omega_n t + \kappa_n \sqrt{2}x)\},$$

$$\kappa_n = \sqrt{\omega_n / 2G}. \tag{12}$$

The physical mechanism of formation of these waves is connected with the influence of the thermal relaxation on phase conditions, which determine the energy dissipation of the thermal motion.

Excitation of these waves is possible in different ways.

The most optimal one is connected with a possible use of local periodic heating at a frequency (11), which correspond to one of such waves. Such system can be based, for example, on the process of interaction of high-frequency electromagnetic wave with a frequency  $\omega_n$  with an absorbing surface. Such surface is a source of undamped thermal waves. It is also possible to use waves with a carrier frequency essentially higher than  $\omega_n$  (e.g., laser radiation), which are modulated by this frequency.

Another simpler case is connected with action on the border between the air and condensed matter by short acoustic pulses with duration  $\Delta t$  less than the time  $\tau$  of relaxation of thermal excitation in the air. In this case in the spectrum of the local thermal waves generated in the area of the local heating, which is formed by the action of these pulses, non-absorbing thermal waves with frequencies corresponding to the condition (11) are present. Such case is realized in the experiments discussed below.

### 3. REGISTRATION AND STUDY OF UNDAMPED TEMPERATURE WAVES IN CAVITATION EXPERIMENTS

The research of the propagation in the air of waves, which are not electromagnetic or acoustic, and the formation of which was stimulated on the target surface by very short mechanical shocks, connected with cavitation phenomena in liquids, was carried out on the basis of several systems used by us during the experiments on cavitation water jets [1, 4, 5, 17, 18].

The scheme of such system is shown in Figure 2.

In this system water under pressure of 250 atm was pumped through channel and through nozzle of small diameter into a cavitation chamber. At the output of the channel cavitation cloud of bubbles appeared, which was formed by the process of growth of cavitation bubbles in a moving jet water. The action of this jet on the inner surface of the metal target caused the formation of intensive shock waves. The inner surface of metal target is at a distance of 14 mm from the channel outlet

opening, while the space between this surface and the nozzle formed the cavitation chamber.

For the registration of thermal waves in the air on the outer border of the metal target broadband acoustic piezoceramic receiver PZT-19 with a diameter of 20 mm and a resonant frequency of 1 MHz was used.

In first experiments the receiver moved along the installation axis in the interval from 5 mm to 21 cm from the outer surface of the metal target. Measurements were made every 1 cm. For control measurements the receiver was turned by 0, 20, 90 and 180 degrees relative to the axis of the experimental setup. In the experiments tungsten and molybdenum targets were used.

**Figure 3** shows the form of signal, detected by the receiver at different distances from a tungsten target. It can be seen that in the space behind the target (in the air) both low-frequency (LF) and high frequency (HF) signals were recorded, whose frequencies changed with the distance weakly.

A simple analysis shows that low-frequency signal with a frequency  $\omega_{LF} \approx 8.3-8.9$  kHz corresponds to a spatial acoustic resonance inside the cavitation chamber. This resonance correspond to "positive feedback loop" during the sequential motion of the shock wave from the target through the walls of cavitation chamber to the nozzle channel and corresponding modulation parameters of this nozzle, affecting the speed of formation of cavitation bubbles in the jet water. This resonance contributed to the formation of the regime of periodic synchronized cavitation of jet liquid, in which the cavitation bubbles are arise

and formed not sporadically, but as synchronized groups.

Such system is similar to the classical electron Van der Pol generator. A small variation of this frequency can occur due to a reverse action of low-frequency acoustic waves reflected from the receiver towards the target.

The amplitude of the low-frequency signal by removing the receiver from the target decreases and is characterized by an approximate coefficient of effective wave attenuation  $\delta_{LF} \approx 0.05 \text{ cm}^{-1}$ . Such damping agrees good enough with the laws of acoustics and is determined by the combined action of two factors: a) "usual" linear damping of low-frequency sound wave; b) diffractive extension of the low-frequency wave front, which is generated by a source of limited aperture.

Fundamentally different situation corresponds to the process of registration of the HF signal, the amplitude of which increases with the increasing of distance of HF wave at removal from the target synchronously with a decrease of amplitude of the LF wave! These results are presented in **Figure 4**.

A possible explanation for this surprising phenomenon may be connected with a hypothetical transfer of heat energy from one wave to another (damping and relaxation of low-frequency thermal excitation leads to the generation of high-frequency thermal wave). The mechanism of this process has not been determined.

At great distances from the target the saturation of amplitude is observed. The maximum value of the amplitude of this wave corresponds to the distance of 21 cm. It is necessary to point

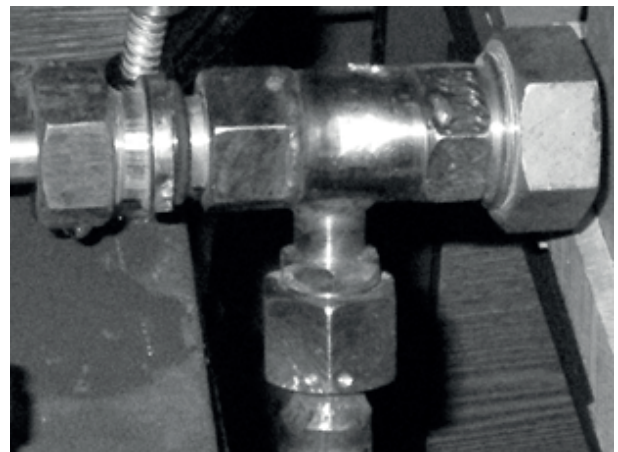
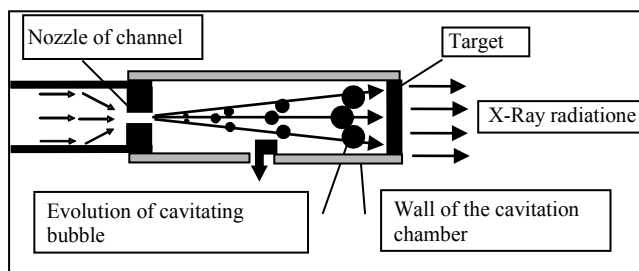


**Fig. 2.** Schematic picture and photo of setup for generating of X-rays at cavitation of water jet in closed chamber.

out that both signals (both low frequency and high frequency) decreased in amplitude when the receiver was turned in vertical and horizontal

planes. It proves that signals were emitted by the target and they were not the background.

It should be noted that the registration of the acoustic signal with a frequency of to  $\sim 80\text{-}85\text{ MHz}$

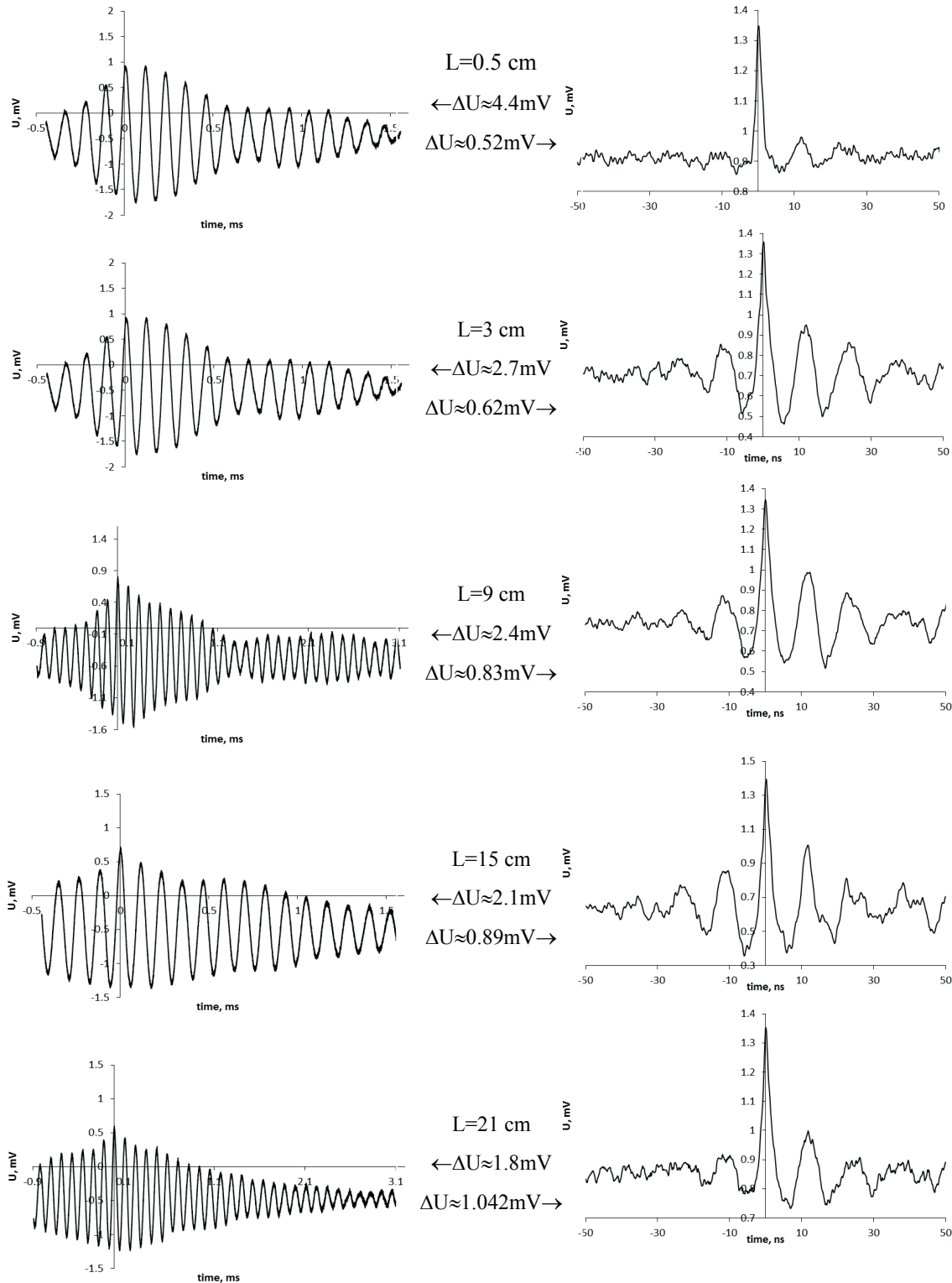
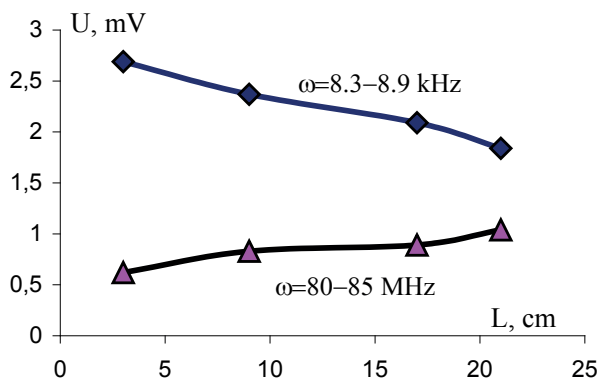


Fig. 3. Low-frequency (left,  $\omega_{LF} \approx 8.3\text{-}8.9\text{ kHz}$ ) and high-frequency (right,  $\omega_{HF} \approx 80\text{-}85\text{ MHz}$ ) signals recorded by an acoustic receiver, which is located in the air at different distances  $L$  from the target. The amplitudes of the recorded signals  $\Delta U$  are presented near the respective plots.



**Fig. 4.** Synchronous change amplitudes of low and high frequency thermal waves in the air when it changes of the distance from the source to the place of registration.

at a distance of  $L = 10-20$  cm from the outer surface of the target (opposite to the direction of water jet falling in the state of cavitation) is a paradox which cannot be explained on the basis of "standard" acoustics. This conclusion follows directly from the expression for sound attenuation coefficient for gases and liquids (eg, [19])

$$\delta(T) = \frac{\omega^2}{2\rho\{c(T)\}^3} \left[ \left( \frac{4}{3}\eta + \xi \right) + \lambda(T) \left( \frac{1}{c_v} - \frac{1}{c_p} \right) \right], \quad (13)$$

where  $c(T) \approx (331.3 + 1.21T^\circ) \cdot 10^2$  cm/sec – the speed of sound,  $\rho$  – air density,  $c_p = 1000$  (J/kg·K) and  $c_v = 717$  (J/kg·K) – specific heat capacity of air at room temperature and normal pressure at constant pressure and volume,  $\eta = 1.9 \cdot 10^{-5}$  (Pa·sec) and  $\xi = 17.2 \cdot 10^{-6}$  (Pa·sec) – coefficients of the shear and bulk viscosity of air,  $T^\circ$  – the temperature in Celsius.

From this formula follows that the hypersound with the frequency  $\omega \approx 80-85$  MHz propagation in the air at room temperature corresponds to a very large damping coefficient  $\delta(T) \approx 10000$  cm $^{-1}$ . Path length of such wave in the air is less than  $\langle L \rangle \approx 1-2$   $\mu$ m, which is in 10000 times (!) less than the experimental results.

This result becomes even more paradoxical taking into account that the resonant frequency of the acoustic detector used was 1 MHz, which is 85 times lower than the frequency of the detected signal and indicates a rather low detection efficiency. So it is evident that the real amplitude of HF signal in the location of acoustic detector was very great.

The second paradox is connected with the discussed above effect of spatial increases of amplitude of the HF wave, which is synchronized with a corresponding decrease of the amplitude of the LF wave.

These paradoxes can be solved if we assume that the HF wave is not the acoustic wave but the undamped temperature wave, which discussed above.

The frequency of this wave is in good agreement with results of calculation.

In the air the relaxation time is defined as by the duration of the process of "maxwellisation"  $\tau_{\max v}$ , as by longer processes of internal and mutual relaxation of vibrational and rotational states of  $N_2$  and  $O_2$  molecules. The value  $t_{\max v}$  depends on the average cross-section  $\sigma \approx \sqrt{2\pi}D^2$  of elastic scattering of similar size molecules  $N_2$  and  $O_2$  (their diameter can be taken as  $D \approx 3\text{\AA}$ ), which are basic molecules in the air, on the average velocity of gas molecules  $v = \sqrt{3kT/m} \approx 4.6 \cdot 10^4$  cm/s and the total concentration of molecules  $n \approx 3 \cdot 10^{19}$  cm $^{-3}$ . Under normal conditions (normal pressure and room temperature) we can find

$$\tau_{\max v} \approx 10/n < \sigma(v)v \gg 10\sqrt{m/3kT}/n < \sigma \gg 2ns. \quad (14)$$

Accounting of the relaxation of the rotational and vibrational states of molecules allows to characterize the time of local relaxation  $\tau \approx 15-20$  ns, which corresponds to the evaluation of the minimum frequency of undamped temperature wave in the range of  $\omega_0 \approx 70-90$  MHz and varies with variations of pressure and humidity.

Another series of research has been carried out using similar experimental equipment, based on the installation of the KMT setup, considered in [17, 18]. The schematic diagram of this setup is similar to setup presented in Fig. 2, and the difference is only in the direction of free outlet of water jet. The purpose of this research was to examine the possibility of extending the temperature waves at substantially greater distances.

**Figure 5** shows a fragment of panoramic spectrum of registered waves in frequency range up to 300 MHz when  $L = 18.5$  cm, as well as fragments of registered signal at a distance  $L = 18.5$  cm and  $L = 198$  cm from the place of

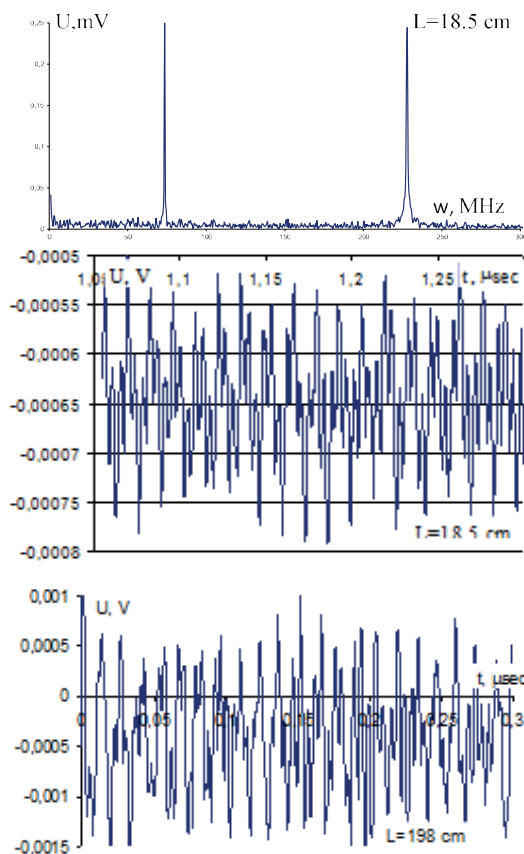


**Fig. 5.** Part panoramic spectrum signals recorded by acoustic detector that located at a distance  $L = 18.5$  cm from the outer surface of the target, and the fragments detected signal at a distance  $L = 18.5$  cm and  $L = 198$  cm.

formation of these waves (the outer surface of the tube, through which a water jet passed). A similar panoramic spectrum was registered and at other distances from the emitting surface (0.5, 18.5, 100 and 198 cm).

The frequencies of the signals registered by the acoustic detector with a resonant frequency of 1 MHz, are respectively  $\omega_0 \approx 74$  MHz and  $\omega_1 \approx 225$  MHz, and are in good agreement with the formula (11), which determines the spectrum of undamped temperature waves. The difference between the lowest frequency of these waves from the frequency  $\omega \approx 80$ -85 MHz, registered in the previous experiment, can be connected with the fact that these frequencies are determined by the thermal relaxation time (14), which varies with the density, temperature of air and air composition. Since in this experiment a jet of water after the generation of shock waves came out into the free space, it has led to high humidity in the space around the experimental setup and, as a result, could change a little relaxation time (from

$\tau = \pi\omega_0/2 \approx 18.4$ -19.6 ns at  $\omega_0 \approx 80$ -85 MHz to  $\tau = \pi\omega_0/2 \approx 21$  ns at  $\omega_0 \approx 74$  MHz). It is obvious that similar reason (in particular, a small change of air temperature near the experimental equipment, which has worked for a long time of the experiment that lasted several hours with concomitant rearrangement and fixing of the detector at different distances, and a corresponding change in concentration of molecules) explains a slight difference of wave frequencies  $\omega_0 \approx 80$ -85 MHz registered at different distances.

Despite the fact that these waves are detected at substantially different distances from the place of formation ( $L = 18.5$  cm and  $L = 198$  cm), their amplitudes at the output of the registration system were identical and were equal to  $U_{\max} \approx 1$  mV, that confirms the absence of their damping in the air.

#### 4. CONCLUSION

Conducted experiments demonstrate the registering of unknown before our work phenomenon – the generation and propagation of undamped HF thermal (temperature) waves with frequency  $\omega_0 \geq 75$ -85 MHz, which are registered by acoustic detector at a great distance (up to 2 meters) from the source.

It should be noted that this distance is limited only by the size of the laboratory, and it is expected that such waves will propagate without attenuation at a much greater distances. These waves are fundamentally different from the "classic" hypersonic waves of megahertz range, which can not propagated in the air and are damped at a very small distance (a units and tens of microns) from the place of excitation.

These undamped thermal waves can be excited and propagated only in environments with a finite (non-zero) time of the local thermodynamic relaxation and their frequency is determined completely by this time.

It was shown that the frequency of these waves depends on the propagation environment parameters (in this case – the air). Condition of excitation of such waves is connected with the obvious requirement that in the spectrum of thermal excitation the spectral components at these frequencies were present. This condition

limits the parameters of thermal pulses – their duration should be small enough so that the needed frequencies were presented in the spectrum.

Used method of excitation of thermal waves by shock waves of cavitation satisfies these conditions because the minimum duration of the leading edge of shock wave is equal  $\Delta t_{\min} \approx \Delta l / v_{\text{SW}}$ , where  $\Delta l \approx 10d$  the length of the shock wave front, which is determined by the average distance  $d$  between atoms or molecules,  $v_{\text{SW}}$  – the speed of the shock wave, that is defined by the Mach number and the speed of sound in this medium.

In metals and other condensed media  $v_{\text{SW}} \approx (2-5) \cdot 10^5$  cm/s,  $d \approx (1.5-2) \text{ \AA}$  and  $\Delta t_{\min} \approx (0.3-0.8) \cdot 10^{-13}$  s. So in the air at normal pressure  $v_{\text{SW}} \approx (0.5-1) \cdot 10^5$  cm/s,  $d \approx n_{\text{air}}^{-1/3} \approx 30 \text{ \AA}$  and  $\Delta t_{\text{(air)min}} \approx 10^{-12}$  s.

From these estimations follow that under optimal conditions corresponding to the formation of shock waves the maximum frequency of undamped thermal waves in the air can reach  $\omega_{\max} \approx 1/\Delta t \approx 1 \text{ GHz}$ . This estimation is in very good agreement with the results of the experiment discussed above. In **Figure 6** a high-frequency part of the general panorama of the spectrum of registered thermal waves is presented, the low-frequency part of it was shown above in Fig. 5.

From the form of this spectrum follows that the maximum frequency of the undamped thermal waves at this method of excitation reaches  $\omega_{\max} \approx 1 \text{ GHz}$ , which coincides with the results of a theoretical estimations.

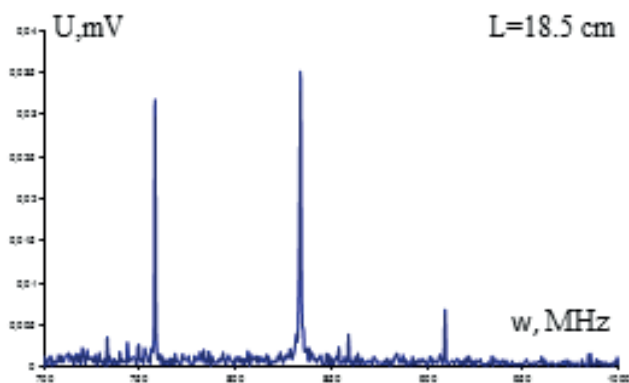


**Fig. 6.** The high-frequency part of the panoramic spectrum of signals recorded by acoustic detector that located at a distance  $L = 18.5$  cm from the outer surface of the target.

These waves have a very small speed of propagation, which is according to estimates much smaller than the speed of normal sound and does not exceed 50-100 m/s.

Finally it is possible to note one more potentially possible factor of pulse generation of thermal waves at the output (outer) surface of screen or tube the inner surface of which is affected by acoustic shock waves caused by cavitation of jets of water. Earlier we considered the process of internal reflection of shock waves from the surface with the corresponding sharp "shaking" and the ionization of surface atoms as the main mechanism of excitation of thermal waves near the outer surface (the right surface of the target in Fig. 2), that leads to the generation of soft X-ray radiation and very rapid heating of the subsurface layer of air.

Recent results show that there is another mechanism of such pulsed heating, which is connected with peculiarities of shock pulse impact on atoms.

In [20-22], it was shown that at rapid (pulse) reversible deformation of the nonstationary harmonic oscillator the formation of coherent correlated states of particles takes place, when these particles are in nonstationary parabolic field of this oscillator. The peculiarities of this state leads to the synchronization of quantum fluctuations in the superposition state and to the formation of a giant fluctuations of momentum and kinetic energy, which are on many orders of magnitude greater than the average values. The result of this process is the sharp increase of the probability of chemical and nuclear reactions between particles in a parabolic field and particles that form this field, and pulsed energy release. In particular, in these works it have been shown that under such modulating action the fluctuations of kinetic energy of particles (in particular atomic nuclei) may reach 10-50 keV at medium thermal (room) energy of target  $kT \approx 0.025$  eV!

Simple analysis shows that the process of shock wave motion through the condensed substance agrees with this scenario of intensified energy release. During the motion of the shock wave through such medium a strong compression

of matter at its leading edge and the extension at the trailing edge takes place. For each atom of the medium, which is surrounded by close neighbors, that is equivalent to the unsteady pulsed deformation of the harmonic oscillator, field of which is formed by nearest neighbors.

Such effect, which leads to the formation of coherent correlated states, plays the main role at the outside (output) surface of the cavitation chamber, where the reflection of shock waves from the border of dense material of the chamber and air takes place. Indirect confirmation of such mechanism of the energy release consist in the detection of foreign chemical elements on the outer chamber surface. These elements were absent before the exposure on the target with the water jet with cavitation bubbles. Such elements may be a result of pulsed nuclear reactions between the nuclei of the target and the nuclei of the atoms of the air. Such process is extremely short and its duration is determined by the time of existence of coherent correlated state [20-22].

We plan to explore this scenario doing additional and longer experiments.

## REFERENCE

1. Vysotsky VI, Kornilova AA, Korneeva Yu V, Krit TB. Issledovanie anomalnykh radiatsionnykh i teplovykh yavleniy pri kavitatsii strui zhidkosti. 1. Anomal'nye efekty pri generatsii rentgenovskogo izlucheniya, stimulirovannogo protsessom kavitatsii zhidkosti [The study of abnormal radiation and thermal phenomena in the cavitation jet fluid. 1. Anomalous effects in the generation of X-rays, stimulate fluid cavitation]. *Inzhenernaya fizika*, 2016, 2:33-45 (in Russ.).
2. Kornilova AA Vysotsky VI, Koldamasov AI, Hyun Ik Yang, Denis B. McConnell, Desyatov AB. Generation of intense directional radiation during the fast motion of a liquid jet through a narrow dielectric channel. *Journal of surface investigation. X-ray, synchrotron and neutron techniques*, 2007, 1(2):167-171.
3. Kornilova AA Vysotsky VI, Sysoev NN, Desyatov AB. Generation of X-rays at bubble cavitation in a fast liquid jet in dielectric channels. *Journal of Surface Investigation. X-ray, Synchrotron and Neutron Techniques*, 2009, 3(2):275-283.
4. Kornilova AA, Vysotsky VI, Sysoev NN, Litvin NK, Tomak VI, Barzov AA. Shock-cavitation mechanism of X-ray generation during fast water stream cavitation. *Moscow University Physics Bulletin*, 2010, 65(1):46-50.
5. Kornilova AA Vysotsky VI, Sysoev NN, Litvin NK, Tomak VI, Barzov AA. Generation of intense x-rays during ejection of a fast water jet from a metal channel to atmosphere. *Journal of Surface Investigation. X-ray, Synchrotron and Neutron Techniques*, 2010, 4(6):1008-1017.
6. Vysotsky VI, Kornilova AA, Sysoev NN. Rentgenovskoe izluchenie pri kavitatsii bystroy strui zhidkosti [X-rays at a fast cavitation liquid jet]. *Radioelektronika. Nanosistemy. Informationnyye tekhnologii (RENSIT)*, 2010, 2(1-2):57-69 (in Russ.).
7. Shashkoff AG, Bubnov VA, Janowski SYu. *Volnovye yavleniya teploprovodnosti: sistemno-strukturny podkhod* [Wave phenomena of thermal conductivity: system-structural approach]. Moscow, Editorial URSS, 2004, 296 p.
8. Telegin AS, Shvydkiy VS, Yaroshenko Yu G. *Teplomassoperenos* [Heat and mass transfer]. Moscow, Akademkniga Publ., 2002.
9. Sobolev SL. Local non-equilibrium transport models. *Physics Uspekhi*, 1997, 40:1043-1053.
10. Cattaneo CR. Sur une forme de l'équation de la chaleur éliminant le paradoxe d'une propagation instantanée. *Comptes Rendus*, 1958, 247:431-433.
11. Vernotte P. Les paradoxes de la theorie continue de l'équation de la chaleur. *Comptes Rendus*, 1958, 246:3154-3155.
12. Samarsky AA, Galaktionov VA, Kurdyumov SP, Mikhaylov AP. *Rezhimy s obostreniem* [The sharpening regimes]. Moscow, Nauka Publ., 1987.
13. Vysotskii VI, Vassilenko VB, Vasylenko AO. Propagation of temperature waves in medium with internal thermal relaxation. *Bulletin of Taras Shevchenko National Univ. of Kyiv, Series Raftiophysics*, 2013, 1:11-14.

14. Vysotskii VI, Vassilenko VB, Vasylenko AO. Periodic heat transfer regimes in active medium. *Bulletin of Taras Shevchenko National Univ. of Kyiv, Series Physics & Mathematics*, 2013, 2:255-260.
15. Vasylenko AO, Vysotskii VI, Vassilenko VB. Heat transfer equation with delay for media with thermal memory. *Intern. J. of Sciences: Basic and Applied Research (IJSBAR)*, 2015, 12(1):160-166.
16. Vysotskii VI, Vasilenko AO, Vassilenko VB, Vysotskyy MV. Nonequilibrium thermal effects during pulsed action on conducting medium. *Inorganic Materials: Applied Research*, 2015, 6(3):199-204.
17. Vysotskii VI, Kornilova AA, Vasilenko AO. Observation and investigation of X-ray and thermal effects at cavitation. *Current Science*, 2015, 108(4):114-119.
18. Vysotsky VI, Kornilova AA, Vasilenko AO, Tomak VI. Detecting and investigation of undamped temperature waves excited under water jet cavitation. *Surface Investigation. X-ray, Synchrotron and Neutron Techniques*, 2014, 8(6):1086-1192.
19. Gurbatov SN, Rudenko OV. *Akustika v zadachakh* [Acoustics in problems]. Moscow, Nauka Publ., 1996.
20. Vysotskii VI, Vysotskyy MV. Coherent correlated states and low-energy nuclear reactions in non stationary systems. *European Phys. Journal. A.*, 2013, 49(8):1-12.
21. Vysotskii VI, Adamenko SV, Vysotskyy MV. Acceleration of low energy nuclear reactions by formation of correlated states of interacting particles in dynamical systems. *Annals of Nuclear energy*, 2013, 62:618-625.
22. Vysotskii VI, Vysotskyy MV. The formation of correlated states and optimization of the tunnel effect for low-energy particles under nonmonochromatic and pulsed action on a potential barrier. *Journal of Experimental and Theoretical Physics*, 2015, 121 (4):559-571.

## FOIRIER IMAGES QUASISYMMETRY OF GENERALIZED TRIADIC KOCH PREFRACTALS

<sup>1,2</sup>Galina V. Arzamastseva, <sup>1</sup>Mikhail G. Evtikhov, <sup>1</sup>Feodor V. Lisovsky, <sup>1</sup>Ekaterina G. Mansvetova

<sup>1</sup>Kotel'nikov Institute of Radioengineering and Electronics, Fryazino Branch, Russian Academy of Sciences, <http://fire.relarn.ru>  
1, Vvedensky sq., 141120 Fryazino, Moscow region, Russian Federation

<sup>2</sup>Modern University for the Humanities, <http://www.muh.ru/>

32/4, Nizhegorodskaya str., 109029 Moscow, Russian Federation

arzamastseva@mail.ru, emg20022002@mail.ru, lisf@df.ru, mansvetova\_eg@mail.ru

*Abstract.* The study of the Fourier-images properties was made by numerical methods for the family of flat triadic geometric prefractals with generator in the form of symmetric four-stage broken line with an arbitrary angle at the apex between the central units and the initiator in the form of a straight line (Koch curve) or in the form of an equilateral triangle (the Koch snowflake). To obtain the Fourier images the pictures of fractals were approximated by a grid function on a uniform grid with cells small enough for adequate mapping of high generation prefractal details, and then were digitized in order to use fast Fourier transform for determination the values of the squared modules of the Fourier component, that is, the spectral intensity distribution of diffraction maxima in the Fraunhofer region. An analysis showed that for the values of the vertex or base angles equal to the integer fraction of 180 degrees, Fourier images are the same as for the perfect crystals with the symmetry axes of the 2-nd, 3-th, 4-th and 6-th order, or as for parquet mosaics or quasicrystals with the axes of quasisymmetry of any order. Really in the Fourier images of the Koch curves with the initiator in the form of a straight line was observed axis of quasisymmetry from 3rd to 9th and 11th order. Similar to the above-described properties are also inherent to Fourier images of the Koch snowflake with the initiator in the form of an equilateral triangle. The configuration of the observed Fourier images can be approximately regarded as a radial-annular, at that in the peripheral ("lattice") of the images is dominated by the radial nature of the frequency distribution of diffraction reflections along the radius, and in the central ("fractal") – a ring with self-similarity. The lattice part has a kind of clustering: all the rays have a strong central chain of reflexes along the radii and parallel to it the weaker satellites on both sides. All Fourier images had the center of symmetry, which is an integral attribute of the diffraction patterns in the Fraunhofer zone for any objects, however, the rotational symmetry was not perfect: the positions of the diffraction reflexes when rotating images at angles that correspond to the order of the symmetry axis remain unchanged, but their intensity could vary. The cause of the observed features is that prefractals, unlike crystals, are not a continuum of point objects but two-dimensional set of equal length line segments with different orientation in space. In this set for the considered configurations of the generator it is possible to allocate several two-dimensional subsets with equally oriented segments, each of which contains a number of partial one-dimensional diffraction gratings formed by segments located along the same line. These parallel lattice in the general case contain a different number of segments, and the degree of filling and the distance between adjacent segments, determining the intensity and diffraction reflections distribution structure along the line, depend on the orientation of the lattice and the generation number of prefractal.

*Keywords:* digital methods, Fourier image, Fraunhofer diffraction, generator, initiator, Koch curve, Koch fractal, Koch snowflake, parquet mosaic, prefractal, quasicrystal, quasisymmetry, scaling invariance, self-similarity, symmetry.

UDC 51.74; 535.42

*Bibliography* – 47 references

*Received* 06.12.2016

RENSIT, 2016, 8(2):207-214

DOI: 10.17725/rensit.2016.08.207

### CONTENTS:

- |   |  |
|---|--|
| <ol style="list-style-type: none"> <li>1. INTRODUCTION (208)</li> <li>2. OBTAINING A FOURIER-IMAGES OF THE KOCH CURVES AND SNOWFLAKES (208)</li> <li>3. CONFIGURATION AND SYMMETRY OF THE FOURIER-IMAGES (209)</li> </ol> | <ol style="list-style-type: none"> <li>4. SCHEME OF THE LATTICE AND FRACTAL PARTS OF THE FOURIER-IMAGES FORMATION (210)</li> <li>5. SUMMARY (212)</li> <li>REFERENCES (212)</li> </ol> |
|---|--|

## 1. INTRODUCTION

Fractal ideology, originally considered only as the basis of exotic branches of abstract mathematics, at the present stage is widely used not only to describe and analyse the various material objects and phenomena [1-4], but persistently intrudes into many areas of human activity. Engineering and technology [5, 6], biology and medicine [7], economics [8, 9], art (music, painting, literature, linguistics, architecture) [10-14] – this list could easily be continued. However, from the point of view of the science of fractals priority areas continue to be math and physics [15].

At the end of XX century there was a marked interest in the study of Fourier-images of flat fractals (i.e., a diffraction pattern in the Fraunhofer zone) (see eg. [16-18]), which remains unabated to this day.

In particular, this is due to the fact that by using Fourier images one can fairly easily determine Hausdorff dimension of the studied objects [16]. Authors of papers [17-18] for the first time performed experiments on the scattering of light by microphotographs of the Koch snowflake in order to get the Fourier-image of it and compared obtained data with the theory using the analytical description of a fractal. The features of Fraunhofer diffraction for other fractal objects (Vicsek fractal, Cantor bar, Sierpinski carpet, etc. [19-24]) were also investigated.

The diffraction method of  $D_f$  determination is widespread, as it is applicable to any objects including real fractals which are not subject to any geometrical or analytical description. However, the utilitarian usefulness of the Fourier transform images is not limited by this, because they can be used to obtain information about the structure and symmetry of abstract fractals, and about phase transitions in real media.

For example, the Fourier images analysis of nonuniform magnetization distributions allowed to detect the phenomenon of biperiodic domain structures amorphization in quasi-uniaxial magnetic films with critical thickness [25], and

the presence of phase transitions of "devil's staircase" type in magnetic films with modulated structure [26]. It is not necessary to ignore the aesthetic factor: often talk about the beauty of fractals [27], but the beauty of their Fourier images is just as impressive [28].

## 2. OBTAINING A FOURIER-IMAGES OF THE KOCH CURVES AND SNOWFLAKES

To obtain Fourier images we used numerical algorithm, the essence of which is as follows. Images of studied fractals are approximated by a uniform grid function with cells small enough for adequate reproduction of the high generations pre-fractals details. For digitized pictures using fast Fourier transform we determined the values of the Fourier component squared modules, i.e. the spectral distribution of intensity  $I$  of diffracted radiation in the zone of Fraunhofer. To display the intensity  $I$  of the diffraction maxima on the 2D-plane, we use representation of  $I$  values in a form of circles with radii proportional to logarithm of  $I$ , where coefficient of proportionality is chosen for reasons of optimal illustrativity of images. With the same purpose Gaussian blur of displaying circles was additionally applied.

The described above procedure of the Fourier images determining was for the first time described and applied by us [29] to study the fractal-like domain structures in opaque magnetic films (see [30-32]), wfs later set forth in public periodicals [25] and tested on the probe objects (mono- and biperiodical domain structures in transparent magnetic films), where these objects and diffraction patterns created by them could be observed visually in the transmission mode and photographed [25, 26]. Using digitized images were obtained Fourier images for many flat geometric and algebraic fractals: the Sierpinski carpet,  $H$ -fractals, Peano curves, bifractals,  $L$ -system fractals, Mandelbrot sets [28, 32, 33-35].

In this article the study of the Fourier-images properties was made by numerical methods for the family of flat triadic geometric prefractals of generation with generator in the form of symmetrical relative to the middle four-stage broken line with an arbitrary angle  $0^\circ < \alpha < 180^\circ$  at the apex between the central units (**Fig. 1a**) and the initiator in the form of a straight line (Koch curve) or in the form of an equilateral triangle (the Koch snowflake); (see Fig. 1b). As an example, in Fig. 1c a view of second generation Koch prefractals is given. To preserve the self-similarity of prefractal by iterations all the segments of generator in a form of broken line must have the same length  $L/3^{N_s}$ . When  $\alpha \rightarrow 0^\circ$ , the broken line becomes delta-shaped, when  $\alpha \rightarrow 180^\circ$ , it merges with a initiator line; case  $\alpha = 60^\circ$  corresponds to the classical Koch curve.

An analysis showed that for  $\alpha = 180^\circ/k_\alpha$  or  $\gamma = 90^\circ - \alpha/2 = 180^\circ/k_\gamma$ , where  $k_\alpha$  and  $k_\gamma$  – any integer numbers, Fourier images are the same as for the perfect crystals with the symmetry axes of the 2-nd, 3-rd, 4-th and 6-th order, or as for parcuet mosaics [36] or quasicrystals [37] with

the axes of quasisymmetry of any order. Really among the Fourier images of the Koch curves with the initiator in the form of a straight line were observed axis of quasisymmetry from 3-rd to 9 th and 11-th order. High quality Fourier image with the axis of quasisymmetry of 10-th order failed to obtain; the reason for this will be discussed next. For integer values of  $k_\alpha$  only axes quasisymmetry of odd order exist (3-rd to 11-th inclusive), while for integer values of  $k_\gamma$  – any axis with the order in the range of 3 to 9. In **Fig. 2** Fourier images of 6-th generations Koch prefractals for  $\alpha = 36^\circ - (a)$ ,  $\alpha = 25.743^\circ - (b)$ ,  $\alpha = 20^\circ - (c)$ ,  $\alpha = 16.2637^\circ - (d)$  are shown.

**3. CONFIGURATION AND SYMMETRY OF THE FOURIER-IMAGES**

The configuration of the observed Fourier images can be approximately regarded as a radial-annular, and, as was first noted by the authors of [17] for a classic example of Koch snowflake, in the peripheral ("lattice") of the images the radial nature of the frequency distribution of diffraction reflects is dominated, and in the central ("fractal") – a ring nature with

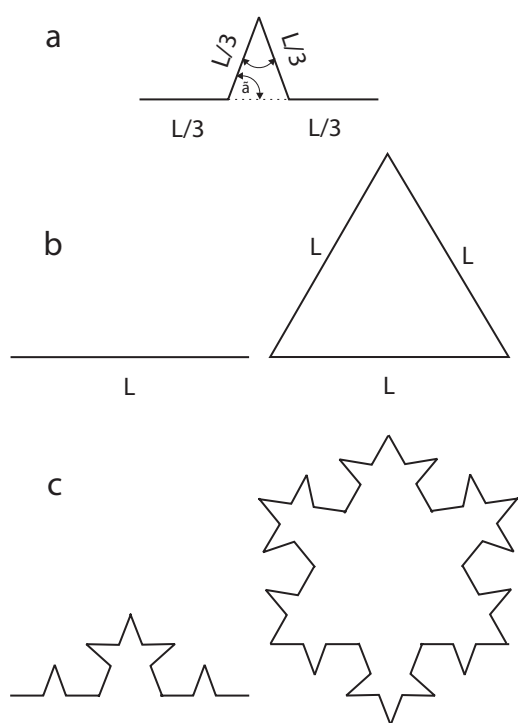


**Fig. 1.** Generator (a), initiators (b) and prefractals of the 2-nd generation for Koch curve and snowflake (c).

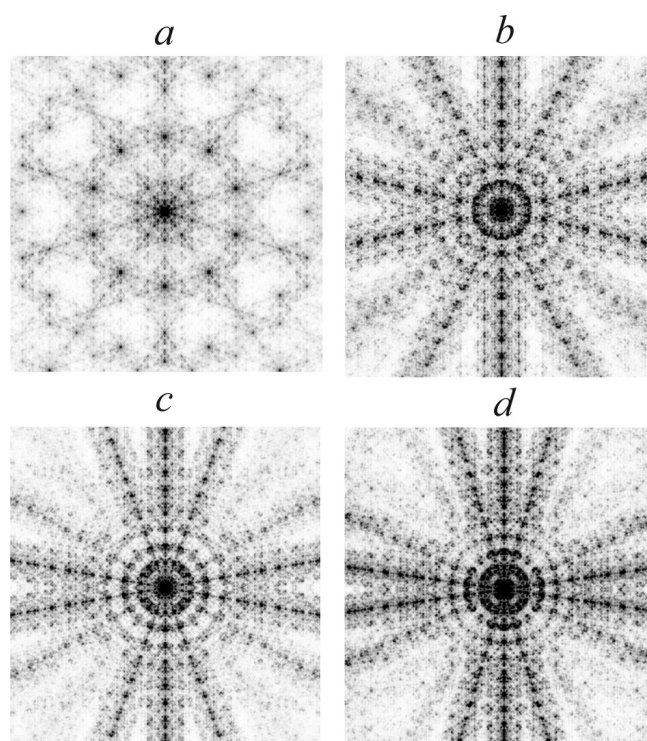


**Fig. 2.** Fourier images of Koch curve prefractals with quasisymmetry axis of 5-th (a), 7-th (b), 9-th (c) and 11-th (d) order.

self-similarity. It was found that the diameter of the central region after each iteration increasing in  $m$  times, where  $m = 2[1 + \sin(\alpha/2)]$  is the scale factor for the considered fractals.

The lattice part has a kind of clustering: all the rays have a strong central chain of reflexes along the radii and parallel to it the weaker satellites on both sides (see Fig. 2*b-d*). Similar features can be traced also in **Fig. 3**, where Fourier images for prefractal of the Koch curves of 6-th (*a*), 5-th (*b*) and 4-th (*c-d*) generations for the values  $k_\gamma = 3, 4, 6$  and 8 are shown.

All Fourier images had the center of symmetry, which is an integral attribute of the diffraction patterns in the Fraunhofer zone for all objects, including non-centrosymmetrical (see eg. [38]), however, the rotational symmetry was not perfect: when one rotates the image around the axis with order of  $k_\alpha$  for angles that are multiples of  $180^\circ/k_\alpha$ , only the positions of the diffraction reflexes coincide, but their intensity could vary. Part (Fig. 2*b*) or full (Fig. 2*c-d*) attenuation of the reflex intensities along some rays (similar to the extinction of the reciprocal lattice nodes in x-ray analysis [39]).

The cause of the observed features is that the objects under consideration, unlike crystals, are not a continuum of point objects (atoms), but a two-dimensional set of line segments with the same length  $L/3^{N_g}$ , but with different orientation in space.

In this set for the integer values of  $k_\alpha$  or  $k_\gamma$  one can select consisting of equally oriented line segments two-dimensional subsets, each of which contains a some number of partial one-dimensional diffraction gratings formed of located along the same line segments. In the general case these parallel lattices contain a different number of segments, and the degree of filling and the distance between adjacent segments, which determine the intensity and structure of the distribution of diffraction reflects along the line, depend on the orientation of the lattice and the generation number of prefractal  $N_g$ .

The presence in each of the two-dimensional subsets of equally oriented segments together several spaced relative to each other parallel one-dimensional lattices leads to a two-dimensional diffraction pattern with reflexes not only along the lattices, but on either side of them (the satellites in Fig. 2 and 4).

#### 4. SCHEME OF THE LATTICE AND FRACTAL PARTS OF THE FOURIER-IMAGES FORMATION

The scheme of formation of the lattice part explains shown in **Fig. 4** the example for Fourier image of 4-th generation prefractal with  $\alpha = 36^\circ$  having pentagonal quasisymmetry. The numbers 1-5 in the image of prefractal

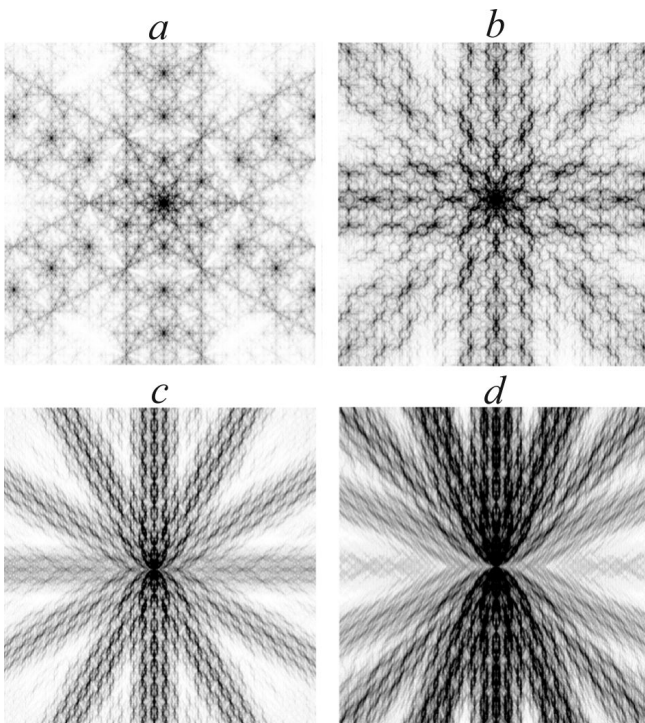


**Fig. 3.** Fourier images of Koch curve prefractals with quasisymmetry axis of 3-rd (*a*), 4-th (*b*), 6-th (*c*) and 8-th (*d*) order.

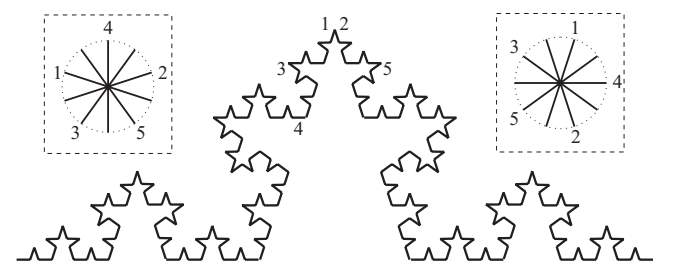


**Fig. 4.** The scheme of formation of the lattice part in Fourier image of 4-th generation Koch curve prefractal with  $\alpha = 36^\circ$  having pentagonal quasisymmetry.

marked 5 orientations of the segments; the inset on the right shows the possible directions of partial diffraction gratings, and the inset on left in the pull – direction of the rays (compare with Fig. 2). The number of partial lattices and the extent of their filling depends on the prefractal generation number. So, it follows from Fig. 4, that the number of partial sublattices in the subset with the direction of the segments of the 1-st type (see right inset) is 21, and three of them contain 6, 7 and 8 segments, two – 4 four – 3, four – 2, and eight – 1.

When  $\alpha = 180^\circ/k_\alpha$  or  $\gamma = 180^\circ/k_\gamma$ , where  $k_\alpha$  and  $k_\gamma$  are any integers, the number of possible orientations of the segments  $N_s$  in the prefractal is determined by the generation number of the latter  $g$ . When one initiates there are only three allowable orientations defined by the generator (Fig. 1a), each subsequent iteration adds two more.

In the case of even values of  $k_\alpha$  or  $k_\gamma$  on the step of the iteration, after which there are no segments with new orientations (i.e., when  $N_s = k_\alpha$  or  $k_\gamma$  is added only one line segment, oriented perpendicular to the initiator. In subsequent iterations, the new directions of the segments are already not formed.

It was found that for even values of  $k_\alpha$  there are  $2k_\alpha$  orientations of the line segments, and, accordingly,  $2k_\alpha$  rays in the lattice region of the Fourier image. For example, if  $\alpha = 22.5^\circ$  instead of 8 rays 16 is formed. We were not able to watch some of the rays due to a small population of the relevant partial sublattices even in prefractals of highest accessible (for technical reasons) generations. For the same reasons, attempts failed to get quality Fourier image with decagonal quasisymmetry.

Similar to the above-described properties are also inherent to Fourier images of the Koch snowflakes (with the initiator in the form of an equilateral triangle) shown in Fig. 5 for some prefractals of 6-th generation with  $\alpha = 120^\circ$  – (a),  $\alpha = 22.5^\circ$  – (b),  $\alpha = 30^\circ$  – (c), and  $\alpha = 12^\circ$

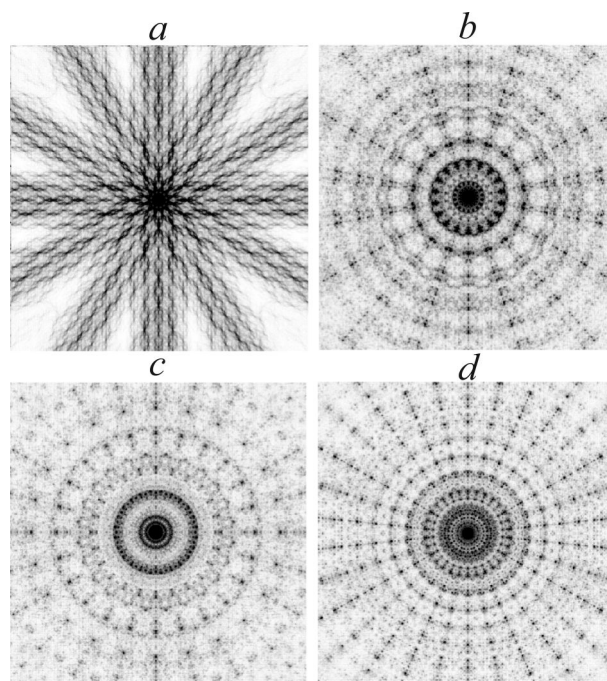


Fig. 5. Fourier images of Koch snowflakes prefractals with quasisymmetry axis of 6-th (a), 9-th (b), 12-th (c) and 15-th (d) order. – (d). Note that obtained in this case Fourier images are not a simple superposition of images from three sides of triangle initiator, as in the case of diffraction waves are summed taking into account phase difference between them.

As can be seen from Fig. 5, using triangle as initiator greatly enhances the filling of the partial sublattices and actually eliminates the difference in the intensity of diffraction spots in symmetry equivalent positions in all the rays of the lattice part of the Fourier image. In addition, in the Fourier images of the Koch snowflake one can more clearly trace the difference in structure of the central and peripheral parts. It is seen for example, that quasisymmetry of high orders manifests itself in the central part in a form of isolated spots, located on concentric circles.

Possessing self-similarity fractal part, the size of which enlarges with increasing angle (under rest equal conditions), is formed by the sum of the central diffraction maxima of all fractal elements. At  $L \rightarrow \infty$  and  $N_g \rightarrow \infty$  the lattice contribution to the Fourier transform of the image disappears, as, in the first, the distance between the forming the lattices line

segments tends to zero, and, in the second, the line segments transforms in the points, the diffraction pattern from which has radial symmetry.

## 6. SUMMARY

The above results convincingly show that the generalized triadic Koch prefractals of sufficiently high generations under certain conditions can have Fourier images with the axes of quasi-symmetry any order like parqued mosaics [36] or quasicrystals [37]. Currently, there are data on realization of the mosaics with the quasisymmetry axis of the 5-th, 8-th, 10-th and 12-th order; in addition to these quasicrystals can have an axis of quasisymmetry of 7-th order [40, 41]. Amazing is the fact that unlike mosaics and quasicrystals Koch curves are generally deprived rotary axes of symmetry, and the Koch snowflakes have the only axis of symmetry of the 3rd order.

However, it has been noticed long ago, that there exist some sibling connections among the fractals and parqued mosaics and also (discovered later) quasi-crystals; and in establishment of these connections, apparently, the decisive role played by self-similarity [40, 42]. And as the axioms are now perceived assertion that mosaics are two-dimensional analogs of quasicrystals, and to the last with any quasisymmetry can be put into correspondence associated fractal structures [43, 44]. Methods of fractal geometry are now used to describe models of quasi-crystalline structures, and tree-graph procedure – to originate them [44, 45].

From the point of view of abstract algebra aperiodic structures (quasi-crystals and mosaic), in contrast to describing by groups ideal crystals, are described by algebraic systems of "field" type, which may have a rotational symmetry and fractal ordering [46]. To describe geometric fractals, one can use the algorithms of so-called  $L$ -systems [47].

## REFERENCES

1. Mandelbrot BB. *The fractal geometry of nature*. San Francisco, Freeman, 1983, 497 p.
2. Olemskoi AI, Flat AY. *UFN*, 1993, 163(12):1-50 (in Russ.).
3. Gouyet J-F. *Physics and fractal structures*. Paris, Ecole Polytechnique, 1995, 234 p.
4. Peitgen HO, Jürgens H, Saupe D. *Chaos and fractals. New frontiers of science*. New York, Springer-Verlag, 2004, 864 p.
5. Levy-Vehel J, Lutton E. *Fractals in Engineering*. London, Springer-Verlag, 2005, 290 p.
6. Potapov AA. *Fractaly v radiofizike i radiolokatsii* [Fractals in Radiophysics and Radiolocation]. Moscow, Logos Publ., 2002, 847 p.
7. *Fractals in Biology and Medicine: vol. IV* (Mathematics and Biosciences in Interaction). Ed. by Losa GA, Merlini D, Nonnenmacher TF, Weibel ER. Basel, Birkhäuser, 2005, 314 p.
8. Hudson RL, Mandelbrot BB. *The (mis)Behavior of Markets: A Fractal View of Risk, Ruin, and Reward*. New York, Basic Book, 2004, 328 p.
9. Almazov AA. *Fractal'naya teoriya. Kak pomenyat' vzglyad na finansovye rynki* [Fractal theory. How to change the view on the financial markets]. Moscow, Admiral Markets, 2009, 209 p.
10. Madden Ch. *Fractals in Music: Introductory Mathematics for Musical Analysis*. Salt Lake City, High Art Press, 1999, 224 p.
11. Bonch-Osmolovskaya TB. *Vvedenie v literaturu formal'nyh ogranicheniy* [An introduction to the literature of formal restrictions]. Samara, Bahrakh-M, 2009, 560 p.
12. Tarasenko VV. *Fractal'naya semiotika. Slepые pyatna, peripetii i uznnavaniya* [Fractal semiotics. Blind spots, the vicissitudes and recognitions]. Moscow, Librokom, 2009, 232 p.
13. Isaeva VV, Kas'yanov NV. *Vestnik DVO RAS*, 2006, 5:119-127 (in Russ.).
14. Shlyk VA. *Izv. Chebyshevskogo nauchnogo tsentra UrO RAS*, 2004, 1(22):231-244 (in Russ.).

15. *Classification and Application of Fractals: New Research*. Ed. by Mitchell EW, Murray SR. New York, October Nova, 2012, 347 p.
16. Alain C, Cloitre M. *Phys. Rev. B*, 1986, 33(5):3566-3569.
17. Uozumi J, Kimura H, Asakura T. *J. Mod. Optics*, 1990, 37(6):1011-1031.
18. Sakurada Y, Uozumi J, Asakura T. *Opt. rev.*, 1994, 1(1):3-7.
19. Uozumi J, Kimura H, Asakura T. *J. Mod. Optics*, 1991, 38(7):1335-1347.
20. Sakurada Y., Uozumi J., Asakura T. *J. Optics. A: Pure Appl. Optics*, 1992, 1:29-40.
21. Chabassier G, Angéli B, Heliodore F, Le Mehauté AS. *J. Optics. A: Pure Appl. Optics*, 1992, 1:41-54.
22. Bo Hou, Gu Xu, Wen W, Wong GK L. *Appl. Phys. Lett.*, 2004, 85(25):6125-6127.
23. Funamizu H., Uozumi J. *J. Opt. Soc. of Amer.: Opt. Express*, 2007, 15(12):7415-7422.
24. Horváth P, Šmid P, Vášková I, Hrabovský M. *Optik*, 2010, 121(2):206-213.
25. Arzamastseva GV, Evtikhov MG, Lisovsky FV, Mansvetova EG, Temiryazeva MP. *ZhETP*, 2008, 134(2):282-290 (in Russ.).
26. Arzamastseva GV, Evtikhov MG, Lisovsky FV, Mansvetova EG. *ZhETP*, 2011, 140(3):516-526 (in Russ.).
27. Peitgen HO, Richter PH. *Beauty of Fractals: Images of Complex Dynamical Systems*. Springer-Verlag, Berlin-Heidelberg, 1986, 199 p.
28. Arzamastseva GV, Evtikhov MG, Lisovsky FV, Mansvetova EG. *Izv. RAS, Ser. fiz.*, 2010, 74(10):1430-1432 (in Russ.).
29. Arzamastseva GV, Evtikhov MG, Lisovsky FV, Lukashenko LI. *Trudy XIX Mezhdunarodnoi shkoly-seminara "Novye magnitnye materialy microelectroniki"* [Proc. of the XX Intern. School-Seminar "New magnetic materials of microelectronics"], Moscow, 2004, p. 632-634 (in Russ.).
30. Dikshtein IE, Kuznetsov DV, Lisovsky FV, Mansvetova EG. *Trudy XVI Mezhdunarodnoi shkoly-seminara "Novye magnitnye materialy microelectroniki"* [Proc. of the XX Intern. School-Seminar "New magnetic materials of microelectronics"], p. II, Moscow, 1998:519 (in Russ.).
31. Lisovsky FV, Mansvetova EG, Lukashenko LI. *Trudy XVI Mezhdunarodnoi shkoly-seminara "Novye magnitnye materialy microelectroniki"* [Proc. of the XX Intern. School-Seminar "New magnetic materials of microelectronics"], Moscow, 2004, p. 838-840 (in Russ.).
32. Lisovsky FV., Lukashenko LI., Mansvetova EG. *Pis'ma v ZhETP*, 2004, 79(7):432-435 (in Russ.).
33. Arzamastseva GV., Evtikhov MG, Lisovsky FV, Mansvetova EG. *Electromagnitnye volny i elektronnye sistemy*, 2012, 17(12):29-32 (in Russ.).
34. Arzamastseva GV, Evtikhov MG, Lisovsky FV, Mansvetova EG. *Electromagnitnye volny i elektronnye sistemy*, 2012, 17(7):48-58 (in Russ.).
35. Arzamastseva GV, Evtikhov MG, Lisovsky FV, Mansvetova EG. *Radioelektronika. Nanosistemy. Informatsionnye tekhnologii (RENSIT)*, 2012, 4(2):93-107 (in Russ.).
36. Penrose R. *Eureka* (Cambridge), 1978, 39:16-22.
37. Shechtman D, Blech LA, Gratias D, Cahn JW. *Phys. Rev. Lett.*, 1984, 53(20):1951-1953.
38. Geht E. *UFN*, 1973, 111(2):355-364 (in Russ.).
39. Umansky YS, Skakov UA, Ivanov AM, Rastorguev LN. *Kristallografiya, rentgenografiya i elektronnaya mikroskopiya* [Crystallography, X-ray and electron microscopy], Moscow, Metallurgiya, 1982, 632 p.
40. Suck J-B, Schreiber M, Haussler P. *Quasicrystals: an introduction to structure, physical properties, and applications*. Springer Verlag, Berlin-Heidelberg, 2010, 564 p.
41. Milman YuV, Efimov NA, Goncharova IV. *Sborn. Nauchn. Trud. Inst. Probl. Materialoved. NAN Ukrainy*, 2012, 18:3-14 (in Russ.).
42. Gardner M. *Penrose Tiles to Trapdoor Ciphers*. Freeman, New York, 1989, 416 p.
43. Lazarev AI, Domrachev GA. *Kristallografiya*, 1994, 39(5):811-844 (in Russ.).

44. Yudin VV, Karygina UA. *Kristallografiya*, 2001, 46(6):1004-1008 (in Russ.).
45. Lazarev AI., Suhanov AU, Domrachev GA. *Kristallografiya*, 1996, 41(5):798-803 (in Russ.).
46. Domrachev GA, Lazarev AI. *Fiz.tverdogo tela*, 1999, 41(5):799 804 (in Russ.).
47. Lindenmayer A. *J. Theor. Biology*, 1968, 18:280315.

## EVOLUTIONARY ASPECTS OF THE GEL APPEARANCE AND ITS FUNCTIONS IN THE CELL CYTOPLASM

**Alexander R. Zaritsky, Galina V. Zaytseva, Marina N. Kirichenko**

Lebedev Fizichesky Institute, Russian Academy of Sciences, <http://www.lebedev.ru>

119991 Moscow, Russian Federation

[zaritsky@sci.lebedev.ru](mailto:zaritsky@sci.lebedev.ru), [zaytseva-gv@yandex.ru](mailto:zaytseva-gv@yandex.ru), [maslova\\_marina@mail.ru](mailto:maslova_marina@mail.ru)

**Vladimir I. Grachev**

Kotelnikov Institute of Radio Engineering and Electronics, Russian Academy of Sciences, <http://www.cplire.ru>

125009 Moscow, Russian Federation

[grachev@cplire.ru](mailto:grachev@cplire.ru)

*Abstract.* In this paper we consider a well-known phenomenon in the life and the evolutionary development of animal cells - the presence in their cytoplasm gel. Described the evolution of the gel appearance with the dynamics of sol-gel phase transitions. Substantiated the main function of the gel in the cytoplasm - providing intensification of the energy metabolism of cells. Shown the role of the gel in the infrastructure of the cell and its compartments, the relationship of the gel and the cytoskeleton, promoting transmembrane exchange of cell with the environment. Shown the role of gel channels in the logistics of water flows and active substances in the cytoplasm, in the regulation of metabolic mechanisms, in particular, in the regulation of the cytoplasm dehydration modes - of sporulation in unicellular organisms and of the drying of human dermal cover in the norm and in various pathologies.

*Keywords:* cytoplasm, sol, gel, structured water, energy metabolism, cytoskeleton, gel channels, waterways, dehydration mechanisms

PACS: 87.32.Kg

*Bibliography* – 34 references

Received 16.11.2016

*RENSIT*, 2016, 8(2):215-222

DOI: 10.17725/[rensit.2016.08.215](http://rensit.2016.08.215)

### CONTENTS

1. INTRODUCTION (215)
  2. EVOLUTIONARY ASPECTS OF THE APPEARANCE OF THE GEL IN THE CYTOPLASM OF CELLS (217)
  3. EVOLUTION INTENSIFICATION GEL ENERGY METABOLISM OF CELLS (218)
  4. THE ROLE OF THE CYTOSKELETON IN THE EVOLUTION OF THE GEL (219)
  5. GEL TRANSPORT STRUCTURES IN THE CYTOPLASM (219)
  6. GEL LIKE CYTOPLASM DEHYDRATION MEANS (220)
  7. CONCLUSION (221)
- REFERENCES (221)

### 1. INTRODUCTION

The internal environment of a living cell - the protoplasm is the subject of intense research today cytophysiology. Another associate of Charles Darwin, Thomas H. Huxley half a

century ago called the protoplasm of the physical basis of life [1]. American cytologist Lewis V. Heilbrunn [2] argued that "if we are able to decipher the mysteries of life and functioning mechanisms, it is only through the study of protoplasm." Extra-nuclear part of the protoplasm – the cytoplasm of the cell and its liquid fraction (without organelles, organelles and metabolites) – cytosol studied so far is not enough [3-5]. The use of nonlinear analysis methods, new spectroscopic, NMR and other techniques and modern computer analysis allow you to implement both quantitative and more qualitative approaches to their problems. It is now known that the cytosol – divided into several compartments, compartments various membranes sol proteins, enzymes, carbohydrates, lipids, low molecular weight (less than 300 Da and 1 nm [6]) of the compounds and inorganic salts in water, with pH 7.0 to 7.4 [7], (= 139/4 mM,

$Na^+_{in}/Na^+_{ex} = 12/145$  mM, etc. [3]  $K^+_{in}/K^+_{ex}$ ) to the asymmetry in the distribution of ions outside the cell cytosol and, metabolites concentration with nonproteinaceous molecules such that their diffusion rate due to collisions is 4 times lower than in pure water [8]. The mechanism of formation of gradients of concentrations and is poorly understood. [9] The structure also includes the cytosol ribosomes - nucleoproteins, synthesizing proteins.

Cytosolic proteins occupy up to 30% of its volume [10], 10 up protein molecules milliardov about 10 to thousands of different cell types [11]. They are in a state of continuous processes of synthesis and decomposition. Free globular proteins and fibrous tape forming colloidal solutions in water, which occupies 70% of the cytosol [12]. At high concentrations of the cytosolic macromolecules water is in a bound state to macromolecules [13, 14]. When this sol may be either non-viscous sol, or viscous, jelly-like gel.

Sol (from the Latin solutio – the solution) – highly dispersed colloidal solution with a liquid dispersion medium in which the volume distributed dispersed phase of organic compounds and ions – Brownian particle size of  $10^{-7}$ - $10^{-9}$  m [3], not related to the spatial structure. When this cell is in the active state. In coagulation, aggregation particulate sol phase transition occurs in the sol gel.

Gel (from the Latin gelo – jell) – structured system of three-dimensional macromolecular grid (skeleton), filled with a low-molecular solvent – dispersion medium, in a cell – water. In the works of Gilbert N. Ling [13] and Gerald H. Pollack [14] showed that in the compartments of the cytoplasm in the adsorption of the active protein (eg, myosin in muscle fibers) ATP, ions and salt monomer actin protein due torn, folded his secondary structure unfolds in oriented parallel to the chain whose carboxyl group adsorb  $K^+$  and polar amino groups and  $NH-CO$ -carbonyl groups of the peptide backbone is already polnorazvernutoyo protein adsorbed layer by

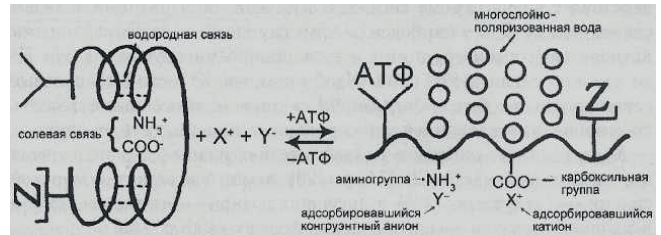


Fig. 1. Scheme of phase transitions sol-gel [13].

layer-oriented and polarized (with a larger dipole moment) water – gel, ie related and structured non-solvent water on nonglobular linear protein (Fig. 1). The multilayer structure of aqueous gel is dynamic, its molecules are constantly moving, changing places, but all movement in her limited interaction between them is stronger than in ordinary water, the structure as a whole is stable and does not mix with the free cells with water, which is virtually non-existent, because . almost all of the water cells included in ordered layers of protein-ion-water complex. When this cell is in a resting state.

High-energy, low-entropy gel thermodynamically unstable: ATP hydrolysis leads to a redistribution of the electron density in the protein molecule, its conformation changes, its amino acid groups are not available water, structural mesh spontaneously breaks down with the release of the liquid phase, the recovered salt due curtail basic protein band in the globule – Gel enters sol liquid colloidal solution.

Colloidal solution of cell proteins is in permanent phase transitions sol-gel – the sol-gel [15] due to the energy of ATP synthesized in the cytosol and in cell ribosomes. These transitions – nonlinear vibration with the ever-changing, varying period. the frequency range or the rhythms of these phase transitions (aggregation rhythms) – from 10-10 sec to-second, minute, okolochasovyh etc. up to seasonal and annual. These transitions are caused by various factors - kosmogeliogeofizicheskimi, rhythm matching between adjacent compartments, a change in pH and salt water mode, etc., and provide dynamic processes and metabolic adaptation all vital cell cycles.

Despite intensive research over the last time water and aqueous colloids of a living cell (see, eg., [16-20] and many others), the evolutionary aspect of these studies is left without attention. In this paper, this aspect is the main subject of study.

## 2. EVOLUTIONARY ASPECTS APPEARANCE GEL IN THE CYTOPLASM OF CELLS

At the final stage of abiogenesis (probable variant), the transition of the first in the world of sustainable separate free energy sources – hydrocarbon nanodroplets aerosol open metabolism and emerging abiogenic organics from planetary autoclave anoxic subsurface air into the aquatic environment of the primary hydrosphere, the cooling of the planet, - lipids and archaic enzymes drops formed from the surface on a turbulent interface between air and water and lipid vesicles (lat vesicula - a vial) containing an aqueous solution of carbon-containing compounds, archaic enzymes, viruses and ribonucleotides with traditional hydrocarbon droplets anaerobic metabolism mechanisms [21, 22]. Anaerobic digestion of glucose polymer glycogen and its aqueous environment of sufficient energy basis turned metabolic activity of vesicles until mitosis. In [23-25] identified a physical factor leading molecular mechanisms of activity and modes of mitosis - change the acidity of the internal environment of the vesicle, which determines the order change processes and phenomena in the fission of the vesicle and change their metabolism modes. The maximum possible capacity of the metabolic processes of groups competing for macroergs in vesicles was achieved in breeding of these groups over time by natural acidification of the internal environment in the synthesis macroergs and forced her alkalization at their disposal. Cyclical vesicles metabolic enzyme selection modes formed by synthesizing catalysis activity higher values in pH, than recycling macroergs catalysis. At a sufficiently high concentration

of peptides and ATP polypeptide structures with low molecular weight fraction ions in vesicles resulting volume pino- phagocytosis and from the external environment and the internal environment in the synthesis of the aqueous solution content in the colloid vesicles was structured with the dynamics of the sol-gel transition. Cyclical vesicles metabolism mode determines the rhythm of these transitions. The liquid crystal gel phase - a universal acceptor osmotic and mechanical, electromagnetic and gravitational fluctuations, which has retained its fundamental role in the evolution and after the emergence of specialized receptor proteins or other receptor structures.

The natural conclusion of this development was the emergence of the first simple cells, anaerobes, and bezhromosomnyh bezyadernyh prokaryotes capable of reproduction [25, 26]. The gradual accumulation of oxygen in the atmosphere to ensure the formation and development in some of the vesicles and anaerobic metabolism of prokaryotes-based photosynthesis, ie aerobic metabolism, which gave rise to the development of the simplest prokaryotes-aerobic. At the time of reaching a partial pressure of oxygen atmosphere at 2 mmHg (Judging by the homeostasis of oxygen levels in the cytoplasm of the modern animal cells) and accumulation of oxygen in the hydrosphere vesicles and archaic prokaryotes with a complex metabolism, including photosynthesis and recycling of energy-intensive substrates anaerobically and aerobically, ousted virtually all other vesicles and have launched the formation and development of eukaryotic (gr . karyon - nucleus) cells [25].

Colloidal structure of compartments of eukaryotes, as well as prokaryotes, optimized whole cell metabolism kinetics of phase transitions through the sol-gel, generating energy in a wide range of the spectrum of electromagnetic and acoustic waves [27-29], very weak intensity of which was seen on the background thermal noise [30, 31, ] – the most

evolutionarily ancient, apparently, the process of information interaction of biosystems. Address information transmission methods have arisen in the course of evolution only in multicellular organisms. Gel one cell compartments can absorb energy signals generated by the sol gel transition neighbor cell compartments, thus passing into the sol. Superweak interactions that determine these processes are currently the subject of intensive research [32]. Phase transitions of the first and second kind are determined by the degree of synchronization of rhythms sol-gel transitions between adjacent cell compartments and matching rhythms of different periods. The study of these rhythms contributes to the formation of modern concepts of fundamental biological problems time and time in general.

Thus the appearance of the gel in the course of evolution in the cytosol was the decisive factor in the optimization of all metabolic processes in the emerging cellular structures.

### 3. EVOLUTION OF IMPROVED ENERGY GEL CELL METABOLISM

The presence and growth of an electric field in the cytoplasmic membrane during evolutionary changes in the cells ensure a steady increase in concentration of the active compounds [33] and, as a consequence, increase the intensity of energy metabolism. Another equally important factor, which used nature for the same purpose, became gel.

In paragraph 2 has been considered a possible variant of the natural appearance of the gel in the internal environment protocellular structures and biological feasibility of its operation in their processes of life, manifesting itself in the optimization of all processes of cell metabolism. Considering the energy metabolism of the leading type of cell metabolism and intensifying its steadfast – the general line of the evolutionary development of the cellular world to the very beginning of its origin, we consider the evolutionary aspects of participation in the process of protein-ion-water complex cells, it

cytosol, existing in a mode of continuous phase transition sol gel – a sol-gel.

If in the initial stages of nucleation protocellular structures in the first lipid vesicles "primeval soup" did not exist a sufficient set of compounds and elements for the organization of an aqueous colloidal solution of necessary concentration, metabolism, which would allow to make stocks of energy-intensive components, then with the emergence of aerobic vesicles and archaic protokariotov sufficient size with the development of metabolic mechanisms of the processes of accumulation of energy reserves can imagine quite likely. In the cell there was a constant factor increase metabolism - gel. Because cytosol in substantially dehydrated gel state, the percentage of free water in the ash is minimized. Accordingly, it is maximal in the concentration of globular proteins that do not participate in the formation of the gel. Their shape structure prevents water on the size level of individual amino acids to the same extent that neglobulyarnye proteins. Because of the presence on the surface of the globules of hydrophobic regions these proteins have a low affinity for the gel has formed. These sol globular proteins directly involved in cellular metabolism. However, their concentration, molecular weight and metabolic rate increases significantly, as an inevitable consequence cytosol separation into two phases - the sol and gel. Increased metabolism in turn leads to the emergence of a chain of causality: the growth of the concentration of ATP in the ash, the acceleration of the work  $K^+/Na^+$  ATP-ase, enhancement of the electric field in the cytoplasmic membrane, causing asymmetry permeability of lipid membranes dipole compounds and, as a consequence, an increase in water flows from the cells (Charakhch'yan effect [33]). These flows are offset by increases in osmotic flows into the cytoplasm resulting increase in the concentration of osmotic sol particles in the gel during formation.

Thus, the growth of the hydrocarbon supply and the development of metabolic mechanisms

of energetic compounds led to the division in the evolution of the cell cytosol to the sol and gel, which, in turn, "reciprocity" has provided steady growth of the intensification of the energy metabolism of cells, ie, follow the general line of the evolutionary development of the cellular world

#### **4. ROLE IN THE EVOLUTION OF GEL CYTOSKELETON**

One of the direct consequences of the intensification of gel activation of intracellular metabolism yavyalyaetsya they form the cytoskeleton elements in the membrane region protocellular formations. Evolutionary chain, in this case can be constructed as follows. The vesicles of the first and prokaryotes supramolecular synthesis is quite likely, broaching polymeric structures consisting of a single type of polypeptide monomers which are already bind water and form, thereby a gel. It is likely also synthesis in the cytoplasm of the primary structures of actin and tubulinopodobnyh protofilaments of amino acids. The sol gelation phase collects the remaining structure under the membrane over its entire area in the chain of the archaic cytoskeletal microfilaments and microtubules, with weak non-covalent bonds of their structural units. Such protein-aqueous matrix ion-dynamically unstable with different effects on cell continuously rearranged in its polymerization-depolymerization threads which are collected from the respective molecules and re-parsed into individual molecules. Polymerization and stabilize the cytoskeleton in the ash provide a gel membrane. Cytoskeletal structure distanced from the lipid membrane protein by bridges, which are connected with both-ankerinami proteins embedded in lipids and proteins with neglobulyarnymi constituting the base gel. Therefore, the gel formed on the cytoskeleton, does not prevent the exchange of cells with transmembrane surrounding aqueous medium or substrates of cell metabolism or water molecules.

In eukaryotes, the presence of organelles and cell volume compartmentation, in cytoskeleton network it appears the third element - intermediate filaments composed of specific polypeptides. Actin and tubulin eukaryotic interact with a large number of regulatory, support, and other motor proteins. It actin is a "champion" among eukaryotic proteins in the number of partner proteins [3]. The intensity of metabolism of the actin-myosin, tubulin and aktinsvyazyvyayuschih proteins provided by the rhythm of the phase transitions of the sol-gel – a gel-sol. The forces acting between the proteins of the cytoskeleton and the liquid phase of the gel cell cytoplasm – the van der Waals forces, hydrophobic interactions, hydrogen bonds, the Coulomb interaction between portions of the charged protein networks and the surrounding ions in an orderly arrangement of components of the cell, forming the cell cytoskeleton that supports it the form and all forms of mobility, transporting motor proteins its organelles involved in receptor function and it significantly increases the resistance of cells to the damaging effects on them of shear flows in the aquatic environment.

#### **5. GEL TRANSPORT STRUCTURES IN THE CYTOPLASM**

Known feature of the cytoplasm of eukaryotic cells – continuous intracellular movement (cyclosis) tumors and decay processes of various substances, microstructures ripple, constantly reaching rhythms sol-gel transition, even in the stationary states the lack of functional activity, ie, in resting cells. Transport of substances in the cytoplasm is realized, as is well known, through the endoplasmic reticulum – a system of long branching tubules penetrating the cytoplasm; continuous cavities which move substances promoting the flow of various processes in different cell compartments. Involved in the cytoskeleton, and transport through its tubulin microtubule hydrophobic molecules provide transfer between separate intracellular

compartments via motor proteins and carrier proteins [34].

However, to explain the targeting of substances within cells, harmonization of metabolism cycles, meeting the enzyme-substrate, etc. these paths together with the simple diffusion and Brownian motion of water-soluble molecules is impossible. Such transport efficiently, with minimal losses, carried out special channels formed gel structure [13, 14, 16], filled with sol, which move metabolites. **Fig. 2** from the GH.Pollack book [16] schematically shows the channel in a helium mass obtained in the experiment of T.Hirai [17]. The channel is surrounded by a layer of structured water in a liquid crystal state (4th phase of Pollack), moves inside the channel with microspheres sol containing metabolites. Such channels will eventually provide the cells in an efficient transfer of water flows of biologically active substances from the places of their synthesis in a remote area of the cytoplasm, where they are most productive to carry out their functions.

## 6. GEL AS A MEANS OF DEHYDRATION CYTOPLASM

Special channels formed gel structure, work on the basis of imbalance of water flows out of the cell to the outside and vice versa, from outside the cell in some areas cytomembranes, sometimes quite distant from each other. Intensification of metabolic cells associated with the synthesis of compounds in the membrane region can locally increase the osmolarity of the aqueous medium in these areas and disrupt the

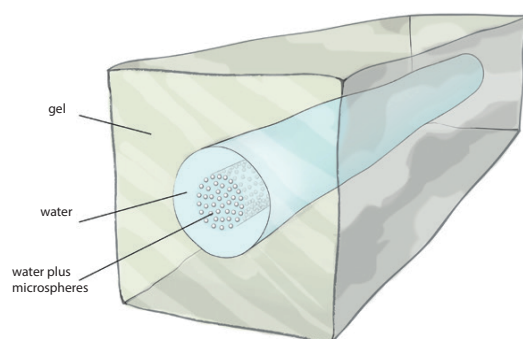


**Рис. 2.** Гелиевый канал в цитоплазме клетки (схема) [16].

balance of water flows through the membrane to the dominance of members of the cell flows. On the other hand, the flow of water balance displacement can be caused by a change of the electric field on the lipid membrane of its individual areas causing asymmetry membrane permeability dipolar compounds and primarily – water (Charakhch'yan effect [33]). With the weakening of the field (for example, in association with the membrane of large organic molecules) will prevail in the incoming cell stream. In other areas of the membrane free of associates, there may be a reverse situation. Here, the electric field intensity in the lipids is much higher than in areas with associated membranes larger particles. In this case the water flow will prevail outside of the cell. As a consequence, it is possible to realize conditions where in some areas of the membrane water "pumped" into the cytoplasm, and in other areas, sometimes quite remote from the first, water, on the contrary, "pumped" from the cytoplasm. It allows the use of the phenomenon of gel structure to form the transport channels for water flow [16, 34].

having cytoplasmic dewatering mechanisms on the basis of the above-mentioned effects. Formation mode of sporulation, which is based on this effect, provided a single-celled organisms survival in periods of drought. Multicellular plants use this effect in the formation of seeds and embryos. Dewatering effect gel filling and skin cells and their subsequent drying and peeling takes place during the formation of silver as a layer of human skin is normal, and in the development of pathologies such as psoriasis and eczema.

## 7. CONCLUSION

This paper considers the option appears in the oxygen-free separation step abiogenesis "cytosol" First protocellular formations – lipid vesicles in the primary hydrosphere of the planet into two phases – the sol and gel. This division was a decisive factor in the optimization of all metabolic processes in the emerging cellular structures. The formation mechanisms

involving the sol-gel structures of evolutionary transformations, which provided the cells following the general line of the evolutionary development of living systems, namely a steadfast intensification of energy metabolism. Identified the principles and beneficial consequences of the actions of such mechanisms. The role of the gel in the formation and functioning of the cytoskeleton, as well as in the formation of optimal structures of metabolite transport. Possible future use of the gel structure to temporarily stop cell metabolism (in the cytoplasm dehydration modes) under conditions unfavorable for their livelihoods.

The analysis covers a huge period of time - by visiting protocellular formation of the first structures of the gel and up to the evolutionary development of prokaryotes and eukaryotes. This analysis is to a certain degree is more schematic and staging character, but this does not diminish its importance. The main result appears to identify the primary function of early evolutionary structure of the gel – optimizing and intensification of the energy metabolism of the cell.

## REFERENCE

- Huxley TH. On the Physical Basis of Life. *Fortnightly Review*, 1869, 5:129.
- Heilbrunn LV. *The dynamics of living protoplasm*. New York, Academic Press, 1956, 336 p.
- Attwood TK, Campbell PN, Parish JH, Smith AD, Stirling JL, Vella F, Cammack R (eds). *Oxford dictionary of biochemistry and molecular biology*. Oxford, UK, Oxford University Press, 2006, 736 p.
- Alberts B, Bray D, Lewis J, Raff M, Roberts K, Watson JD. *Molecular Biology of the Cell. Vol. 2*. NY-London, Garland Publ., 1989, 541 p.
- Lyuin B, Cassimeris L, Lingappa VR, Plopper G. (eds). *Cells*. Sudbury, Jones&Bartlett Publ., 2007, 951 p.
- Goodacre R, Vaidyanathan S, Dunn WB, Harrigan GG, Kell DB. Metabolomics by numbers: acquiring and understanding global metabolite data. *Trends in biotechnology*, 2004, 22(5):245-252.
- Bright GR, Fisher GW, Rogowska J, Taylor DL. Fluorescence ratio imaging microscopy: temporal and spatial measurements of cytoplasmic pH. *The Journal of cell biology*, 1987, 104(4):1019-1033.
- Verkman AS. Solute and macromolecule diffusion in cellular aqueous compartments. *Trends in biochemical sciences*, 2002, 27(1):27-33.
- Weiss JN, Korge P. The cytoplasm: no longer a well-mixed bag. *Circulation research*, 2001, 89(2):108-110.
- Ellis RJ. Macromolecular crowding: obvious but underappreciated. *Trends in biochemical sciences*, 2001, 26(10):597-604.
- Luby-Phelps K. Cytoarchitecture and physical properties of cytoplasm: volume, viscosity, diffusion, intracellular surface area. *International review of cytology*, 2000, 192:189-221.
- Persson E, Halle B. Cell water dynamics on multiple time scales. *Proceedings of the National Academy of Sciences of the United States of America*, 2008, 105(17):6266-6271.
- Ling GN. *Life at the Cell and Below-Cell Level: the Hidden History of a Fundamental Revolution in Biology*. New York, Pacific Press, 2001, 373 p.
- Pollack GH. *Cells, Gels and Motors Life. The New Unifying Approach to Cell Function*. Ekaterinburg, Tokmas-Press, 2009, 386 p.
- Zaguskin SL, Nikitenko AA, Ovchinnikov SA, Prokhorov AM, Savranskii VV, Degtyarev VP, Platonov VI. About period range microstructures of living cells hesitation. *Dokl. Academy of Sciences of the USSR*, 1984, 277 (6):1468-1471.
- Pollack GH. *The Fourth Phase of Water: Beyond Solid, Liquid, and Vapor*. Seattle, Ebner & Sons Publ., 2013.
- Suzuki D, Kobayashi T, Yoshida R, Hirai T. Soft actuators of organized self-oscillating microgels. *Soft Matter*, 2012, 8(45):11447-11449, DOI: 10.1039/C2SM26477C.
- Giudice E, Del, Tedeschi A, Vitiello G, Voeikov V. Coherent structures in liquid water close to hydrophilic surfaces. *Journal of Physics: Conference Series*, 2013, 442(012028):1-5.
- Voeikov VL. Active oxygen, water, and organized processes of life. *Proc. II Intern. Congress "Low and super-low fields and radiations in biology and medicine"* Saint-Petersburg, Tuscarora, 2000, p. 1-4.
- Pershin SM, Bunkin AF. Observation of temperature evolution of relative concentration

- ortho/para spin-isomers H<sub>2</sub>O by four-photon spectroscopy. *Laser Physics*, 2009, 19(7):1-5.
21. Zaritskii AR, Grachev VI, Vorontsov YuP, Pronin VS. Energeticheskie aspekty abiogeneza v atmosfere na nanokaplyakh uglevodorodnogo aerolya [Energy aspects of abiogenesis in the atmosphere on hydrocarbon aerosol nanodroplets]. *Radioelektronika. Nanosistemy. Informatsionnye tekhnologii (RENSIT)*, 2013, 5(2):105-125 (in Russ.).
  22. Zaritskii AR, Grachev VI, Vorontsov YuP, Pronin VS. Abiogenez na etape perekhoda iz atmosfery v vodnyu sredu: ot vesikul k protokletkam [Abiogenesis transition from the atmosphere into the hydrosphere: from vesicles to protocells]. *Radioelektronika. Nanosistemy. Informatsionnye tekhnologii (RENSIT)*, 2014, 6(2):221-231; DOI: 10.17725/RENSITe.0006.201412f.0221 (in Russ.).
  23. Zaritskii AR, Pronin VS. Biophysics major modes of cellular metabolism. Functional cell modes: a state of rest and activity. *Bulletin of the Lebedev Physics Institute*, 2006, 12:8-18.
  24. Zaritskii AR, Pronin VS. Biophysics major modes of cellular metabolism: mode of cell division (mitosis). *Bulletin of the Lebedev Physics Institute*, 2006, 12:19-27.
  25. Zaritskii AR, Grachev VI, Vorontsov YuP, Kirichenko MN, Pronin VS. Anaerobny etap evolyutsionnogo razvitiya zhitnoy kletki [Anaerobic stage of the evolutionary development of animal cell]. *Radioelektronika. Nanosistemy. Informatsionnye tekhnologii (RENSIT)*, 2015, 7(1):87-99; DOI: 10.17725/RENSITe.2015.07.087 (in Russ.).
  26. Doolittle WF, Zhaxybayeva O. On the Origin of Prokaryotic Species. *Genome Res.*, 2009, 19:744-756.
  27. Lipeschkin WW. My opinion about protoplasm. *Protoplasma*, 1930, 9:269.
  28. Gurvich AG. *Problema mitogeneticheskogo izlucheniya kak aspekt molekulyarnoy biologii* [The problem mitogenetic radiation as an aspect of molecular biology]. Leningrad, Medicine Publ., 1968, 240 p.
  29. Kaznacheev VP, Mikhailova LP. *Sverkhslabye izlucheniya v mezhkletochnykh vzaimodeystviyakh* [Superlow radiations in cell-cell interactions]. Novosibirsk, Nauka Publ., 1981, 144 p.
  30. Burlakov AB, Burlakova OV, Golichenkov VA. Distantionnye vzaimodeystviya raznovozrastnykh embrionov v'yuna [Distant interaction uneven loach embryos]. *DAN*, 1999, 368(4):562-564.
  31. Burlakov AB, Burlakova OV, Golichenkov VA. Vozmozhnost' izmeneniya individual'nogo biologicheskogo vremeni slabymi elektromagnitnymi izlucheniyami [Ability to change of individual biological time by low electromagnetic radiations]. *Proc. V Int. Congress "Weak and super-weak fields and radiations in biology and medicine"* (29.6-3.7.09), St.-Petersburg, Russian State Hydrometeorological University Publ., 2009, p. 41-47.
  32. Congress Website "Weak and super-weak fields and radiations in biology and medicine", St.-Petersburg, Russia: <http://www.biophys.ru/congress-2015>.
  33. Zaritskii AR, Zaitseva GV, Grachev VI, Kirichenko MN. Elektricheskoe pole v tsitomembrane kak faktor intensivatsii metabolizma kletok [Electric field in the cytoplasmic membrane as factor for improved cell metabolism]. *Radioelektronika. Nanosistemy. Informatsionnye tekhnologii (RENSIT)*, 2016, 8(1):91-103, DOI: 10.17725/rensit.2016.08.91.
  34. Gitai Z. The new bacterial cell biology: moving parts and subcellular architecture. *Cell*, 2005, 120(5):577-586.

## GRAFENIKA [GRAPHENICS] RUSSIAN GUBIN'S SEMINAR (MOSCOW)

Elena Yu. Buslaeva

VNIIAlmaz, <http://www.vniialmaz.ru/>, Ltd. AkKoLab, <http://www.akkolab.ru>

107996 Moscow, Russian Federation

Kurnakov Institute of General and Inorganic Chemistry, Russian Academy of Sciences, <http://www.igic.ras.ru>

117991 Moscow, Russian Federation

[eyubuslaeva@inbox.ru](mailto:eyubuslaeva@inbox.ru)

**Russian Seminar "GRAPHENE: MOLECULE AND CRYSTAL (material, physics, chemistry, electronics, photonics, biomedical applications)"** under the direction of prof. SP Gubin operates from November 2011. Seminar sessions are held once a month, mainly in the boardroom VNIIAlmaz in Gilyarovskogo str., 65 (metro station "Rizhskaya"). The seminar is supported by LLC "AkKoLab" and the VNIIAlmaz. Programms of seminars are available at <http://www.akkolab.ru>. The seminar organizers see it as a discussion platform to discuss new ideas and concepts, review the results and the exchange of experience of researchers in the booming grafenika - an interdisciplinary field of modern science. Anticipated publication of an annual compendium of seminar materials, creating Programs of research in this area with possible access to financing. The seminar was attended by officials from various scientific institutions of Moscow - Kurnakov Institute of General and Inorganic Chemistry RAS, Nesmeyanov Institute of Organoelement Compounds of RAS, Semenov Institute of Chemical Physics RAS, Kotel'nikov Institute of Radio Engineering and Electronics RAS, National Research Centre "Kurchatov Institute", Moscow State University Department of Chemistry, Moscow Institute of Physics and Technology, National Research Nuclear University "MEPhI", People's Friendship University of Russia, LLC "AkKoLab", Open Joint Stock Company (JSC) "VNII ALMAZ", LLC "Karbonlayt", JSC NIIgrafit and others, as well as invited members of scientific institutions in Russia, Commonwealth of Independent States (CIS) and foreign countries. The audience for each session - about fifty participants. In the four- hour meeting with a break heard and discussed the 3-4 reports, news review and submitted poster presentations. The journal RENSIT is published semi-annual reports of this seminar: list of reports indicating affiliated authors and submitted abstracts.

PACS: 01.10 Fv

*RENSIT*, 2016, 8(2): 223-224

DOI: 10.17725/rensit.2016.08.223

### 25th SEMINAR, 13.10.2016

1. Svintsov DA (PhD Phys&Math), V'yurkov VV, Ryzhii VI, T.Otsuji. (MIPT, FTIRAN, Tohoku Univ., Sendai, Japan). **PROMISING DEVICES FOR NANO - AND OPTOELECTRONICS BASED ON GRAPHENE HETEROSTRUCTURES.**

The unique electronic properties of graphene and optical properties of layered semiconductors can be successfully combined into a new composite materials called van der Waals heterostructures. The report will provide an overview of the devices, nano - and optoelectronics on the basis of heterostructures: as a functioning and planned for implementation. Special attention will be paid to devices based on resonant tunneling: tunneling transistors, cascade - infrared photo-detectors and sources of terahertz radiation.

The report will show how "relativistic" spectrum of charge carriers in graphene can dramatically improve the performance of devices based on graphene structures are compared with counterparts based on compounds III-V semiconductors.

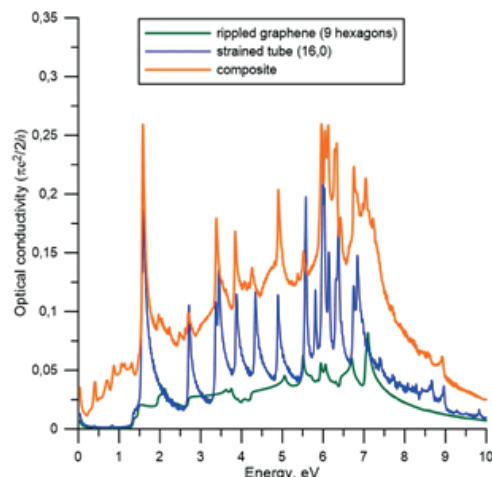
2. Amirov RKh, Isakaev EK, Shavelkina MB (PhD Tech) (JIHT RAS). **DIRECT SYNTHESIS OF HYDROGENATED GRAPHENE IN THERMAL PLASMA.**

Shown the possibility of direct synthesis of hydrogenated graphene materials in plazmotrona reactor. The materials obtained in the free state by decomposition of hydrocarbons with the plasma torch constant current at a pressure close to atmospheric. Elemental analysis, scanning electron microscopy, spectroscopy Raman scattering and

x-ray photoelectron spectroscopy showed that the synthesized samples present molar ratio of hydrogen relative to carbon of 1:4. When heated samples is the release of hydrogen, as illustrated by thermogravimetry in an inert gas atmosphere.

### 3. Glukhova OE (Dr Sci Phys&Math, Saratov Univ.) HYBRID 2D/3D NANOCOMPOSITES BASED ON GRAPHENE WITH A POSITION OF APPLICATION IN OPTO - AND EMISSION ELECTRONICS.

The optical and electronic properties of 2D graphene hybrid nanocomposite-nanotubok material and a new topological form 3D porous glass-like carbon material formed by graphene flakes and fullerenelike fragments. Methods modeling was performed by the molecular mechanical method and the quantum method AIREBO SCC DFTB2. Static study conducted using the software package DFTB+ (<http://www.dftb-plus.info>), dynamic - with the domestic open source KVAZAR (<http://nanokvazar.ru>). Installed the thermodynamically stable form of 2D graphene-nanotubok composite structural components which are the nanotubes of type (n,0) located between the two monolayers of graphene and related covalent (n=10, 12, 14,16, 18, 20). The calculated band structure showed that the composite has a conductivity characteristic of metals (like graphene). The exception is the topological model of composite with tubes (10,0), the conductivity of which is of a semiconductor character with a gap in conditioning the structure of 0.08-0.1 eV, depending on the step of distancing tubes. Calculated the complex optical conductivity, dielectric permittivity showed that the 2D graphene-nanotubki the composite is a very high quality filter and a polarizer, in comparison with graphene and separate the individual nanotubes (see figure). It was also found that in the UV and optical range of the composite is almost not reflected (reflection is less than 0.2 % for H-waves), and the absorption reaches 8-9 %, which makes the composite promising in the development of optical nanoantenna and solar cells.



For other graphene nanocomposite - porous glass-like carbon 3D material identified ways to control the emission properties. Established ways of filling the pores with atoms of alkali metals, the maximum concentration of these atoms reduces the work function by 1 eV or more. Identified as critical oxygen concentration, increasing the work function by more than 0.5 eV. All studies were performed on atomistic material models, built as a result of heating and compressing a porous mixture of graphene flakes and deformed fullerene fragments.

### 26th SEMINAR, 15.12.2016

1. **Kuznetsova IE** (Dr Sci Phys&Math, prof RAS, IRE RAS). **HIGHLY SENSITIVE ACOUSTOELECTRIC SENSOR OF HUMIDITY WITH A LAYER OF GRAPHENE OXIDE.**

2. **Chervonoborodov SP** (PhD Phys&Math) **THE MESSAGE ABOUT THE ROUND TABLE AT THE INTERNATIONAL CONGRESS "RENEWABLE ENERGY XXI CENTURY: ENERGY AND ECONOMIC EFFICIENCY."** SKOLKOVO, 13 -14 OCT 2016. "CAN CARBON MATERIALS (GRAPHENE-BASED) IS FUNDAMENTALLY CHANGING THE ENERGY OF ANY ELECTROCHEMICAL DEVICES?"

3. **D'yachkova TP** (PhD Chem, Tambov GTU). **PHYSICO-CHEMICAL ASPECTS OF FUNCTIONALIZATION AND MODIFICATION OF CARBON NANOMATERIALS.**

Radioelectronics. Nanosystems. Information Technologies (abbr. RENSIT)

Certificate El. no. FS77-60275 on 19.12.2014 of the Ministry of Telecom and Mass Communications of Russian Federation, Moscow  
ISSN: 2414-1267online. [Http://www.rensit.ru](http://www.rensit.ru). Publisher - Vladimir I. Grachev. 2016, 30 December.

Computer printing, page-proofs, graphics, photos of work - the editors RENSIT